Designing a Giant Stress Impedance (GSI) Strain Sensor for Monitoring Intermediate Level Nuclear Waste (ILW) Packages

Patrick Yu Chen Pan

Supervisor: Dr Thomas Hayward and Prof Claire Corkhill
Industrial Supervisor: Dr Gary Bolton

A report submitted in partial fulfilment of the requirements for the degree of Doctor of Philosophy

Faculty of Engineering
Department of Materials Science and Engineering
The University of Sheffield
July 30, 2023

Abstract

In this thesis the practicality and viability of a giant stress impedance (GSI) sensor was studied on three amorphous magnetic ribbons. The GMI effect between the three amorphous magnetic ribbons was investigated, initially, to understand the influence of the GMI behaviour between materials of varying magnetic properties, especially the different chemical structure and, their respective, magnetostriction coefficients (a variable that describes a magnetic material's magnetoelastic properties) (λ_S); $Co_{66}Si_{15}B_{14}Fe_4Ni_1$ ($\lambda_S = < 1\times10^{-6}$), $Fe_{81}Si_{13.5}B_{13}C_2$ ($\lambda_S = 30\times10^{-6}$) and $Ni_{40}Fe_{40}Si+B_{19}Mo_{1\text{-}2}$ ($\lambda_S = 8\times10^{-6}$).

Initial characterisation of the GMI effect was difficult due to the dimensions of the samples being larger compared to previous studies investigating the GMI effect of their studied samples. It used a trial-and-error approach to improve the characterisation technique to the point it could repeatably measure a consistent GMI response of the samples. The characterisation technique for measuring the GSI effect followed a similar procedure but with little time remaining it was incomplete to achieve the desired reliability.

The influence of the geometry, λ_S and fabrication process of the samples on their GMI behaviour was explored. It was observed that the Co-rich sample had a higher GMI response compared to Fe- and Ni-rich ribbon samples. This was related to the difference in domain structures where a negative (near

zero) λ_S domain structure promotes transverse permeability (μ_T), thus having a higher GMI response. A critical aspect ratio (l/w = 20) was observed for all three samples where at the critical aspect ratio all samples exhibited their highest GMI response. In addition, it was observed the GMI response of the three samples would be impeded by the presence of permanent damages (such as plastic deformation) caused by the fabrication process. The varying GMI behaviour between the ribbon samples was discussed using the competing effects between the shape anisotropy and demagnetisation factors, influencing the ribbon sample's transverse permeability (μ_T).

The suitability of using the GSI effect to detect the expansion of intermediate-level nuclear waste (ILW) packages was investigated by applying stress/strain on the sensing material directly. The influence of the magnetostriction coefficients (λ_S) to the GSI effect of the three samples displayed similar responses to their GMI behaviours; where the Co-rich ribbon sample exhibited the highest magnitude in GSI ratio compared to the Fe- and Ni-rich ribbon samples. This implies the lower the magnetoelastic effects the higher GSI response. Although, the data suggests a more complicated interaction between the transverse permeability (μ_T) to the shape and stress anisotropies (magnetoelastic effects). The GSI performance between all three samples was explored at stresses/ strains up to 400 MPa/ 10×10^{-3} at frequencies between 0.1 – 10 MHz.

Finally, the demonstration of the feasibility of the selected material (Co-rich) as a strain sensor on monitoring globally expanding ILW nuclear waste packages was investigated. Simulating the strains that were comparable to a globally expanding ILW waste package (referenced from Sellafield Ltd) the strain sensor observed a clear noticeable trend when undergoing strain at 0.4 Ω decrease at 0.25% strain. This demonstrated a proof-of-concept of using a GSI strain sensor to monitor the expansion of a nuclear waste package

using the change in the stress impedance of the sensor – where high and low impedance values signify the early and late stages of the waste package expansion. This is under the assumption the sensor will be used to monitor the waste package within an approximate time period of a decade.

The experimental results and the existing literature on using the GSI effect for strain sensing applications suggest the technology is applicable for structural health monitoring for detecting very small changes of strain that are not (typically) noticeable by the naked eye. This is possible from their high sensitivity to detecting minor external changes in the material, which includes minor changes of strain. In addition, it is possible to adjust the strain-sensing capability of the material by either adjusting its magnetic or mechanical properties, such as heat treatments or Young's modulus. As a result, this is considered a viable solution for the current application of monitoring the expansion of intermediate-level nuclear waste (ILW) packages since it has been reported by the staff at Sellafield, the expansion becomes noticeable after decades of observation [1].

Acknowledgement

Firstly, I would like to thank my family, my father, mother and little brother for always supporting me throughout my PhD – especially during the pandemic where they would always find the time to visit me all the way to Sheffield when I was by myself. I would like to give a special thanks to my talented little brother for helping me in some of the heavy loading when dealing with a large set of data.

Secondly, I am extremely grateful and appreciative to my incredible supervisor Dr Thomas Hayward for his guidance, critical remarks and patience for my slow uptake on the subject. I have learned from his scientific meticulousness on how to critically think and observe the results in literature (as well as my own results) and I hope to use this experience in my future career. I would like to deeply thank Dr Thomas Hayward for always providing aid whenever possible, giving me a sense of security and confidence that he would always be available whenever I am facing difficulty. I wish him great fortune and success in his career and hope to stay in contact in the future.

I would also like thank my other supervisor Dr Claire Corkhill and Dr Gary Bolton for the providing the materials and knowledge, at the initial stages of the project, which greatly helped me understand on the subject of nuclear waste and the procedures regarding to it. I have learned immensely from the subject of the nuclear waste industry and will hope to make use

of this newfound knowledge in my future career. I am extremely grateful for my industrial supervisor Dr Gary Bolton for his provided network and knowledge on the nuclear waste industry and the annual discussions between me, Gary and Tom. In addition, I would like to thank the Senior Technology Manager, Operation Technical, John Jowsey at Sellafield Ltd for providing the information in regards to the expanding ILW nuclear waste packages. Without his input the project would have not reached at the current stage so I am extremely thankful for him finding the time to provide the information in regards to the expanding ILW waste packages with me and Tom. Finally, I would like to thank Dr Robert Moorehead for using his time to analyse the surface topography of my samples. It was thanks to his contributions that my first paper was published to the Journal of Applied Physics!

The project was financed by the Nuclear Decommissioning Authority (NDA) and supported by the National Nuclear Laboratory (NNL) which I am forever grateful. I am thankful for the chance to work on this PhD project and be working alongside many other PhD students in a similar position as me. I am appreciative of the financial support for my attendance to multiple conferences for both Nuclear Waste and Magnetism where I can meet many other academics and learn from the knowledge they can provide. I am indebted to them for providing extra funds during the pandemic enabling the PhD project to have reached this current stage and the financial security for completing the writing of this thesis.

These three to four years in Sheffield have been the most exciting and one of my greatest achievements yet, in my life. I will definitely reflect back to these days fondly and treasure the experiences and lessons learned during those times. Though it felt like I was alone in my PhD journey it quickly dissipated thanks to the members of the Functional Magnetic Materials (FMM) group for their friendly spirit, support, knowledge and keen insight. In all

honesty, some of the topics discussed in this thesis came from their insight and knowledge so I am very grateful for their support (big or small, it all made some contribution!). Moreover, I am grateful of the new friendships that I have forged over the years in the Sheffield Anime Society for which granted me an enjoyable university student life in Sheffield. Joining in the society gave me a great stress-relief to distract myself from my research and provided a sense of comfort.

Finally, I hope that this research will benefit somebody else who is also following down a similar research path or that somebody can continue this project where the sensor technology for the intended application can come to fruition. As for me, I will definitely take these experiences from the past few years and use them to contribute humanity for the far future – no matter how vast or minuscule those contributions would be!

Previously published works

Previously published papers were used as chapters for this thesis. All author names are sorted in alphabetical order.

- Influence of geometry on the giant magnetoimpedance of high-aspect ratio amorphous magnetic ribbons. Patrick Pan, Robert D. Moorehead, and Thomas J. Hayward. Journal of Applied Physics (JAP 2020).
- Comparative study of the giant stress impedance behavior of commercial amorphous ribbons for strain sensing applications. Patrick Pan and Thomas J. Hayward. Journal of Applied Physics (JAP 2022).

Nomenclature

ILW	Intermediate level (nuclear) waste
GDF	Geological Disposal Facility
GF	Gauge Factor
GMI	Giant magnetoimpedance
GSI	Giant stress impedance
λ	Magnetostriction coefficient (ppm)
λ_S	Saturation Magnetostriction (ppm)
$\boldsymbol{K_\sigma}$	Magnetoelastic anisotropy
$\boldsymbol{K_U}$	Magnetocrystalline anisotropy constant
$\boldsymbol{H}$	Applied (external) field
$\boldsymbol{H_C}$	Coercivity or Coercive field
$\boldsymbol{H_K}$	Anisotropy field
$\boldsymbol{H_W}$	Weiss Field
$\boldsymbol{M}$	Magnetisation

$\boldsymbol{M_S}$	Magnetisation Saturation
χ	Magnetic suscpetiblity
μ	Magnetic permeability
μ_0	Permeability of free space
μ_r	Relative magnetic permeability
μ_T	Transverse permeability
μ_ϕ	Circumferential permeability
μ^{dw}	Domain wall contribution to magnetic permeability
μ^{rot}	Magnetisation rotation contribution to magnetic permeability
E_{ex}	Exchange energy
A	Exchange Stiffness
E_K	Magnetocrystalline anisotropy energy
E_M	Magnetostatic energy
E_Z	Zeeman energy
E_{ME}	Magnetoelastic anisitropy energy
E_T	Total magnetic energy
E	Young's Modulus (GPa)
σ_{dw}	Surface energy of a domain wall
σ	Tensile mechanical stress (MPa)

ϵ	Tensile mechanical strain
AC	Alternating current
DC	Direct current
Z	Complex impedance
Z_{P}	Parasitic impedance
Z(H)	Impedance with respect to applied field H
δ_{m}	Classical skin depth of conductor
S/DLEC	Single/Double longitudinal edge cuts

Contents

Chapter 1

Introduction

The safe storage of nuclear waste is an important and ongoing issue. There is substantial waste that is now labelled as "legacy waste" [2] due to the continuous accumulation of the generated nuclear waste since the mid-1900s. In the early stages of generating nuclear energy, there was little to no regard to managing the generated waste which has created substantial problems for future generations to resolve [2]. The combination of negligible waste management and the accumulation of legacy waste has caused increasing concern for the safety of the environment and human health from any potential leaks. The Energy Act 2004 was the UK's response to properly manage and minimise any potential dangers caused by the accumulated legacy waste [2].

The majority of nuclear wastes are generated from nuclear power plants which generate power via the splitting of the Uranium-235 (^{235}U) isotope atoms after the impact of a slow neutron (n):

$$^{235}_{92}\mathrm{U} + {}^{1}_{0}\mathrm{n} \longrightarrow \mathrm{A} + \mathrm{B} + x{}^{1}_{0}\mathrm{n} + 200\mathrm{MeV}. \qquad [2]$$

This reaction is self-sustaining because of the generated neutrons x from

the splitting of the initial ^{235}U atom, that can be used to split further (^{235}U) atoms (also called a chain reaction). The splitting process of the (^{235}U) atom releases energy in the form of heat which heats up the water to steam that turns the turbines to produce electricity. However, during this process the (^{235}U) atom splits into two smaller atoms (labelled as A + B for simplicity in the equation above) which are unstable and radioactive, these are the unwanted products that are considered nuclear waste. The waste is typically categorised into three categories; low (LLW), intermediate (ILW), and high-level (HLW) nuclear waste [3].

The categorisation between the three levels differs between the regulatory body of each nation but typically is based on the concentration of radionuclides and half-life of the nuclear waste. Each category represents the amount of radioactivity (radioactivity includes: High energy Alpha (α), Beta (β), and neutron (n) particles and Gamma (γ) waves [4]) present in the nuclear waste and the level of attention required for the disposal of each waste package. HLW waste packages are the most radioactive requiring extreme caution and care to monitor (and dispose of) because of the high concentrations of radionuclides present in the waste. In addition, the high concentration of radionuclides gives rise to radiogenic self-heating – the wasteform heats up from the high radioactivity – thus extreme caution is required when interacting with HLW waste packages, which includes: shielding, personnel protection, remote handling and countermeasures of the generated heat (typically the temperature at the core of waste can go as high as 100°C [5]). However, these wastes occupy very little volume (of space) of the total waste produced (as in 2019 it was measured that HLW waste only occupies 0.03% of the total volume [6]) so it is easier to manage the HLW waste packages due to their small package size. ILW waste packages have lower radioactivity than HLW waste packages but still require special considerations, such as shielding, remote handling, and personnel protection. On the other hand, they are safer

to handle since the heat generated from ILW waste packages is low enough not to harm the surrounding environment (the surface of ILW waste packages is the same as room temperature [1]). Although, the volume the waste occupies is around (as of 2019) 5.4% which is orders of magnitudes higher than the HLW waste [6]. Typically, a single ILW waste package unit can contain up to ∼400 L (∼0.4 m^3) worth of nuclear waste [1]. Hence, there is a higher concern about handling and monitoring the large volume of ILW waste because of the (potential) damage that radioactive waste can cause. LLW waste packages are (relatively) the safest to handle without requiring special precautions since the low concentration of radionuclides generates little heat and has low/ negligible radioactivity [2], [6].

Since the Energy Act in 2004, there has been a massive research activity on both short- and long-term plans for monitoring, storing, and disposing of nuclear waste whilst creating the minimum impact on the environment and human health for future generations. Specifically, this has focused on ILW and HLW nuclear wastes based on their influence to the surrounding environment from their radioactivity and half-life (which can last up to 100,000 years or more [2]). Currently, the long-term plan is to dispose of ILW and HLW nuclear waste into geological disposal facilities (GDF) but this is dependent on the surrounding rock type that will be hosting the facility. This requires careful consideration to ensure the GDF can securely store the ILW and HLW nuclear waste without causing potential leaks from the containers to impact the surrounding environment outside the GDF. As a result, the GDF is still in the design stages with a time span of decades until being developed. Therefore, short-term solutions are required to monitor, store and dispose of any legacy waste packages that have reached their "limit" (global strains of up to 40%) which could potentially endanger the surrounding environment. Currently, waste packages reaching their "limit" are closely monitored at "interim storages" (a licensed and highly secured location) where all waste packages

– planned for disposal – are remotely monitored, periodically.

At present, the nuclear industry monitors the ILW nuclear waste packages visually. This is achieved by physically moving individual waste packages (using a crane) to an isolated chamber where all observations of the nuclear waste package are conducted from afar. Any defects, such as localised or global expansions, are identified using sight alone, and this can be difficult to achieve, as is illustrated in the photo of an ILW canister in Fig. 1.1(a). The designs of the ILW nuclear waste packages are in accordance with a strict set of guidelines that ensure that the nuclear waste they contain will not be leaked. Overall, the process of monitoring every ILW waste package requires a huge time investment since the total number of ILW waste package units is around (as of 2021) 126,000 units – which contributes to 71% of the total fraction of total waste package units for all waste groups [7]. In addition, the risk of maneuvering each waste package to an isolated chamber introduces potential accidents and hazards, such as a waste leakage from dropping the waste package during moving. Therefore, to mitigate these unnecessary risks there is massive research in regards to the safety of storing, monitoring, and disposing of ILW waste packages due to its influence on the surrounding environment by radioactive waste leakage if handled poorly. Most of the research on ILW waste packages has a major point of interest to find a more effective solution to monitor the evolution progress for a large number of waste packages until a GDF is developed.

Information regarding to the design and time evolution of ILW waste packages are rarely reported, and without this information, it is difficult to simulate their swelling to assess alternative monitoring strategies. To address this, a staff member from Sellafield Ltd, John Jowsey (Senior Technology Manager, Operation Technical, Sellafield Ltd), was contacted as a source of information about ILW nuclear waste packages, including:

1. The dimensions of an ILW nuclear waste package and its shape.
2. The specific chemical reaction that causes global and local expansion of the ILW nuclear waste packages.
3. The evolutionary progress of the ILW nuclear waste packages over time.
4. The point at which an ILW nuclear waste package would be considered to have expanded to a concerning degree.

The following summarises the information obtained from these discussions.

A schematic sketch of a typical ILW waste package is shown in Fig. 1.1(b). ILW nuclear waste packages are typically made out of a stainless-steel drum with a diameter of 800 mm and a total height of 1166 mm. They are designed with two sections: the main body for containing the nuclear waste and the lid which prevents the nuclear waste from expanding outwards. The main body (shaded in grey) consists of an 800 mm diameter cylinder with a height of 868mm which connects to a bottle-neck shape of an inclined angle, with a neck (shaded in blue) height of 148 mm preventing global or localised expansion occurring near the lid of the waste package. The ILW nuclear waste packages are sealed off with a circular lid of a diameter of 738 mm [1].

ILW nuclear waste consists of metallic waste encapsulated by wet cement (typically Portland Cement) which then solidifies and effectively immobilises the metallic waste. The metallic waste consists of steels, graphite, concrete, cement and sand, sludges, ion exchange resins, and flocculants. In addition, items and equipment used for nuclear fission such as fuel cladding and reactor components are included as metallic waste [6]. Both the contaminants and the metallic waste both react with the water of the cement and produce corrosion products as well as hydrogen gas [2], [8]. The corrosion products

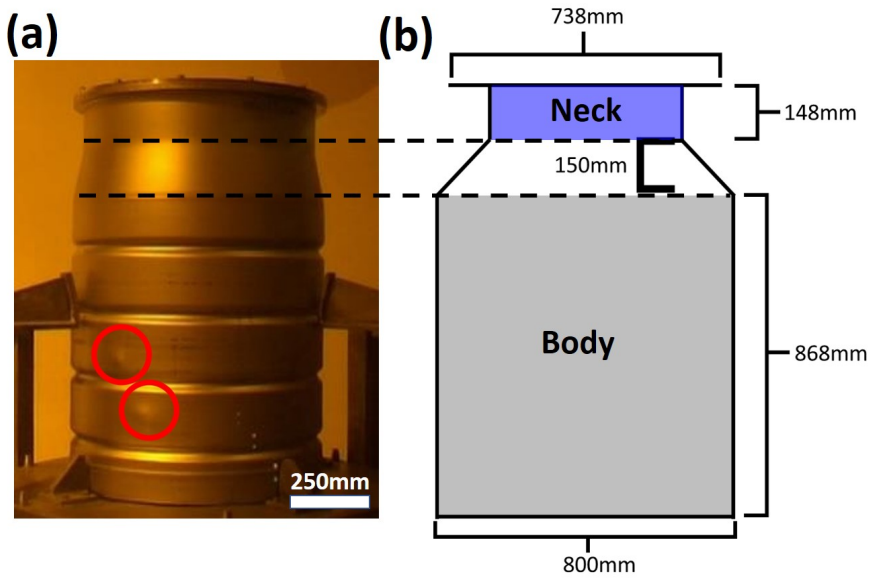

Figure 1.1: Comparison between (a) on-site photo of an ILW waste package with localised expansion (highlighted in red) and (b) schematic sketch on the dimensions and design of the same waste package. The dotted lines are a visual guide to approximate the sections of the body and neck between the schematic and photo of an ILW waste package.

occupy more volume than the initial material which causes the global and local expansion deformation to occur on the ILW nuclear waste package. Local expansions are protrusions that appear on the surface of the waste package (Fig. 1.2(a)) with a displacement of, approximately, 2 mm whereas global expansions occur when the diameter of the waste package expands with a change of 2 mm (Fig. 1.2(b)) [1]. There have been observations of both global and localised expansions that occur on the ILW waste package where the visible deformation on the waste package is located at the bottom third of the waste package. Although, John Jowsey has mentioned that the majority of the waste package will undergo global expansion at some point -

based on the past decade he (and the staff at Sellafield Ltd) have monitored them [1].

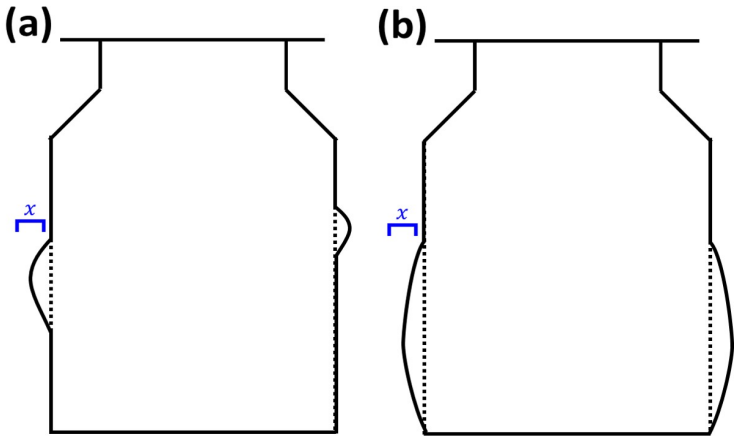

Figure 1.2: Schematic sketch of (a) localised expansion and (b) global expansion of waste package of displacement x. The dotted line highlights the original dimensions of the waste package. Sketches of deformation are highly exaggerated to visually show the difference.

The creation of corrosion products and an increase in the pressure of hydrogen gas is the source of the expansion of the waste packages. This causes concern for their mechanical stability, especially as the accumulating pressure of hydrogen gas could potentially leak out causing a fire hazard. To avoid this hazard the staff at Sellafield Ltd provided a guideline where any waste package reaching 40% strain needs to be disposed of, but there has not been any waste package that has reached that value. John Jowsey explained that from his (and other Sellafield Ltd staff) observations the rate of localised and global expansion is very slow. He provided a rough calculation – based on visual estimations of the size of the expansion to the time the waste package was created – and concluded the rate of change the ILW waste package undergoes; a change in diameter of about 2mm and/or a change in height

of about 2.1mm, every decade. Hence, resulting in strains of roughly 0.25% and 0.24% of the waste package walls over this period [1]. This indicates the global expansion of the ILW nuclear waste packages is slow and does not cause any short-term harm, but an accurate measurement of the rate of expansion is still required to ensure any new ILW waste packages that are formed can be monitored with an educated approximation when it reaches its limit of 40% strain. Furthermore, there is little information on the expansion evolution of these ILW waste packages as time scales up to (potentially) centuries. Hence, it is important to find an accurate and sustainable monitoring method to properly grasp the behaviour of the expanding ILW waste packages before any unforeseen circumstances have happened. This is especially the case where it will be easier to monitor large numbers of waste packages and accurately record the rate of expansion for each of them.

Therefore, particular properties that are required for a sensor technology when monitoring ILW waste packages will need to have:

- Instantaneous response when expansion occurs.
- Exhibit a noticeable change in signal when under strains up to (minimum) 0.25%.
- Flexible enough to be applied on a curved surface of an ILW waste package.
- Easy to obtain the technology for mass production in order to monitor thousands of waste packages.
- Can cover a large surface area on the waste package body.

The details of the criteria are discussed later in the thesis.

In this thesis, we propose using a magnetic strain sensor as a solution to monitor the swelling of ILW waste packages. Magnetic sensors have been studied extensively in recent decades based on their wide applicability and high performance in measuring magnetic effects. Examples of sensing technologies include: induction sensors [9, 10, 11, 12], fluxgate sensors [13, 14, 15, 16], Hall-effect magnetic sensors [17, 18, 19, 20, 21], magneto-optical sensors [22, 23, 24, 25], giant magnetoresistive (GMR) sensors [26, 27, 28, 29], resonance magnetometers [30, 31, 32], superconducting quantum interface devices (SQUID) gradiometers [33, 34, 35, 36, 37], giant magnetoimpedance (GMI) sensors [38, 39, 40, 41, 42] and giant stress impedance (GSI) sensors [43, 44, 45]. Fundamentally, a magnetic sensor converts a magnetic field into a voltage or change of resistance under (generally) a DC current supply, with the field sensitivity having a key role in determining its operating regime and key applications [46].

In recent decades the research on flexible magnetic strain sensors had an increasing interest due to their flexible and sensitive detection capabilities. This is especially so for magnetostrictive sensors (such as GMR, GMI, and GSI, etc.) due to their very high gauge factors (GF >100) when detecting strains as small as 0.25%. These metrics show promise for their applications for monitoring nuclear waste packages. Here, it is proposed the magnetic sensor will use the GSI effect to monitor the changes in strain. Initially, the design for the magnetic sensor was to be a ribbon-shaped material that wrapped around the whole waste package (Fig. 1.3(a)), thus allowing monitoring of its whole surface area. However, this was considered inefficient and cost-intensive since the size of a single waste package was 800 mm in diameter and 868 mm in height [1] and requires complete coverage of the waste package surface to ensure the whole package can be monitored. An alternative approach would be to design the sensor material to a size that covers the area of interest and monitor the expansion (Fig. 1.3(b)).

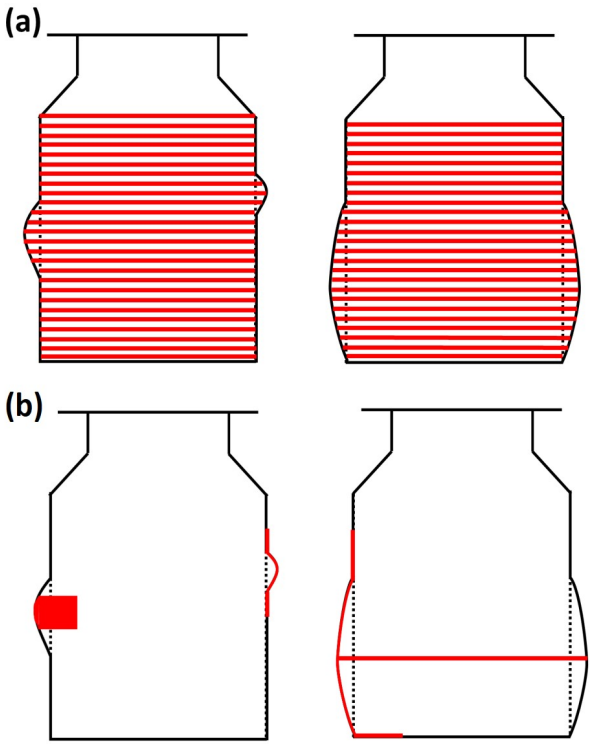

Figure 1.3: Schematic sketch of applying the sensor (in red) on the waste package using (a) the initial method of wrapping around the whole canister and (b) the alternative method of designing the sensor for a specific size that covers the area of interest for both expansion deformations. The size of the red line is a visual guide and not to scale.

Although it is sensible to use ribbon pieces to cover the areas of interest to monitor the rate of expansion it raises an important question on the influence the geometry of the ribbon sensor has on the material's GSI behaviour. This is one of the research topics that was investigated in this study as there was a lack of knowledge on the relation between the aspect ratio to the GSI effect, but the GSI effect has close parallels to the GMI effect. Therefore, any behaviours observed by the GMI effect with changing aspect ratio would have

a similar result to the GSI effect [43, 47, 48]. Considering the bottom third of the waste package initially undergoes expansion the sensor needs to be at (a maximum) length of either 300 mm (1/3 of the waste package body height) or 800 mm (diameter of the waste package) to monitor any expansions that occur. Hence, for a sensor with a width of 10 mm, the aspect ratio (l/w) can range between 30 to 80 (and possibly higher if a smaller width was used). This is considered very large compared to typically studied ribbons where they are studied at aspect ratios around 20 or lower [49, 48]. This showed a gap in the research on the GMI and GSI behaviour of the size and aspect ratio of an amorphous ribbon with lengths over 200 mm and 20, respectively. This was closely studied, in this thesis, since the size (and shape) of the strain sensor has a large impact on the sensing performance of the GSI strain sensor.

Furthermore, the thesis also investigates other variables that influence the GMI and GSI performance, which include the chemical structure, geometry, and stress/strain. Both GMI and GSI effects were investigated for all ribbon samples in the study since the literature on the GSI effect is not as extensive compared to the GMI effect. The influence of chemical composition was studied by exploring GMI effects in three different ferromagnetic amorphous metals (which were obtained commercially from GoodFellow) with each having a higher concentration of one of the ferromagnetic elements than the other (cobalt, iron, and nickel). This gave insight to the role of the magnetostriction coefficient (λ_S) on both the GMI and GSI effects. The effects of geometry were conducted on the same three amorphous ribbon samples, with the ribbon samples having different aspect ratios (ranging between 2 to 150). This touches on the influence of shape anisotropy and demagnetizing field effects on GMI behaviour. The relation between the GMI and GSI performances to mechanical strain was also investigated. The three amorphous ribbon samples were comparatively studied in order to identify which material had the best GSI sensing performance for strains up to 10×10^{-3}. Moreover,

observations on the GMI and GSI behaviour to the mechanical strain identified a complex underlying behaviour between the three amorphous samples. The complex underlying behaviour was discussed which revolved around the magnetoelastic anisotropy ($\boldsymbol{K}_\sigma$), the magnetostriction coefficient (λ_S), and the anisotropy field ($\boldsymbol{H}_K$) [50].

The observed results provided crucial insight when designing an amorphous ribbon GSI strain sensor with optimal sensing capabilities when monitoring ILW waste packages (including other similar-sized applications). These findings were then used to model the ability of an amorphous magnetic ribbon sensor to detect changes in expansion of ILW waste packages, as a proof-of-concept. The sample that performed the best in GMI and GSI response was selected to be tested as a prototype strain sensor to detect strains of up to 0.25% (and potentially higher). In addition, if the material was capable of emitting two distinct signals that represent the two extreme states of the waste package; no expansion (absence of strain) and expansion (under strain). This was analysed using signal-to-noise ratio (SNR) analysis.

This thesis is organised as follows: chapter 2 describes the basic theory of magnetism and discusses the difference between diamagnetic, paramagnetic, and ferromagnetic behaviour along with the four magnetic energies: exchange energy, magnetocrystalline anisotropy, magnetostatic energy, and the Zeeman energy. The chapter also discusses the different magnetic properties of hard and soft magnetic materials. Chapter 3 presents a literature review on the state-of-the-art flexible strain sensors and their suitability for monitoring ILW waste packages followed by basic theory of the GMI and GSI effect. Chapter 4 will present the experimental methodology and characterisation techniques used to characterise samples in this thesis. Chapter 5 will discuss the challenges and obstacles of developing an experimental methodology that allowed accurate, precise, and reliable measurements of GMI and

GSI effects in macro-scale ribbons. Chapters 6 and 7 then discuss the fundamental GMI and GSI behaviours of the three amorphous ribbons, and how these respond to various variables. More specifically, chapter 6 investigates the influence of the ribbon sample's chemical anatomy (which involves their crystal structure and magnetic properties) and aspect ratio on their GMI behaviours, while chapter 7 investigates the ribbons' responses to stress and strain. Chapter 8 presents the proof-of-concept of a magnetic ribbon sensor technology that is capable of detecting changes in an applied strain that would be expected were a ribbon sensor mounted to the surface of an ILW waste package.

Finally, chapter 9 will present the conclusions of the thesis and summarises the major findings from the results presented in this study. This will be followed by a brief discussion of the outlook for creating a usable sensor device for the proposed application.

Chapter 2

Basic Theory of Magnetism

2.1 Outline

The chapter provides an introduction to the basic theory of magnetism at a variety of length scales, spanning the atomic length scale, which is defined by quantum mechanical interactions between electron spins, up to macroscale length scales which are defined by the collective behaviours of magnetic moments.

The chapter first covers the different types of magnetism: diamagnetism, paramagnetism, and ferromagnetism. It then proceeds to a more detailed description of ferromagnetism based on four magnetic energy terms: the exchange, magnetocrystalline anisotropy, magnetostatic, and Zeeman energies. Each of these magnetic energies is discussed in detail to provide insight into the complex interplay between all four energies that define magnetic behaviour. Lastly, the chapter discusses the differences between hard and soft magnets and the physical origins of these.

2.2 Origins of Magnetism

Magnetism is a physical phenomenon of attractive and repulsive forces between moving electrical charges, mediated via a magnetic field ($\boldsymbol{H}$). A magnetic field is a vector field that describes the magnitude and direction of the magnetic forces on a magnetic body with the definition: "A unit of field strength (Oe) is one which exerts a force of 1 dyne (1×10^{-5} N) on a unit pole (unit pole is where one magnetic body exerts 1 dyne of force on another magnetic body at a distance of 1 cm)" [51]. Therefore, a magnetic body with two poles in a magnetic field is subjected to a magnetic force with motion or rotation if the field is non-uniform or uniform, respectively.

2.2.1 The relationship between magnetization, magnetic field, and magnetic moment

A "magnet" typically refers to any physical entity that is magnetized when subjected to an external magnetic field ($\boldsymbol{H}$). As such, a physical entity that is magnetized responds to the direction and strength of a magnetic field and will preferentially align itself parallel to the field. The magnitude of the torque describes the magnetic strength of the physical entity and is labelled as the magnetic dipole moment ($\boldsymbol{m}$). It is easier to visualise the interaction by replacing the magnetic body with a bar magnet since a bar magnet is defined to be always magnetized. A bar magnet typically has a dipole (a north and south pole) where each pole has a finite pole strength (p) and both interact with the magnetic field with equal and opposite forces. This creates a couple on the magnetic body by producing a net moment of pure rotation with no resultant force (Fig. 2.1).

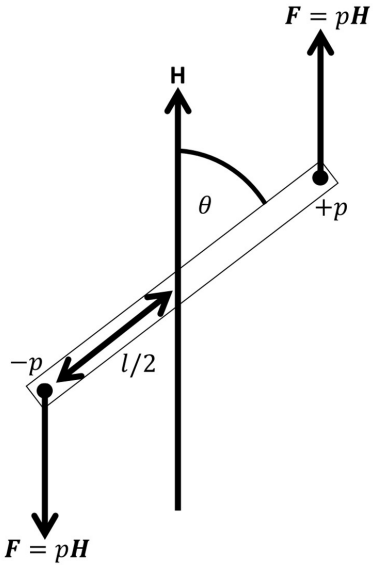

Figure 2.1: Schematic diagram on the calculation of a magnetic dipole moment on a bar magnet under an applied magnetic field [51]

.

A couple is a pair of equally in magnitude and oppositely directed forces (F) times the total perpendicular distance (l) of the rotating object with the pair of forces is the product of the magnetic field strength ($\boldsymbol{H}$) and the pole strength (p), as shown in Fig. 2.1). Therefore, the torque on the magnetic body can be expressed as:

$$\tau = pl\boldsymbol{H}\sin\theta = \mu_0 \boldsymbol{m}\boldsymbol{H}\sin\theta. \tag{2.1}$$

The magnetic dipole moment ($\boldsymbol{m}$) is defined as the moment of the couple exerted on a magnetic body when it is perpendicular to a uniform field of 1 Oe. Therefore, the product of the pole strength (p) and the length of the magnetic body (l) defines $\boldsymbol{m}$. The total energy (E) required to rotate a magnetic dipole moment from orthogonal alignment to an angle (θ) to the

applied field is expressed as:

$$\begin{aligned} E &= \int_{\pi/2}^{\theta} \mu_0 \boldsymbol{m}\boldsymbol{H} \sin\theta \, d\theta \\ &= -\mu_0 \boldsymbol{m}\boldsymbol{H} \cos\theta = -\mu_0 \boldsymbol{m} \cdot \boldsymbol{H}. \end{aligned} \tag{2.2}$$

All magnetic bodies exhibit a magnetic moment when under a magnetic field. At the atomic scale each atom has a magnetic dipole moment that depends on its electron configuration due to quantization of the orbital angular momentum (l), magnetic quantum number (m_l), and spin (m_s) of each electron. (l) and m_l both describe the magnitude and orientation of the angular momentum of electrons orbiting around the nucleus whereas m_s describes the electron spin orientation. The orbital motion of the electron behaves like a circulating electric current which generates a magnetic field generating a magnetic moment (called an orbital moment) and this is coupled with the magnetic moment of the electron as a result from its own spin, via spin-orbit coupling. The spin-orbit varies in strength depending on the size of the atom. For lighter atoms (with an atomic number of $Z < 30$) the spin-orbit coupling is weak and thus the total angular momentum is best calculated by considering the total spin angular momentum ($\boldsymbol{S}$) of all electrons and the total orbital angular momentum ($\boldsymbol{L}$) of all electrons – this is known as the $\boldsymbol{LS}$ coupling. However, in heavier atoms the spin-orbit coupling of the electrons is stronger so the total angular momentum is best modelled via the sum of the individual total angular momentum of each electron ($\sum_i \boldsymbol{j}_i$) – this is labelled as jj coupling. As a result, spin-orbit coupling determines the total angular momentum of all the electrons in an atom which influences the overall magnetic moment of the atom. The spin-orbit coupling is also the fundamental origin of magnetocrystalline anisotropy (section 2.4.2) [51].

Calculating an atoms total angular momentum, and thus the net mag-

netic moment requires knowledge of how valence electrons occupy the subshell orbitals (m_l). This follows Hund's rules, which describes the lowest energetically favoured electron configuration in an atom.

Hund's first rule states that the electron populate states so as to maximise their total spin, thus each orbital is occupied by a single electron with all electrons spinning parallel to each other until all orbitals contain one electron. When a half-filled shell is achieved and there are leftover electrons to fill the remaining space each electron is then forced to "pair up" with another electron, with its spin being the opposite to its neighbour, occupied in the same orbital, this follows Pauli's exclusion principle in which to prevent two pairs of electrons having the same quantum state the spin of the two electrons are anti-parallel to each other.

Hund's second rule states that for a given spin arrangement of the electrons, the total atomic orbital angular momentum must be at its highest. This is to reduce the overall energy of the repulsion between electrons from the coulomb force. This is achieved with the electrons orbiting in the same direction since (on average) the distance between the electrons instead of orbiting in opposite directions. In the latter case, the (average) distance between orbiting electrons is smaller so increases the overall coulomb force which adds potential energy to the electrons, thus increasing the overall energy.

The third rule, states when the electron configuration of the atom has less than a half-full shell, the lowest total angular momentum is energetically favourable. When the configuration is over a half-full shell, the highest total angular momentum is energetically favourable. This is related to the spin-orbit coupling where the orientation of the spin and orbit of adjacent electrons become either parallel or anti-parallel based on the number of electrons filling the shell. The combination of these three rules defines the ground state of

the atom in which the combination of paired and unpaired electrons as well as their arrangement in the orbitals affects the electron exchange interaction determining the atom's magnetic behaviour. Simply put, an atom with totally filled orbitals of paired electrons has no total magnetic moment giving rise to diamagnetic behaviour whereas half-filled orbitals with unpaired electrons does have a resultant total magnetic moment. This could give rise to either paramagnetic, ferromagnetic, ferrimagnetic, or anti-ferromagnetic behaviours depending on the strength of the exchange energy (each magnetic behaviour will be discussed in section 2.3).

At the macroscale (typically over tens of nm) a material's magnetic behaviour is generated on the net magnetic moment from its collective atoms. Therefore, a new parameter, magnetization ($\boldsymbol{M}$) is defined. The magnetization of a bulk material can be considered as the magnetic "density" of the material, which can be expressed as

$$\boldsymbol{M} = \frac{\boldsymbol{m}}{V} \tag{2.3}$$

where $\boldsymbol{m}$ is the magnetic dipole moment and V is the material's volume with units, emu/cm^3.

To characterise the magnetic behaviour of different materials one can plot the magnetization ($\boldsymbol{M}$) of the material as a function of the applied field ($\boldsymbol{H}$). The curve observed then identifies the type of magnetic behaviours a material exhibits (e.g. diamagnetic, paramagnetic, and ferromagnetic) (Fig. 2.2).

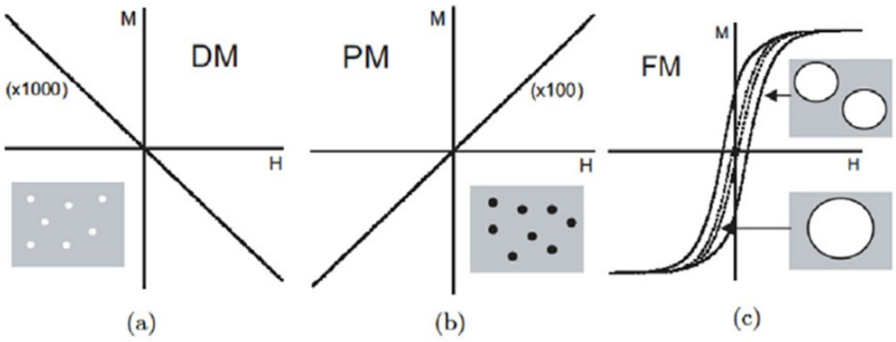

Figure 2.2: Magnetization curves of (a) diamagnetic, (b) paramagnetic, and (c) ferromagnetic beads. The data was from the study done by Pankhurst et al. (2003) [52] where these figures are only used to identify the different magnetization ($\boldsymbol{M}$) responses between diamagnetic, paramagnetic, and ferromagnetic materials with respect to field ($\boldsymbol{H}$). A magnetization response from diamagnetism and paramagnetism are smaller by (x1000) and (x100), respectively, compared to ferromagnetism.

The response of a medium to applied field ($\boldsymbol{H}$) is described by the magnetic induction ($\boldsymbol{B}$), measured in Gauss (G). $\boldsymbol{B}$ increases proportionally to the combination of applied field ($\boldsymbol{H}$) and magnetization of a ferromagnetic material ($\boldsymbol{M}$), expressed in Eq. 2.4

$$\boldsymbol{B} = \boldsymbol{H} + 4\pi\boldsymbol{M}. \tag{2.4}$$

In SI units the equation is expressed as $\boldsymbol{B} = \mu_0(\boldsymbol{H} + \boldsymbol{M})$ where μ_0 is the magnetic permeability of free space (in a vacuum). The value of μ_0 is 1 - dimensionless in centimetre-gram-second (cgs) units - or $4\pi \times 10^{-7}$ H/m (Henry per metre) in SI units.

If there is an applied field with no ferromagnetic material present then

the magnetization ($\boldsymbol{M}$) is zero, thus the magnetic induction ($\boldsymbol{B}$) is linearly proportional to $\mu_0\boldsymbol{H}$. Thus, in free space, the ratio between B and H is the magnetic permeability of free space (μ_0) but, other than free space the ratio between $\boldsymbol{B}$ and $\boldsymbol{H}$ is μ (magnetic permeability). Therefore, μ describes how magnetic a medium is by its magnetic flux density ($\boldsymbol{B}$) when under a magnetic field ($\boldsymbol{H}$). The higher the value the more magnetic the medium is.

Another quantity that can analyse the magnetisation behaviour of a magnetic material under a changing field is its magnetic susceptibility (χ). The magnetic susceptibility is the ratio of $\boldsymbol{M}$ and $\boldsymbol{H}$ expressed as

$$\chi = \frac{\boldsymbol{M}}{\boldsymbol{H}}, \tag{2.5}$$

measured in emu/Oe·cm^3.

The susceptibility indicates how responsive a material is when applied under a magnetic field, i.e. materials with higher susceptibility exhibit larger values of $\boldsymbol{M}$ for the same value of $\boldsymbol{H}$. Using Eq. 2.5 to substitute in Eq. 2.4 provides a linear relationship between relative permeability and susceptibility (χ), expressed as

$$\mu = 1 + 4\pi\chi, \tag{2.6}$$

in which the $1 + 4\pi\chi$ equates to the ratio of the material's magnetic permeability (μ). In SI units, the equation for permeability (μ) is $\mu_0(1 + \chi)$ thus relative permeability will be expressed as $\mu_r = \mu/\mu_0$

2.3 Type of Magnetism

Understanding the relationship between the magnetic moment, magnetization, and magnetic field relative to free space can identify the various magnetic behaviours in materials. These magnetic behaviours include: diamagnetism, paramagnetism, ferrimagnetism, ferromagnetism, and anti-ferromagnetism. In this section, simple models to explain diamagnetic, paramagnetic, and ferromagnetic phenomena will be discussed.

2.3.1 Diamagnetism

Diamagnetism is a quantum mechanical effect where applying a magnetic field ($\boldsymbol{H}$) induces a magnetisation that is opposite to the field (i.e., a positive field produces a negative magnetisation and vice-versa). This opposing nature of the magnetisation is a consequence of Lenz's law in which the magnetic field induces a change in the current (of a neutral conductor) and the direction of the induced current always goes in the direction to oppose the change. This applies to many atoms with totally filled orbitals of electron pairs because of their electron orbital motion. Paired electrons have no total magnetic moment, but the electrons still orbit around the nucleus which can be considered a current loop. As a result, when applying a magnetic field to a current loop, it induces a change in the current which creates an electromotive force to oppose the change. The electromotive force is linearly proportional to the applied field strength and its nature to oppose the direction of the change in current from the magnetic field results in a magnetisation that behaves opposite to the direction of the field (as seen in Fig. 2.2(a)). This effect is very weak so the magnetic permeability of these materials is, typically, very low, $\mu < 1$.

Using Langevin theory of diamagnetism, the change in the magnetic moment, from the diamagnetic effect, for a single atom, can be expressed as:

$$\Delta \boldsymbol{m} = -\frac{e^2 r^2 \mu_0}{4 m_e} \boldsymbol{H} \tag{2.7}$$

where e is the charge of the electron, r^2 is the "average value of the square of the projection of r onto the field direction" [53] (which reduces the effective magnetic moment by a factor of 2/3), and m_e is the mass of the electron.

If multiple electrons, in a single atom, contribute to the diamagnetic effect the change in the magnetic moment is then,

$$\Delta \boldsymbol{m} = -\frac{Z e^2 \langle r^2 \rangle_{av} \mu_0}{6 m_e} \boldsymbol{H} \tag{2.8}$$

where Z is the number of electrons in the atom and $\langle r^2 \rangle_{av}$ is the average value of the mean square distance (of all electrons) from the nucleus. The bulk magnetization of the material can be calculated by multiplying the number of atoms per unit volume, N, to Eq. 2.8 ($N = N_A \rho / A$, where N_A is the Avogadro's number, ρ is the density of a unit cell, and A is the atomic weight). Therefore, the diamagnetic susceptibility for a bulk material can be expressed as:

$$\Delta m = -\frac{N Z e^2 \mu_0}{6 m_e} \langle r^2 \rangle_{av} \tag{2.9}$$

The Langevin theory qualitatively models the susceptibility response of the diamagnetic effect in materials and shows it being independent of any influences of temperature [54].

This type of magnetism is present in all materials, but it gets overshad-

owed by stronger interactions such as paramagnetism and ferromagnetism due to unpaired electrons in the orbitals in those materials where atoms carry magnetic moments. Generally, this type of magnetism is observed in materials that have no net magnetic moment where the atoms have a full shell configuration. Examples include monoatomic rare gases (He, Ne, Ar, etc.), polyatomic gases (O_2, N_2, etc.), ionic solids like NaCl, and covalently bonded molecules. As such, the response from the diamagnetic effect is typically small with the relative susceptibility being at magnitudes of $\chi = -10^{-5}$ (per unit volume) range (e.g. Bismuth has a susceptibility of -16.6×10^{-5}).

2.3.2 Paramagnetism

Paramagnetism is one of the magnetic behaviours with a net magnetic moment – from the spin of unpaired electrons. As a result, when a magnetic field is applied, the magnetic moments will start to align to the field with only a fraction of them aligning parallel to the field with the remainder showing a weaker response to the field. Only at higher magnetic fields is the paramagnetic material fully magnetised with all magnetic moments aligning parallel to the field. This weak interaction between applied field and magnetic moments is associated to the weakly coupling of the magnetic moments (this is related to its exchange interaction which is discussed in section 2.4.1). The weak coupling of magnetic moments means in the absence of a magnetic field the magnetic moments are randomly oriented due to the thermal energy overcoming the weak exchange interaction. In the presence of a magnetic field, there is competition between applied field and thermal energy which explains the fraction of magnetic moments aligning parallel to the field with the remainder weakly rotating to the field (Fig. 2.3).

The material can reach full magnetization when the field strength over-

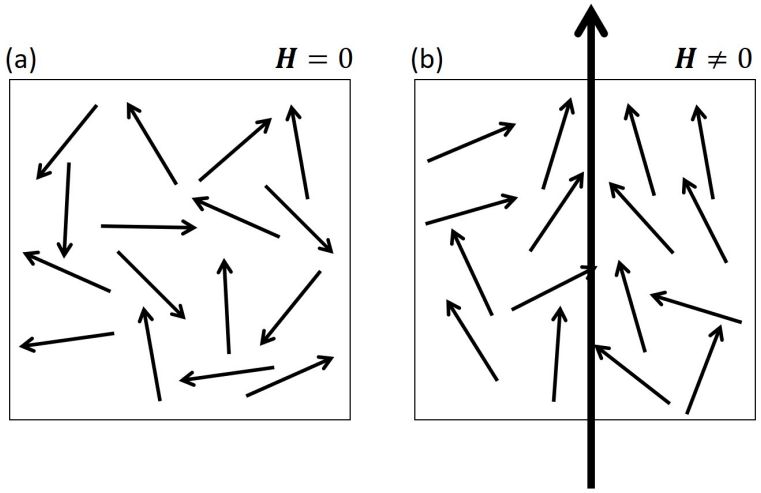

Figure 2.3: Schematic diagram of the behaviour of a paramagnetic material when (a) no field is applied and (b) when field is applied. The arrows indicate the direction of the magnetic moments of the atoms in the material. In an absence of field, the alignment of the magnetic moments are randomly disordered from the thermal energy of the environment. Under an applied field, the magnetic moments are partially attracted to the field but some are still disordered from the thermal energy [51].

comes the thermal energy or if the environmental temperature around the material is very low, i.e. near 0 K. On the other hand, when the temperature is high the increase in thermal energy overcomes the magnetic moment's weak coupling and all magnetic moments are randomly orientated unless magnetized by a magnetic field. The Langevin localized-moment model assumes the atomic magnetic moments are not interacting with each other and are randomly orientated by the thermal energy. Thus, the model assumes for a unit volume of atomic magnetic moments a fraction of these moments will align to the magnetic field (as shown in Fig. 2.3(b)).

Under these conditions the magnetization of a paramagnetic material can

be expressed as:

$$\boldsymbol{M} = NmL(\alpha) \tag{2.10}$$

where $\alpha = m\boldsymbol{H}/k_BT$, and $L(\alpha)$ is the Langevin function which represents the fraction of magnetic moments aligned to the field. $\boldsymbol{M}$ depends on α, where the higher α is (e.g. by increasing the applied field or decreasing the temperature) the more magnetically saturated the paramagnetic material becomes, as shown in Fig. 2.4.

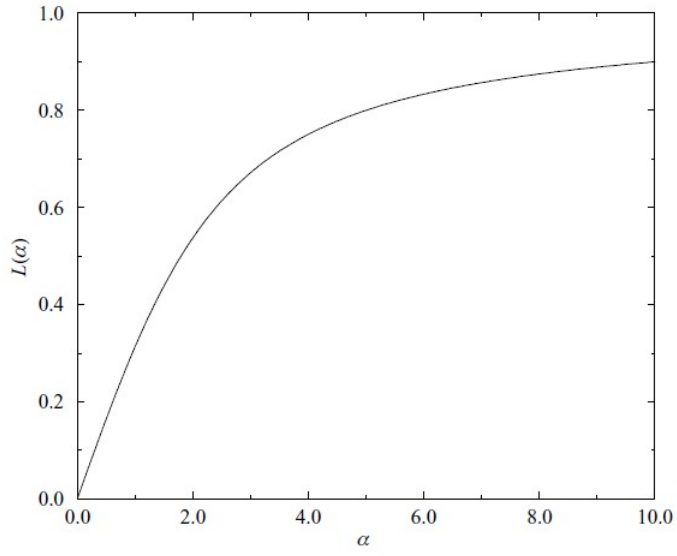

Figure 2.4: Graph plotting the Langevin function, $L(\alpha)$, with respect to the value of α [51].

The Langevin theory of paramagnetism shows the susceptibility of paramagnetic materials to be inversely proportional to temperature, $\chi = C/T$ – which is Curie's law, where C is the Curie constant ($Nm_{eff}^2/(3k_B)$, where m_{eff}^2 is the effective magnetic moment and k_B is the Boltzmann constant).

However, not all paramagnetic materials obey this law since at a low enough temperature some materials can exhibit ferromagnetic properties [55]. In such materials one can adopt Weiss molecular field theory which assumes a hypothetical magnetic field ($\boldsymbol{H}_W$) (representing the material's internal magnetic field generated by the electron interaction) exists in the material, and allows a generalised theory of paramagnetic materials was created. The magnitude of $\boldsymbol{H}_W$ is assumed to be proportional to the material's magnetization with via molecular field constant, γ. Thus, the total magnetic field on a magnetic material would be

$$\boldsymbol{H}_{total} = \boldsymbol{H} + \boldsymbol{H}_w = \boldsymbol{H} + \gamma \boldsymbol{M} \tag{2.11}$$

and, the susceptibility of this material would be

$$\chi = \frac{\boldsymbol{M}}{\boldsymbol{H} + \gamma \boldsymbol{M}} \tag{2.12}$$

where a simultaneous equation between Eq. 2.12 and Curie's Law, provides the Curie-Weiss law (Eq. 2.13) where $C_\gamma = T_C$,

$$\chi = \frac{C}{T - T_C} \tag{2.13}$$

where T_C is the Curie temperature of the material, and T is the absolute temperature of the material. Therefore, the Curie-Weiss law shows when $T < T_C$ the material behaves ferromagnetically, with spontaneous ordering, and when $T > T_C$ the material behaves like a paramagnet where it has no spontaneous ordering.

The Langevin theory of paramagnetism and the Curie-Weiss law provides

the magnetization of an ideal paramagnet which describes the paramagnetic behaviour of materials that have a net magnetic moment due to incomplete outer shells of localized unpaired electrons. However, it neglects the quantum effects present within the material in regards to quantisation of angular momentum. Instead, the theory assumes the magnetic moments can point in any direction on a 3D sphere which quantisation doesn't allow. As such the model cannot predict the paramagnetic behaviour at very low temperatures or at high fields regimes – both regimes represent the full alignment of the magnetic moments.

Furthermore, such a theory cannot be applied to transition and rare-earth metals since the valence electrons in these materials are delocalised. Here, the mechanism for susceptibility is dominated by the valence electrons and these metals are called Pauli paramagnets. The behaviours of these materials can be described using the band theory (or collective-electron theory) which describes how the energy levels for electrons change when isolated atoms are brought together into a crystal lattice. For an isolated atom the electrons are configurated by discrete energy levels at their respective orbitals. However, as multiple atoms bond together and form crystal lattices (where the interatomic distance, d, decreases to d_0) multiple discrete energy levels are formed which functions as a continuous band of allowed energy levels for each subshell (Fig. 2.5), with the highest energy level at T = 0 K being the Fermi level, E_F.

The broadness of these bands is based on the number of overlapping electrons in the same orbital. This broadness increases at higher energy levels because the number of electrons that can fill one orbital is much higher compared to lower energy levels closer to the nucleus. This is a consequence of Pauli's exclusion principle. Thus, in a crystal lattice, multiple electrons that can occupy the same orbital have varying energy levels to prevent having

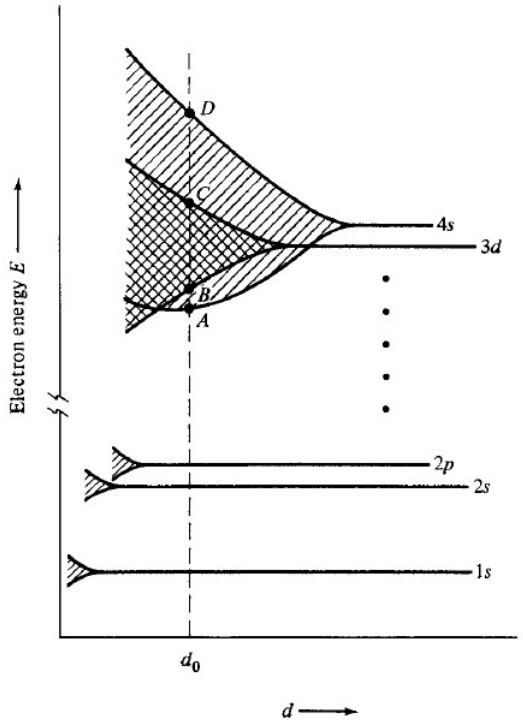

Figure 2.5: Schematic diagram illustrating the splitting of electron energy levels as the interatomic distance (d) decreases. d_0 is the closest distance between atoms [53].

identical wavefunctions. For transition metals the broadness between the 3d and 4s subshell greatly overlap since the 4s subshell is the furthest away from the nucleus, illustrated in Fig. 2.5. The result of this overlap enables valence electrons to occupy the 3d-4s bands interchangeably as "free moving electrons" (which are referred as a "sea of electrons"). For transition metals, the partial filling of the 3d-4s subshell defines where E_F lies in between the continuous band of allowed energies which can be quantified by the density of states (DOS), which describes the number of electron energy levels of a given energy range (in this case the Fermi level). The DOS, at the Fermi level, represents the lowest energy levels for all up- and down-spin electrons

of a given crystalline material with a net magnetic moment and this describes the evolution of magnetic behaviour when in absence of a magnetic field and under a magnetic field.

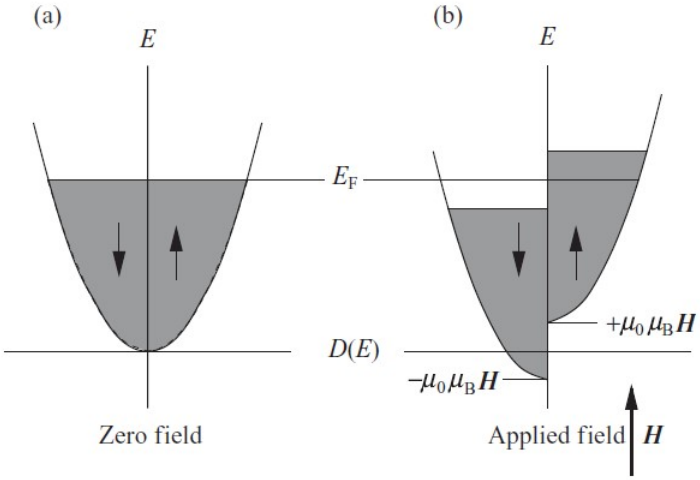

Figure 2.6: Schematic diagram illustrating the density of states (DOS) between (a) absence of field and (b) presence of field. In an absence of field, the DOS are in equilibrium with an equal number of states with opposite spins. When a field is applied the spin states that are parallel to the field increase in energy (repulsion) and the down spin states decrease in energy (attraction) [51].

In the absence of applied field both up- and down-spins have the same energy (Fig. 2.6(a)) due to the weak exchange interaction between magnetic moments. However, when a field is applied a Zeeman-splitting occurs, where the energy of the up- and down-spin energy states is unbalanced, with spins that align parallel to the direction of the field having a lower energy and spins antiparallel to the field will have a higher energy. The splitting is caused by increasing the exchange interaction between the magnetic moments from the Zeeman energy (discussed in section 2.4.4). Quantitatively, this splitting

is given by, of $\pm\mu_0\mu_B\boldsymbol{H}$ (where $\mu_B = m\boldsymbol{H}cos\theta$ or a Bohr magneton) (Fig. 2.6(b)). This shift of energy provides a net magnetization for the paramagnet as valence electrons (that have energies close or at E_F) switch spin states to be parallel to the magnetic field. This net magnetization (magnetic moment per unit volume) can be expressed as:

$$\boldsymbol{M} = \frac{\mu_0\mu_B^2\boldsymbol{H}}{V}D(E_F) \tag{2.14}$$

where D(E_F) is the DOS of electrons at the Fermi level, thus the susceptibility of a Pauli paramagnet is [51],

$$\chi = \frac{\mu_0\mu_B^2}{V}D(E_F). \tag{2.15}$$

The susceptibility of paramagnetic materials is generally between the order of 10^{-5} to 10^{-3} because only a small fraction of magnetic moments are aligned to the applied magnetic field. Eq. 2.15 shows that, unlike in Langevin theory, the susceptibilities of Pauli paramagnets are independent of temperature since the effects of thermal energy only excite valence electrons to higher (vacant) energy levels but this can apply to both up- and down spin electrons.

2.3.3 Ferromagnetism

For all of the materials discussed so far, the magnetisation is zero in the absence of an applied field. However, ferromagnetic materials exhibit a spontaneous magnetisation even when no field is applied. In metallic ferromagnetic materials this can be understand using band theory in a similar way to a Pauli paramagnet, with the major difference that in ferromagnetic materials there is an inherent imbalance between the energies of up and down spins

even in absence of an applied field ($\boldsymbol{H}$). This behaviour indicates a stronger interaction between electron spins – the exchange interaction – compared to a paramagnet and the imbalance of energy density of up and down spins is described as exchange-splitting.

Classically, a ferromagnet can be considered as a paramagnet with a larger internal molecular field. Thus, a ferromagnet exhibits strong interactions between the atomic magnetic moments that can resist thermal energy, producing spontaneous ordering. This can be understood using the Weiss molecular field theory ($\boldsymbol{H}_W = \gamma \boldsymbol{M}$) and Langevin theory of paramagnetism, illustrated in Fig. 2.7.

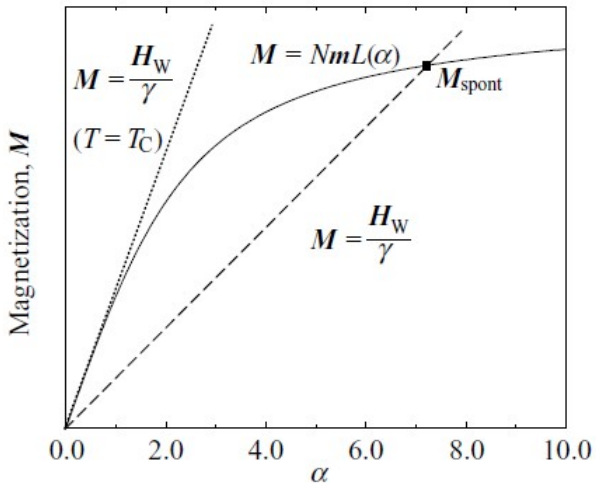

Figure 2.7: Graph plotting the Weiss field ($\boldsymbol{H}_W = \gamma \boldsymbol{M}$) using the Langevin function, $L(\alpha)$, as the limit and γ representing the temperature (T) of the ferromagnet material ($= T_C/C$). At low temperatures, the two functions intersect to represent spontaneous magnetization and when the temperature reaches the Curie temperature (T_C) the two functions are tangential to each other which represents behaving as a paramagnet [51].

The intersection between the lines defined by Langevin theory and the definition of the Weiss molecular field (away from the origin) represents the physical solution of spontaneous magnetization for a ferromagnetic material at a given temperature. This is based on the theory the magnetization of a ferromagnetic material with its own internal molecular field ($\boldsymbol{H}_W$) is the same magnetization observed in paramagnetic materials with an applied field ($\boldsymbol{H}$). The Langevin function represents the limits of the ferromagnetic behaviour with respect to temperature thus as temperature increases to the point where the gradient of α becomes tangential to the Langevin function where no real solutions are found. At this point, the temperature has reached the Curie temperature (T_C) where the ferromagnet behaves as a paramagnet with thermal energy randomly orientating the atomic magnetic moments (seen in Fig. 2.3(a)). Although the Weiss molecular field and the Langevin theory of localized moments are able to describe the general magnetic behaviour of ferromagnetic materials and its dependence on temperature, it is unable to identify the mechanism that differentiates ferromagnetic and paramagnetic behaviour. The understanding of the difference between ferromagnetism and paramagnetism can be generally explained using the collective-electron theory.

As mentioned in section 2.3.2, transition metals have overlapping 3d and 4s subshells, and the configuration of the valence electrons, in the overlapping subshells, determines the transition metal having either a paramagnetic or ferromagnetic behaviour. This difference depends on the energy of the electrons and the fermi level (E_f) for each transition metal. This can be visualised by plotting the density of states (DOS) to energy (E) between the 3d and 4s subshell as shown in 2.8.

Fig. 2.8 illustrates the DOS between the 4s and 3d subshells for both up- and down-spin electrons. The 4s subshell displays a symmetrical energy

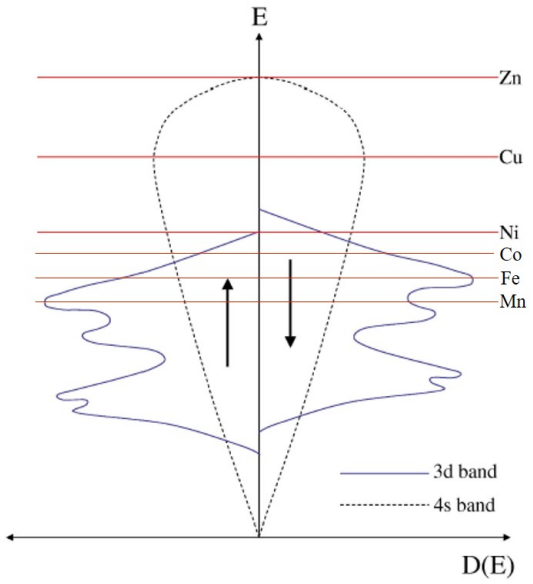

Figure 2.8: Schematic diagram on the splitting of DOS between 3d and 4s bands in transition metal. The existence of an intermolecular field causes splitting of the 3d bands more than the 4s band which creates net magnetization for the transition metal. This figure was adapted from [56] with information from [51].

level between both spins whereas the 3d subshells have an asymmetrical energy level between both spins. The asymmetry can be associated with the exchange interaction (detailed physics of the exchange interaction will be discussed in the following section) a consequence of the internal molecular (Weiss) field – thus described as exchange-splitting. Therefore, a ferromagnet's DOS with no applied field is similar to that of a Pauli paramagnet with an applied field (Fig. 2.6(b)). The exchange-splitting of the DOS enables a net magnetization for transition metals, but it is dependent on the metal's E_F level; the closer it lies to the exchange energy ($+\mu_0\mu_B \boldsymbol{H}_W$) the more likely it is that an electron can reverse its spin to align parallel to the field

($\boldsymbol{H}_W$).

The reason the exchange-splitting is prominent in the 3d subshell instead of the 4s subshell is the difference in the energy gaps between their available orbitals. Despite the 4s subshell having one orbital – two electrons – whilst the 3d subshell has five orbitals – ten electrons – the band energy of the 4s subshell is much higher than the 3d subshell, at the fermi level. Therefore, the energy cost to reverse the spin of an electron in the 4s subshell is higher compared to an electron in the 3d subshell. This model can be used to explain the different magnetic behaviour between Copper (Cu) and Nickel (Ni). The E_f level for Cu lies above the 3d band (meaning it has fully filled 3d subshell) thus there are no exchange interactions within the 3d subshell and despite having a half-filled 4s subshell, the exchange-splitting is not as prominent, so no exchange interaction occurs. Whereas the E_f level for Ni is within the 3d band (meaning a partially filled 3d subshell) thus it has electrons that can (spontaneously) reverse its spin which promotes exchange interaction and exchange-splitting to occur. However, this does not apply to all transition metals that have an E_f level lying in the 3d band, such as Manganese (Mn). Despite, Mn having a partially filled 3d subshell it is still paramagnetic (at room temperature) because it has a lower exchange energy (compared to Iron) which is insufficient to promote parallel spin of neighbouring atoms. Therefore, the prerequisite for a ferromagnetic behaviour is to have a partially filled 3d subshell with an electron configuration that has a strong exchange interaction – thus having the exchange energy – to promote parallel spin of neighbouring atoms.

Iron (Fe), Cobalt (Co), and Nickel (Ni) are the only three transition metals that are ferromagnetic since they "naturally" achieve the conditions, with a high exchange energy to promote spontaneous ordering and a net magnetization in the absence of a field. As a result, the susceptibility of

ferromagnetic materials is very high that can reach up to values around $\chi = 10^4$ [56] and because ferromagnetic have spontaneous ordering in an absence of a field, their interaction under an applied field leads to their unique hysteresis loops (unlike paramagnets and diamagnets). These interactions under an applied field are discussed in section 2.4.

2.4 Magnetic energies in ferromagnets

The magnetic behaviours of ferromagnetic, ferrimagnetic and antiferromagnetic materials are the result of magnetic energy terms which work in competition to minimise the total free energy (E_T) of the material. These competing mechanisms can be understood via four magnetic energy terms, the exchange energy (E_{ex}), the magnetocrystalline anisotropy energy (E_K), the magnetostatic energy (E_M), and the Zeeman energy (E_Z).

2.4.1 Exchange energy

Ferromagnetic materials behave differently from paramagnetic and diamagnetic materials because of the exchange energy from the exchange interaction between electrons. The exchange interaction is a quantum mechanical effect and fundamentally electrostatic in origin and can be parametrised by the exchange integral/constant (J_{ex}). Electrons exhibit either positive or negative exchange constants depending on whether they favour ferromagnetic or antiferromagnetic spin alignment [53].

The phenomenon was understood, in 1928, when Heisenberg tried to understand the stability of a hydrogen (H_2) molecule. A hydrogen atom simply consists of a proton (as a nucleus) and one electron so when two hydrogen atoms are within a particular distance to each other both atoms are

electrostatically repelled due to the same charges – i.e., both electrons and protons repel each other. Although, when sharing the same electron (covalently bonded) the electrostatic force of repulsion is overridden and becomes an attractive force instead. This is a consequence of the Pauli exclusion principle where two electrons can only occupy the same energy state when both have the opposite spins. This attractive force gives rise to the stability of the hydrogen molecule which originates from the electrons "exchanging" with each other. The "exchange" arises from the consideration that electrons are indistinguishable from each other, thus not only electrons 1 and 2 can orbit around protons 1 and 2, respectively, but electron 1 can orbit around proton 2 and vice-versa. This behaviour introduces the exchange energy (E_{ex}) term that creates a favouring of the electron spin orientation – and is part of the total energy of the molecule. For the hydrogen molecule case, the exchange energy between the two electrons is represented as

$$E_{ex} = -2J_{ex}S_iS_j = -2JS_iS_j\cos\phi \tag{2.16}$$

where J_{ex} is the exchange integral, J is the exchange coupling constant, S_iS_j is the spin angular momentum of atoms i and j, and $\cos\phi$ is the angle between the spins of the electrons sharing the same energy state. Eq. 2.16 calculates the exchange energy between two hydrogen atoms which is the simplest molecule thus calculating the exchange energy of a crystal is very difficult due to the number of electron spin interactions [53].

Nevertheless, the J_{ex} and the E_{ex} provides a general insight on how magnetic materials have spontaneous ordering, such as ferromagnetism, antiferromagnetism and ferrimagnetism. It is understood when J_{ex} is positive with $\cos\phi = 1$ (parallel spins) the exchange energy is at its minimum and if $\cos\phi = -1$ (anti-parallel spins) the exchange energy is at its largest (i.e., fer-

romagnetism). When J_{ex} is negative the lowest exchange energy is when the electron spins are anti-parallel (i.e. antiferromagnetism or ferrimagnetism).

In 1930 John C. Slater proposed the relationship between interatomic distance and exchange integral (J_{ex}) [57]. In 1933, a heuristic explanation was used with the Bethe-Slater curve (Fig. 2.9) [58] showing the ratio of the interatomic distance (r_a) to the radius of the 3d electron shell (r_{3d}) to J_{ex} contributes to metals having either ferromagnetic or anti-ferromagnetic behaviour.

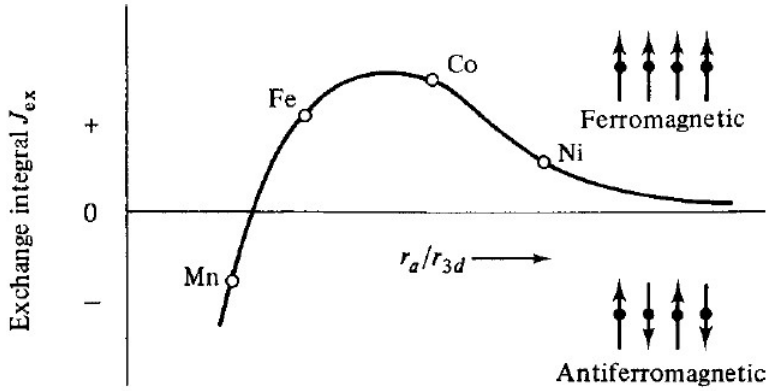

Figure 2.9: Schematic of the Bethe-Slater curve where the ratio of the interatomic distance (r_a) to the radius of the 3d electron shell (r_{3d}) increases the exchange integral (J_{ex}) becomes positive promoting parallel spins of adjacent magnetic moments – thus exhibiting ferromagnetic behaviour [53].

The Bethe-Slater curve correctly separates the transition metals that have ferromagnetic – Fe, Co, and Ni – and antiferromagnetic behaviours – Mn and Cr – using the Heisenberg Hamiltonian model of magnetism. However, a study by Cardias et al. [59] reported the underlying physics of the exchange interaction between neighbouring atoms is more complex with exchange interaction following the Heisenberg model as well as non-Heisenberg. Overall, the Bethe-Slater curve provides convincing evidence the interatomic distance

does have a huge impact on the exchange couple between electrons of neighbouring atoms.

In a crystal lattice, the exchange energy varies depending on the positions between the magnetic moments on the crystal lattice axes. At high exchange energies, a region of magnetic moments would align parallel to the preferred direction which would be resilient to other magnetic interactions, such as resisting an applied field with the direction perpendicular to the preferred direction. This property is described as the exchange stiffness constant (Å) and this constant varies depending on the crystal structure since the exchange interaction is dependent on the atomic distance between neighbours. Therefore, A can be expressed as nJS^2/a (where n is the number of atoms per unit cell, and a is the lattice parameter) [53]. The exchange energy for a crystal lattice can then be expressed as,

$$E_{ex} = A \int_V ((\nabla m_x)^2 + (\nabla m_y)^2 + (\nabla m_z)^2)\, dV \tag{2.17}$$

where $\nabla m_{x/y/z}$ are the components of the magnetic moment ($\boldsymbol{m}$) along the cartesian axes and the integral is over the volume of the material. Eq. 2.17 is used in micromagnetic simulations to understand the exchange behaviour of magnetic materials of varying crystal lattices and to other magnetic energies.

2.4.2 Magnetocrystalline anisotropy energy

The magnetocrystalline anisotropy energy (E_K) is the energy difference per unit volume between the magnetized easy and hard axes in a magnetic material. The energy difference between both axes is a result from a phenomenon known as the magnetocrystalline anisotropy which is the tendency of the

magnetization to align itself along a preferred crystallographic direction [51]. The origin of the magnetocrystalline anisotropy is the coupling of the magnetic moment's to the crystal lattice of the material via spin-orbit coupling [51]. This is observed in magnetization ($M - H$) measurements when the applied field is along the sample's hard axis the hysteresis curve has a shallower gradient with the saturation of magnetization ($\boldsymbol{M}_S$) reached at a higher applied magnetic field ($\boldsymbol{H}$) (Fig. 2.10).

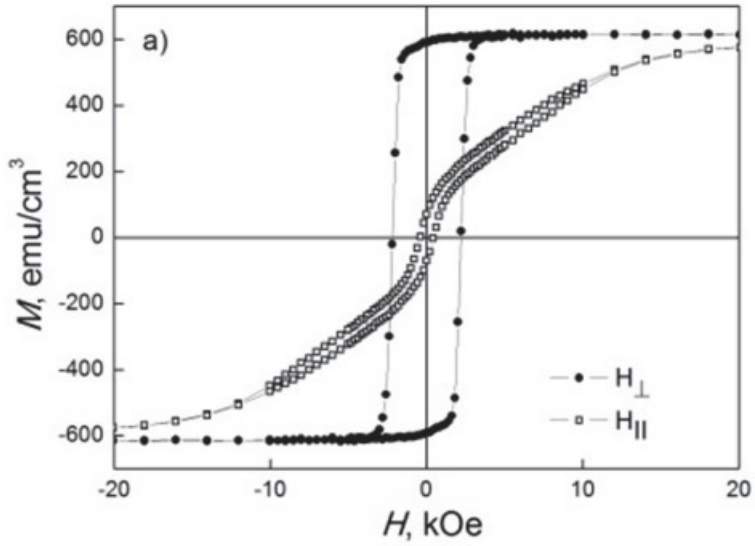

Figure 2.10: Magnetization (M-H) loop measured in perpendicular ($\boldsymbol{H}_\perp$) and parallel ($\boldsymbol{H}_\parallel$) applied field to the sample. The sample measured was a Cobalt/Palladium (Co/Pd) multilayer thin film with a chemical structure of Pd/[$\mathrm{Co}_{0.3\ \mathrm{nm}}$/$\mathrm{Pd}_{0.55\ \mathrm{nm}}$]/Pd [60].

The magnetocrystalline anisotropy energy varies depending on the crystal lattice. For a cubic crystal lattice, the magnetocrystalline anisotropy energy can be expressed in terms of a series expansion of the direction cosines (α_i) of the saturation magnetization ($\boldsymbol{M}_S$) relative to the crystal axes, thus for a

cubic lattice the magnetocrystalline anisotropy can be expressed as

$$\frac{E_K}{V} = K_0 + K_1(\alpha_1^2\alpha_2^2 + \alpha_2^2\alpha_3^2 + \alpha_3^2\alpha_1^2) + K_2(\alpha_1^2\alpha_2^2\alpha_3^2) + ..., \tag{2.18}$$

where K_0, K_1, K_2,... are anisotropy constants (K_i). The first term K_0 is independent of angle and is typically ignored since the main interest is the rotation of axis of the $\boldsymbol{M}_S$ vector relative to the crystal axes. Therefore, K_1 and K_2 are good estimates to the magnetocrystalline anisotropy of the ferromagnetic material relative to its crystal lattice with higher powers not included due to the very small values. This can be seen in Table. 2.1.

$[u\ v\ w]$	α_1	α_2	α_3	E_K/V
[100]	1	0	0	K_0
[110]	$1/\sqrt{2}$	$1/\sqrt{2}$	0	$K_0 + K_1/4$
[111]	$1/\sqrt{3}$	$1/\sqrt{3}$	$1/\sqrt{3}$	$K_0 + K_1/4 + K_2/27$

Table 2.1: An example of increasing magnetocrystalline anisotropy energies (E_K/V) when rotating spin-orbit coupling from the easy axis [100] to other crystallographic directions $[u\ v\ w]$ in a cubic lattice structure in terms of anisotropy constants (K_i). The field is assumed to be applied away from the [100] direction.

Hexagonal and tetragonal lattices typically have uniaxial anisotropy i.e., only a single easy axis along the c-axis of the crystal lattice. As such, the magnetocrystalline anisotropy energy for a hexagonal lattice can be expressed as a function of θ, the angle between the magnetisation vector and the c-axis:

$$\frac{E_K}{V} = K_0 + K_1 \sin^2\theta + K_2 \sin^4\theta + ... \tag{2.19}$$

The direct relationship between the easy and hard axes to the crystal lattice structure is not explicitly clear [53], but it is known that the symmetry of a materials magnetocrystalline anisotropy is always the same as its crystal lattice [51]. For example, a cubic lattice (i.e., body-centred cubic (BCC) and face-centred cubic (FCC) show cubic symmetry. Alternatively, in a crystal lattice with only a single line of symmetry (such as hexagonal close-packed (HCP) lattice) the magnetocrystalline anisotropy only favours a single easy axis. The direction of the easy and hard axes relative to the crystal lattice is dependent on the sign of the anisotropy constants, K_1 and K_2 (Table 2.2).

(a) K_1 ($K_2 = 0$)	Cubic		Hexagonal	
	$+K_1$	$-K_1$	$+K_1$	$-K_1$
Easy	<100>	<111>	[0001]	(0001)
Hard	<111>	<100>	(0001)	[0001]

(b) K_1 ($K_2 \neq 0$)	Cubic			
	$+K_1, +K_2$	$-K_1, -K_2$	$+K_1, -K_2$	$-K_1, +K_1$
Easy	<100>	<111>	<111>	<110>
Hard	<111>	<100>	<110>	<111>

Table 2.2: (a) Crystallographic directions for easy and hard axes for cubic and hexagonal lattices when changing signs of anisotropy constant (K_1) when (top) $K_2 = 0$. (b) Crystallographic directions for easy and hard axes for cubic lattice when signs of K_1 and K_2 change.

Unlike the cubic lattice the K_1 and K_2 constants for a hexagonal crystal lattice have a more complicated behaviour. An example is seen in Table 2.2.a. when K_1 is negative the magnetocrystalline anisotropy favours the easy axis orthogonal to the c-axis which are all crystal directions in the (0001)

plane. Hence, it is considered as an easy plane of magnetization which is the basal plane for the hexagonal lattice. Therefore, when K_2 is non-zero the combination of K_1 and K_2 provide multiple phases of anisotropies present in the hexagonal structure depending if either are positive, negative or opposite signs to each other (Fig. 2.11).

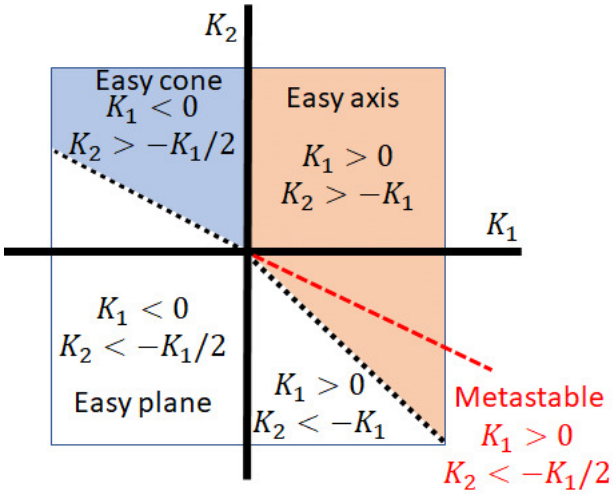

Figure 2.11: Phase diagram of magnetocrystalline anisotropy energy for uniaxial anisotropy crystals. For hexagonal lattice the magnetocrystalline anisotropy of K_1 and K_2 can give rise to three different easy directions: easy axis, easy plane, and easy cone. A metastable phase exists as well and it is when the easy axis and easy plane are in coexistence. The diagram was from the study done by P. Nieves et al. [61].

Table. 2.2. shows the strongest magnetocrystalline anisotropy effect when observed in ferromagnetic materials with a monocrystal structure. However, synthesised ferromagnetic materials are either amorphous or polycrystalline containing multiple grains with different magnetocrystalline anisotropies which weakens the overall anisotropy of the material. It is possible to synthesise polycrystalline ferromagnets with a more uniaxial anisotropy by inducing the

grains to a specific orientation. This can be achieved by various fabrication techniques, such as annealing under an applied magnetic field, to orientate the grains to a specific direction achieving a more uniaxial anisotropy, which improves the magnetocrystalline anisotropy of the material significantly.

Other anisotropies that contribute to the material's magnetic behaviour apart from its magnetocrystalline anisotropy are the shape anisotropy and magnetoelastic effects. Shape anisotropy is a magnetostatic effect that relates to the aspect-ratio of the ferromagnetic material where the magnetization favours the long axis, whereas magnetoelastic effects induce a magnetoelastic anisotropy which involves the magnetostrictive effects of the material, more details are explained in the following section.

with the magnetocrystalline anisotropy is , such as magnetoelastic effects. Shape anisotropy is a magnetostatic effect that relates to the aspect-ratio of the ferromagnetic material where the magnetization favours the long axis, whereas magnetoelastic anisotropy involves the magnetostrictive effects of the material which exhibits localised strains and stresses around the magnetic domains and crystal grains of the material.

2.4.2.i Magnetostriction

Magnetostriction (λ) is a magnetoelastic phenomenon where a ferromagnetic material undergoes tensile or compressive strain when under a magnetic field (Fig. 2.12).

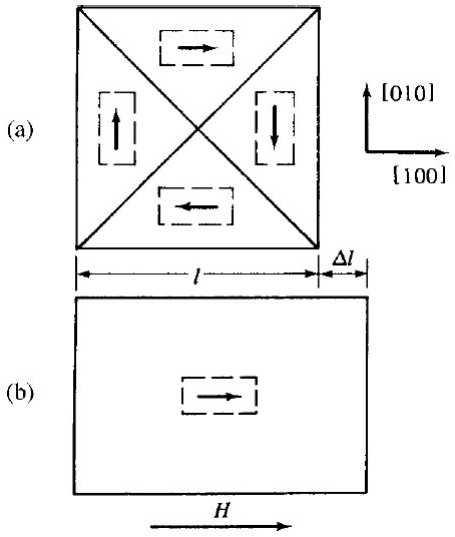

Figure 2.12: Schematic diagram of the magnetostriction phenomenon when applying a field ($\boldsymbol{H}$) on (a) a demagnetized iron (BCC) monocrystal in the [100] crystallographic direction. (b) After saturation the domain continues to expand elongating the crystal lattice and straining the ferromagnetic material by Δl [53].

The magnetostriction constant (λ) is defined as a fractional change in length which is expressed as

$$\lambda = \frac{\delta l}{l} \tag{2.20}$$

where l is the length of the material and δl is the change in length from the applied magnetic field. When a magnetic material reaches its maximum mechanical strain and is magnetically saturated ($\boldsymbol{M}_S$) (i.e., the change in length cannot undergo further strain) the value of λ is called the saturation magnetostriction (λ_S). λ_S is typically in the range of 10^{-5} - 10^{-6} which is a small effect from the competing effects of the elastic stiffness of the crystal lattice

and the minimisation of magnetic energy. However, these deformations give a noticeable impact on the magnetic behaviour of ferromagnetic materials since any slight movements between neighbouring atoms within the material influence the magnetic energies between magnetocrystalline anisotropy and exchange energy [53].

This is manifested where the material exhibits magnetostrictive effects from its own magnetisation as stray fields (or demagnetising field, discussed in section 2.4.3). The stray fields induce a strain to the material in which the direction of the strain is dependent on the crystal lattice and crystal direction; thus, regions of the material would strain either horizontally or vertically. Fig. 2.13 illustrates this effect where the region of the crystal direction strains horizontally and vertically is represented as magnetic domains. The domains that are orthogonal to each other will have competing effects to elongate on the preferred orientation which adds an elastic strain energy component to the total free energy (highlighted in dotted lines on Fig. 2.13). To minimise the strain energy the domains of closure have to be smaller (Fig. 2.17(a)), but this introduces new domains which increases the magnetostatic and exchange energies to form the new domains. As a result, the magnetostriction influences the magnetic domain structure of the magnetic body due to elastic strain energy (which is also related to the magnetoelastic anisotropy) [51, 53].

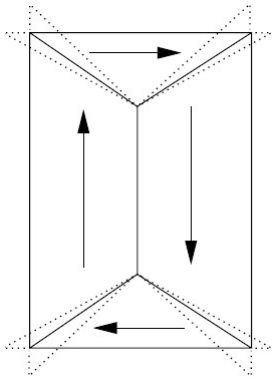

Figure 2.13: Magnetostriction occurring in a demagnetized state of a BCC iron. The elongation effects between horizontal and vertical domains are highlighted in the dotted area. The competing elongation subtly strains and deforms the crystal structure changing its own magnetization. The diagram was taken from [51].

Magnetostriction is an anisotropic property where different crystallographic directions have their own magnetostriction constants. For a single crystal with cubic symmetry the total magnetostriction along a given direction, can be expressed using the Becker-Döring equation [62], written as

$$\lambda_S = \frac{3}{2}\lambda_{100}(\sum_i \alpha_i^2\beta_i^2 - \frac{1}{3}) + 3\lambda_{111}\sum_{i\neq j}\alpha_i\alpha_j\beta_i\beta_j \tag{2.21}$$

where λ_{100} and λ_{111} are magnetostriction constants that contain the crystal elastic stiffness and are included since either direction could be the easy axis depending on the anisotropy constant ($\boldsymbol{K}_i$), $\alpha_{i/j}$ are cosine angles of the saturation magnetisation ($\boldsymbol{M}_S$) relative to the crystal axes, and $\beta_{i/j}$ is the cosine angle of measured magnetostriction relative to the crystal axes. Both $\alpha_{i/j}$ and $\beta_{i/j}$ measure the angles for crystallographic directions [100] and [111]. For a hexagonal symmetry the magnetostriction equation involves more mag-

netostriction constants and further considers the cosine angles orthogonal to the c-axis as well as the hexagonal axes [63].

In a polycrystal (or amorphous) structure the saturation magnetostriction is dependent on the individual grain and domain structures within the ferromagnetic material. When a polycrystal is saturated by an applied field the different orientations and structures of neighbouring grains and/or domains will strain magnetostrictively in the direction of the field at varying amounts. Therefore, the saturation magnetostriction of a polycrystal is considered the average of saturation magnetostriction of all individual grains/domains in the material. In this case, the magnetostriction for these materials behave more in an isotropic manner [64] than anisotropic, thus the magnetostriction along the <100> and <111> directions are considered equal. Hence, the isotropic magnetostriction can be expressed as

$$\lambda_{isotropic} = \frac{3}{2}\lambda_S(\cos^2(\theta) - \frac{1}{3}), \tag{2.22}$$

where $\lambda = \lambda_{100} = \lambda_{111}$ and the direction of magnetization is only considered the relative angles between $\alpha_{i/j}$ and $\beta_{i/j}$ is simplified to $\cos^2(\theta)$.

The magnetostriction constant of an amorphous or polycrystal ferromagnet can either be positive or negative depending on if the overall strains from the grains are tensile or compressive, respectively. However, ferromagnets with higher crystallinity can possess both negative and positive magnetostrictions depending on the direction the strain and magnetization is relative to the crystal axes.

2.4.2.ii Inverse magnetostriction (Villari effect)

Magnetostriction is a phenomenon that deforms the crystal lattice, domain, and grain structures which rotates the magnetisation of the material. It is expected that applying a mechanical stress/strain onto the material should also induce an anisotropy that does the same effect of rotating the material's magnetisation. This is known as the inverse magnetostriction (or the Villari effect) where the magnetic properties of a ferromagnet changes from applied stress/strain (Fig. 2.14).

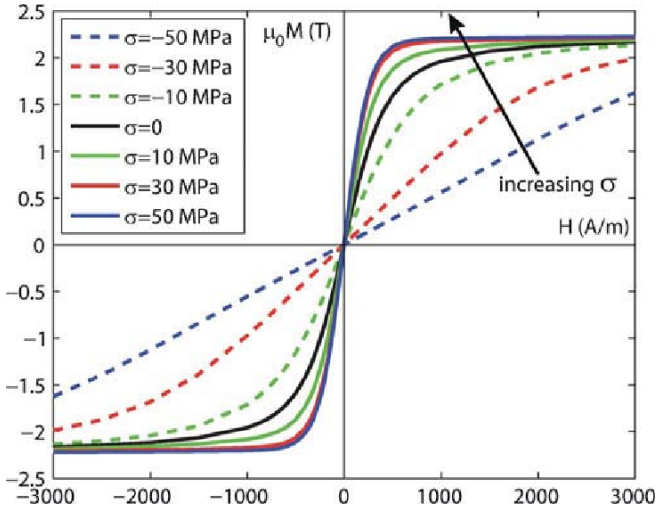

Figure 2.14: Modelling a magnetization curve of a magnetic material (defined as a set of magnetic domains, of known $\boldsymbol{M}_S$, with random orientation) under uniaxial mechanical stress (σ). The applied field ($\boldsymbol{H}$) is simulated to be parallel to the direction of the applied uniaxial stress (σ). The increasing stress from compressive to tensile improves the magnetization of the material. The data was done by Bernard et al. [65].

Fig. 2.14 illustrates the change material's $M - H$ curve changes when transitioning from compressive to tensile stresses, and illustrates how applied stresses influence the ferromagnet's magnetic permeability (μ). In the

absence of stress, the ferromagnet's behaviour is controlled by the magnetocrystalline anisotropy of its crystal lattice. The transition from compressive to tensile stress displays a decrease in the work done for the magnetic field to saturate the material. This indicates the applied mechanical stress introduces additional anisotropy (stress anisotropy) which influences the magnetocrystalline anisotropy by rotating the easy and hard axes of the material. The correlation between mechanical strain to the changing magnetisation behaviour of the material can be described as the magnetoelastic coupling effect.

The relationship between the magnetoelastic effects to the magnetocrystalline anisotropy can be written as

$$E_T = E_K - E_{ME}, \tag{2.23}$$

where E_T is the total free energy of the ferromagnet and E_{ME} is the magnetoelastic energy from the applied stress. Therefore, for a cubic lattice structure the equation can be expanded into

$$\begin{aligned} E_T = K_1(\alpha_1^2\alpha_2^2 + \alpha_2^2\alpha_3^2 + \alpha_3^2\alpha_1^2) - \frac{3}{2}\lambda_{100}\sigma(\alpha_1^2\gamma_1^2 + \alpha_2^2\gamma_2^2 + \alpha_3^2\gamma_3^2) \\ -3\lambda_{111}\sigma(\alpha_1\alpha_2\gamma_1\gamma_2 + \alpha_2\alpha_3\gamma_2\gamma_3 + \alpha_3\alpha_1\gamma_3\gamma_1) \end{aligned} \tag{2.24}$$

where α_i and γ_i are the direction cosines of magnetization ($\boldsymbol{M}_S$) and applied stress, respectively, relative to the crystal axis. Eq. 2.24 approximates the combination of magnetocrystalline anisotropy and the magnetoelastic effects. The formula describes the energy of a ferromagnet at varying strengths of stress where at low (or in the absence of) stress the material only possesses magnetocrystalline anisotropy or a combination of magnetocrystalline

and magnetoelastic anisotropy at finite stress/strain. Note the stress applied is assumed to be within the elastic limit of the material since permanent deformation involves permanent changes to the crystal lattice which in turn change the ferromagnet's saturation magnetostriction.

Stress anisotropies on ferromagnets that possess a monocrystal structure have magnetostrictions that are dependent on the direction of the stress relative to the crystal structure, whereas polycrystals and amorphous structures typically have a more isotropic behaviour. The mathematical form of the magnetoelastic energy can be simplified if the magnetostriction of the material is isotropic and the magnetostriction constants λ_{100} and λ_{111} are the same:

$$E_{ME} = \frac{3}{2}\lambda_s \sigma \cos^2\theta \tag{2.25}$$

Depending on the sign of the product of $\lambda_s\sigma$ the easy and hard axes of the material will be reoriented, as in Fig. 2.14, where the samples susceptibility is increased under tensile stress whereas compressive stresses decreases it.

In summary, when applying either a tensile or compressive stress to a ferromagnet induces a stress anisotropy ($\boldsymbol{K}_\sigma = \frac{3}{2}\lambda_s\sigma$). When the stress anisotropy is equivalent to the magnetocrystalline anisotropy the magnetic behaviour of the ferromagnet is then dominated by the magnetoelastic anisotropy instead of the magnetocrystalline anisotropy. The stress required to overcome the magnetocrystalline anisotropy can be expressed in Eq. 2.26,

$$\sigma = \frac{2}{3}\frac{K_1}{\lambda_s} \tag{2.26}$$

Stress (σ) represents the total combination of external and internal stresses i.e., applied mechanical stresses and internal residual stresses from the mate-

rial fabrication processes respectively. As discussed in the previous section, the magnetostriction of a material depends on the crystallinity of a material. The higher the crystallinity (single crystal) the more anisotropic the magnetostriction because of the presence of the magnetocrystalline anisotropy from the high concentration of long-range ordering of atoms. Alternatively, the lower the crystallinity (polycrystalline) the more isotropic the saturated magnetostriction because of increasing concentration of short-range ordering of atoms, reducing the magnetocrystalline anisotropy. In a material that is fully amorphous (absence of any long-range ordering) the magnetostriction of the material is considered to be completely isotropic.

2.4.3 Magnetostatic energy

The magnetostatic energy (E_M) is the energy to magnetize a ferromagnetic material against its own magnetic field. This field is defined as the "demagnetising field", $\boldsymbol{H}_d$. $\boldsymbol{H}_d$ is directly proportional to the magnetization ($\boldsymbol{M}$) of the ferromagnet and the demagnetizing coefficient (N_d),

$$\boldsymbol{H}_d = -N_d \boldsymbol{M}_S. \tag{2.27}$$

The demagnetizing factor (N_d) is a geometry dependence constant that describes the strength of the demagnetizing field along a particular cartesian axis of the ferromagnet, thus the higher the demagnetizing factor the higher the demagnetizing field on that axis. Therefore, the demagnetization field on each axis is proportional to a corresponding demagnetizing factor of that axis. The total of the demagnetization factors at each cartesian axis should equal 4π [53],

$$N_x + N_y + N_z = 4\pi, \tag{2.28}$$

in SI units the total of $N_x + N_y + N_z$ is 1.

The difference in the demagnetization factors is dependent on the symmetry of the ferromagnet between all three cartesian axes. The more symmetrical it is (such as a sphere) the more equal the demagnetization factors are to each other (for example a sphere has $N_x = N_y = N_z = 4/3\pi$). Therefore, when a body's shape is less symmetrical and has one side longer than the others the demagnetization factors change accordingly where the longest axis has the lowest demagnetization factor. This is known as the shape anisotropy. Shape anisotropy determines the strength of the demagnetizing field of the ferromagnet based on the aspect-ratio of the material. As a consequence, the demagnetization field is weakest along the longest axis and strongest on the shortest axis with a net shape anisotropy being prominent along the longest axis. The shape anisotropy is more prominent in polycrystal and amorphous crystal structures where the material does not have a strong magnetocrystalline anisotropy but for monocrystals, the shape anisotropy competes with the magnetocrystalline anisotropy energy on the direction of magnetization.

The total magnetostatic energy (per unit volume) in a magnetically saturated ferromagnet is expressed as

$$\frac{E_M}{V} = -\frac{1}{2}\mu_0 \boldsymbol{M}_S^2 H_d = \frac{1}{2}\mu_0 N_d \boldsymbol{M}_S^2. \tag{2.29}$$

The magnetostatic energy differences between two cartesian axes can be expressed as:

$$E_M = \frac{1}{2}\mu_0 \boldsymbol{M}_S^2 N_d + \frac{1}{2}\mu_0 \Delta N \boldsymbol{M}_S^2 \sin^2(\theta), \tag{2.30}$$

where $\Delta N = N_{d(x,y,z)} - N_{d(x,y,z)}$. Eq. 2.30 displays an angle-dependent term similar to the magnetocrystalline anisotropy and magnetoelastic anisotropy where $\frac{1}{2}\mu_0 \Delta N \boldsymbol{M}_S^2$ represents the shape anisotropy ($\boldsymbol{K}_S$) of the material. The first term indicates the "easy-axis" for the shape anisotropy, i.e., the least amount of energy required to align the anisotropy, and the second term defines the difference in energy when measuring the shape anisotropy away from its "easy-axis".

To reduce the magnetostatic energy ferromagnetic materials often form multi-domains states which reduce the size of $\boldsymbol{H}_S$ (Fig. 2.15(b) . Flux-closed configurations where the magnetisation forms a closed loop reduce $\boldsymbol{H}_S$ further (Fig. 2.15(c)), and these will be discussed in more detail shortly.

The exchange energy, magnetocrystalline anisotropy, and magnetostatic energy influence the size and number of the domains (and domain wall thickness) of a material. Exchange energy favours parallel spins between adjacent magnetic moments which competes with the magnetocrystalline anisotropy on preferring the magnetic moments to lie along the easy crystallographic axis. As a result, both exchange and magnetocrystalline anisotropy energies prefer fewer domains as possible to minimise both of their energies. However, magnetostatic energy prefers as many domains as possible to minimise its demagnetizing field. These competing effects between exchange, magnetocrystalline, and magnetostatic energies can be used to identify the "effective domain width" (d_w) and the number of domains present a ferromagnet could produce. The effective domain width (d_w) can be expressed as

$$d_w = L\sqrt{\frac{\sigma_{DW}}{\mu_0 \boldsymbol{M}_S^2 t C}} \tag{2.31}$$

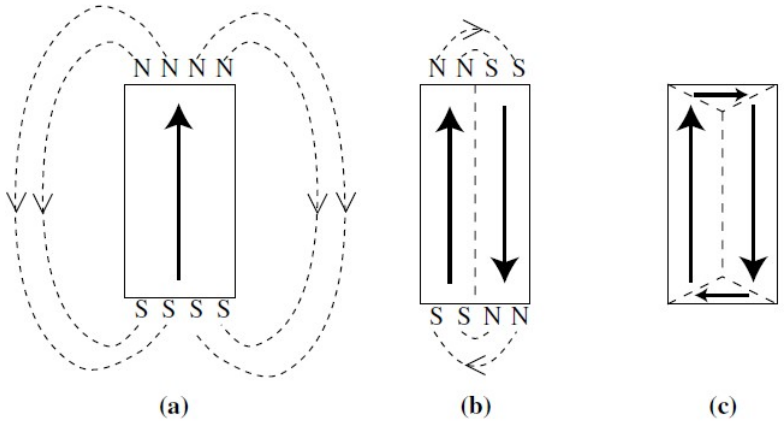

Figure 2.15: Schematic diagram on domain formation from the material's own (a) magnetic field demagnetizing its own magnetization – known as a demagnetizing field ($\boldsymbol{H}_d$) (dotted lines), with (b) vertical domains of opposing magnetisation reduce the magnetostatic energy to the ends of the magnetic material (dotted lines connected between North and South poles) until (c) horizontal domains are formed to form a closed-flux state with no fields produced from the magnetostatic energy [51].

where L is the length of the material, t is the thickness of the material, C is a constant (derived from calculating the magnetostatic energy of multi-domain crystal) [66], and σ_{DW} is the surface energy of a domain wall.

Domain walls are the boundaries between two neighbouring domains in which the size of the boundary can influence the number of magnetic domains as well as the domain type – 90° and 180° domain walls – of the bulk ferromagnet. Domain walls are formed between competing energy contributions of exchange energy and magnetocrystalline anisotropy energy. The boundary is formed by the slow rotation of the exchange energy between two neighbouring domains with anti-parallel magnetic moments (Fig. 2.16).

The formation of a domain wall can be described by expressing the energy

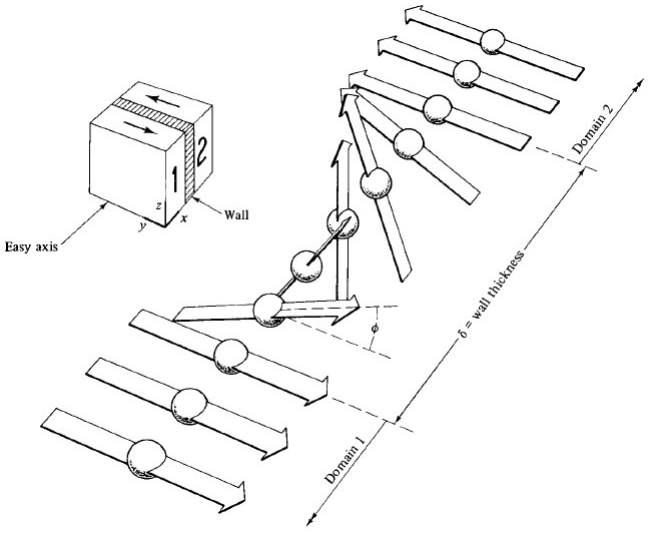

Figure 2.16: Schematic diagram of a 90° domain wall between domain 1 and domain 2. The wall has a thickness (δ) which is defined by the competing effects between exchange energy and magnetocrystalline anisotropy energy. The thicker the wall the more gradual the rotation of magnetization between two opposing magnetizations (90° domain walls) and the thinner the wall the more rapid the magnetisation rotation (180° domain walls) [53].

density required to form a domain wall (σ_{DW}) as

$$\sigma_{DW} = \sigma_{ex} + \sigma_K = \frac{A\pi^2}{\delta} + \boldsymbol{K}_U\delta \tag{2.32}$$

where δ is the domain wall thickness, $\boldsymbol{K}_U$ is the magnetocrystalline anisotropy constant, and A is the exchange stiffness. Rearranging Eq. 2.32 where both exchange and anisotropy energies are equal determines the "effective domain wall thickness" (δ_0), which is expressed as

$$\delta_0 = \pi\sqrt{\frac{A}{\boldsymbol{K}_U}} = \pi L_{ex} \tag{2.33}$$

where L_{ex} is the ferromagnetic exchange length that describes the minimum distance for the magnetisation to change direction without involving the exchange energy. Hence, substituting Eq. 2.33 into Eq. 2.32 provides the energy density of a domain wall of equal exchange and magnetocrystalline energies to be $\sigma_{DW} = 2\pi\sqrt{A\boldsymbol{K}_U}$.

Therefore, a higher magnetocrystalline anisotropy would have low domain wall thickness with higher exchange energy having a large domain wall thickness. This is because the magnetocrystalline anisotropy prefers the magnetic moments to align parallel to the easy-axis, thus it prefers a narrow domain wall thickness to minimise moments align away from the easy-axis. However, exchange energy prefers parallel alignment between as many magnetic moments as possible, thus favouring wider domain wall thickness. Depending on the dominating energy two types of domains are formed which are the 90° and 180° domain walls and a combination of these two domain walls can form a close loop domain structure (Fig. 2.15). Close loop domain structures are domain structures that minimises the demagnetizing field as much as possible by preventing any pole regions to form. There are two types of close loop domain structures; closure domain structures and vortex-domain structures.

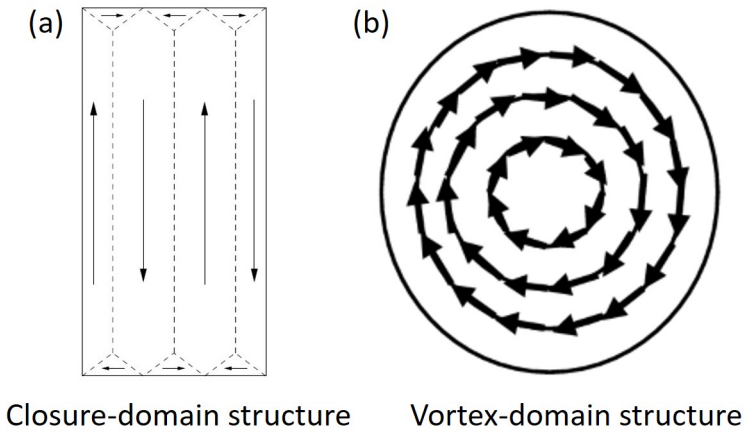

Figure 2.17: Schematic diagram of domain structures that minimises stray fields; (a) closure-domain structure [51] and (b) vortex-domain structure [67]. The closure-domains are different from Fig. 2.13 with larger vertical domains and shorter horizontal domains based on the magnetostrictive energies present in the system.

In summary, the formation of domain patterns reduces the magnetostatic energy. The volume, number of domains, and domain wall thickness are controlled by the competing effects of exchange and magnetocrystalline anisotropy energies where the effective domain width and wall thickness is the equilibrium between the two energies. As a result, when applying an external magnetic field to the system it is possible to move the domain wall throughout the ferromagnet since it promotes exchange energy and reduces anisotropy, this is further described in section 2.4.4.

2.4.4 Zeeman energy

The last magnetic energy term is the Zeeman energy (E_Z), it is the potential energy of the magnetization of a ferromagnet to an externally applied

magnetic field (H). The Zeeman energy can be derived from Eq. 2.2 by the integral of the energy required to rotate a dipole moment (parallel to the magnetisation) by the volume of the magnetic body (V), giving the expression,

$$E_z = -\mu_0 \int_0^V \boldsymbol{M} \cdot \boldsymbol{H} \, dV. \tag{2.34}$$

When a magnetic field is applied to a magnetic material it competes with the other energy terms, dominating at high fields and being less significant at lower fields. These phenomena give rise to the unique properties and features of the material's hysteresis loop (Fig. 2.18).

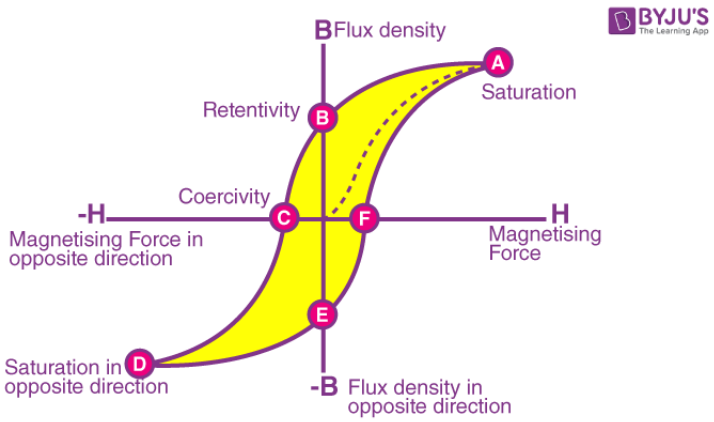

Figure 2.18: Schematic diagram of a magnetization curve of a typical ferromagnetic material [68].

Fig. 2.18 illustrates an example of a typical magnetic hysteresis loop, including an initial stage of magnetisation from a demagnetised state. Initially, the material starts in a fully demagnetized, multi-domain state. When applying the field to the ferromagnet, existing domains will expand via domain wall motion whilst domain nucleation also forms from magnetization

rotation. Before reaching saturation (point A) if the magnetization of the domain is not aligned to the field it will undergo magnetization rotation where the magnetization reorients itself parallel to the field. Once at saturation, the ferromagnet is a single domain with its magnetization aligning parallel to the field.

When the field decreases the ferromagnet begins to demagnetize itself by nucleation of multiple domains with magnetizations along the easy axis to reduce the magnetostatic energy, but at zero field the ferromagnet still has remanence (or retentivity) ($\boldsymbol{M}_r$) of its magnetization because of a combination of exchange and magnetocrystalline energy that favour parallel spins (point B and E) along the easy-axis. To fully demagnetize the ferromagnet a field pointing in the opposite direction has to be applied where it reverses the magnetisation rotation and domain dynamics back to its (close to) initial state when reaching zero magnetization (or flux density) (points C and F) – the field at which the ferromagnet becomes completely demagnetised is called the coercive field ($\boldsymbol{H}_c$). If the field increases in the opposite direction the existing domains will start expanding with domain nucleation until near saturation the domain undergoes magnetization rotation until aligning parallel to the applied field (point D). The domain structure at saturation will be the same as point A but the direction of magnetization will be in the opposite direction. The same behaviour can be observed in Fig. 2.19 where (a) is the demagnetized state of the ferromagnet, (b) is domain expansion, and (c) to (e) is magnetization rotation. Moreover, at Fig. 2.19, part (d) is the point when the Zeeman energy is equal to the magnetocrystalline anisotropy energy and this is called the anisotropy field ($\boldsymbol{H}_k$) – the (theoretical) field required to align the magnetization of the material orthogonal to the easy-axis – this is further discussed in detail in chapter 3, section 3.5.1.vi.

A hysteresis loop presents many of the defining properties of a magnetic

material such as its saturation magnetization ($\boldsymbol{M}_S$), magnetization remanence ($\boldsymbol{M}_r$), the anisotropy field ($\boldsymbol{H}_k$), coercive field ($\boldsymbol{H}_c$), and its magnetic susceptibility (χ). Furthermore, the hysteresis loop can provide information on whether a material should be classified as "soft" or "hard" ($\boldsymbol{H}_k$ and $\boldsymbol{H}_c$) (Fig. 2.20) and on the orientation of easy- or hard-axes if angularly resolved measurements are performed ($\boldsymbol{M}_S$, $\boldsymbol{H}_k$, and χ) (Fig. 2.9). Collectively, these properties define the suitability of a magnetic material for any given application and provide insight into the competing anisotropies in the material.

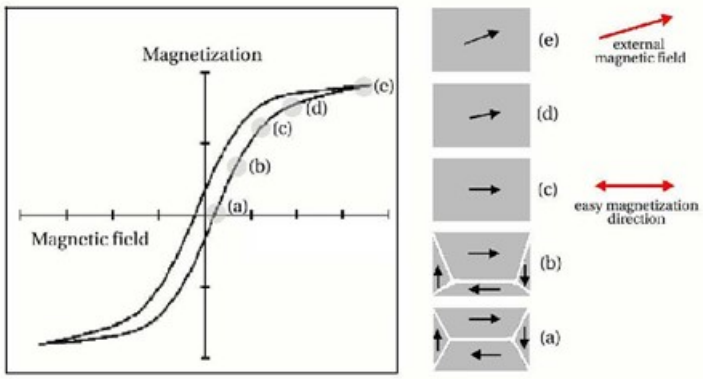

Figure 2.19: Magnetization curve done by F. Colaiori [69] on a soft ferromagnetic sample with the domain structure changing with respect to applied field ($\boldsymbol{H}$). (a) Initially, the sample is demagnetized with a closed-flux state and (b) when increasing the applied field, the domain with magnetization parallel to the field direction expands via domain wall motion until (c) the sample is a single domain. To reach magnetization saturation (d) the magnetization on the single domain starts to rotate to align itself parallel to the field direction and (e) after undergoing magnetization rotation the sample reaches saturation of magnetization ($\boldsymbol{M}_S$).

Applying other external stimuli to a ferromagnetic material may also change its hysteresis loops by affecting the various magnetic anisotropies. These external could include thermal, electrical, chemical, mechanical stimuli, or a combination of the four. The influence of these variables on the behaviour of ferromagnetic materials is discussed in Chapter 3, section 3.5.1.

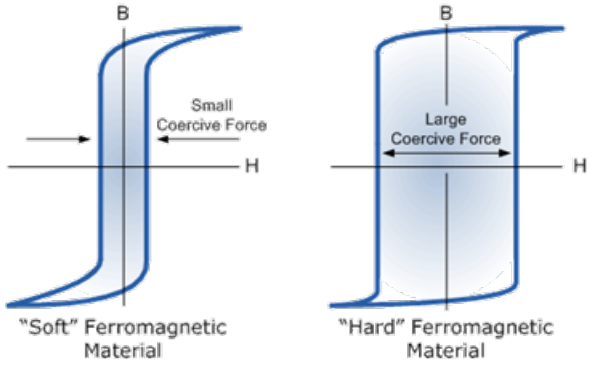

Figure 2.20: Schematic diagram of magnetization curve profiles of typical "soft" and "hard" ferromagnetic materials [70].

2.5 Hard and soft magnetic materials

The difference between "hard" and "soft" magnetic materials is the amount of applied field to demagnetize the material from $\boldsymbol{M}_r$, also known as the coercivity, $\boldsymbol{H}_C$. Simply, the higher the $\boldsymbol{H}_C$ the harder the magnetic material becomes and vice versa. The typical $\boldsymbol{H}_C$ value for a hard (or permanent) magnet would be over 100 Oe [71] and anything under that range would be categorised as a soft magnet [72]. The variation in $\boldsymbol{H}_C$ is dependent on the dynamic interaction between the magnetic energies; magnetocrystalline anisotropy (E_K), the exchange energy (E_{ex}), magnetostatic energy (E_M), and magnetoelastic energy (E_{ME}) which influences the dynamic behaviour of domain formation, domain wall motion, and magnetisation rotation [73].

These energies can be manipulated by adjusting the microstructure via grain size, crystallinity, chemical composition, and crystal and/or surface defects which either enhance or diminishes coercivity.

In the following, the factors affecting the coercivity in materials with different degrees of crystallinity are discussed. Crystallinity describes the degree of structural order between atoms. There are three distinct crystalline structures; single (mono) crystal, polycrystal, or an amorphous crystal structure [71], [72].

2.5.1 Single (mono) crystalline materials

Single crystal materials have a homogeneous crystal lattice and thus in the absence of local defects have a uniform magnetic behaviour throughout the material. Therefore, any changes to the material's crystal lattice/structure can cause changes in the balance of the magnetic energies and thus its coercivity. Possible changes here include crystal lattice distortions, surface effects, and the size of the material.

Anti-phase boundaries (APB) are one such defects that can increase the coercivity of a single crystal material [74], [75]. An anti-phase boundary is when the symmetry of an ordered phase breaks into two separate domains in which the atomic positions are the same as before, but of a different chemical nature (which extends to magnetic nature). The breaking of symmetry affects the local exchange and magnetocrystalline anisotropies at the boundary regions which influences the coercivity. In this case, the coercivity increases the higher the density of APB's due to the changing domain structure. At low densities, the magnetocrystalline anisotropy energy dominates with a preference for 180° domain labyrinth-like structures and with increasing density the magnetocrystalline anisotropy decreases with magnetic vortices being

preferred at the APB regions. The magnetic vortices obstruct the domain wall motion, thus the higher the number of APB on the material the higher the coercivity.

Another variable of changing the coercivity of single crystal materials can be the distortion of the crystal lattice. This was studied by Patelli et al. [76] where the coercivity in single crystal Fe-Co alloy nanoparticles changed when increasing the atomic concentration of cobalt. The increase in the concentration of cobalt atoms distorts the BCC crystal lattice and increases the coercivity from 376 to 752 Oe. The increase in coercivity was attributed to the distortion of the crystal lattice from a BCC crystal lattice (cubic anisotropy) to an HCP crystal lattice (uniaxial anisotropy) evident by the increased intensity of the (321) miller indices which increases the magnetocrystalline anisotropy. The relation between the increasing atomic concentration of a specific element and crystal lattice distortion comes from the atomic substitution between two atoms with similar atomic radii [77]. Furthermore, atomic substitution also influences the exchange interaction between neighbouring atoms due to both the change of the interatomic distance and concentration of ferromagnetic atoms. Gorbachev et al. observed the coercivity decreasing for M-type hexaferrite nanoparticles when increasing the atomic concentration of aluminium. Apart from crystal lattice distortions the decrease in coercivity was also contributed by the different concentrations between the ferromagnetic atom (in this case it was iron) and aluminium – which is a paramagnetic atom. Therefore, the increase in aluminium weakened the exchange interaction between the ferromagnetic atoms resulting in the lowering of the coercivity.

It is also well known that the coercivity is size dependent, especially for nanoparticles [78], [79]. As the size of the particles changes, so does the coercivity as it becomes affected by changes to the particles' domain

structure and by the ability of the magnetisation to resist perturbations by thermal energy. Critical length scales here are the single-domain limit and the superparamagnetic limit, respectively [80], [81]. The single domain limit (D_C or D_S) is when the physical size of the material is so small it becomes energetically unfavourable to form closure domains (or multiple domains) so the material exhibits only a single domain. Coercivity depends differently on particle size above and below D_C:

$$H_C = a + \frac{b}{D} \quad (when\ D > D_c) \tag{2.35a}$$

$$H_C = c + \frac{d}{D^{3/2}} \quad (when\ D < D_c) \tag{2.35b}$$

where a,b,c, and d are constants [79]. For particles lower than D_C the coercivity rapidly decreases due to thermal energies (room temperature, 293 K) overcoming the particle's magnetostatic energy becoming superparamagnetic, labelled as D_P (Fig. 2.21). Although, the coercivity can be restored or enhanced when reducing the surrounding temperature of the magnetic particle to nearly 0 K [74], [81], [82].

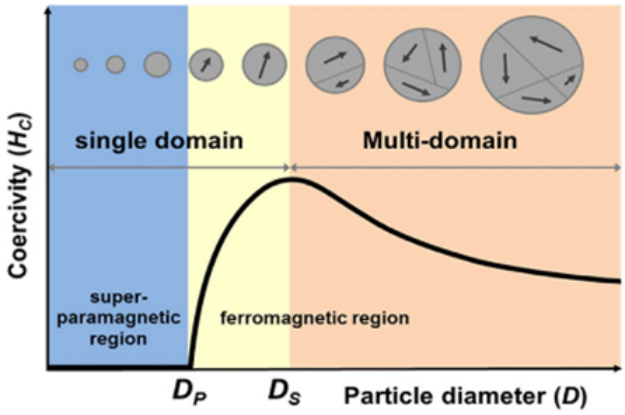

Figure 2.21: Schematic diagram of the particle diameter (D) with respect to coercivity [79].

In an ideal scenario, the shape and size of the nanoparticles would be identical in which the overall coercivity of the nanoparticles would be identical. In reality, nanoparticles will have some distribution of varying particle sizes and spherical shapes. Depending on the width of the distribution for both particle size and spherical shape the coercivity would be lower or than expected. Patelli et al. discussed the nature of the distribution where a wider distribution translates to a small fraction of nanoparticles having superparamagnetic behaviour or with multiple domains which lower the expected coercivity. Particles that are not spherical will induce a shape anisotropy due to one axis being longer than the others. The introduction of a shape anisotropy increases the coercivity since it orients the magnetic moments along the long axis. Therefore, it is possible to improve the coercivity even higher by having ellipsoidal nanoparticles with a very small distribution of the particle size with the majority being in the single domain.

The relation to size and coercivity applies to all materials regardless of crystallinity, but for single crystals, the change in coercivity is more signif-

icant, as studied by Dar et al. [81]. It was observed that the coercivity for a single crystal nanoparticle was a magnitude higher compared to their bulk counterparts, with coercivities of 818 Oe and 150 Oe, respectively. This large difference was considered to be the stronger exchange interaction at smaller length scales.

2.5.2 Polycrystalline materials

Polycrystalline materials contain multiple grains all of which generally have the same basic crystal structure. The origin of multiple grains is from multiple nucleation sites located at crystal defects found within the crystal lattice, resulting in the disorder of the uniform lattice [83]. Each grain will have its own axis of magnetocrystalline anisotropy and the material as a whole will exhibit "effective anisotropy" resulting from the average across many grains. This makes the magnetic behaviour of a polycrystalline material more isotropic and the coercivity of these materials is more dependent on the grain size instead of the crystal lattice.

The relationship between the grain size and coercivity can be explained using Herzer's model of random anisotropy [84], [85]. The random anisotropy model assumes a characteristic volume of sizes equal to the exchange length (L_{ex}) (Eq. 2.33). Each grain has a random easy-axis with a corresponding magnetocrystalline anisotropy, K_U, and all the grains are exchange coupled. As a result, the overall anisotropy (or the effective anisotropy), K_{eff}, would be reduced by a factor of $1/\sqrt{N}$ due to the different easy-axes in each grain (Fig. 2.22).

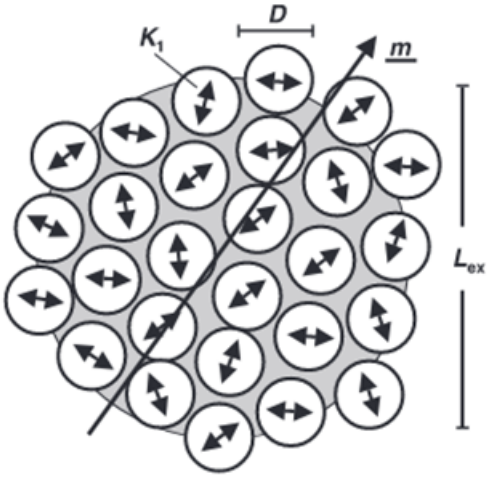

Figure 2.22: Schematic representation of the random anisotropy model of average grain size (D) in a soft ferromagnetic matrix within a ferromagnetic correlation volume determined by the exchange length (L_{ex}). The double arrows indicate the randomly fluctuating magnetocrystalline anisotropy axis ($\boldsymbol{K}_1$) and the magnetization ($\boldsymbol{M}$) is constant [86].

Hence, K_{eff} can then be expressed as

$$\boldsymbol{K}_{eff} \approx \frac{\boldsymbol{K}_U}{\sqrt{N}} \tag{2.36}$$

The number of grains (N) is the volumetric ratio between the exchange length and average grain size, expressed as L_{ex}^3/D^3 substituted into Eq. 2.36 gives the expression

$$\boldsymbol{K}_{eff} \approx \frac{\boldsymbol{K}_U}{\sqrt{N}} = \boldsymbol{K}_U \left(\frac{D}{L_{ex}}\right)^{\frac{3}{2}}. \tag{2.37}$$

Depending on the average grain size (D) relative to the exchange length ways in which the coercivity varies with grain size can manifest. Knowing

the coercivity strength is proportional to the anisotropy field $\rho 2K_{eff}/\boldsymbol{M}_S$ and setting the conditions for D to either be smaller or equal to L_{ex} or larger than effective domain wall width (δ_0) highlights three behaviours regimes (Eq. 2.38)

$$\boldsymbol{H}_C \approx \rho \frac{\boldsymbol{K}_U^4}{A^3 \boldsymbol{M}_S} D^6, \quad when\ D < L_{ex} \tag{2.38a}$$

$$\approx \rho \frac{\boldsymbol{K}_U}{\boldsymbol{M}_S}, \quad when\ D \cong L_{ex} \tag{2.38b}$$

$$\approx \rho \frac{\sqrt{A\boldsymbol{K}_U}}{\boldsymbol{M}_S D}, \quad when\ D > L_{ex} \tag{2.38c}$$

ρ is the dimensionless factor related to the crystal structure.

When the average grain size is smaller than the exchange length the model describes a rapid change in coercivity proportional to the sixth power of the average grain size, D^6. This rapid change in coercivity comes from the exchange energy overcoming the magnetocrystalline anisotropy due to the increase interaction of magnetic moments between the grains. This impedes the orientation of the magnetic moments along the easy-axis instead favouring parallel orientation, with each other, with respect to the magnetisation of the material. As a result, the effective anisotropy of the material spans over multiple grains with the domain dynamics being influenced by the magnetostatic energy, magnetoelastic anisotropy, and exchange energy. Average grain size equalling the exchange length will have the coercivity being independent from D and is only proportional to K_U. Average grain size over the domain wall width enables magnetic domains to form within the grains. Therefore, the change in coercivity is proportional to the energy density of the domain wall $\sqrt{(AK_U)}$ which changes their pinning [87]. Domain wall pinning happens when the domain wall is obstructed by pinning sites – non-magnetic inclusions – such as defects in the crystal lattice, precipitates within

the material, etc, which increases the material's coercivity. Hence, when the grain size gets smaller it will increase the number of grain boundaries which increases the coercivity (Fig. 2.23) [88], [89].

Fig. 2.23 illustrates the differentiation between hard and soft magnets is determined by the exchange length. The coercivity reaches its maximum when the average grain size is equal to the exchange length exhibiting hard magnetic properties. The grain size to achieve the highest coercivity varies depending on the exchange length of the material. For example, a study done by Vopsaroiu et al. [85] calculated the exchange length for a polycrystalline CoFe thin film to be 18.4 nm whereas Han et al. [90] calculated the exchange length for NdFeB nanocrystalline ribbon to be 4.2 nm, thus the maximum coercivity for both of these materials will have different average grain sizes. The exchange length is dependent on the exchange stiffness (A) and magnetocrystalline anisotropy (K_U) which can be optimised by the chemical configuration [91], [92] and the atomic radii [93].

Overall, it is evident that coercivities are smallest happens when the average grain size is at the nanoscale range either close to or under the exchange length, i.e. when materials are nanocrystalline.

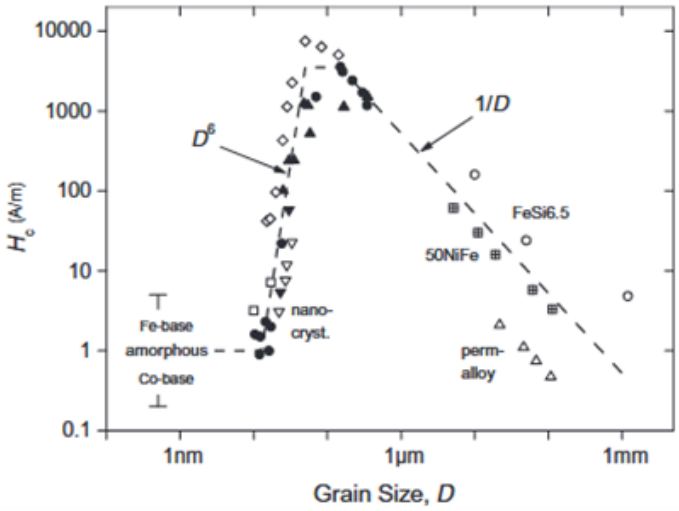

Figure 2.23: Relationship between the average grain size (D) and coercivity. The dotted line represents the random anisotropy model with good correlation to the experimental data of various soft magnetic alloys of varying grain sizes. The data was used from ref. [86].

2.5.3 Nanocrystalline and amorphous materials

Nanocrystalline materials with average grain sizes (D) ranging between 1 – 100 nm [94]. One of the methods to create these materials is to prepare them initially in an amorphous state using fabrication methods such as rapid solidification and deposition techniques, and then inducing crystallisation via annealing treatments [92], [95], [96]. Hence, nanocrystalline materials typically have two-phase microstructures, containing both amorphous and nanocrystalline phases. Herzer adjusted the random anisotropy model for a two-phase microstructure nanocrystalline material where the effective anisotropy is

$$\boldsymbol{K}_{eff} \approx (1 - V_{am})^2 \frac{\boldsymbol{K}_U^4}{A^3} D^6 \tag{2.39}$$

where V_{am} is the volume fraction of the amorphous phase. Eq. 2.39 implies the presence of an amorphous phase weakens the effective anisotropy by assuming the exchange stiffness of the amorphous phase was comparable to the crystalline phase. However, this does not apply to all materials, as reported by Suzuki and Cadogan [97], where they observed an increase in coercivity with an increasing volume fraction of the amorphous phase (up to 0.53). The authors identified the exchange stiffness of the amorphous phase to be much weaker. As a result, the two-phase random anisotropy model was extended to consider a more realistic scenario with the effective anisotropy contributed by local exchange stiffnesses from both phases

$$\boldsymbol{K}_{eff} \approx \frac{1}{\varphi^6}(1-V_{am})^4 \boldsymbol{K}_U^4 D^6 \left(\frac{1}{A_{cr}^{1/2}} + \frac{(1-V_{am})^{-1/3}-1}{A_{am}^{1/2}} \right)^6 \tag{2.40}$$

where φ is the parameter reflecting the symmetry of $\boldsymbol{K}_{eff}$ and the spin angle rotation of L_{ex}.

The random anisotropy model can accurately predict the relation between coercivity to the average grain size for all materials at varying dimensions (e.g., ribbons, thin films, and nanowires) with the power-law behaviour of the coercivity being different depending on the dimensionality of the exchange-coupled region. Therefore, Eq. 2.37 can be generalised to

$$\boldsymbol{H}_C \approx \boldsymbol{K}_U \left(\frac{D}{L_{ex}} \right)^{2n/(4-n)} \tag{2.41}$$

where n is the dimensionality of the exchange-couple region [97], [98]. As a result, the coercivity for thin films (n=2) and nanowires (n=1) would be proportional to the second (D^2) and one-third power ($D^{(1/3)}$) of the average grain size, respectively [99], [100]. However, the model assumes the average

grain size represents the actual size of every grain, i.e., a uniform grain size. Typically, a material would have a range of grain sizes that deviates from the mean which influences the effective anisotropy of the material. The relation of the power-law behaviour of coercivity to the average grain size distribution was investigated by Bolyachkin et al. [101] using micromagnetic modelling. They measured the relation of n to the deviation of grain sizes ($\sigma/\langle D\rangle$) with the range of values between $0 < \sigma/\langle D\rangle < 0.16$, where 0 and 0.16 are defined as monodisperse and polydisperse grains, respectively. The study observed a decreasing trend from n=6 to n=3.2 from a monodisperse to a polydisperse grain structure with the reasoning of competing effects between random and induced anisotropies from the varying grain sizes (Fig. 2.24).

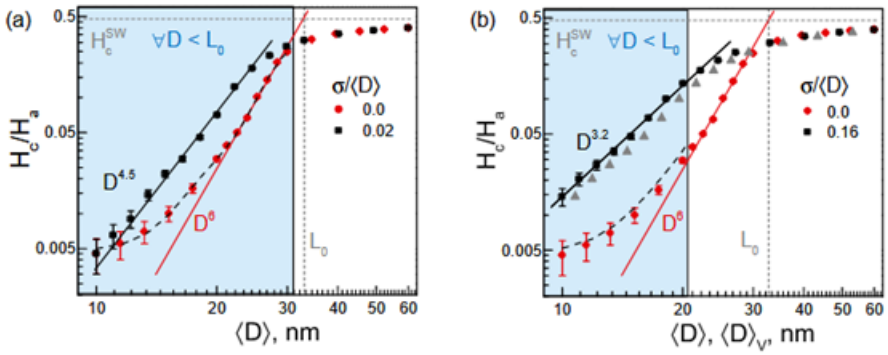

Figure 2.24: Micromagnetic modelling the relationship of the reduced coercivity on the average grain size of the monodisperse ($\sigma/\langle D\rangle = 0$) and polydisperse ensemble of (a) $\sigma/\langle D\rangle = 0.02$ and (b) $\sigma/\langle D\rangle = 0.16$. L_0 is the exchange length with the coloured region representing the grain sizes that are smaller than the exchange length [98].

Therefore, a polydisperse grain structure would have grains larger and smaller than the exchange length which induces either a magnetocrystalline anisotropy or random anisotropy. The non-uniformity of the grain size potentially increases the coercivity which would require further reduction of the

grain size to achieve a magnetically soft material of near-vanishing magnetocrystalline anisotropy. Although, this is easily accomplished in amorphous magnetic materials.

Amorphous materials are non-crystalline solids with an atomic arrangement similar to a liquid lacking any long-range ordering. The lack of long-range ordering (i.e., a crystal lattice) achieves a near-vanishing magnetocrystalline anisotropy with the exchange energy dominating the magnetisation behaviour of the material. Therefore, the magnetisation behaviour of the amorphous material is dependent on the exchange interaction between spins of neighbouring unpaired electrons between ferromagnetic atoms [102]. The strength of the interactions varies depending on the interatomic distance between the atoms correlating to the Bethe-Slater model on the exchange integral (Fig. 2.9), which would affect the material's coercivity. The interatomic distance between ferromagnetic atoms can be manipulated by adding other metallic elements into the matrix, such as metalloids, which dilute the concentration of the ferromagnetic atoms by atomic substitution, increasing the average distance between the unpaired electrons of ferromagnetic atoms. The magnetisation of a random atomic magnetisation can be approximated using the mean-field theory by considering that magnetisation is contributed only by the exchange interactions of magnetic metals (i.e., transition metals and rare-earth metals). The relation between magnetisation to the exchange interactions can be expressed as [103], [104]

$$\boldsymbol{M}_S = \frac{8 \times 10^{-7} \pi \rho}{\boldsymbol{H}_{ex} R_a^2} A \tag{2.42}$$

where $\boldsymbol{H}_{ex}$ is the (unchanged) exchange field, R_a the length over which the local anisotropy axes are correlated (short-range structural order) [105], and ρ the density of the material. Consequently, the exchange stiffness (A) is proportional to the saturation magnetisation (M_S) and the exchange stiffness

can be approximated using the mean-field theory, in conjunction with the curie temperature (T_C), using Hasegawa's model as the basis [106]. The equation for the exchange stiffness for an amorphous magnetic material can be expressed as

$$A = \frac{C_m S_m k_B T_C}{4(S_m + 1) r_{m_i - m_j}} \tag{2.43}$$

where C_m is the concentration (in atomic percent) of the ferromagnetic metal, S_m is the spin moment of the metal, k_B the Boltzmann constant, T_C is the curie temperature, and $r_{(m_i - m_j)}$ is the interatomic distance between two (closest) neighbouring magnetic atoms at sites i and j. The spin moment (S_m) can be calculated by using the formula

$$M(\mu_B) = 2 S_m C_m \mu_B \tag{2.44}$$

where $M(\mu_B)$ is the magnetic moment of the material in Bohr magnetons. However, this relation is only valid if there is only one ferromagnetic metal in the amorphous alloy (such as Fe, Co, or Ni atoms). If the amorphous alloy contains multiple magnetic metals (FeCo- or FeNi-based alloys, etc.) the effective magnetic moment of the material will be described as

$$M(\mu_B) = w M_1(\mu_B) + (1 - w) M_2(\mu_B) \tag{2.45}$$

where $M_1(\mu_B)$ and $M_2(\mu_B)$ are the magnetic moments of two different magnetic atoms (labelled with indices 1 and 2) and w is the atomic fraction ($w = M_1/M_1 + M_2$). According to Hasegawa's model of the mean-field theory, an amorphous alloy consisting of two magnetic elements (M_1 and M_2) exhibits two magnetic sublattices that interact with each other which consist of three short-range exchange interactions: m_1 – m_1, m_2 – m_2, and

m_1 – m_2 (where m_1 and m_2 are two different magnetic metals with one being ferromagnetic). Hasegawa's mean-field model provides a good description of the changing magnetisation of the material based on the relation between the exchange stiffness and concentration of the magnetic atom(s) (Fig. 2.25(a)).

Furthermore, the change in Curie temperature with relation to the exchange stiffness can also be related back to the concentration of the magnetic atoms [102], [103]. The variation of the curie temperature can be modelled using the mean-field theory (not the same as Eq. 2.43) by relating the curie temperature to the magnetic interactions of the two sublattices [107],

$$3k_B T_C = a_{11} + a_{22} + [(a_{22} - a_{11})^2 + 4a_{12}a_{21}]^{1/2} \tag{2.46}$$

in which

$$a_{11} = C_{m_1} Z_{m_1} J_{m_1 - m_1} S_{m_1}(S_{m_1} + 1) \tag{2.47a}$$

$$a_{22} = C_{m_2} Z_{m_2} J_{m_2 - m_2} S_{m_2}(S_{m_2} + 1) \tag{2.47b}$$

$$a_{12}a_{21} = C_{m_1} C_{m_2} Z_{m_1} Z_{m_2} (J_{m_1 - m_2})^2 S_{m_1}(S_{m_1} + 1) S_{m_2}(S_{m_2} + 1) \tag{2.47c}$$

where C_{m_i} is the concentration (in atomic percent) of the respective metal, Z_{m_i} are the coordination numbers of the metal, $J_{mi} - m_j$ is the exchange integral between the respective metals, and S_{m_i} is the spin moment of the respective metal. Eq. 2.46 displays a high correlation to the measured experimental data of changing curie temperature in relation to the changing concentration of the magnetic atom(s) (Fig. 2.25(b)).

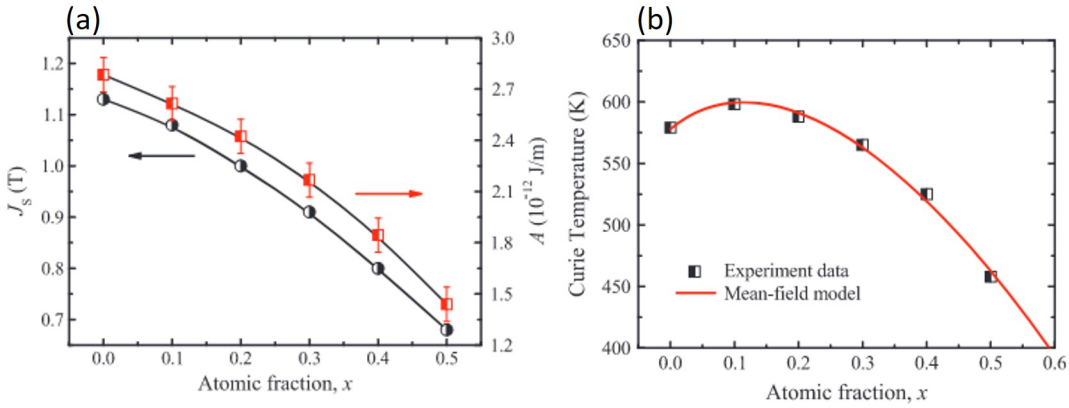

Figure 2.25: The influence of atomic fraction of the ferromagnetic atom with respect to (a) saturation magnetisation and exchange stiffness and (b) the curie temperature on bulk metallic glass $Fe_{1-x}Ni_x$-based alloy [103].

The coercivity of an amorphous material can be associated with its saturation magnetisation in relation to the exchange stiffness which encompasses the overall (average) strength of short-range exchange interactions between magnetic atoms. In addition, the influence of short- and long-range ordering has a significant influence on the magnetoelastic anisotropy by affecting both the saturation magnetostriction coefficient and the residual stresses inside the material [108], [109].

The magnitude (and sign) of the saturation magnetostriction coefficient of an amorphous material is influenced by the chemical composition of the material. This phenomenon was explained using models at the microscopic and macroscopic level of the material [110]. At the microscopic level, the magnetostriction of an amorphous material can be explained using quantum mechanical theory on the single-ion crystal field effect and two-ion anisotropic exchange [111]. The macroscopic level assumes the amorphous material is composed of many "clusters" of atoms – each "cluster" approximates a few

atomic distances – and it's treated like a grain with a magnetostriction coefficient. Each grain will have a random orientation of the magnetostriction and when the material is magnetized the grain exhibits saturation magnetostriction. During this process, all grains would rotate to minimise their local anisotropy. The grains obstructing each other's rotation induce spontaneous strain and internal stresses between them which collectively exhibits a macroscopic strain – or the magnetostriction (Fig. 2.26) [112].

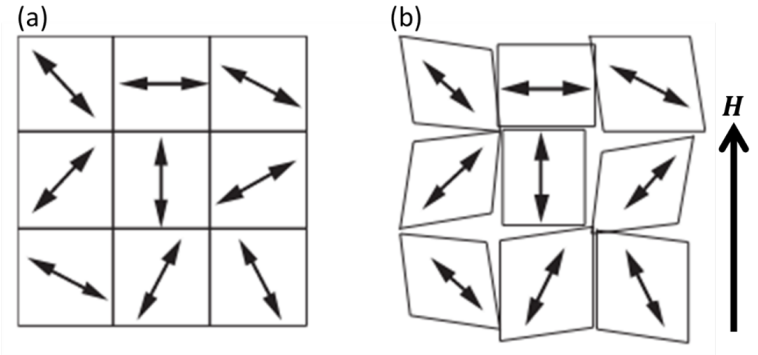

Figure 2.26: Schematic representation of the macroscopic level of the magnetostriction of amorphous metal (a) at demagnetized state and (b) magnetized state. Each block represents the "cluster" of atoms that behave as a grain with the double pointed arrow representing the local magnetostriction of the grain. The deformation of the block represents the local magnetostrictive effects in which the spontaneous localised strain and stress appear in between the grains [110].

The single-ion crystal field effect and two-ion anisotropic exchange describes the difference of the sign for the magnetostriction depending on the ferromagnetic atom (e.g., Fe-based alloys are positive magnetostriction and Co-based alloys are negative magnetostriction) and correlates the temperature dependence to the magnetostriction coefficient. The "cluster" of atoms with respect to the magnetisation describes the magnitude of the magne-

tostriction coefficient based on the total number of obstructions to each grain's rotation and correlates stress dependence to the magnetostriction. Typically, the saturation magnetostriction coefficient for amorphous materials are higher than nanocrystalline materials because of the higher number of short-range interactions with higher concentrations of residual stress in the system (Fig. 2.27).

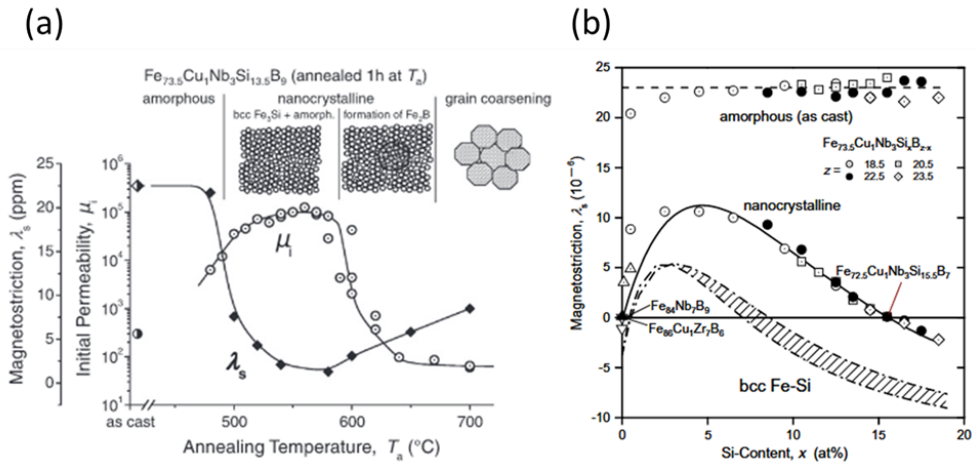

Figure 2.27: Saturation magnetostriction of amorphous and nanocrystalline of FeCuNbSiB alloy with respect to (a) annealing temperature and (b) atomic fraction of Si. The hatched area in the dashed-dotted lines in (b) is the estimate of the local magnetostriction within the BCC grains. The open triangle, solid triangle, and open nablas are the experimental data of other Fe-based alloy samples from another study [86].

Residual stress is the imbalance stress-profile throughout the volume of the material where the surface layer applies tension to the bulk with the bulk applying compression to the surface. This can be relieved through thermal annealing which is discussed in Chapter 3, section 3.5.1.iv. A near-zero magnetostriction material (softest magnetic properties) can be achieved

by a combination of stress relieving and chemical composition of particular ferromagnetic atoms within the alloy.

Overall, the effective anisotropy for an amorphous material would be dependent on the magnetoelastic anisotropy and the exchange energy. To achieve the lowest coercivity the exchange interactions have to be diluted by adding in other metallic materials that are not ferromagnetic typically metalloids (Si, Al, B etc.) and/or transition metals (Mn, Cu, etc.). These materials are selected because of their atomic size as well as their ability to stabilise (or improve) the material's glass forming ability (GFA) [113]. On the other hand, the stress relief of residual stresses within the amorphous crystal structure as well as balancing out the positive and negative magnetostrictive effects from Fe and Co atoms have to be considered as well. This is desirable for a magnetic strain sensor because of the isotropic magnetostrictive effects which translate to an isotropic magnetic behaviour throughout the material. Furthermore, the softer the material the easier it is to induce a spontaneous change in the magnetic behaviour from external mechanical stresses. The performance of an amorphous magnetic strain sensor is discussed in Chapter 3.

Chapter 3

Materials for flexible strain sensors and fundamental theory of the GMI and GSI effect

3.1 Outline

The chapter discusses functional "smart materials" and their unique properties that make them ideal for use in sensing technology. The sensing performance of existing strain sensors is investigated (involving their detectable strain range, strain sensitivity, ease of access to the technology, and dimensions) and their applicability to monitoring the expansion of nuclear waste packages. The chapter discusses the comparability of the performance of magnetostrictive strain sensors to existing flexible strain sensors.

The chapter then moves on to review existing literature on the GMI and GSI effects and the physical variables that influence these, with a particular emphasis on how these would affect the ability of the sensor based on these

effects when detecting strain.

3.2 Smart materials in sensor technology

Smart materials (also known as advanced or intelligent materials) are used in sensor technology because of their ability to respond to changes in their environment. Smart materials are difficult to uniquely define [114] because different materials that experience the same external stimuli may exhibit fundamentally different physical responses. For example, applying strain to a magnetostrictive material or a piezoelectric material results in changes in different properties. Although, smart materials possess a common behaviour to revert back to their original form when removing the external stimuli, it (strictly) cannot be used as a definition because of the different physical phenomena that enable them to revert back to their original form. The general consent from the science community is to define smart materials as "advanced materials that can respond smartly to environment changes" [114].

It is easier to categorise smart materials by their response to external stimuli which may be either active or passive in nature. Passive smart materials do not rely on the changes to their own material properties but on changes in the medium they interact with e.g., optical fibres are used as a smart material by detecting the changes in the environment from the way light propagates through them (light). Active smart materials are materials that can alter one form of energy to another form of energy e.g., piezoelectric materials can produce electrical charge when under external mechanical strain. These materials are capable of performing either in a sensor or an actuator configuration (i.e. a transducer,) where in the former cases the material undergoes a mechanical deformation and exhibits a non-mechanical response, while in the latter a non-mechanical external stimulus prompts a

mechanical deformation from the material [115]. Furthermore, these materials are able to retain their original shapes when the external stimulus is removed classifying these types of smart materials as shape memory materials (SMMs). SMMs have great versatility since their properties make them:

- Adaptable - they can respond to various types of external stimuli.
- Immediate – any change to the materials environment produces a near immediate response.
- Noticeable – the material can change appearance when any of its material property changes.
- Automated – they can function with little to no human intervention.
- Reused – can be used multiple times without becoming damaged.

There are various SMMs that are categorised as shape memory alloys, thermostrictive materials, electrostrictive materials, magnetostrictive/ magnetoelastic materials, piezoelectric materials, electroactive polymers, and electro/magnetorheological fluids. Each of these materials has a unique response to applied, external, stimulus but all have a common property of retaining their original shape in the absence of the stimulus. Smart memory materials would be convenient to use as a sensor technology for monitoring the evolving expansion of nuclear waste packages due to their; adaptability to the harsh radioactive environment, immediate change to their material property in response to an external stimulus (in this case mechanical stress/strain), automation in which the sensor can keep on functioning without human intervention, and reusable so that it can be used again if the material isn't permanently damaged/ or plastically deformed.

3.3 Applicability of flexible strain sensors on monitoring ILW waste packages

As discussed in Chapter 1, the desired properties required from a strain sensor when monitoring ILW nuclear waste packages were:

- Instantaneous response when expansion occurs.
- Flexible enough to be applied on a curved surface of an ILW waste package.
- Exhibit a noticeable change in electrical signal when under strains up to (minimum) 0.25%.
- Can cover a large surface area on the waste package body.
- Easy to obtain the technology for mass production in order to monitor thousands of waste packages.

These criteria were based on the information shared by John Jowsey [1] where the rate of strain was observed to be at least 0.25% per decade. The criteria are used as the specification for the desired strain sensor that is capable of monitoring ILW waste packages. The performance of existing state-of-the-art flexible strain sensors (of the last decade) was investigated [116, 117, 118, 119, 120, 121, 122] and summarised in Table 3.1. The flexible strain sensors and their applicability to monitoring ILW waste packages were discussed.

The first criterion "Instantaneous response when expansion occurs" is requiring the sensor technology to show a change in signal the moment it undergoes an external stimulus – in this case, mechanical strain. In order

to achieve an instantaneous response, a specific intrinsic material property that is directly (or indirectly) related to the mechanical strain or change in geometry is required. One of these intrinsic properties that fits this criterion is the resistivity of the material which relates the electrical resistance to the cross-sectional area and length of the material. As a result, strain sensors use the change of their electrical resistance as an indicator of when a material undergoes strain. Many of the investigated strain sensors use resistivity to respond to changes in strain with other sensors using capacitance or voltage to detect changes in strain. Typically, capacitive strain sensors are used to detect changes in pressure such as the hydrogel-based strain sensor ACC/PAA/Na alginate mineral hydrogel which has a sensitivity measured in per kPa. However, all sensors displayed the capability for instantaneous change when subjected to mechanical stress/strain.

The second criterion "Flexible enough to be applied on a curved surface of an ILW waste package" relates to the compliance of the sensor which defines the detectable strain range. As a result, very compliant materials such as elastomers and hydrogels can reach very high strains up to 900% or 18100%, respectively, whereas less compliant materials like carbon-based and magnetostrictive sensors reach strains at 8.1×10^{-3}% or 1.4%, respectively. Typically, higher compliance is favourable for a larger operating range, but for the application on monitoring waste packages lower compliance is favourable. Considering the rate of expansion is 0.25%, per decade, means to reliably monitor the growth of the expansion the material must be capable of detecting strains as small as 1%. Moreover, considering the time-span for monitoring the waste packages could last centuries it is probable to have a material that has an operating strain as high as 2.5%. Hence, elastomer-based, hydrogel-based, and a few textile-based strain sensors are not desirable for the application considering their high operating strains. This can be circumvented by adding stiffer materials (such as carbon nanoparticles) to reduce

the operating strain, but this could also compromise their sensitivity – as observed between LM-MRE and CNT/Ecoflex strain sensors.

The third criterion of "Exhibit a noticeable change in electrical signal when under strains up to (minimum) 0.25%" which describes the sensitivity of the sensor. For a minimum strain of 0.25%, the sensor must display a significant signal change in which the user can identify the different stages of the waste package life-cycle. This can be measured by the gauge factor (GF) which is calculated by

$$Gauge\ Factor\ (GF) = \frac{\Delta S}{S_0 \varepsilon} \tag{3.1}$$

where ΔS is the change in signal (typically between a strained and unstrained state of the sensor), S_0 is the signal before strain and ε is the applied tensile strain on the sensor. The change in signal is typically the electrical resistance (R). The gauge factor defines the fractional change of the material's electrical signal per strain. Considering the minimum strain required for the sensor to detect is 0.25% a GF value of 1 indicates an observed fractional change in signal is 2.5×10^{-3}. GF values higher than 1 are preferable since it is less susceptible to the noisiness in the measurement even if S_0 does not exhibit a high signal. Thus, sensors with a GF value in the double digits or higher are more desirable to avoid any unreliable measurements when tracking the expansion of ILW waste packages – unnecessarily increasing risk.

The fourth criterion is "Easy to obtain the technology for mass production in order to monitor thousands of waste packages". The accessibility of the technology is important since the number of waste package units is in the thousands and still rising it is vital to manufacture as many sensors as possible to keep track the many of waste packages that are undergoing expansion. Commercially available strain sensing technologies are highly favourable since

they can be used immediately with the desired quantity. In addition, if the fabrication process for the strain material is inexpensive and simple then it is just as favourable. As such, the carbon-based, PVDF (PEDOT+CNT coating)/Ag/PET, paper-based, some polymer-based, and magnetostrictive sensors are suitable considering they are either commercially available or have simple fabricating methods for mass production.

The last criterion is "Can cover a large surface area on the waste package body" which is relevant for waste packages undergoing global expansion. John Jowsey (and the other members of Sellafield Ltd) have confirmed that at some point waste packages that initially expanded locally will transition to a global expansion. To monitor global expansion the sensor has to cover a sufficient surface area that can accurately monitor either the change in diameter or height of the waste package. In addition, the staff at Sellafield Ltd have observed the start of the expansion consistently begins at the bottom third of the waste package body. Therefore, the length of the sensor has to be (maximum) 300 mm or 800 mm in length when monitoring the expansion. Currently, many of the flexible strain sensors were designed with dimensions of 100 mm in length which is too small for monitoring global expansion (especially around the diameter). Potentially, polymer-based strain sensors such as GWF/PDMS, paper-based, or magnetostrictive materials can be designed at much higher lengths than their reported dimensions because of their simple fabrication methods. The more inexpensive the starting materials the easier it is to mass produce and fabricate large strain sensors, such as the graphite/paper sensor can increase in size by having a larger A-size paper (i.e., A0).

Overall, the best candidates that are considered to be applicable as strain sensors for monitoring ILW waste packages are GWF/PDMS, rGO/PDMS, graphite/paper, and cobalt-based alloy smart materials. In this thesis, mag-

netostrictive materials were selected as the material of study as strain sensors for monitoring ILW waste packages.

3.4 Magnetostrictive strain sensors

In recent years there has been a large interest in researching magnetostrictive materials as possible stress/strain sensors. In these proposals a material's magnetoelectric properties change when they are subjected to an external mechanical stimulus [45]. This phenomenon is based on the inverse magnetostrictive effect (Villari effect) where an applied external mechanical stimulus induces a change in the material's magnetic anisotropy. This may then manifest via a number of different magnetoelectric effects: the anisotropic magnetoresistance effect (AMR), the giant magnetoresistance effect (GMR), the tunnel magnetoresistance effect (TMR), the giant magnetoimpedance effect (GMI), and the giant stress-impedance effect (GSI) [123]. Each of these magnetoelectric effects was investigated as a possible strain sensor examining the existing literature and their sensor performances were compared to each other, as shown in Table 3.2.

Table 3.2 reveals multiple studies on the influence of stress/strain effects on magnetostrictive materials. However, the strain measured is typically around 1% or smaller which may explain the lack of inclusion amongst the recent flexible strain sensors, considering the function of a strain sensor requires a high operating strain as possible. A caveat among the researched literature for magnetostrictive strain sensing materials was that some of the literature on the GMI and GSI effects did not include a GF nor E values as part of their report when investigating the material's sensing performance. Hence, it was not possible to compare the sensor performance of these materials directly to the others. However, a conservative estimate can be applied

to them by applying a E value for a typical Co-based amorphous metal ribbon/wire under cold-worked treatment. This would not be perfectly accurate as it is known the Young's modulus differs between ribbon and wire-shaped samples [124, 125]. As a result, the data in Table 3.2 reflects the order of magnitude of the material's sensitivities, rather than precise values. Assuming the calculated GF values are at the correct magnitude indicates that magnetostrictive sensors have a lot of promise for high-performing low strain sensors.

Using the five criteria, the best candidate for monitoring nuclear waste packages was the Co-based alloy ribbon with 1.4% strain detection and a GF value of -80. Other candidates of magnetostrictive materials were not selected either because of the low operating strain, geometry of the material, or complex fabrication process. Magnetic materials with a strain under 0.25% were ignored since it would not operate long enough to sufficiently monitor a visible change on the expanding waste package. Furthermore, any magnetic strain sensors that operate only in a wire-form were not considered since it would not be capable of covering a surface area compared to ribbon-form sensors. This can be improved by using a composite material with the magnetostrictive wire embedded in a polymer matrix, such as glass-coated CoFeSiB within 913 E-glass prepreg which can cover a larger surface area, though, this could lower the sensing performance of the wire material. Lastly, considering the number of waste packages that have to be monitored, materials with a simple fabrication process (or commercially available) are preferred for mass production purposes. AMR, GMR, and TMR had fabrication processes that require specific magnetic materials that can exhibit these magnetoelectric effects. Through the process of elimination, GMI and GSI strain sensors were the only viable options that can fulfil all criteria. Of the two, only the Co-based (CoFeSiB) ribbon alloy was considered the best.

In order, to understand the GSI effect and its magnetic behaviour on amorphous ribbons a literature review on the physical variables of the GSI effect was conducted. However, currently, there are not many studies on the application of GSI strain sensors with more studies on investigating the physical variables influencing the GSI effect, such as annealing and applied stress/strain. The amount of research on the GSI effect is not as extensive compared to the GMI effect, but, fundamentally, the GSI effect has very close parallels to the GMI effect. Hence, a literature review on both the GMI and GSI effects was investigated to identify all physical variables that have an impact on optimising the sensing performance of a GSI strain sensor.

Classification of flexible material	Smart material	Type of response	Material Composition	Synthesised or commercially available	Size (l x w x t)	Detectable strain range (%)	Sensitivity
Polymer-based	Nanographene film	Resistive	Graphene on top of PMMA substrate	Synthesised	500 µm x 500 µm x ~1 µm	0 – ~1.6	GF – ~600
	GWF/PDMS	Resistive	Graphene woven fabrics (GWF) embedded in a PDMS matrix	Synthesised	Not reported	0 – 8	GF – ~10^3 (between 2 – 6% strain) GF – ~10^6 (strains higher than 6%)
	FGS/SBS/Ag	Resistive	Fragmentized graphene sponges (FGS) in poly(styrene-block-butaidene-block-styrene) (SBS) matrix with absorption and reduction of silver (Ag) precursor to form nanoparticles	Synthesised	Not reported (Estimated length and width to be 15 mm and 4 mm, respectively, from image length scale. Thickness cannot be estimated)	10 – 120	GF – ~10^7
	PU/AgNW/rGO	Resistive	Reduced graphene oxide (rGO) and silver nanowires (AgNW) hybrid particles in polyurethane matrix (PU)	Synthesised	30 mm x 5 mm x 300 µm	0 – 1	GF – ~560 (at 0.6% strain)
	rGO/PDMS	Capacitive	Reduced graphene oxide (rGO) nanoparticles in a polydimethylsiloxane (PDMS) matrix	Synthesised	40 mm x 10 mm x 500 µm	0 – 4	GF – (-)18.6
	Ag/ HfO_2/n-ZnO	Resistive	Sensor Zinc oxide (ZnO) micro/nanowires coated with hafnium(IV) Oxide (HfO_2) with silver (Ag) contacts Substrate Polyethylene terephthalate (PET)	Synthesised	Sensor Diameter: ~8 µm (thickness of coating ~1.8 nm) Substrate 30 mm x 5 mm x 150 µm	0 – 0.10	GF – ~4.8×10^5
	PVDF (PEDOT+CNT coating) /Ag/PET	Potential	Sensor Polyvinylidenefluoride (PVDF) film both sides coated with Poly(3,4-ethylenedioxythiophene) (PEDOT) & carbon nanotubes (CNT) composite. Both sides further coated with silver (Ag) contacts. Substrate Polyethylene terephthalate (PET)	Commercially available (Fils, Korea)	Sensor Length and width not reported (Presumed to be ~10 x 10 mm^2) Thickness: 80 µm Substrate Length and width not reported (Presumed to be ~10 x 10 mm^2) Thickness: 10 µm	0 – 25	8.92 V/mε
Elastomer-based	Graphene/NR	Resistive	Graphene infused into natural rubber (elastic bands)	Synthesised	Width not reported Length: 15 mm Thickness: 450 – 500 µm	0 – ~800	GF – 35

Table 3.1: List of recent flexible strain sensing technologies (of the past decade) with reported strain and sensitivity performances. References are ordered [126, 127, 128, 129, 130, 131, 132, 101]

Elastomer-based	LM-MRE	Resistive	Liquid metal (LM) GaInSn is placed inside a channel of a magnetorheological elastomer consisting of 60 wt% carbonyl iron particles (CNP) in a polydimethylsiloxane (PDMS) matrix elastomer (MRE).	Synthesised	Magnetorheological elastomer (MRE) 50 mm x 15 mm x 1 mm Channel for liquid metal 100 mm x 500 µm x 300 µm PDMS layer 50 mm x 15 mm x 2 mm	2 – 10	GF – ~3.53
	CNT/Ecoflex	Resistive	Carbon nanotube (CNT) yarn on Ecoflex substrate (covered by a thin coat of Ecoflex)	Synthesised	Not reported	0 – 960	GF – 0.54 (between 2 – 400% strain) GF – ~64 (between 400 – 960% strain)
Hydrogel-based	ACC/PAA/Na alginate mineral hydrogel	Capacitive	Amorphous calcium carbonate (ACC) nanoparticles cross-linked by polyacrylic acid (PAA) and (sodium) alginate chains	Synthesised	Not reported	0 – ~55	~0.17 kPa^{-1}
	AgNWs/AAM	Resistive	Silver nanowires are embedded in a polymer network of polyacrylamide (AAM) matrix	Synthesised	2.5 mm (gauge length) x 10 mm x 2.5 mm	0 – 18100	GF – 0.71
	MXene + PDA/Ni^{2+}	Resistive	Silver (Ag) nanowire in nanocomposite film made from Mxene titanium carbide ($Ti_3C_2T_x$) nanosheet "brick" and poly(dopamine) (PDA)/Ni^{2+} "mortar" structure	Synthesised	20 mm x 3.5 mm x ~0.8 µm	0 – 15 15 – 35 35 – 60 60 – 77 77 – 83	GF – ~256.1 GF – ~433.3 GF – ~1160.8 GF – ~2209.1 GF – ~8767.4
Textiles-based	CNT yarn	Resistive	Carbon nanotube (CNT) ribbons woven into a yarn	Synthesised	Length: 10 mm Diameter: 3 – 30 µm	0 – ~1	GF – ~0.5
	CNT/EVA	Resistive	Ethylene vynil acetate (EVA) fibres coated with carbon nanotubes (CNT)	Synthesised	Length not reported Diameter: ~203 µm (CNT have lengths ranging between 20 – 30 nm)	0 – 88 88 – 190	GF – ~3.25 GF – ~33.29
	ZnONW/PET (coated in CNT/rGO)	Resistive	Polyethylene terephthalate (PET) fibres coated with carbon nanotubes (CNT) and reduced graphene oxide (rGO) with zinc oxide (ZnO) nanowires grown on the surface	Synthesised	CNT/rGO coated textile fibre Diameter: 40 µm Pore size: 50 x 50 $µm^2$ Zno nanowire Diameter: ~80 µm Length: ~1.8 µm	0 – ~6.2	GF – ~7.64
Carbon-based	Carbon-carbon composite (Sigrabond C/C)	Resistive	Biaxially woven carbon fibre carbon-matrix composite	Commercially available (SGL Carbon)	203.2 mm x 152.4 mm x 1.4 mm	0 – $8.1x10^{-3}$	GF – (-)7804 ± 429

Table 3.1 continued. References for each strain sensor are ordered [133, 134, 135, 136, 137, 138, 139, 140, 141]

Paper-based	Graphite/Paper	Resistive	Drawing graphite lines using a graphite pencil on Xerox paper	Synthesised	40 mm x 5 mm x ~100 µm	0 – 0.62	GF – ~60.7 (for strains up to 0.32%) GF – ~536.6 (for strains higher than 0.32%)
Magnetostrictive/ Magnetoelastic	Cobalt-based alloy	Resistive	Melt-spun ribbons with chemical composition of CoFeSiB	Synthesised	100 mm x 530 µm x 66 µm	0 – 0.75	N/A **{GF ~(-)8}***
	Cobalt-based alloy	Resistive	Melt-spun ribbons with chemical composition CoFeSiB	Synthesised	50 mm x 0.53 mm x 66 µm	0 – 1.4	GF – (-)80

Table 3.1: continued. *The gauge factor was estimated based on the change in signal to strain that was reported in the literature. References are ordered [142, 143, 43]

Magnetic Sensor	Underlying physics	Material used	Size (l x w x t)	Strain range (%)	Sensitivity
Anisotropic magnetoresistance (AMR)	The resistance change of the material is dependent on the relative angle of the directions between the magnetization of the material and the direct current.	Sensor: Thin film of Permalloy (Py) strips wrapped around in gold (Au) at 45° angle (barber pole formation). Substrate: Polyethylene terephthalate (PET)	Sensor 800 µm x 300 µm x 130 nm Substrate Length and width not reported Thickness: 100 µm (*Device can be used on an index finger*)	~0.25 – 1	GF ~ 29.6
Giant magnetoresistance (GMR)	The resistance of a structure, consisting of a non-magnetic conductor sandwiched between two magnetic layers, can change depending on the relative orientation between the magnetization direction between the two magnetic layers with respect to the driving current. These sensors have their layers designed with one layer having a fixed magnetization direction (known as a pinned or reference layer) and the other layer having a free-moving magnetization in relation to the external stimulus, in this case applied stress/strain.	Sensor: Co/Cu/Py trilayer thin film (with the addition of Tantalum (Ta) and Platinum (Pt) layers) Substrate: Polyethylene naphthalate (PEN)	Sensor 200 – 350 µm x 30 µm x 16 nm Substrate Length and width not reported Thickness: 38 µm	0 – ~1	GF ~ 2.5 (with an applied field of 200 Oe)
Tunnel magnetoresistance (TMR) or tunnel magnetic junction (TMJ)	Structurally similar to GMR, but instead of a non-magnetic conductor the layer consists of an insulator/ tunnel barrier. The probability of electrons tunnelling through the barrier depends on the relative orientation between the magnetization direction between the two magnetic layers.	Sensor: CoFeB/MgO/CoFeB (CoFeB reference layer was magnetically stabilised using MnIr/CoFe/Ru layers) Substrate: Si/SiO	Sensor & Substrate Diameter: 11.3 µm (Thickness of substrate was not reported but sensor was ~6 nm)	0 – 0.6	GF ~ 400 (up to 0.2% strain)

Table 3.2: List of flexible magnetostrictive strain sensors with reported (or estimated) strain and sensitivity performance. References are ordered [144, 145, 146]

Giant magnetoimpedance (GMI)	The change in the material's electrical impedance when subjected under an applied magnetic field with a driven alternating current.	CoSiFeB	Length: 50 mm Diameter: 28 µm	Not available **{0 – 0.07}***	N/A **{GF ~600}***
		Glass coated CoFeSiB within 913 E-glass prepreg – Glass fibre and epoxy resin matrix (4 layers)	CoFeSiB Diameter: 29.4 µm Length: 10 mm 913 E-glass 10 mm x 20 mm x 640 µm	Not available **{0 – 0.43}***	N/A **{GF ~245}***
		CoFeNiSiPB	20 mm x 0.8 mm x 25 µm	Not available **{0 – 0.17}****	N/A **{GF ~168}****
Giant stress-impedance (GSI)	The change in the material's electrical impedance when subjected under an applied tensile stress with a driven alternating current.	Glass coated CoFeSiB within 913 E-glass prepreg – Glass fibre and epoxy resin matrix (4 layers)	CoFeSiB Diameter: 29.4 µm Length: 10 mm 913 E-glass 10 mm x 20 mm x 640 µm	Not available **{0 – 0.43}***	N/A **{GF ~145}***
		CoFeNiSiPB	20 mm x 0.8 mm x 25 µm	Not available **{0 – 0.17}****	N/A **{GF ~210}****
		CoFeSiB	50 mm x 0.53 mm x 66 µm	0 – 1.4	GF ~-80

* The literature does not provide a measured strain nor GF value for their sample(s) thus are labelled "not available", but a conservative estimate for measured strain and GF value can be calculated by determining a "typical" Young's modulus (E) for a Co-based amorphous microwire, which was reported to be ~140 GPa, based on [13]. Strain of the material would be calculated using $\varepsilon = \sigma/E$ and sensitivity would be calculated using $GF = \Delta S/S_0\varepsilon$, where ΔS is the difference in signal before and after applied strain and $S_0$is the signal before applied strain.

** Unlike microwires, Co-based amorphous metals with a ribbon geometry typically have a lower E value. Basing it on studies done by J.Konieczny et al. [14] a conservative estimate for a Co-based amorphous ribbon can be ~60 GPa.

Calculated values for applied strain and GF values are allocated in {}.

Table 3.2: Continued. References for each strain sensor are ordered [147, 148, 149, 148, 149, 43]

3.5 GMI and GSI effect

The GMI and GSI effects are both defined as a change in the impedance of the magnetic conductor when under an external stimulus [150, 45]. The GMI effect is expressed as [150]

$$GMI = 100\% \times \frac{Z(H) - Z(H_{max})}{Z(H_{max})} \tag{3.2}$$

whereas the GSI effect is expressed as [45]

$$GSI = 100\% \times \frac{Z(\sigma_{max}) - Z(0)}{Z(0)} \tag{3.3}$$

$Z(H)$ is the measured impedance at an applied field, $Z(0)$ is the measured impedance in an absence of stress, $Z(H_{max})$ and $Z(\sigma_{max})$ are both measured impedance at the maximum applied field and tensile stress, respectively.

Both the GMI and GSI effects are determined by the classical skin effect which is expressed as,

$$\delta_m = \sqrt{\frac{2\rho}{\mu_{\phi/T}\omega}} \tag{3.4}$$

where δ_m is the skin depth, ω is the angular frequency ($2\pi f$) of the AC current, ρ is the electrical resistivity of the magnetic conductor, and $\mu_{\phi/T}$ is the circumferential (ϕ) or transverse (T) permeability of a circular (wires) or planar (ribbons and films) magnetic conductor, respectively [46]. The skin effect contributes to the varying impedance of the conductor based on the relative distance the skin depth is to the surface of the magnetic conductor. The closer the skin depth is to the surface the larger the impedance and the

further the skin depth is from the surface the smaller the impedance. The skin depth of the magnetic conductor is dependent on the circumferential or transverse permeability of the conductor – depending on its shape geometry. The permeability is proportional to susceptibility (χ) which can change depending on the ratio between the magnetization ($\boldsymbol{M}$) of the magnetic material and applied field ($\boldsymbol{H}$), according to Eq. 2.5 and 2.6.

Therefore, both the GMI and GSI effects have, fundamentally, identical phenomenological behaviour. The differences are from the external stimulus in which the permeability changes either from applied magnetic field (Zeeman energy) or applied mechanical stress/strain (magnetoelastic anisotropy).

3.5.1 Variables that influence the GMI effect

A number of variables influence the GMI effect of magnetoelastic materials, which include:

- The frequency of the driven alternating (AC) current
- The magnetostriction coefficient (λ_S)
- The fabrication technique
- The annealing treatment
- The aspect ratio

3.5.1.i Frequency

The underlying physics of the GMI effect can be split into three different regimes depending on the frequency of the applied AC current [46, 151, 152, 153]:

(i) Low-frequency regime (Quasistatic model) ($f < 1$ MHz)

(ii) Intermediate-frequency regime (Eddy current and domain model) ($\sim 0.01 \leq f \leq 1000$ MHz)

(iii) High-frequency regime (Electromagnetic and exchange-conductivity model) ($f \geq 1000$ MHz)

Each model describes the varying GMI behaviour with relation to the changing magnetic permeability (μ) in which the larger the change the higher the GMI signal. All models use the assumption the magnetic permeability of the material is contributed by the dynamic interaction between the domain wall motion (μ^{dw}) and magnetisation rotation (μ^{rot}), expressed as

$$\mu = \mu^{dw} + \mu^{rot} \tag{3.5}$$

The quasistatic model assumes the GMI behaviour is dependent on the change of the material's inductance (L) termed as the "magnetoinductive effect" [152, 154]. At this regime the skin effect is very weak where the skin depth exceeds the radius/thickness of the magnetic conductor.

Squire et al. [155] and Knobel et al. [152] explained the interaction between the domain wall motion and magnetisation rotation at frequencies lower than 1 MHz, based on the assumption of the minimization of free energy where the domain structure ignores the dynamic effects related to the rapid motion of magnetisation. As a result, the quasistatic model assumes the domain wall motion and magnetisation rotation are at an equilibrium state at all moments with respect to applied field [152, 155, 156], (Fig. 3.1). As a result, the higher the applied field the lower the magnetic susceptibility (χ) of the material – decreasing the magnetic permeability of the material – which increases the GMI ratio. The accuracy of the model to the experimental data

displayed good correlation observed by Machado et al. [157] when studying the GMI behaviour of a CoFeSiB ribbon at frequencies under 1 MHz (Fig. 3.2(a)).

Unlike the quasistatic model, the eddy current and domain model includes consideration of dynamic magnetisation effects, for example those of domain wall motion and magnetisation rotation. This becomes relevant at frequencies between ∼0.01 MHz to 1000 MHz. Including the dynamic effects between the magnetisation rotation and domain wall motion involves the presence of a damping factor where the domain wall motion gets dampened by eddy currents which becomes more dominant at higher frequencies – typically over 1 MHz [46, 152, 158]. Eddy currents are formed by the induced changing magnetic field from the AC current, in the conductor, thus the higher the frequency the faster the switching of the induced field which increases the eddy currents present – further dampening the domain wall motion. The interaction between domain wall motion, magnetisation rotation, and the damping factor with increasing frequency is related to the skin effect of the magnetic conductor. The skin effect at this frequency regime is dominant and depending on the skin depth relative to the thickness/radius of the magnetic conductor the GMI response will vary.

The correlation of the model to the experimental data was observed by Panina et al. [159] by observing the GMI behaviour of amorphous FeCoSiB wires between 0.01 MHz to 100 MHz frequency range. The model displays a good correlation to the experimental data in which the shape of the GMI curves were similar, but not at the correct magnitudes (Fig. 3.2(b)). Although not highly precise, it implies the underlying physics in the GMI effect between the 0.01 to 100 MHz frequency range is accurate. Another study done by Gonzalez-Legarreta et al. [160] observed the eddy current and domain model can be observed and modelled at frequencies up to 1000 MHz,

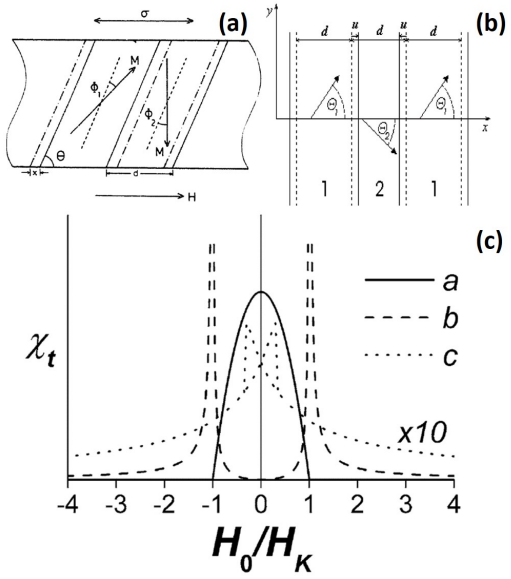

Figure 3.1: (a) Squire et al. [155] illustrated the geometry of domain structure in the quasistatic model where θ is the angle of easy axis relative to the x - axis, $\phi_{1,2}$ represent the angle of rotation of the magnetic moment $\boldsymbol{M}$ with respect to the easy axis θ, d is the domain size where the motion of the domain wall is represented by x, $\boldsymbol{H}$ is the applied field to the magnetic material along the x-axis and the σ is the applied stress to the magnetic material. (b) Knobel et al. [152] illustrated the change in angle of rotation of magnetic moment when either an applied field $\boldsymbol{H}$ or stress σ is subjected to the material which is indicated by $\Theta_{1,2}$ and the change in domain d wall motion u [155, 156], [51]. (c) Relationship of the transverse susceptibility χ_t to the external field $\boldsymbol{H}_0$: (a) $\boldsymbol{H}_0$ $\perp$easy axis ($\theta = 0$): domain wall motion, (b) $\boldsymbol{H}_0$ $\perp$easy axis ($\theta = 0$): magnetisation rotation, (c) $\boldsymbol{H}_0$ $\|$easy axis ($\theta = 90$): magnetisation rotation [151, 152].

albeit with similar precision as the previous study.

At frequencies over 1000 MHz the observed GMI behaviour can be described using the electromagnetic and exchange-conductivity model where it includes the exchange interaction with the magnetisation rotation on the assumption the domain wall motion is completely damped. Hence, the permeability of the magnetic material is dependent on the magnetisation rotation in relation to the exchange interaction which is difficult to be modelled since it requires the exact solutions between the Maxwell and Landau-Lifshitz equations (i.e. understanding the complexity of the magnetic domain structure, inhomogeneous electrical and magnetic properties and the exchange interactions between the material and applied field [150, 46, 151, 152]). However, Yelon et al. [161] reported the GMI effect could be modelled easier if the resonant condition of the material was achieved – the magnetization between the internal magnetic field of the material and the magnetic moments are in resonance – since the ferromagnetic resonance (FMR) phenomenon takes into account the exchange phenomenon. This was proven by Menard et al. [162] where the model displayed high precision to the experimental data at frequencies up to 6000 MHz (Fig. 3.2(c)).

The frequency of the AC current has a huge impact on the GMI response of the material and depending on the frequency regime the material may exhibit its maximum GMI ratio, which is sometimes labelled as the critical frequency (f_0) [48, 49]. The critical frequency of an amorphous metal is heavily dependent on other variables, such as the aspect ratio, magnetostriction coefficient, and the annealing treatment of the amorphous metal.

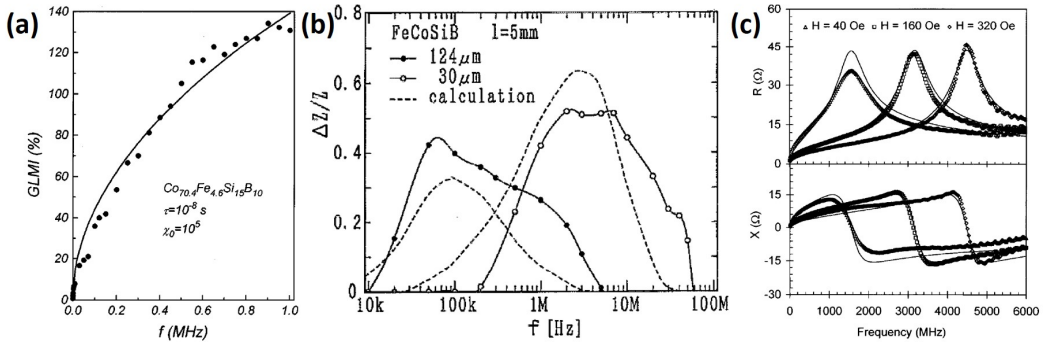

Figure 3.2: Comparison between the theoretical model and the experimental data using (a) quasistatic model [157], (b) eddy current and domain wall model [159], and (c) the electromagnet and exchange-conductivity model [162]. The samples used for the experimental data for each model were; amorphous CoFeSiB ribbon, Fe-Co-Si-B amorphous wire with common length of 5 mm with differing diameters; 124 μm as-cast wire (close dots) and 30 μm tension annealed wire (open dot), and 125 μm diameter amorphous CoFeSiB wire at three applied fields, respectively.

3.5.1.ii Magnetostriction coefficient

The magnetostriction coefficient describes the material's magnetoelastic anisotropy behaviour defined by the internal residual stress distributions of the material from fabrication processes [110]. In amorphous materials, the overall magnetostriction coefficient is the average of localised magnetostrictive anisotropies from the exchange interactions between a "cluster" of ferromagnetic atoms. Depending on the microstructure and the chemical elements the material's magnetostriction coefficient can change in both magnitude and sign (chapter 2, section 2.5.2), which results in different GMI behaviours.

The difference in GMI behaviour is (typically) attributed to the sign of the magnetostriction coefficient where a material can either possess a positive, negative, or near-zero (vanishing) magnetostriction. The sign of the coefficient causes differing domain structures within the magnetic material. Cylindrical magnetic materials (such as wires) possess two domain structures located at the central (inner core) and surface (outer shell) regions. The inner core is dominated by axial anisotropy (which is magnetostatic in origin [163]) which results in a domain structure parallel to the wire axis (labelled as "Axial domain" in Fig. 3.3). This is present regardless of the sign of the magnetostriction coefficient. However, the outer shell domain structure would change depending on the sign where a positive sign would have radial orientated domains, perpendicular to the wire axis, whereas a negative sign would have circumferential orientated domains, on the circumferential surface of the wire (labelled as "Shell domain" in Fig. 3.3). Planar magnetic materials (such as ribbons) with positive magnetostriction possess more domains oriented longitudinally (parallel to the ribbon long axis), and with negative magnetostriction, domains are more transversely orientated (perpendicular to the ribbon long axis) throughout the surface of the ribbon [46] (Fig. 3.3).

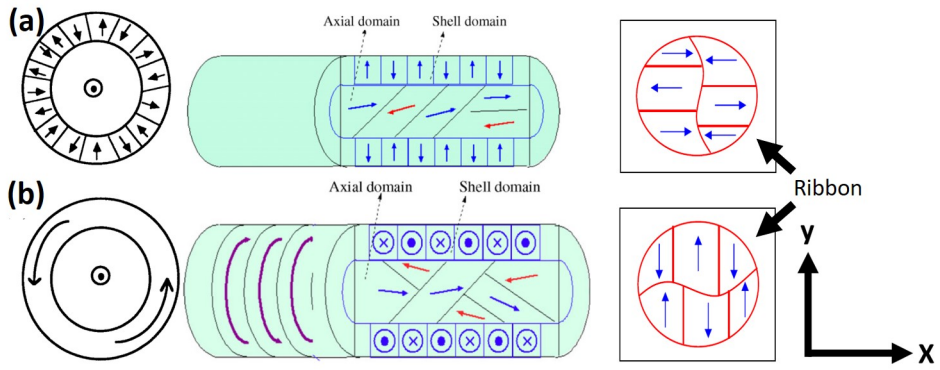

Figure 3.3: Schematic of domain structure configuration for (a) positive magnetostriction and (b) negative magnetostriction for cylindrical and planar magnetic conductor [46, 164, 165]. The cross-section highlighting the axial and shell domain structures is orientated parallel to the cylindrical axis but is shown perpendicularly for convenience. The ribbon axis is along the x-axis.

A near-zero magnetostriction is slightly different depending on the form of the material. For wires, the domain structure was reported to be similar to a negative magnetostrictive wire, but its true domain structure was not physically well defined [46]. For ribbons with near-zero magnetostriction both longitudinal and transverse domains are reported to be present in the material [46] (Fig. 3.4).

The difference in magnitude of the GMI ratio is dependent on the transverse permeability (or circumferential permeability) of the material. Therefore, the larger the change in the transverse permeability with the applied field the larger the change in the skin depth which will drastically increase the GMI ratio of the material. This was observed by Garcia et al. [166] where the magnitude of the GMI ratio between three wires with different magnetostriction coefficient signs (Fig. 3.5).

Evidently, a material that has a domain structure predominantly in the

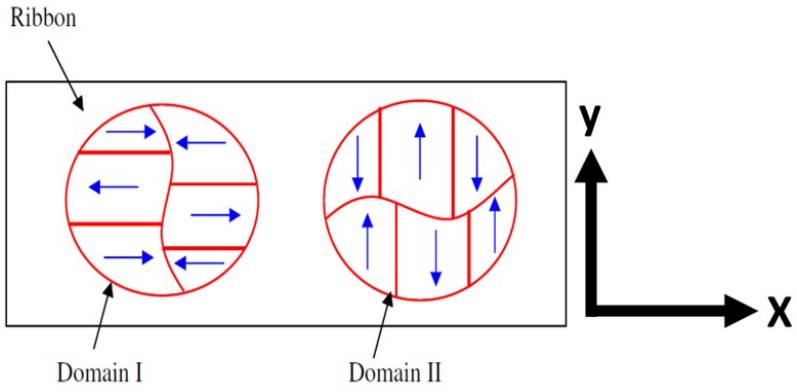

Figure 3.4: Schematic of near-zero (vanishing) magnetostrictive domain structure of an annealed amorphous ribbon illustrating containing both positive and negative domain structures as domain I and domain II, respectively [46], [165].

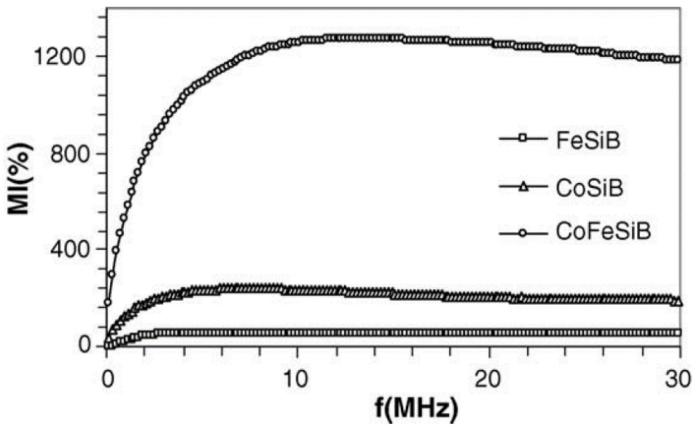

Figure 3.5: Difference in magnitude of the magnetoimpedance ratio between positive (FeSiB, $\lambda_S \approx 25 \times 10^{-6}$), negative (CoSiB, $\lambda_S \approx -3 \times 10^{-6}$), and near-zero (CoFeSiB, $\lambda_S \approx -0.1 \times 10^{-6}$) magnetostrictive wires [166].

transverse orientation displays a higher GMI ratio compared to a domain structure having a longitudinal orientation. However, the magnitude of a negative magnetostriction coefficient does not correlate to a higher GMI ratio as shown with the near-zero magnetostrictive wire exhibiting a GMI ratio about ten orders of magnitudes higher. This huge difference in ratio is based on the magnetic softness associated with the magnetic interactions occurring in the microstructure of the material [167] (discussed in chapter 2, section 2.5.2). Magnetic softness, comparable to near-zero magnetostriction, can be achieved by a combination of fabrication techniques and annealing treatments in which the key parameter is to have a domain structure that is transverse as much as possible.

3.5.1.iii Fabrication techniques

The materials that have been discussed, are categorised as metallic glasses which are described as metallic materials with an amorphous (or nanocrystalline) crystal structure. These are also suitable for magnetostrictive sensors because of their soft magnetic properties. The "soft" nature means the material's magnetic anisotropy can easily change when modest magnetoelastic anisotropies are introduced, thus when applying either a tensile stress/strain or a magnetic field the magnetoelectric behaviour of the material changes accordingly. This magnetic softness is due to the low coercivity due to the grain size being smaller than the exchange length (l_{ex}), as discussed in chapter 2, section 2.5.2.

There are many fabrication techniques that can produce metallic glasses at varying thicknesses and forms. Apart from specific techniques, the common method to achieve nano-scale grain size is to quench the molten alloy as soon as it is drawn to the desired morphology. The cooling rate from quenching can range between 10^3 – 10^8 K/s depending on the technique.

Each technique is presented in Table. 3.3 with a summarised detail on the procedure, product, and range of cooling rates.

The magnetic properties of metallic glasses are dependent on the chemical composition and the structural arrangement of atoms, which affect the total magnetic anisotropy. The structural arrangement of atoms can be manipulated by cooling rate [183], glass layer thickness [184], and chemical configuration – particularly metalloids. Chapter 2, section 2.5.3, briefly mentions the glass forming ability (GFA) where the inclusion of metalloids (i.e., silicon, boron, carbon etc.) stabilises the amorphous state of the material. This was observed by Geng et al. [185] where the glass transition temperature (T_g) increased by ∼70 K when increasing the Zr atomic concentration from 0 to 0.6% in Fe-B-Si-Zr alloy. The increasing presence of Zr introduced more atomic pairs with the silicon atom which contributed to the thermal stability of the amorphous phase. As a result, this reduces the chance of any grain nucleation and maintains a near-vanishing magnetocrystalline anisotropy, thus keeping its soft magnetic behaviour. Moreover, the inclusion of other small atomic radii metalloids such as aluminium, boron, and copper also improves the magnetisation saturation of the metal which further improves the softness of the material [113].

The influence of surface roughness on the GMI response of the material has been observed especially at frequencies where the skin effect is dominant (0.01 – 1000 MHz range). The skin effect describes the distribution of the AC current throughout the conductor, as such when the skin depth gets smaller the higher the current density is at the surface of the conductor. Hence, at higher frequencies where the skin depth is close to the surface of the conductor the GMI behaviour is mainly contributed by the magnetic behaviour at the surface – also known as surface anisotropy. Jiang et al. [186] explain the impact of surface anisotropy is contributed by the surface magnetization of

Technique	Process	Form of the product	Typical thickness/diameter (μm)	Typical cooling rates (K/s)
Melt spinning	Molten alloy is ejected as a melt stream and cooled rapidly (by a cooling fluid) and is collected on a rotating drum.	Wire	1 – 300	$10^4 – 10^6$
In-rotating water spinning	Molten alloy is ejected into a rotating drum covered with water (the cooling fluid).	Wire	30 – 300	$10^5 – 10^6$
Taylor-wire process	The metal alloy is placed inside a glass tube and is then melted by induction heating. The molten liquid softens the glass in the glass tube which is then drawn as a glass-covered molten liquid. The product gets cooled by a cooling fluid and gets collected on a rotating drum.	Wire	2 – 100	$10^3 – 10^6$
Glass-coated melt spinning	A modification of the Taylor-wire technique where the molten alloy is placed into an already softened glass cover which is immediately drawn. The product is cooled by a water jet immediately after the product is formed.	Wire	3 – 50	$10^4 – 10^7$
Electrodeposition	A solution of a magnetic alloy (e.g., FeNi) is used to coat the surface of a non-magnetic conductor (e.g., Cu) by using current between two electrodes. Afterwards the product is pressed between two rotating rollers to obtain a smooth surface. Additional layers of magnetic material could be applied.	Wire, ribbon, or thin film	20 – 1000	-
Single roller melt spinning	Molten alloy is ejected onto a single copper drum roller. The copper drum is cooled by the cooling fluid (typically a liquid).	Ribbon	15 – 25	$10^6 – 10^8$
Sputtering	The atoms of the of the surface of a magnetic alloy are removed from the impact of energetic ions. These atoms are then captured on a substrate where a thin film of magnetic material is formed. Typically, a multiplayer thin film of multiple magnetic materials is formed with this method.	Thin film	0.1 – 10	-

Table 3.3: List of fabrication techniques used to design different forms and thickness/diameter of amorphous metals. References for each fabrication technique are ordered [168, 169], [170, 171], [172], [173, 174, 175], [176, 177], [178, 179], [180, 181, 182]

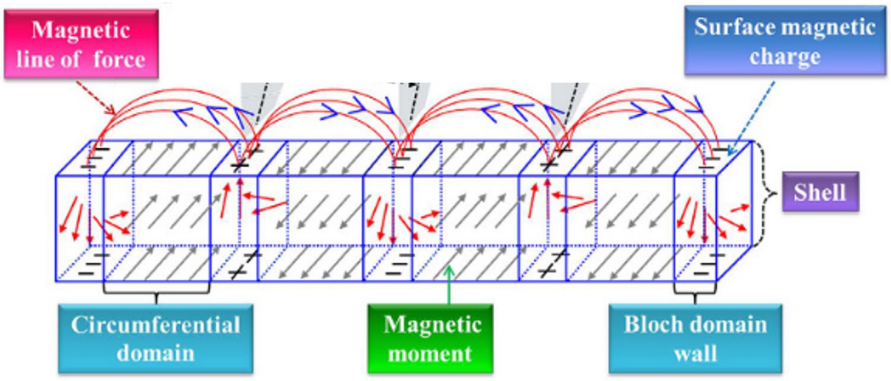

Figure 3.6: Schematic diagram of the surface anisotropies on a Co-rich microwire with stray fields generated by the surface magnetization of the Bloch domain walls [186]. The magnetization of the circumferential domain does not contribute to the generation of stray fields because of its circular nature, as shown in Fig. 3.3 [186].

the domain and domain walls where stray fields are generated by the domain walls – where the magnetization rotation takes place (Fig. 3.6).

The irregularity of the surface roughness generates localised magnetic fluxes [187] that induce more stray fields which pins domain wall motion, thus increasing the anisotropy field of the material (reducing the transverse permeability), as explored in thin films [188]. Therefore, reducing the surface roughness reduces localised magnetic fluxes, in turn, reducing induced stray fields. However, this is difficult to control considering the chemical composition [189] as well as the fabrication process [187] can modify the surface roughness.

These can be circumvented by coating the material with cobalt (Co) or a cobalt alloy (which is known to have a low surface roughness) which improves the GMI response where the peak GMI response occurs at higher frequencies compared to without the coating. This was observed by Taysioglu et al. [190]

where the CuO coating of Co-rich ribbons displayed an improvement of the GMI response with the maximum GMI ratio occurring at 0.5 MHz higher than their no coating counterparts. An alternative solution is by sputtering [182], electrodeposition [191], or other fabrication techniques that are capable of adjusting the atomic weight percent of the alloy ingot [186].

In this study, the samples were obtained commercially (from GoodFellow) but there was a lack of information on the fabrication technique used. Considering the dimensions of the bulk foils it was safe to assume they were fabricated from the single roller melt spinning method. The crystal structure and surface roughness of each sample was investigated and discussed in chapter 6.

3.5.1.iv Annealing treatments

Annealing treatments are also used to improve the GMI response of material by either inducing the domain structure [46, 192] to be more transversely orientated or by alleviating the internal stresses [46, 193] within the material. Both of these methods improve the magnetic softness of the material by enhancing the transverse permeability which increases the GMI ratio. The list of annealing techniques that can improve the magnetic softness of a material is presented in Table. 3.4.

Annealing technique	Process	Influence to magnetic material
Conventional annealing	Sample is heated in an inert environment (such as nitrogen or vacuum).	Redistributes the internal stresses of the material by nucleation and growth of grains within the material.
Field annealing	Sample is heated in an inert environment whilst under a magnetic field at a specific orientation relative to the sample axis.	Along with redistributing internal stresses the magnetic field reorientates the domain structure relative to the sample axis.
Current (or Joule) annealing	Sample is heated in an inert environment from the resistance of the material when subjected under a large DC current.	The heating redistributes the internal stresses and the current induces an internal magnetic field from the material which promotes domain growth along the field direction.
Stress annealing	Sample is heated undern an inert environment and is subjected under an applied tensile stress.	The heating redistributes the internal stresses and the applied stress further redistributes the internal stresses via physically rearranging the crystal structure of the material.

Table 3.4: List of annealing techniques used to improve the GMI ratio for an amorphous metal. Each annealing technique reference is ordered [194, 195, 196, 197, 198]

Although annealing does improve the GMI ratio it can also reduce it significantly when heated at an extended period of time or at a higher annealing temperature. The reduction of the GMI ratio is by magnetically hardening the material from the increasing average grain size (over the ferromagnetic exchange length) which increases its magnetic coercivity of the material [46, 194, 197]. This was observed in two studies by Zhukova et al. [197] and Phan et al. [165] where the GMI ratio increases at specific annealing time and temperature before decreasing at either longer annealing time or higher temperatures (Fig. 3.7).

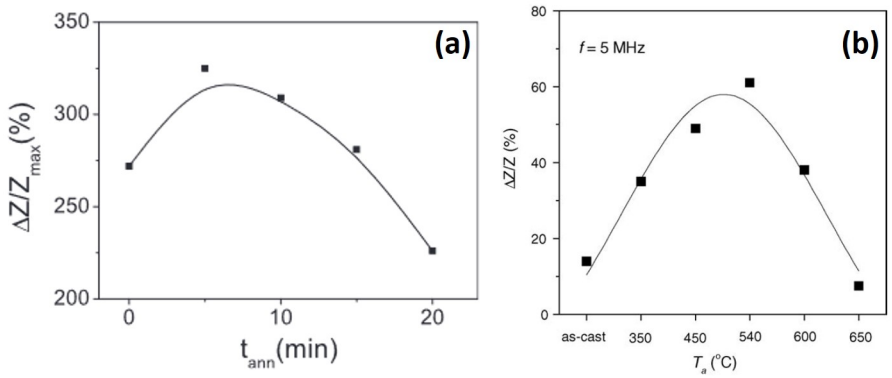

Figure 3.7: Variation of the GMI response with respect to (a) annealing time for an amorphous glass-coated CoFeBSiC microwire (100 mm length x 30.2 μm diameter) at 300°C annealing temperature (200 MHz frequency) [197] and (b) annealing temperature for FeCuNbSiB amorphous ribbon (4 mm width x 15 μm thickness) when annealed for 45 minutes (5 MHz frequency) [165].

In this study, the influence of annealing and its limitations were studied and discussed in chapter 6.

3.5.1.v Aspect ratio

The aspect ratio of the magnetostrictive material does influence the GMI behaviour for both wires and ribbons. For ribbons the maximum GMI ratio depends on the length, width, and thickness; for wires, it depends on the length and diameter – of the magnetic material [48, 184, 198, 199] (Fig. 3.8).

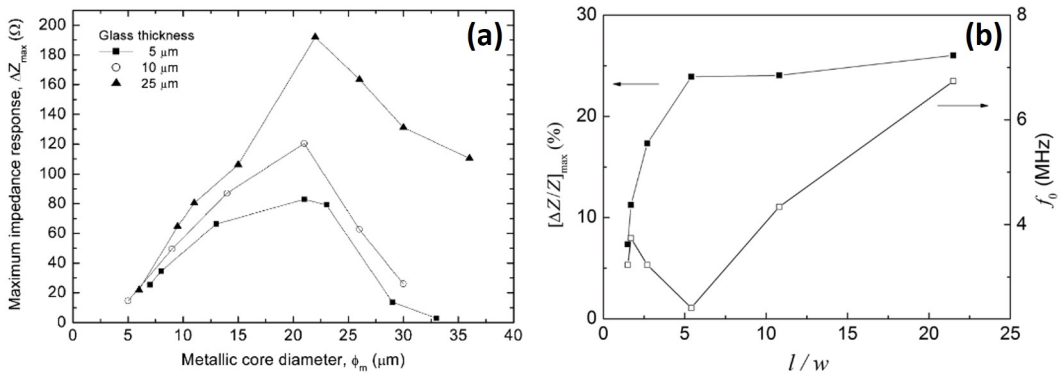

Figure 3.8: Variation of magnetoimpedance response for (a) amorphous glass-covered CoFeSiB wires with varying metallic core diameters and thickness of glass-shell (at 1 MHz frequency) [199] and (b) amorphous FeCoSiB ribbons (43 mm length x 30 μm thickness) with varying widths (at varying f_0) [48].

Both studies in Fig. 3.8 display a common trend of a maximum magnetoimpedance response as they increase in diameter and width, respectively, before either decreasing or plateauing at even larger sizes. The observed behaviour was related to the change in the material's magnetization from the changing shape anisotropy. Chiriac et al. [199] associated the increase in the GMI response with increasing diameter to the circumferential anisotropy. At smaller diameters, the GMI response was contributed by the axial anisotropy – which has magnetostatic origins – but at larger diameters, the circumferential anisotropy becomes dominant due to the increasing circumferential surface region. For higher diameters, it has been reported the critical frequency reduces to achieve the maximum GMI response. Ding et al. [48] reported the changing GMI response to the demagnetizing effects from the shape anisotropy. Therefore, at low aspect ratios the demagnetization field was dominant which decreased the material's transverse susceptibility, thus a lower GMI response. Alternatively, as the aspect ratio increased the shape anisotropy dominated and the GMI response rapidly increased until a "criti-

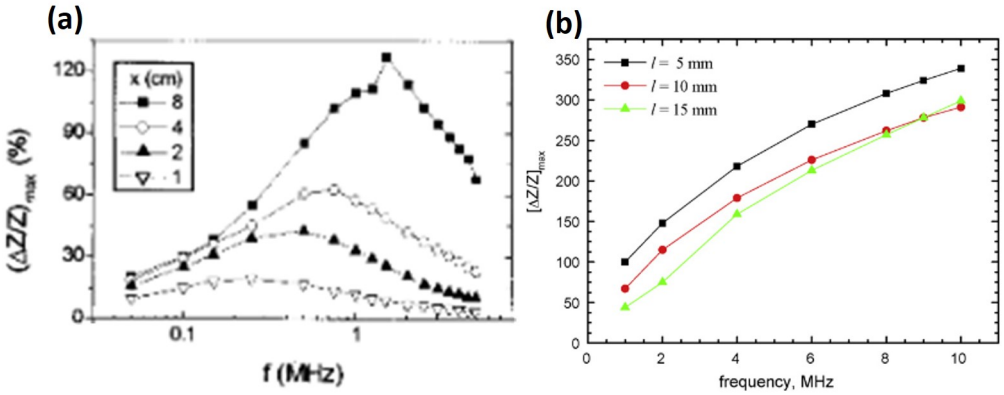

Figure 3.9: Influence on wire length studied by (a) Vazquez et al. [200] and (b) Qin et al. [201] on the GMI behaviour with respect to frequency, up to 5 MHz and 10 MHz, respectively.

cal aspect ratio" in which the GMI response was consistent.

The length of a wire and the thickness of a ribbon also affect their GMI behaviour. However, there is a lack of consensus in the existing literature on the nature of these effects. For wires, there were two studies that observed different GMI behaviours when increasing the length of the wire sample. The first study, by Vazquez et al. [200], observed a decrease in the GMI response when decreasing its wire length from 80 mm to 10 mm, including an increase in critical frequency for the maximum GMI response. On the other hand, the study done by Qin et al. [201] observed the opposite where the GMI response increased when decreasing the wire length from 15 mm to 5 mm, and no critical frequency was observed (Fig. 3.9).

The difference in the GMI response could be attributed to either, or a combination, of the chemical composition of the studied samples and the fabrication technique to synthesise the samples. The sample studied by Vazquez et al. was a Fe-rich amorphous wire with a diameter of 112 μm and 80 mm

length where the sample was cut into smaller lengths and remeasured at each cut. The other study investigated multiple amorphous glass-coated Co-rich wire with a 29.2 μm diameter metallic core and 7.5 μm glass thickness. Each wire was synthesised until the desired length was acquired. Both used different fabrication techniques where one used the in-rotating-water technique and the other used the modified Taylor-Ulitovski method. As a result, it is possible that these variables may have influenced their sample's magnetic properties (such as magnetostriction coefficient and surface roughness) contributing to differing domain structures when increasing their lengths.

It is also difficult to find a consensus on the effect of thickness of an amorphous ribbon on its GMI behaviour among the existing literature. Currently, the literature suggests the GMI behaviour would change depending on the techniques used to reduce the ribbon's thickness. Park et al. [202] used etching techniques on the ribbon resulting little to no change in its GMI response, whereas Amalou et al. [203] reported the GMI response increased for their ribbon samples when using polishing and chemically thinning techniques. Amalou et al. suggested that the increase in GMI ratio for lower thicknesses was due to weaker demagnetizing effects promoting the transverse permeability of their samples. In this thesis, the influence of the aspect ratio on the studied ribbon samples was investigated, with a focus on aspect ratios that are much larger than those typically observed in the literature (chapter 6). As the ribbons were obtained commercially, it was not possible to study the effect of the ribbon's thickness on its GMI behaviour.

3.5.1.vi Tensile stress/strain, and anisotropy field ($\boldsymbol{H}_K$) and angle (θ_K)

In the existing literature, the relationship between the GMI behaviour and applied tensile stress was correlated to changes in the anisotropy field ($\boldsymbol{H}_K$)

and its anisotropy angle (θ_K) within the material [204, 205]. The anisotropy field is expressed as $\boldsymbol{H}_K = 2\boldsymbol{K}/\boldsymbol{M}_S$ where $\boldsymbol{K}$ is the anisotropy constant and $\boldsymbol{M}_S$ is the saturation magnetization [206] and the anisotropy angle is the relative angle between the material's easy-axis to its transverse direction (perpendicular to the material's long axis) [207, 208] (Fig. 3.10). $\boldsymbol{H}_K$ represents the total free energy contributed from the combination of multiple (competing) magnetic anisotropies present within the magnetic material (such as magnetocrystalline anisotropy, shape anisotropy, magnetoelastic anisotropy etc) and its influence on rotating the easy-axis away from the transverse orientation of the material [209]. Hence, changing the anisotropy field influences the magnetic domain structure of the material by rotating its easy-axis, which subsequently changes its GMI behaviour. Such changes in the GMI behaviour are exhibited by a combination transitioning between single- (SP) to double-peak (DP) GMI curves [210, 211], and/or varying magnitudes of the GMI ratio [211, 212].

Zhao et al. [210] loosely references θ_k when discussing the transition from an SP to a DP GMI curve profile using the phenomenological model of magnetostrictive energy in CoFeNiSiB and FeSiBNbCu amorphous ribbons (15 mm length x 4 mm width x 22 μm thickness). Depending on the sign of the magnetostriction coefficient the strength of $\boldsymbol{H}_K$ varies; it is weaker for positive magnetostrictive (FeSiBNbCu) ribbons and stronger for negative magnetostrictive (CoFeNiSiB) ribbons (Fig. 3.9(a)). This difference in strength is due to the orientation of the domain structure where a more transverse orientated domain structure (negative magnetostriction) has a higher anisotropy field compared to a longitudinal domain structure (positive magnetostriction). The difference in the anisotropy field relates to the single- (SP) and double-peak (DP) GMI response between these materials. This indicates the anisotropy field is contributed by the magnetoelastic anisotropy in which the magnetostrictive effects of a negative magnetostrictive material will resist

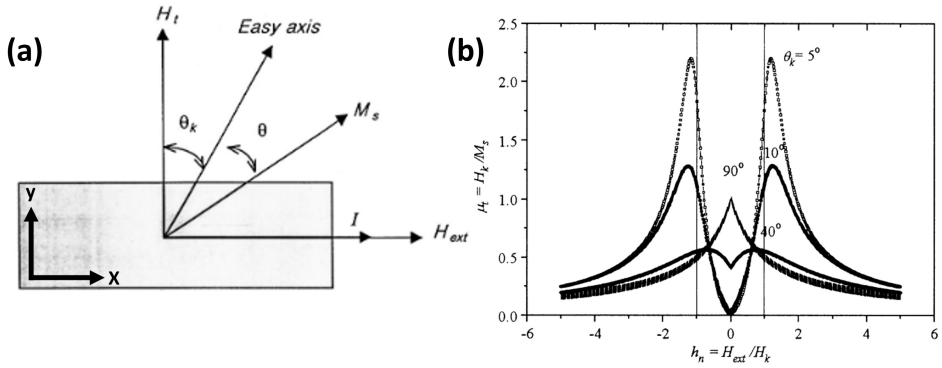

Figure 3.10: (a) Schematic of an in-plane view for a rotational magnetization of an amorphous ribbon with a uniaxial anisotropy (H_t – transverse field, M_s – saturation magnetization, H_{ext} – external applied field, θ_k – anisotropic angle) and (b) the transverse susceptibility (μ_t) with relation to H_{ext}/H_k [208].

the rotation of the magnetic domains (as well as domain wall motion) to align parallel to the field because it favours transverse orientation. When the field overcomes the magnetoelastic anisotropy the maximum transverse permeability is achieved and a DP behaviour is observed. On the other hand, a positive magnetostrictive material favours a longitudinal domain structure, thus the magnetoelastic anisotropy and the field are in parallel. Therefore, the field enhances the magnetostrictive effects which reduce the transverse permeability resulting in an SP behaviour.

Another study closely investigated the effect of varying θ_k on the GMI behaviour of an amorphous FeZrBCu ribbon was performed by Yoon et al. [208]. The study calculated the transverse susceptibility of the sample to its anisotropy angle and observed a DP to SP transition where the angle of the easy-axis was more perpendicular to the ribbon long axis - more transversely orientated (Fig. 3.10).

It is important to note, both studies mention the contribution of the shape anisotropy to θ_k. The shape anisotropy intrinsically has demagnetization effects that reduces the anisotropy angle reinforcing the easy-axis to be more aligned to the shape anisotropy which is always the longest side of the material.

Yoon et al. investigated the effect of the magnitude of $\boldsymbol{H}_K$ on the ribbon's GMI behaviour by annealing the ribbon at various temperatures (up to 600°C) with an annealing time of one hour. They observed the magnitude of $\boldsymbol{H}_K$ decreasing and the GMI response of the material increasing until 400°C, where the GMI ratio began to decrease with temperature (Fig. 3.11(a)). The improvement of the GMI response was due to the relaxation of the internal stress within the material which reduced $\boldsymbol{H}_K$. However, at higher annealing temperatures the GMI ratio decreased because the average crystalline grain size grew, making the material harder, as mentioned in section 3.5.1.iii. A similar result was observed by Ryu et al. [212] when they increased the Fe-content of amorphous FeNbB ribbons (reducing the atomic concentration of boron) resulting in the GMI ratio increasing as the magnitude of $\boldsymbol{H}_K$ decreased (Fig. 3.11(b)). Ryu et al. correlated the coercivity to $\boldsymbol{H}_K$ of the FeNbB sample and observed a positive linear trend which implies the magnitude of $\boldsymbol{H}_K$ reflects the magnetic hardness of a material (relative to the transverse orientation).

It is evident the strength of the magnetoelastic anisotropy from the residual stresses present in the amorphous material (from fabrication processes) has a significant impact on the anisotropy field and angle. Hence, it is expected, the inverse magnetostriction effect should also influence the anisotropy field. In the literature, there is a correlation between the anisotropy field and the magnetostriction coefficient: the lower the coefficient the magnetically softer the transverse orientation of the magnetic material. Therefore, it is

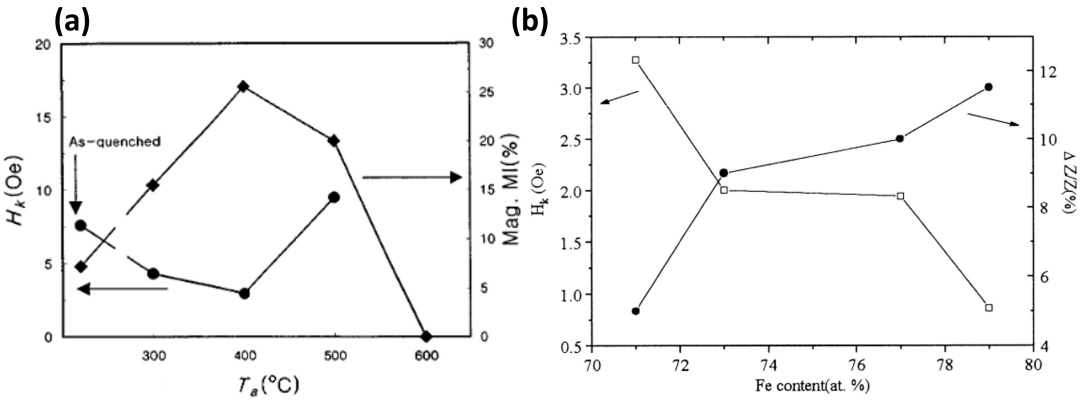

Figure 3.11: Relationship between $\boldsymbol{H}_K$ and GMI ratio with respect to (a) annealing temperature [208] and (b) atomic weight percent of Fe-content [212].

safe to assume increasing the tensile stress/strain also should induce magnetic hardening which reduces the GMI response of the material due to the increasing magnetoelastic anisotropy. This was observed in multiple studies [204, 205, 213, 214] where the GMI response of an amorphous material monotonically decreased as the stress increases. However, a study by Moradi et al. [215] displayed an increase in the GMI ratio with increasing stress (Fig. 3.12).

Mansourian et al. [211] calculated the anisotropy field of the samples and discovered that the anisotropy field does not increase linearly with stress. The exact origin for the non-monotonic behaviour is difficult to untangle since there are many factors to include, such as; interactions between the exchange energy and local anisotropies within the microstructure, the relaxation effects from local structural rearrangement, grain-to-grain variations of induced stress and anisotropy, and pinning of domain walls from defects in the alloy. The same non-monotonic behaviour on the GMI behaviour to was also observed and is discussed in chapter 7.

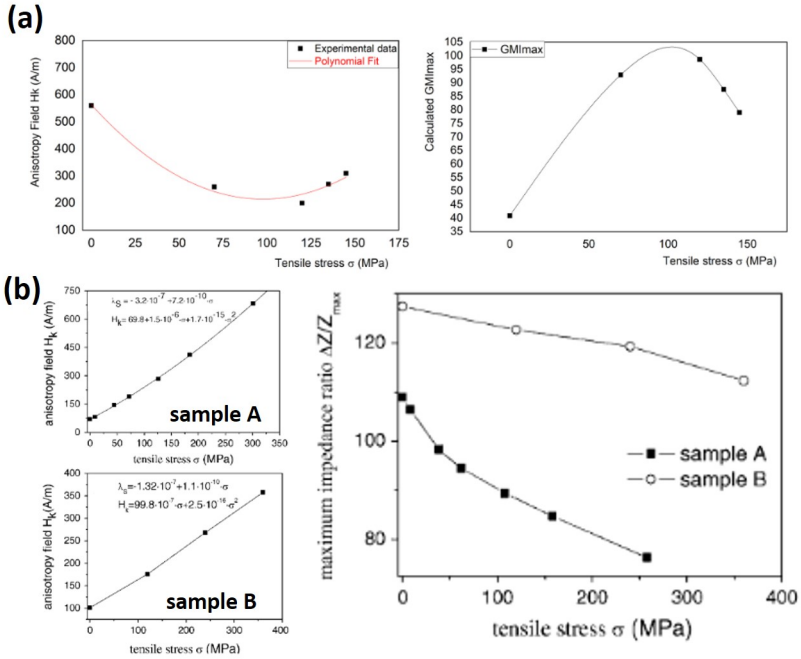

Figure 3.12: Stress dependence on the anisotropic field and GMI ratio with trends as either (a) non-monotonic [211] and (b) monotonic [205]. The samples used in both studies were Co-rich (CoFeSiB) amorphous ribbon (40 mm length x 0.81 mm width x 28.8 μm thickness) and glass-coated Co-rich (CoFeNiBSiMo) amorphous wires (sample A: metallic nucleus diameter 16.4 μm, and total diameter 19.4 μm; sample B: metallic nucleus diameter 21.4 μm, and total diameter 26.2 μm), respectively. The frequency for the measured GMI ratio was 1 MHz and 10 MHz, respectively.

3.5.2 Similarities between the GMI effect to the GSI effect

The effect tensile stress/strain has on the GMI effect indicates a close relation to the changing anisotropy field and anisotropic angle of the material. Thus, it would be expected, that the GSI effect would also behave similarly where the lower the anisotropy field and angle the higher the GSI response of the material when under an applied tensile stress. This was observed by Li et al. [207] where they have calculated the theoretical GSI response of a nanocrystalline FeCuNbSiB ribbon (65 mm length x 0.6 mm width x 25 μm thickness) based on its anisotropic field and angle with respect to applied tensile stress and compared it to the experimental data (Fig. 3.13).

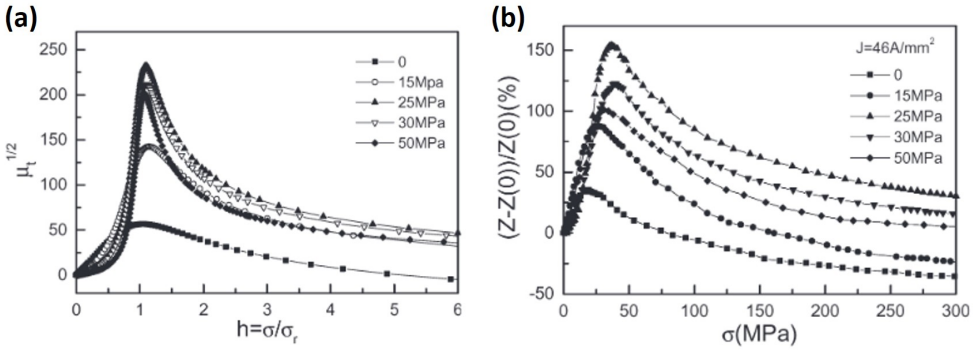

Figure 3.13: (a) Theoretical estimation on the transverse permeability of an amorphous FeCuNbSiB ribbon with increasing tensile stress ($h = \sigma/\sigma_r$, where σ is the applied tensile stress and σ_r is the residual stress in the ribbon) using the values of the anisotropic field and angle at 0.69 Oe and 5.5°, respectively. (b) The experimental data of the GSI ratio with increasing tensile stress. The sample was Joule annealed (at a current density of 46 A/mm^2) under different tensile stresses with a common frequency at 10 MHz [207].

Fig. 3.13 displays qualitative agreement between the theoretical estimation and the experimental data. This provided strong evidence that the GSI effect is influenced by the anisotropy field and its orrientation. The study further demonstrated the anisotropy field and angle could be reduced to very low values by applying a complex annealing process by Joule heating the ribbon at 46 A/mm^2 whilst under a tensile stress (of 50 MPa) followed by a DC magnetic field (of 70 Oe), parallel to the ribbon length, for 20 seconds each. The magnitude of the GSI ratio increased considerably from 100% to 286% at an applied tensile stress of ∼30 MPa. This correlated with an earlier study done by the same authors [44] where they thermally annealed an amorphous ribbon of the same chemical composition (Fig. 3.14).

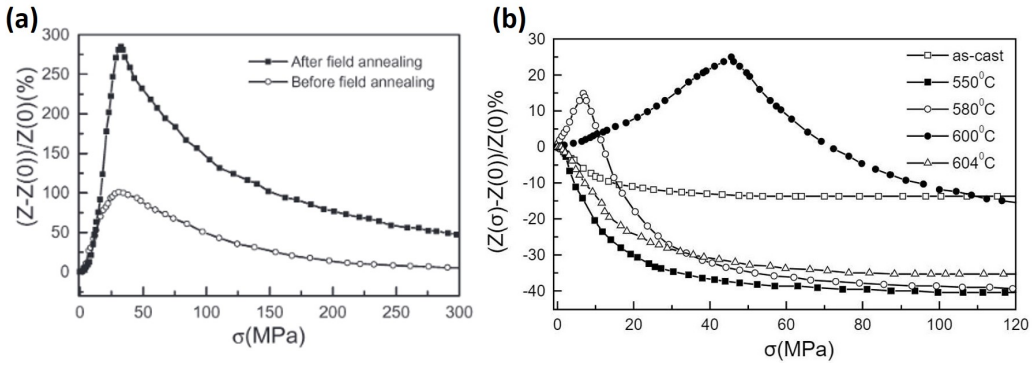

Figure 3.14: (a) GSI ratio with respect to tensile stress before and after field annealing at 46 A/mm^2 and 70 Oe DC field [207]. (b) GSI ratio with respect to tensile stress at various (conventional) annealing temperatures (for 30 minutes) on an amorphous ribbon with the same chemical composition but with different dimensions (65 mm length x 1 mm width x 35 μm thickness) [44]. The frequency measured was 10 MHz and 0.3 MHz, respectively. Both used the identical FeCuNbSiB ribbon sample.

A study by Kaviraj et al. [216] investigated the frequency dependence

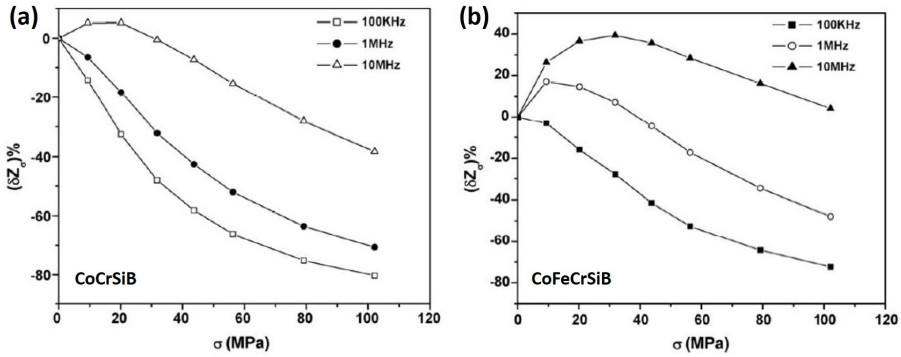

Figure 3.15: Stress dependence on the GSI ratio of amorphous ribbons at various frequencies for (a) CoCrSiB (80 mm length x 6.41 mm width x 33.5 μm thickness) and (b) CoFeCrSiB (80 mm length x 6.347 mm width x 32.5 μm thickness) [216].

on the GSI effect on two amorphous ribbons with chemical compositions of CoCrSiB and CoFeCrSiB (Fig. 3.15).

Fig. 3.15 illustrates the changes in the GSI behaviour between frequencies of 0.1 MHz and 10 MHz. A monotonic behaviour was observed at 0.1 MHz, while a non-monotonic behaviour was a observed at 10 MHz. Currently, there are no studies that have explained the exact underlying physics of this changing behaviour at different frequencies, which is similarly observed in chapter 7. However, it is clear that at higher frequencies the maximum GSI ratio decreases, which was also observed by Hu et al. [217] for two amorphous ribbon samples with different chemical compositions of FeCuNbSiB and FeCuNbVSiB.

Kaviraj et al. discussed the difference in GSI behaviour between two ribbon samples with a CoCrSiB ribbon having a sharper decrease in the GSI ratio compared to the CoFeCrSiB ribbon at all three frequencies measured. This difference was attributed to the different magnetostriction coefficient

magnitudes where CoCrSiB and CoFeCrSiB had magnetostriction coefficients (calculated) to be -0.63×10^{-6} and -0.24×10^{-6}, respectively. Both samples possessed a negative magnetostriction coefficient but CoFeCrSiB had a lower magnitude of the magnetostriction coefficient, thus exhibiting a slow decrease in the GSI ratio. However, both samples had a maximum GSI ratio of $\sim$-80% at 0.1 MHz. When compared to an as-cast amorphous FeCuNbSiB ribbon (with a positive magnetostriction coefficient) the measured GSI ratio was $\sim$10% at 0.3 MHz. Similar to GMI the magnetostriction coefficient also impacts the GSI behaviour of metallic glass materials where it appears negative magnetostriction manifests a higher magnitude GSI ratio than positive magnetostriction.

At present, there is no literature on the influence between the surface roughness nor aspect ratio on the GSI behaviour of amorphous metals. However, both variables have been investigated on the GMI behaviour of these materials in which the surface roughness contributes to the increase in the anisotropy field by inducing stray fields which acts as pinning sites for domain wall motion. The aspect ratio illustrates the influence of shape anisotropy to the GMI behaviour, where at low aspect ratios the shape of the material has stronger demagnetizing effects which reduces the transverse permeability significantly, in turn reducing the GMI response. Fundamentally, the GSI effect changes with transverse permeability it can be safe to assume it would respond as similarly to the GMI effect.

The GMI and GSI effects both displayed very similar behaviours for either ribbon or wire geometries. Therefore, it was expected to be possible to design a magnetostrictive sensor using the GSI effect which would perform similarly to a GMI strain sensor and would be more convenient since it directly detects changes in stress/strain of the medium.

3.6 Summary

Flexible shape memory smart materials are optimal for strain sensing technology, as their unique response to external mechanical stimuli can be used to detect changes in strain. These materials were assessed against a set of criteria for the desired strain sensor that could monitor the expansion of an ILW nuclear waste package. After investigating multiple flexible strain sensors, the smart material that fulfilled the majority of the criteria were either polymer-based (GWF/PDMS and rGO/PDMS), paper-based (graphite/paper), and magnetostrictive/magnetoelastic (cobalt-based alloy) smart materials. Magnetostrictive/magnetoelastic materials were chosen for study since we were interested in their capability to function as a GSI strain sensor.

To understand the GSI effect and its behaviour with other physical variables a literature review was conducted. However, it was immediately obvious the studies on the GSI effect were limited compared to the GMI effect which has been thoroughly studied. The physics between the GMI and GSI effect were, fundamentally, the same where both of them exhibit a change in impedance from changing transverse permeability. The only difference was the external stimulus for this change was an applied field for the GMI effect and applied stress for the GSI effect. Therefore, a literature review on the GMI effect was also included to identify the many variables that can influence both the GSI and GMI behaviour. The variables that influenced the GMI behaviour (which could also influence the GSI behaviour) were: the frequency of the AC current, the magnetostriction coefficient, the annealing treatment, the fabrication process, the aspect ratio, and applied tensile stress/strain. These were then used to experiment with the GMI and GSI responses of the studied samples for optimal sensing performance.

Chapter 4

Characterisation Techniques and the Experimental Method of Measuring GMI and GSI

4.1 Outline

This chapter will introduce the fabrication and characterisation techniques used to perform the experimental studies in this thesis. The chapter is separated into three sections: The first section discusses the specification of the material characterised as well as the techniques used for sample preparation. The second section provides a brief description of each material characterisation technique used and how they were utilised in this work. Finally, the third section describes the basic experimental approach used to characterise giant magnetoimpedance (GMI) and giant stress impedance (GSI) in this study. A more detailed description of the development of an experimental system to characterise the GMI and GSI of large-scale amorphous ribbons

can be found in chapter 4.

4.2 Sample Preparation

The aim of this thesis was to develop a sensor technology to detect the rate of expansion of either a localised or global deformation on the surface of an ILW nuclear waste package. Hence, to effectively monitor both deformations the sensor must be capable of covering a large surface area on the surface of the ILW waste package (as shown in Fig. 1.3). Therefore, it was decided the magnetostrictive sensor would be ribbon-shaped.

As discussed in chapters 2 and 3 the material properties that influence the sensing performance of a magnetostrictive sensor are:

- The crystal structure of the material
- The magnetostriction coefficient (λ_S)
- The coercivity ($\boldsymbol{H}_{\mathrm{C}}$) and saturation magnetisation ($\boldsymbol{M}_{\mathrm{S}}$) which are both related to the anisotropy field ($\boldsymbol{H}_{\mathrm{K}}$)
- Curie temperature ($\mathrm{T_C}$)

In addition, the mechanical properties of the material (such as tensile strength and Young's modulus) are just as important to identify their strain range and mechanical failure.

Commercialised metallic glass bulk foils were purchased from GoodFellow with three different compositions. Each chemical composition had a different ferromagnetic element (cobalt, iron, or nickel) having the highest concentration. These materials were selected due to their relatively large differences in

their magnetic properties such as the magnetostriction coefficients, coercivity, saturation magnetisation, etc, in Table 4.1. The crystal structure for all three metallic glass foils are amorphous which was confirmed when characterising each foil using X-ray diffraction (Fig. 4.4). All three bulk foils had a common thickness of 25 μm with varying widths. The Co-rich and Ni-rich foils had widths of 250 mm, while the Fe-rich foil had a width of 500 mm.

To prepare ribbons from the precursor foils the following procedure was followed: Each bulk foil was laid out at a desired length measured with a ruler. The bulk foil was mechanically cut (using a retractable utility knife) to produce foil pieces with the desired length and the respective bulk foil width. Further mechanical cuts were made in order to make ribbon samples of desired widths. Moreover, depending on the cut of the foil ribbon samples had either a single or double longitudinal edge cut (S/DLEC) which represents the longitudinal edge profile of the ribbon samples after cutting them from the bulk foil. The procedure of using a utility knife to cut a metallic foil into ribbon-shaped samples of high-aspect ratios (as high as 150) leads to permanent damage at the ribbon edges. However, there are some manufactured ribbons with an edge from the precursor foil and the other edge being damaged by the cutting process creating two sets of samples with the first set having one edge (SLEC) damaged and the other set having both edges (DLEC) damaged. This brings an interesting topic of the relation between the physical state of the ribbon sample and its GMI response, which will be discussed in chapter 6.

Chemical composition of foil	Electrical resistivity ($\mu\Omega$cm)	Magnetostriction Coefficient (λ_S) ($\times 10^{-6}$)	Curie Temperature (°C)
$Co_{66}Si_{15}B_{14}Fe_4Ni_1$ (Co-rich)	142	<1	205
$Fe_{81}B_{13}Si_{3.5}C_2$ (Fe-rich)	30	370	480
$Ni_{40}Fe_{40}(Si + B)_{19}Mo_{1\text{-}2}$ (Ni-rich)	8	260	450
Chemical composition of foil	Crystallisation Temperature (°C)	Tensile Strength (MPa)	Young's Modulus (GPa)
$Co_{66}Si_{15}B_{14}Fe_4Ni_1$ (Co-rich)	550	>700	61
$Fe_{81}B_{13}Si_{3.5}C_2$ (Fe-rich)	135	>700	58
$Ni_{40}Fe_{40}(Si + B)_{19}Mo_{1\text{-}2}$ (Ni-rich)	135	1500 - 2000	150

Table 4.1: Material properties of Co-rich, Fe-rich, and Ni-rich bulk foils as quoted by the supplier (Good-Fellow) [218].

The range of sample geometries studied was as follows:

- Ribbon length: 20 - 300 mm
- Ribbon width: 2 - 10 mm
- Single and double longitudinal edge cuts (S/DLEC) of ribbon samples.

This provided a range of aspect ratios between 2 to 150 for all amorphous ribbons in which the GMI response in relation to the range of aspect ratios was studied in chapter 6.

4.3 Material Characterisation Techniques

4.3.1 X-ray diffraction (XRD)

X-ray diffraction (XRD) is a non-destructive characterisation technique that can be used to identify the crystal structure and characterise the microstructure of materials. In this study, XRD was used to characterise the crystal structure of the three materials studied obtained and identify any difference between them. This was expected to provide insight into potential differences in their electrical and magnetic properties performance between them.

In XRD samples are placed in the path of monochromatic (single wavelength) and collimated beams of X-rays. The beams scatter after interacting with the sample and are then detected with a detector, shown in Fig. 4.1. The scattering of the incident beams from sample creates a diffraction pattern which identifies their crystal structure [219].

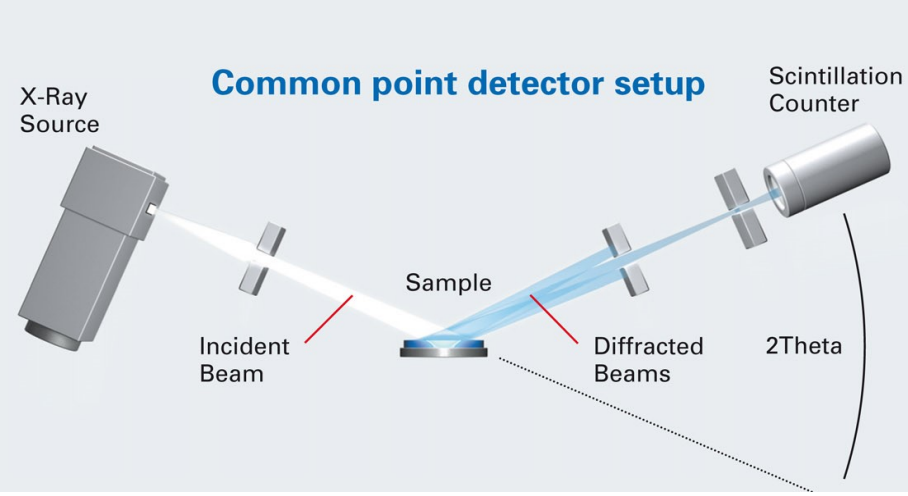

Figure 4.1: Schematic diagram of how XRD operates in the Bruker 2D Phaser [220].

The diffraction pattern is produced from the combination of constructive and destructive interference from the scattered beams, where the scattered beams have a different direction and intensity compared to the incident beams [221]. Fig. 4.2. illustrates how the scattered beams could interfere with each other under the assumption that,

- the incident beams are monochromatic and parallel to each other
- the angle of incidence (θ) is the same as the angle of diffraction
- the material has a perfect crystal lattice structure with no grains i.e. a single, perfect crystal.

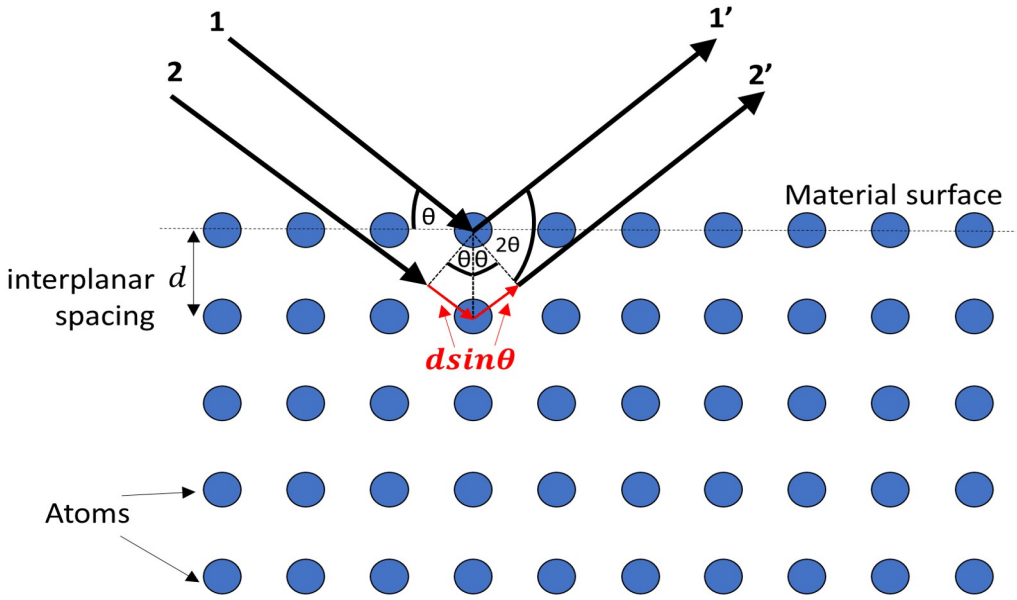

Figure 4.2: Illustration of incident beams (1 and 2) are scattered (1' and 2') when interacting with a perfect single crystal lattice and assuming the diffraction angle is the same as the angle of incidence.

In this case, incident beams 1 and 2 are in phase and will interact with two atoms. After being scattered beams 1' and 2' remain coherent but the total path distance travelled differs between the two. The difference is equated to 2dsinθ and this change in distance dictates if the interference is constructive or destructive to beam 1' based on the number of wavelengths that have traversed. Therefore, for constructive interference (where both 1' and 2' are in phase) an integer of wavelengths needs to traverse the distance of 2dsinθ and n/2 wavelengths become destructive interference. The collection of only constructive interference is then detected as peaks in the diffraction pattern (Fig. 4.3).

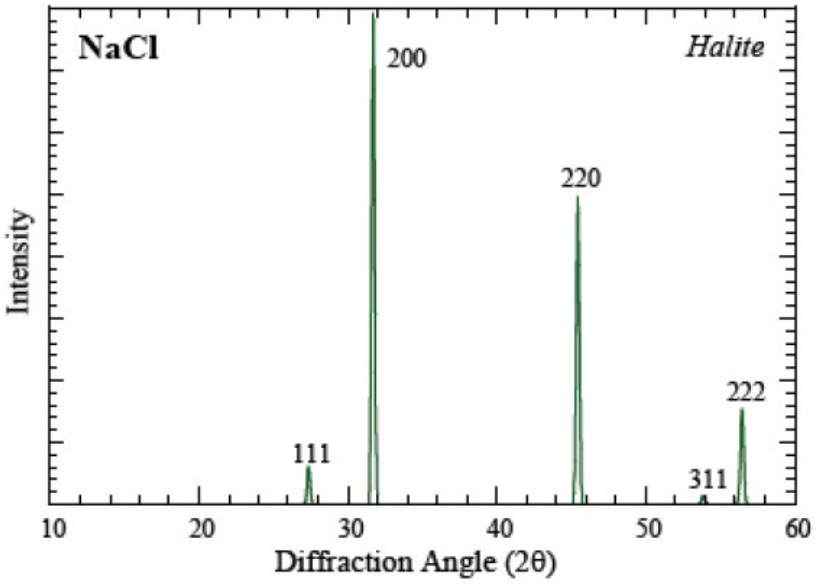

Figure 4.3: Diffraction pattern of Halite (NaCl) in XRD where each narrow peak are constructive interference waves detected at their respective angle (2θ) [221].

This behaviour can be defined by Bragg's Law of diffraction which is expressed as,

$$n\lambda = 2dsin\theta \tag{4.1}$$

where n is the integer number of wavelengths traversed, λ is the wavelength and d is the interplanar spacing in the crystal lattice. Rearranging this equation provides the conditions required to obtain a diffraction pattern of any crystal structure so long the wavelength is equal to or lower than $2d$ for an angle of incidence between 0 to 90 degrees. To ensure a diffraction pattern is always produced regardless of what d is, λ is set to be at a size equal to or smaller than an atom (or the smallest size of a crystal unit cell)

which is around 0.1 nm, thus the selection of using X-rays to characterise a material's crystal structure. As a result, each material's diffraction pattern is defined by the regular interplanar spacing d which changes depending on the crystal structure.

In this thesis XRD was performed using a Bruker D2 Phaser in the θ-2θ geometry using Kα X-rays from a copper source (average wavelength of 1.54184 Å). The bulk foils were cut into 30 mm x 30 mm squares, all having a common thickness of 25 μm. The XRD spectra for all three bulk foils show a common single broad peak which indicates the absence of long-range ordering and a lack of a crystal phase (Fig. 4.4). The single broad peak is the result of X-ray scattering of irregular interplanar spacing d within the crystal structure with a statistical preference for a particular interatomic distance indicated by the 2θ angle [222]. Fe-rich and Ni-rich foils exhibited a broad peak at a 2θ angle of around 45°and the Co-rich at around 44°angle. This correlates to existing literature where amorphous ribbons exhibit a broad diffraction peak with a 2θ angle around 44°[223, 224] or 45°[49, 225, 47].

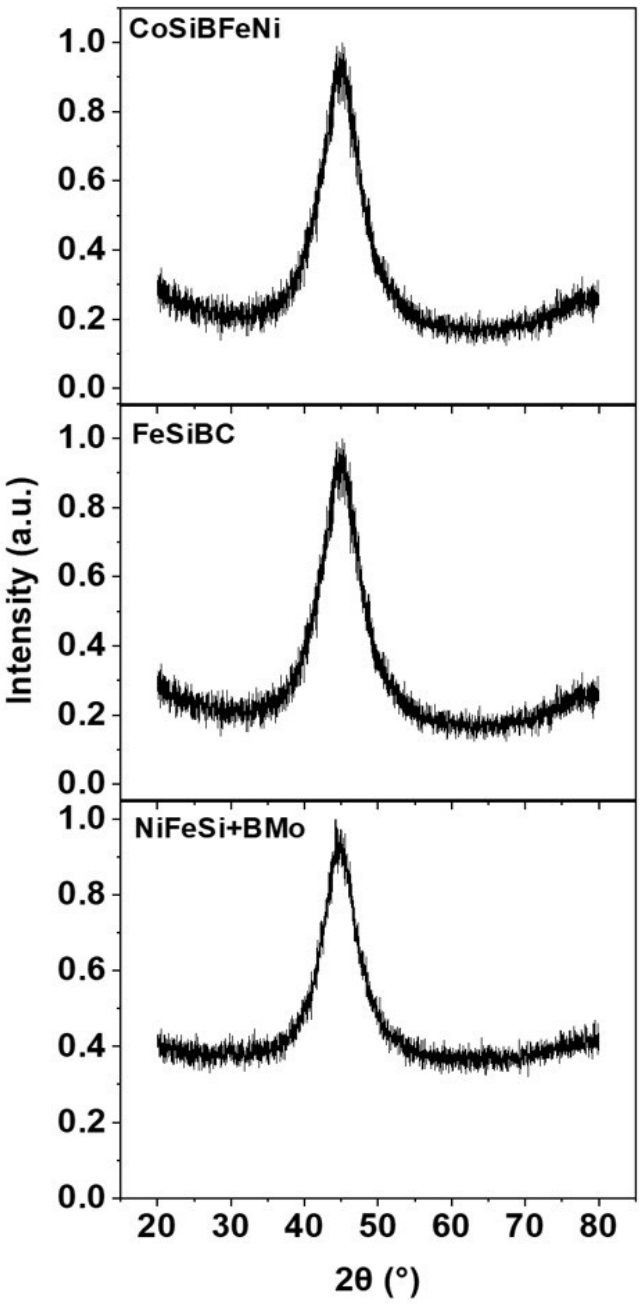

Figure 4.4: XRD patterns of samples (a) Co-rich, (b) Fe-rich and (c) Ni-rich foil samples at ambient temperatures – data was copied from ref. [218].

4.3.2 Atomic force microscopy (AFM)

Atomic Force Microscopy (AFM) is a scanning probe-based imaging technique that visualises the topography of a material's surface using the interaction of atomic forces between a sharp cantilever tip and the material surface (Fig. 4.5). In this study AFM was used to characterise the surface roughness of the metallic glass foils/ These measurements were performed to investigate the possibility of a correlation between the giant magnetoimpedance (GMI) ratios of materials and surface roughness which is reported in the literature [189, 226].

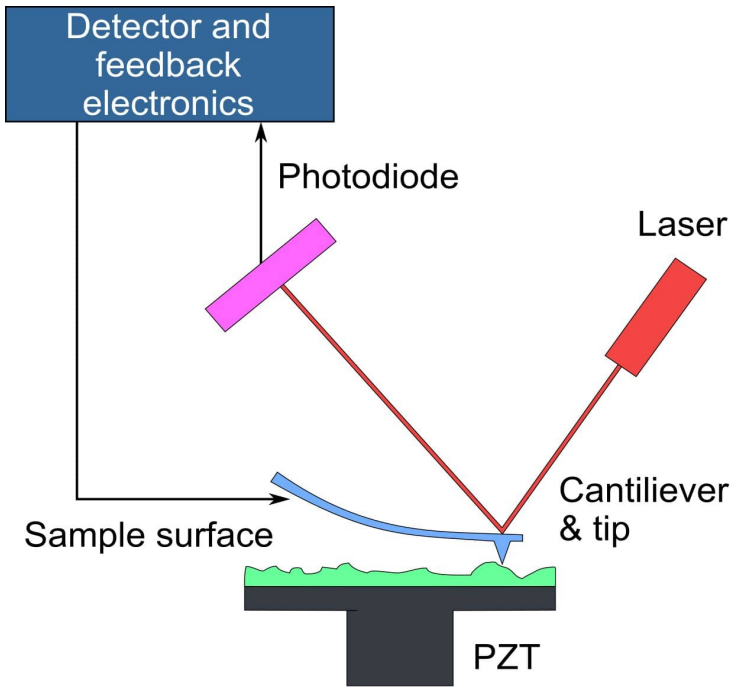

Figure 4.5: Schematic diagram illustrating the operation procedure for AFM [227].

The AFM instrument uses a laser source, a photodiode, and a cantilever with an incredibly sharp (typically a few atoms thick) tip to measure the surface roughness of the sample. The cantilever has a reflective mirror on top (above the tip) where the laser reflects off and gets detected by the photodiode. The photodiode connects to a detector that measures the current based on the intensity of the laser. Therefore, as the cantilever deflects, under the influence of the atomic forces (typically van der Waal forces) between the atoms from the tip and sample surface, the intensity of the laser decreases which creates a change in current. When the instrument detects a change in current it sends a feedback loop to the piezoelectric platform which adjusts its position to ensure the intensity of the laser is restored. A piezoelectric material (an example of a piezoelectric material is PZT - Lead zirconate titanate) is used as a platform because of its property to detect minuscule changes in potential (V) within the circuit. This property is used to adjust the position of the piezoelectric platform to ensure the distance between the sample surface and the tip of the cantilever is constant. Adjusting the parameters between the deflection of the cantilever and the movement of the piezoelectric enables many different methods to produce an image of the sample's surface.

The measurements in this thesis were performed using an AFM in "Tapping mode". Tapping mode is a non-destructive technique where the tip of the cantilever is only in brief, periodic contact with the surface of a sample at a consistent rate. This ensures that the surface of the sample is not damaged or contaminated during scanning. This is calibrated by initially finding the natural resonance frequency of the cantilever and by monitoring the rate of change of its frequency, as the tip gets closer to the sample surface. The point at which this change becomes negligible defines the frequency (f_{eff}) for tapping mode. When maintaining a constant frequency and excitation strength the amplitude of the tip oscillation varies when its height above the surface

varies due to the force gradient of the van der Waal interactions between the atoms of the cantilever tip and the sample surface (Fig. 4.6).

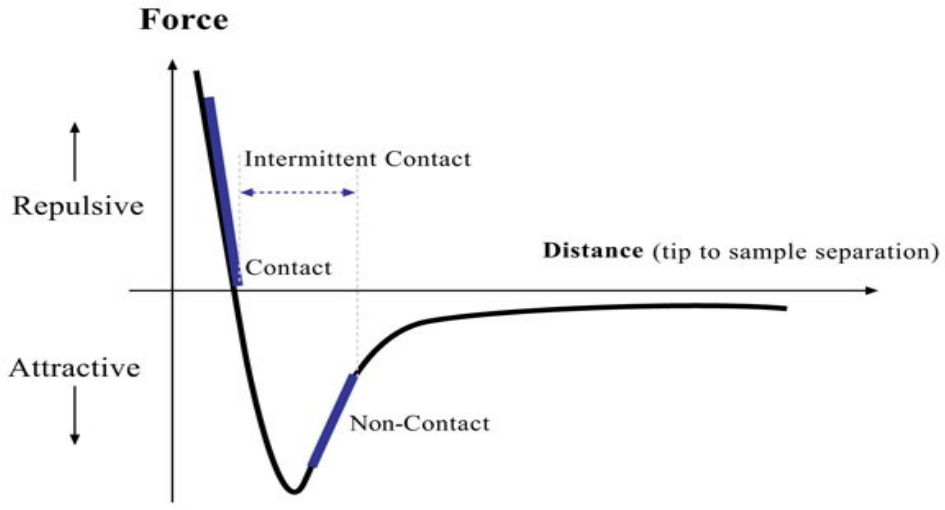

Figure 4.6: Graph that describes the atomic force interaction with distance between the tip of the cantilever and the sample surface. The non-contact trendline of the graph shows the force gradient with respect to distance and when it starts to plateau is where the tapping mode frequency f_{eff} is defined [228].

The image is constructed by monitoring the deviations from f_{eff} (observable by changes in the tip oscillation amplitude) when scanning over the sample surface and, when deviations are observed, using the feedback loop of the instrument to use a piezoelectric material to move the sample away or closer to the tip until f_{eff} is reached [229]. To ensure the image has a very high-resolution the cantilever tip needs to be sharp to the atomic scale whilst the cantilever needs to be stiff enough to consistently oscillate without failing [230].

In this study AFM was conducted by Dr Robert Moore who analysed the

Sample	Root mean square (R_q) (nm)
CoSiBFeNi (Co-rich)	4.15
FeBSiC (Fe-rich)	15.3
NiFeSi+BMo (Ni-rich)	14.8

Table 4.2: Surface roughness of each sample scanned in tapping mode on AFM - data was copied from ref. [218].

surface roughness topography of the samples using the Bruker Fastscan® AFM, in tapping mode. The surface roughness of each sample was scanned over a common scanning area of 3×3 μm, 10×10 μm, and 30×30 μm. Following the literature it is considered the scanning area of 3×3 μm was a good representation of the surface roughness of the whole ribbon sample [226, 231]. This was selected for the reason of a smaller scanning range provided a higher image resolution of the topography of the sample's surface. Thus, providing a more detailed image with higher accuracy to measure the surface roughness of each sample (Fig. 4.7).

The surface roughness was quantified using the root mean square value (R_q). Roughness for each of the materials characterised is displayed in Table 4.2. The sample roughness was investigated on the three bulk foils which have been reported to have an impact on the GMI behaviour (chapter 3, section 3.5.iii) on the impact of a ribbon's surface roughness on the GMI effect.

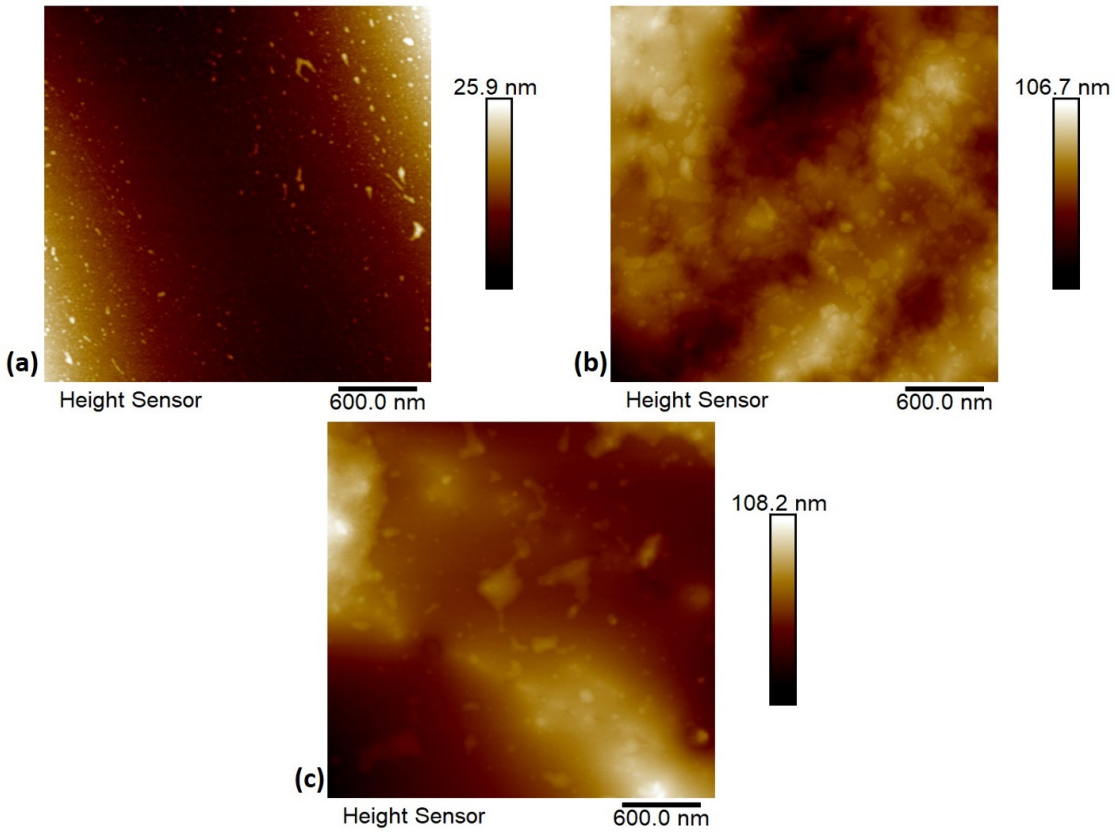

Figure 4.7: AFM images of surface roughness for (a) CoSiBFeNi, (b) FeSiBC and (c) NiFeSi+BMo samples with a common scanning area of 3×3 μm – data was copied from ref. [218].

4.3.3 Superconducting Quantum Interference Device – Vibrating Sample Magnetometry mode (SQUID-VSM)

Superconducting Quantum Interference Device – Vibrating Sample Magnetometry mode (SQUID-VSM) is a magnetometry technique that combines the basic principles of VSM with those of SQUID in order to obtain an exquisitely sensitive probe of a samples magnetic moment. In this thesis, SQUID-VSM was used to obtain the hysteresis loops of the ribbon samples' magnetic moment (Fig. 4.11).

Conventional vibrating sample magnetometry (VSM) operates by using pickup coils to detect a sample's change in the magnetic moment when the sample vibrates between them (Fig. 4.8). This method follows Faraday's Law of induction by detecting the induction in the pickup coils when the sample is vibrating between them. Initially, the sample is mounted and positioned at the centre between the top and bottom pickup coils, with no physical interaction between them. Then the sample is magnetised by the applied external uniform dc field (produced by an electromagnet) with a sample's magnetic domains and, or individual magnetic spins aligning to the field. The magnetisation of the sample induces "magnetic stray fields" due to the dipole moment present in the sample. The magnetic stray fields are the magnetic field lines surrounding the sample and the strength of these stray fields is proportional to the strength of the sample's magnetisation. Therefore, the strength of the sample's magnetisation is dependent on the strength of the uniform applied field. When vibrating the sample (in a sinusoidal manner) the magnetic stray fields change direction depending on the position of the sample. The moving stray field lines induce a changing magnetic flux which is detected from the pickup coils. The changing magnetic flux behaves as

an alternating field which induces a current in the pickup coils (according to Faraday's Law of induction) thus a larger induced current represents a larger magnetisation of the sample. The transimpedance amplifier and lock-in amplifier amplifies the signal of the measured induced current to the computer interface. The computer interface uses specific software (such as LabVIEW or RTForc^{TM}) that communicates with the various components of the VSM (such as the lock-in amplifier, power supply, etc.) to automate the measurements and collects the data. The data is then plotted as a hysteresis loop of magnetisation ($\boldsymbol{M}$) to the applied field ($\boldsymbol{H}$) [232, 233].

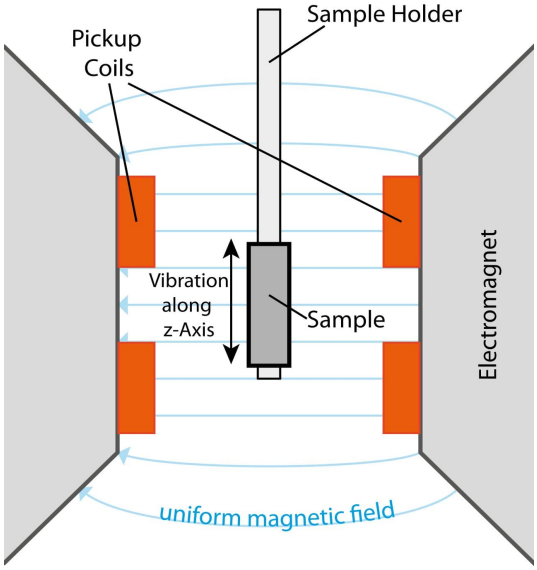

Figure 4.8: Schematic illustrating a VSM measuring the sample's magnetic moment where the sample is held by a sample holder isolated by the pickup coils and when it vibrates along the z-axis. Pickup coils are inducted from Faraday's law of induction and the measured signals are compared to the reference signal (from a Lock-in amplifier), before the sample was placed [234].

To measure materials with very soft magnetic properties the SQUID-VSM technique was used. The SQUID uses two superconductors separated by a thin insulating layer to form two parallel Josephson junctions under a biasing current (Fig. 4.9(a)).

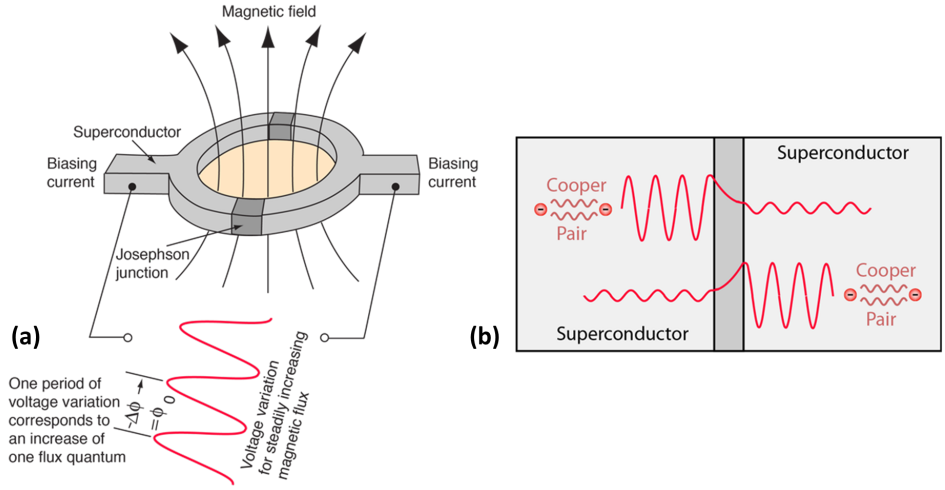

Figure 4.9: Illustration of (a) superconducting coil with Josephson junctions with (b) quantum tunnelling of cooper pair electrons happens at the Josephson junction at a critical temperature of the superconductor [235].

According to the Meissner effect, at temperatures that are under the critical temperature (T_C), a material in a superconductive state will expel magnetic field lines (i.e., magnetic flux) from its own body when under a magnetic field (Fig. 4.10(b)) [35]. If a superconducting ring-shaped material is under a magnetic field the field lines outside the ring get expelled, but the magnetic field lines inside the ring gets trapped. As such, when the applied magnetic field is gone a current (I_0) is induced within the ring-shaped material which retains the magnetic flux inside the ring. Normally, the current decays over time from the material's electrical resistance ($I(t) = I_0 e^{-tR/L}$, where t is time, R is the electrical resistance, and L is the inductance of the

conductor). However, in a superconductor the current doesn't decay over time, thus it will keep on maintaining the current, also called a persistent current (Fig. 4.10(c)). The persistent current is proportional to $-\Phi/L$, with L being the inductance of the material. The trapped magnetic flux inside the ring has unique properties in which the level of magnetic flux cannot be changed in a continuous manner. In other words, the trapped magnetic flux is a quantized variable that can only increase in multiples of the flux quantum ($\Phi_0 = 2\pi\hbar/2e = 2.068 \times 10^{-15}$Wb) [35].

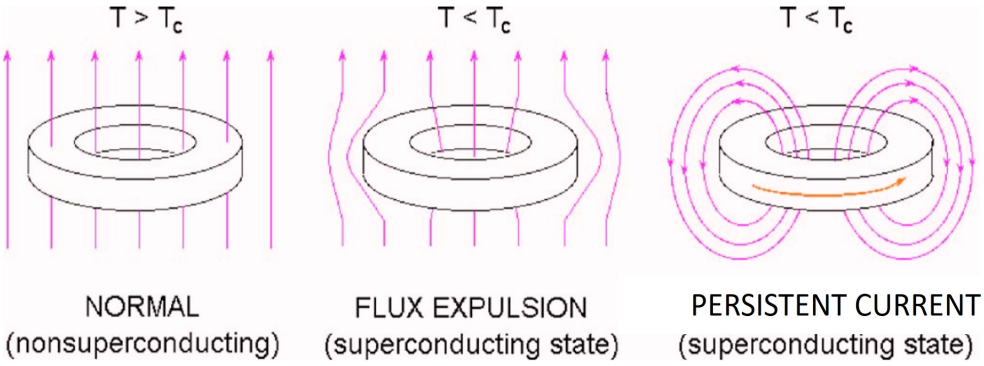

Figure 4.10: Schematic illustration of the Meissner effect in a ring-shaped superconductor under an applied magnetic field when the temperature (a) is over the critical temperature and (b,c) under the critical temperature [35].

The SQUID uses the Josephson effect which describes the electron (Cooper pair electrons) can quantum tunnel through the Josephson junction with no voltage as long as the material is in a superconductive state. However, at high enough currents (over the critical current, I_C) the material loses its superconductive behaviour and becomes resistive, following Ohm's law. Hence, ideally, when the current reaches critical the material should immediately exhibit a voltage signal (i.e., a vertical line), but realistically it is a steep gradient when the current goes over the critical limit (Fig. 4 .11(a)).

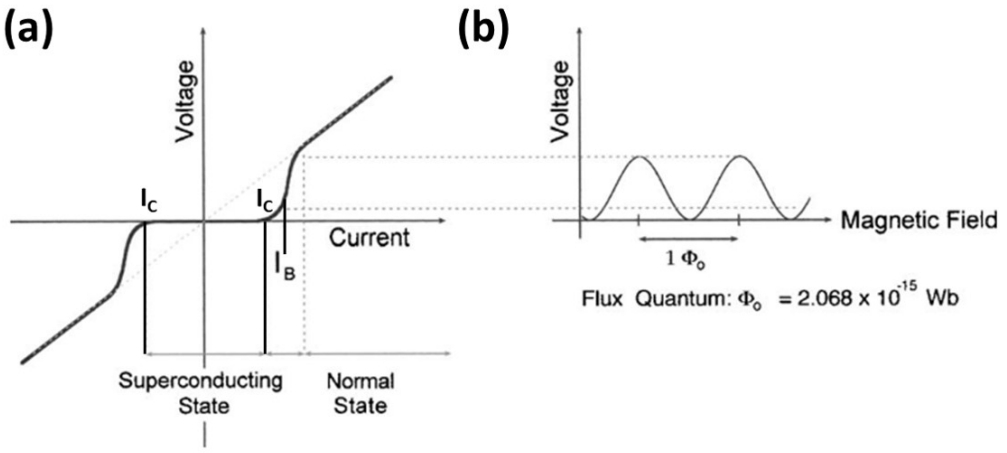

Figure 4.11: (a) Biased current (I_{B}) for Josephson junction with the normal state indicating the Ohm's law resistive behaviour of the material. (b) The voltage vs externally applied flux at a constant bias current [35].

Therefore, when applying a bias field over the critical current the superconducting ring exhibits a periodic voltage signal where the period is proportional to a multiple of the flux quantum (Fig. 4.11(b)). This can then be locked into state can be locked by a feedback loop and is considered the reference point when comparing the change in periodicity of the voltage signal ($\Delta\Phi$).

The SQUID-VSM mode follows a similar principle to conventional VSM where the sample oscillates in a sinusoidal manner and is magnetised under a uniform magnetic field. However, the pickup coils that detect the stray fields from the sample is a second order gradiometer, in which the sample only oscillates at the centre (or x-position = 2cm, in Fig. 4.12) where the signal is at its highest. The oscillation of the sample induces a change in current within the detection coils and this gets relayed to the SQUID sensor (the superconducting ring with Josephson junctions) in which the change in

current induces a change in the magnetic flux which changes the periodic manner of the voltage signal and the voltage change is compared to the reference point (Fig. 4.12).

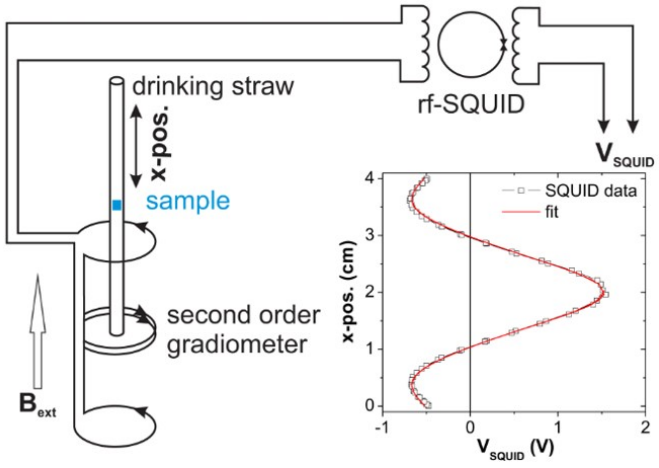

Figure 4.12: Schematic setup of a SQUID system with the second order gradiometer detection coils, rf-SQUID (rf meaning the Josephson junction is biased by an AC current), and feedback loop that produces the signal measured (in this case V_{SQUID}. The inset shows the response of the SQUID to the sample position (x-pos.) where x=2 cm is the centre of the second-order gradiometer detection coils [236].

As a result, the magnetisation of the sample can be calculated by the change in flux quantum, $\Delta\Phi$, from the reference to the applied magnetic field strength. As a result, the setup of the SQUID-VSM enables very high sensitivity that can detect stray fields down to 10^{-14}T [235].

In this study, SQUID-VSM was performed using a Quantum Design MPMS3 Magnetometer. The samples were cut into dimensions of 10 mm $\times$ 2 mm $\times$ 25 μm and were placed inside plastic capsules filled with cotton wool to limit the sample movement as it vibrates inside the SQUID. The cap-

sule was then inserted into a plastic straw and the capsule positioned at the centre of the gradiometer in the SQUID to ensure maximum signal could be detected. The sample was subjected to a sweeping field between +/- 150 Oe at ambient temperature with 4 Oe/sec steps to ensure any small changes to the sample's magnetic moment were detected. Each sample's hysteresis loop was obtained with the Co-rich ribbon sample having the softest magnetic properties, followed by Fe-rich and then Ni-rich ribbon samples, respectively (Fig. 4.13).

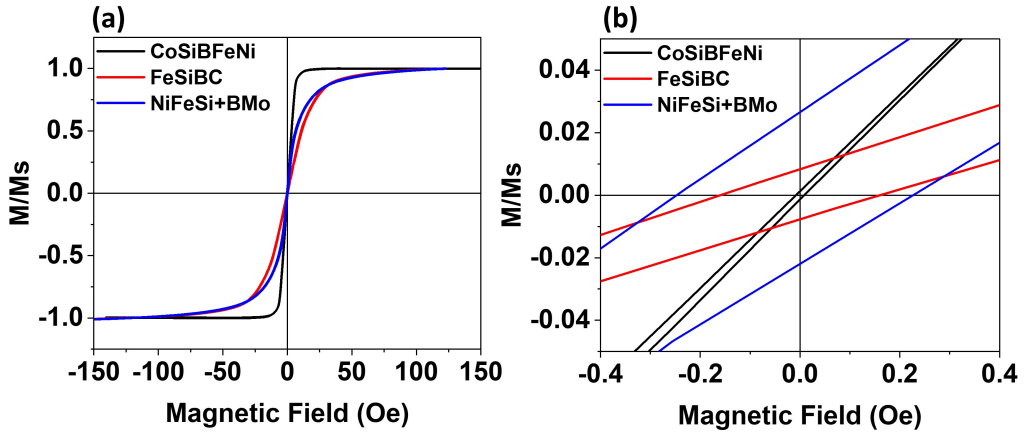

Figure 4.13: Normalised hysteresis loops of (a) CoSiBFeNi, FeSiBC and NiFeSi+BMo ribbon samples and (b) a more detailed image of the same graph that illustrates very small coercive fields measured by the SQUID-VSM.

Fig. 4.13 displays the normalised hysteresis loops of all three samples with Co-rich reaching magnetisation saturation ($\boldsymbol{M}_{\mathrm{S}}$) at a faster rate (at field $\sim \pm 23$ Oe) compared to Fe-and Ni-rich samples with fields reaching saturation at $\sim \pm 115$ Oe. From this, it can be implied the susceptibility (χ) of the Co-rich sample is much higher compared to Fe- and Ni-rich samples. In addition, the coercivity of the Co-, Fe-, and Ni-rich samples was measured

to be 10 mOe, 160 mOe, and 230 mOe, respectively. This indicates the Co-rich sample to be more magnetically softer than the other two samples with Ni-rich being the hardest magnetic sample. Based on the coercivity of each sample, this implies the Co-rich material would exhibit the highest GMI/ GSI response with Ni-rich being the lowest in response. This was investigated and discussed in chapters 6 and 7, in which chapter 6 investigated the GMI response and chapter 7 investigated the GSI response for each material, with respect to their magnetisation and magnetostriction values.

4.4 Characterisation of GMI and GSI

The literature describes many bespoke experimental systems that have been designed to characterise GMI, where the specific details of each design reflected the geometry and design of the magnetic sample to be characterised [237, 238, 239]. However, all of these have been designed with the fundamental definition of GMI as their basis. GMI is defined as the change of the magnetic material's electrical impedance ($|Z|$) as a function of applied magnetic field (H), at frequencies between 0.01 – 1000 MHz [46]. Therefore, all GMI measurement systems must reflect the basic circuit diagram shown in Fig. 4.14, where the impedance of a sample is measured by using a voltmeter to measure the potential difference of the sample with an alternating current (AC) of 20 mA, and whilst subjected to an applied field (H_{dc}). This is typically achieved using an impedance analyser.

A similar approach must be taken to characterise giant stress impedance (GSI) [43, 44, 45]. The definition of GSI is the change in a magnetic material's electrical impedance ($|Z|$) as a function of applied tensile stress (σ), at frequencies between 0.01 – 100 MHz [45]. In general, a GSI setup will resemble that shown in Fig. 4.14, but instead of an applied field, tensile

stress (σ) is applied.

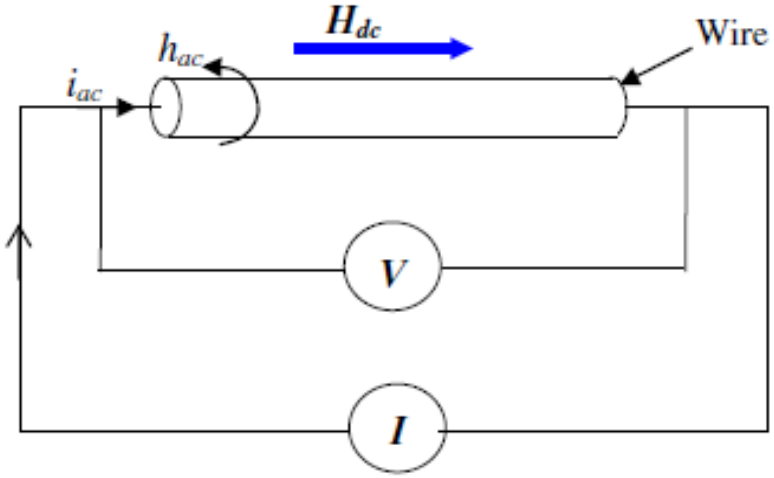

Figure 4.14: The circuit diagram illustrates the definition for measuring GMI. H_{dc} is the applied direct current (DC) uniform field and h_{ac} is the induced alternating field from the wire sample when subjected under a flowing alternating current (i_{ac}) [46].

In this study, rigs were developed to measure both GMI and GSI. However, additional challenges resulted from the geometry and sizes of the ribbon samples. Compared to the literature, the samples that were prepared for this study are much larger (typically of lengths 200 mm or longer) thus it adds further difficulties to design a rig that could provide a reliable and accurate GMI measurement of the ribbon samples [49, 225, 47, 240]. Details on the development of the custom-made rigs to accurately and reliably measure GMI and GSI can be found in chapter 5. In this chapter, a short description of the equipment used and how these rigs were operated will be described.

GMI was characterised by designing a setup illustrated in Fig. 4.15 with a flowchart that shows how it was operated. LabVIEW (refer to Ap-

pendix 1 for further details on using LabVIEW) was used to operate both an impedance analyser (Agilent 4294A Precision Impedance Analyser) and a bipolar power supply (KEPCO BOP 72-6D-802-E DC power supply) in order to measure the GMI in a changing field. Before any measurements were taken the adapter (16048H Adapter) and the test leads (0.14 m long BNC (Bayonet Neill-Concelman) to crocodile clip test leads) had to be calibrated. The adapter was calibrated using a PHASE and LOAD compensation whereas the test leads were calibrated using an OPEN, SHORT, and LOAD compensation, further details on compensation are found in chapter 4. After the calibrations, the ribbon sample was placed inside the electromagnet whilst connected to the impedance analyser with a four-point terminal connection. Next, a uniform dc magnetic field was produced by the electromagnet where the magnetic field strength was defined by the voltage and current values set by the power supply. Afterward, the impedance ($|Z|$) of the sample was measured and saved by the impedance analyser. The process was then repeated with the power supply setting a new voltage and current value (and thus applying a different field) after every impedance measurement. Once a full magnetic field sweep was completed the operation ended.

Fig. 4.15 illustrates how GSI was characterised with a flow chart showing its operation procedure. As in Fig. 4.16 the process began with the adapter and test leads of the impedance analyser being calibrated by LabVIEW. After calibration both ends of the ribbon sample are clamped to the manual tensile test machine (Mark-10 ES30 Precision Hand Wheel Test Stand) where a tensile force was manually applied to the sample, monitored by a force gauge (Mark-10 Series-5 Advanced Digital Force Gauge) with a precision of 0.05 N. Once the desired tensile force was set, the impedance ($|Z|$) of the sample was measured and saved by the impedance analyser. The process was then cycled with the tensile force being manually increased after every impedance measurement. The operation ended either when the desired tensile force had

been reached or the sample broke.

After measuring the changes of impedance $|Z|$ at each applied magnetic field (H_{dc}) or applied tensile stress (σ). The GMI or GSI ratios were calculated using the following formula:

$$GMI = \frac{|Z(H)| - |Z(H_{max})|}{|Z(H_{max})|} \times 100\% \tag{4.2}$$

$$GSI = \frac{|Z(\sigma)| - |Z(0)|}{|Z(0)|} \times 100\% \tag{4.3}$$

where H_{max} was the maximum applied field (at $\pm$150 Oe) and $Z(0)$ was the impedance for an applied tensile stress = 0 MPa on the ribbon sample whereas $Z(\sigma)$ was the impedance of a sample for any given applied tensile stress. H_{max} was set at $\pm$150 Oe in reference to Fig. 4.13 where all three samples reached magnetisation saturation at $\pm$150 Oe or lower. The GMI and GSI ratio of the various ribbon sample characterised can be found in chapters 6 and 7 where both are discussed in detail.

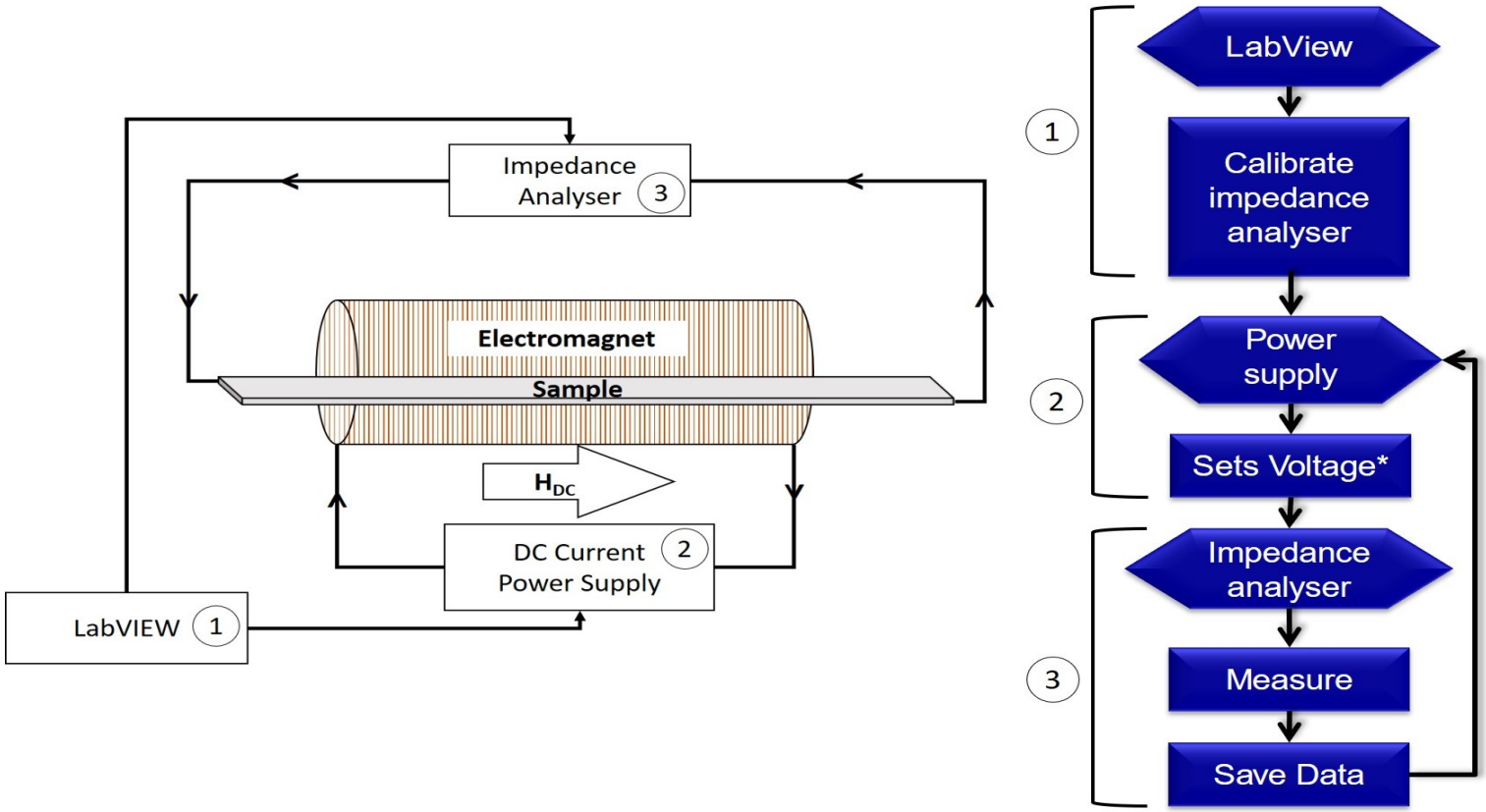

Figure 4.15: Schematic diagram (left) for characterising GMI with flowchart (right) illustrating the operating procedure. *Setting the voltage provides the magnetic field strength of the electromagnet.

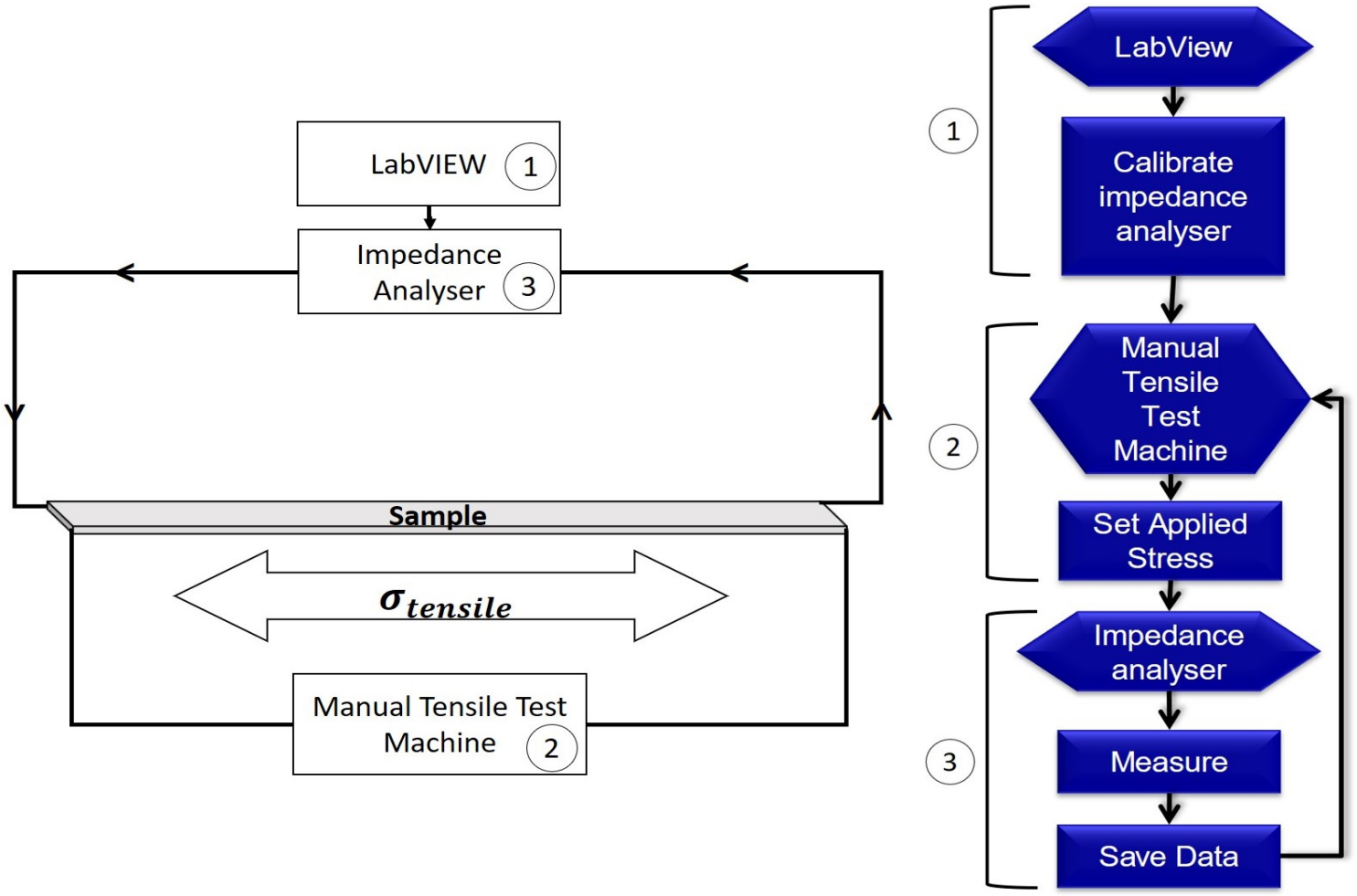

Figure 4.16: Schematic diagram (left) for characterising GSI with flowchart (right) illustrating the operating procedure.

Chapter 5

Development of Experimental Infrastructure for GMI and GSI Measurements in Macroscale Ribbon Samples

5.1 Outline

The project described in this thesis required the measurement of the electrical impedance of macroscale (>100 mm long) ribbon samples with high precision and repeatability. This presented substantial additional challenges over more standard studies of giant magnetoimpedance and giant stress-impedance, where samples are typically <50 mm, in length [43, 241, 46, 242, 243]. From them, the two challenges that proved difficult in obtaining reliable measurements for such samples were: (1) compensating for the parasitic impedance of the test lead cables and contacts, which were typical of a similar order of

magnitude to the samples under test, and (2) immobilisation of the (highly flexible) ribbons, as (minor) distortions were found to produce substantial changes in impedance. Overcoming these challenges was necessary to obtain repeatable and accurate measurements for both the GMI and GSI behaviour of the studied samples.

The chapter discusses the progressive steps taken to improve the characterisation technique for both GMI and GSI measurements using quantitative data and referring to the literature for every measurement taken for the studied samples.

5.2 Developing GMI and GSI measurement systems

As discussed in chapter 4, studies of the GMI and GSI effect typically use bespoke systems to characterise their sample(s). These bespoke systems were designed around the size and shape of the sample(s), such as wires [244, 245, 246], ribbons [43, 247, 198], meandering strips [248], etc.

For GMI measurements every bespoke system always had two common components:

1. An impedance analyser producing an alternating current (AC) capable of producing MHz bandwidth driven frequency to characterise the impedance of the samples.

2. An electromagnet (such as a solenoid or Helmholtz Coil) driven by a power supply to apply direct current (DC) magnetic fields to the sample(s) under test.

For GSI measurements it is also necessary to apply, compressive or tensile stresses ($\boldsymbol{\sigma}$) to the samples under test instead of or in addition to magnetic fields.

In this study, a system for characterising the GMI effect in macroscopic ribbons was developed first and then adapted to allow characterisation of GSI effects. Development was performed in this order because:

1. The literature on the GMI effect was more extensive compared to the GSI effect, allowing the validity of the results to be checked against previous studies.

2. The bespoke system for measuring the GMI effect can easily be adapted for measuring the GSI effect by implementing a tensile tester.

Measurements with an initial test rig produced unreliable data, and substantial time was spent attempting to identify flaws by comparing measured data to literature sources and testing prospective solutions. Ultimately, the factors contributing to reliability were found to be the poor immobilisation of the ribbon sample within the measurement rig and poor compensation for the parasitic impedances of the impedance analyser adaptor and test leads. It is of note that both of these factors were particularly acute for the large-scale ribbon samples that were under test. The size of these samples made immobilisation difficult resulting in unreliable connections to the impedance analyser (i.e., without changing the impedance of the test leads) and the ribbons had intrinsically low impedances (typically $\sim$13 Ω) meaning that even smaller parasitic impedances had large impacts on the measured data.

This chapter will first illustrate these difficulties in section 5.2.1, before demonstrating how incremental changes to the experimental approach allowed reliable measurements to be obtained.

5.2.1 The initial experimental approach to characterising GMI

The system used to characterise GMI and GSI was originally designed for measuring the impedance of ceramic-based samples with very large impedance values (measured in kΩ). The system consisted of an Agilent 4294A precision impedance analyser connected via a 16048D adapter to BNC to crocodile clip test leads. The ceramic-based sample the system was designed for only had two electrical contacts and thus a two-terminal (2T) connection was used. The parasitic impedance of the test leads was compensated via a manual, three-step process; First, the open and short circuit impedances of the test leads were characterised in the range of 40 Hz to 110 MHz. Then, the impedance of the sample was measured via a 2T connection. An Excel spreadsheet was then used to manually calculate the samples' compensated impedance values using a simple network model. Further details on modelled networks and compensating parasitic impedances are discussed in section 5.3.3.i "Terminal configurations". In general, the high impedances of the ceramic samples meant that residual parasitic impedance left in the measurement due to the 2T configuration and crude, manual compensation procedure were irrelevant. However, these had much larger impacts on the measurements of metallic samples with impedances <100 Ω.

This system was used to pilot GMI measurements on a ribbon chemical composition of CoSiFeMo (Fig. 5.1). The magnetic ribbon sample was placed inside a solenoid – connected to a power supply (KEPCO BOP 72-6D-802-E) – with test leads connected to the sample in a 2T configuration to the impedance analyser. The solenoid was created from a 100 mm length polyvinyl chloride (PVC) tube with a 20 mm diameter aperture, with 1000 turns of copper wire coiled around the tube. The power supply (KEPCO

BOP) supplied a DC current to the solenoid to enable a uniform DC magnetic field onto the sample. The strength of the field was varied by manually changing the driving current from the power supply and at each field strength the impedance of the sample was measured. The test leads and adaptor were both compensated using the aforementioned methodology which were then used to calculate the corrected impedance of the magnetic ribbon sample measured, at each magnetic field strength applied.

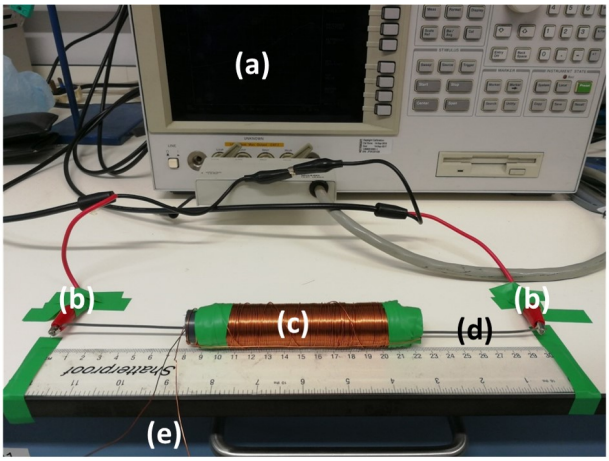

Figure 5.1: The initial setup for characterising GMI; (a) an Agilent 4294A precision impedance analyser, (b) BNC to crocodile clip test leads, (c) a (homebuilt) solenoid, (d) the sample and (e) connection to a KEPCO BOP 72-6D-802-E DC power supply (outside the image).

The corrected data were used to calculate the absolute impedance ($|Z|$) of the sample before and after the applied field ($\boldsymbol{H}$), which was then used to calculate the GMI ratios at each applied field of the sample (Eq. 3.2).

Fig. 5.2 compares the difference of the measured GMI response ($\Delta Z/Z$) with respect to the field ($\boldsymbol{H}$) of a commercialised amorphous ribbon sample, CoSiFeMo, of length 200 mm, width 3 mm, and thickness of 25 μm, using

the initial system to a typical GMI (with respect to the field) measurement found in literature, in this case, a study done by Lu et al. [249]. This latter study investigated the GMI response for a melt-spun (in vacuum) amorphous ribbon sample, CoFeCrSiB, annealed at 400°C for 20 minutes (in a vacuum) of length 5 mm, width 1 mm, and thickness of 23 μm.

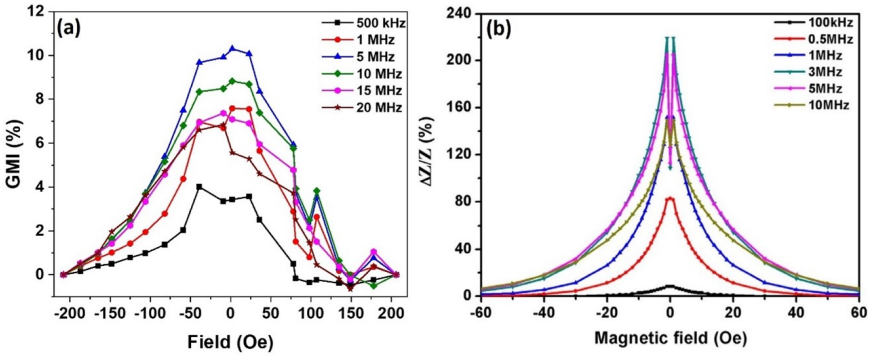

Figure 5.2: Comparison between two measured GMI responses ($\Delta Z/Z$) with respect to field (H) at various driven frequencies between (a) the initial experimental system and (b) literature source taken from [249]. Both samples have amorphous crystal structures and Co-rich compositions, where (a) was CoSiFeMo and (b) was CoFeCrSiB. Dimensions for the ribbon sample in (a) were 200 mm length x 3 mm width x 25 μm thickness and for (b) were 5 mm length x 1 mm width x 23 μm thickness.

Fig. 5.2 illustrates the difference between the measurement taken using the initial experimental system and the GMI data published by a previous study by Lu et al [249]. The similarities the initial GMI measurement has in common with the published data were:

1. Basic peaked behaviour close to the zero field.

2. Broad single peaks in the measured data compared to sharp single or

double peak(s) in the published data.

3. The measured GMI response was significantly lower than the published data – by a factor of 20.

Comparatively, many noticeable differences were observed, which were:

1. Asymmetricity of the GMI curve with the rig exhibiting noise in the data.

2. The highest GMI response occurred at ∼5 MHz frequency.

The asymmetricity of the initial measurement was quantified by comparing the GMI values at the negative field ($-\boldsymbol{H}$) to the positive field ($+\boldsymbol{H}$) as shown in Fig. 5.3 for frequencies 500 kHz, 5 MHz, and 15 MHz frequencies.

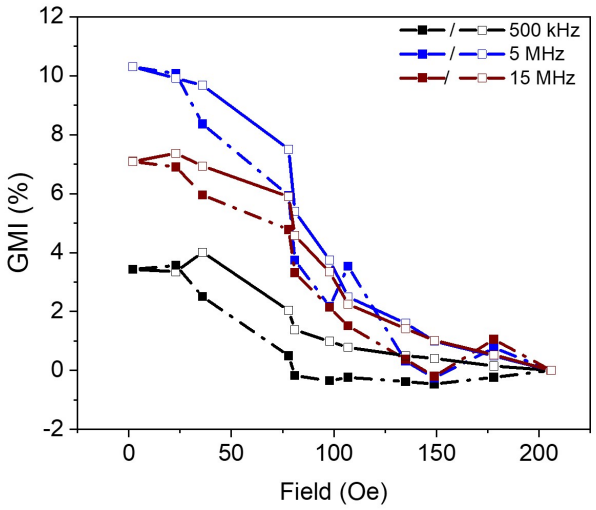

Figure 5.3: Comparing the measured GMI response between negative fields (open dots) to positive fields (filled dots) for 0.5 MHz, 5 Mhz, and 15 MHz frequencies. The data was adapted from Fig. 5.2(a).

ΔGMI (%) = GMI (%) (at -H) – GMI (%) (at +H)											
±H (Oe)	**2**	**23**	**36**	**78**	**81**	**98**	**107**	**135**	**149**	**178**	**206**
Frequency (MHz)											
0.5	0	-0.21	1.50	1.54	1.55	1.34	1.01	0.88	0.87	0.39	0
1	0	-0.86	1.32	1.49	1.27	1.15	-1.21	0.83	0.75	0.03	0
5	0	-0.15	1.31	1.58	1.66	1.57	-1.04	1.29	1.25	-0.28	0
10	0	-0.20	0.96	1.04	1.23	1.20	-1.36	1.00	0.98	0.95	0
15	0	0.46	0.98	1.12	1.26	1.20	0.74	1.04	1.22	-0.52	0
20	0	1.57	1.99	2.08	2.20	2.15	2.18	2.14	1.65	0.12	0

Table 5.1: Differences of measured GMI ratios between positive and negative fields.

The difference in GMI values (ΔGMI) was calculated by taking the difference between them, as shown in Table 5.1.

For a symmetrical GMI profile, the difference between GMI values at both positive and negative fields should be at 0. For the preliminary measurement (excluding 2 and 206 Oe) the differences were all non-zero, thus illustrating the asymmetry in the data. The largest difference was shown at the 20 MHz frequency with a 2.20% difference at a field of $\pm$81 Oe.

Table 5.2 lists each of the differences noted between the preliminary data and the published data of a previous study, suggests potential causes and identifies possible solutions. In the following sections, these solutions are implemented and their effectiveness is examined both quantitatively and qualitatively.

Inaccuracies in Fig. 5.2(a)	Differences to Fig. 5.2(b)	Type and (potential) cause of error(s) (Systematic error = S and Human error = H)	Potential solution(s)
Highest GMI response of the Co-rich sample reached ~10%	GMI responses for Co-rich samples are very high with the lowest being around 80% [17] up to values over 300% [18].	S1) Improper terminal configuration and calibration procedure which inadequately compensated the measured impedance from internal (parasitic) impedances in the impedance analyser and its components, such as the adapter, coaxial cable, and test leads. S2) Ratio of ribbon under field compared to outside of field resulted in a low signal GMI response from partial saturation of the sample.	S1) Proper calibration of an open, short, and load circuit to compensate the parasitic impedance in the impedance analyser and its components. S2) Ensure the sample is completely subjected under a DC magnetic field for full magnetization saturation of the sample.
Unclear distinction of a single-peak (SP) or double-peak (DP) GMI curve profile	GMI curves with respect to applied field (***H***) typically have either SP and/or DP GMI curves that indicate the magnetic behaviour of the sample at changing frequencies. The literature displays an example of both SP and DP curve profiles at different frequencies.	S3) Field resolution was too low to identify any distinguishable SP or DP GMI curve features. S4) Lack of a zero-field (0 Oe) data point to differentiate the SP or DP GMI curve.	S3) Design and use an automated control system capable of high field resolution, e.g. deploying multiple fields with increments of every 0.5 Oe within the desired field for all frequency ranges. S4) Inclusion of a zero-field data point to differentiate a SP and DP GMI curve.
Lack of symmetry of the GMI curve between positive and negative fields, with inclusion of noise	All GMI curves are symmetrical with the line of symmetry at the zero-field data point. This is expected since the magnetic behaviour of the sample should be identical with the difference being the direction of the magnetization vector.	H1) Impedance measurement was inconsistent throughout the sample during measurement. Causes of sample movement in the middle of measurement are from the rigidity of test lead cables where any movement from the cables deforms (and moves) the ribbon sample.	H1) Design a mount that effectively immobilises the sample during measurement.

Table 5.2: Summary of errors present in the GMI response measured from the initial experimental approach with solutions to resolve them for a more accurate and representable GMI response of the measured ribbon sample.

5.3 Refining the approach to GMI measurement

5.3.1 Power supply and electromagnets

5.3.1.i Resistive load KEPCO power supply

The 400 W KEPCO power supply used in this study was capable of supplying a current of up to ±6 A and voltage of up to ±72 V. This ensured that DC magnetic fields were large enough to magnetically saturate the sample, allowing complete GMI curves to be measured. To prevent applied fields from drifting due to resistive heating during a measurement cycle the KEPCO is used in current controlled, rather than voltage controlled mode. However, during preliminary measurements, it was noticed that the application of magnetic fields caused audible vibration of the ribbon samples (∼4 kHz). This occurred because the purchased KEPCO unit was optimised for resistive loads rather than inductive loads. The result of this was that when supplying a higher current (>1 A), the current oscillated, creating oscillations in the magnetic fields applied and driving high-frequency sample motion. These vibrations were clearly an under-desirable feature for high-precision impedance measurement.

The cause of these oscillations was the voltage and current outputs were out of phase due to the inductive effects of the solenoid. The inductive effects slowed the rate at which current can respond to changes in the applied voltage causing a lag in the control circuit. Adding a resistor and capacitor in parallel to the inductive solenoid cancels the reactive elements of the load which brings the voltage and current to be back in phase. As a result, the induced acoustic noise became inaudible i.e., the vibration of the sample in

the electromagnet was suppressed. Further immobilisation of the sample, to suppress lower frequency vibrations, will be discussed in section 5.3.4.

5.3.1.ii Electromagnets

Two types of electromagnets were used in the project, an existing Helmholtz coil pair and home-built solenoids. In the following sections, the design and calibration of the field strength and uniformity are discussed.

5.3.1.ii.1 Solenoid

The solenoid used for the initial GMI characterisation was wound around a PVC tube with an aperture of 20 mm and a length of 100 mm. Copper wire, of 24 AWG (0.5 mm diameter), was coiled around for 1000 turns evenly distributed along its length, with a measured average resistance of ∼13.6 Ω. However, this was too short to apply a uniform field for samples with lengths that exceeded 100 mm, and the solenoid also deformed due to resistive heating when applying strong magnetic fields, due to the low glass transition temperature (T_g) of the PVC tube (around 80° C). To prevent the deformation, the plastic material was changed to PC (polycarbonate) plastic, which had a higher T_g temperature (around 145°C), and a second coil was created with an increased length of 200 mm. For this solenoid 1600 turns of coiled copper wire were used, which had a measured average resistance of ∼21.7 Ω (Fig. 5.4). The number of turns per unit length was maintained in order to maintain similar applied field strengths to the original solenoid. The coiling of the copper wire was also improved to improve the uniformity of the applied field.

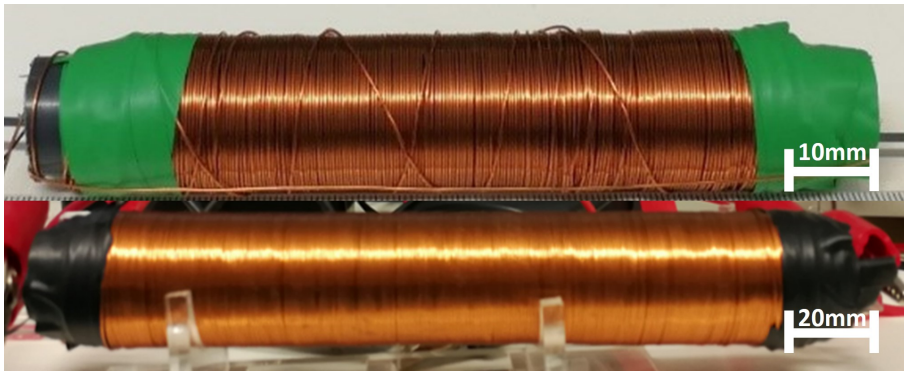

Figure 5.4: (Top) Solenoid used for the initial GMI measurements with 100 mm length; PVC tubing as the base. (Bottom) refined solenoid design with 200 mm length and PC tubing as the base.

The uniformity of the magnetic field was characterised by using a gauss-meter equipped with an axial Hall probe. For both solenoids magnetic field strength was measured and mapped throughout the solenoid in 10 mm increments in the centre of the solenoid (Fig. 5.5).

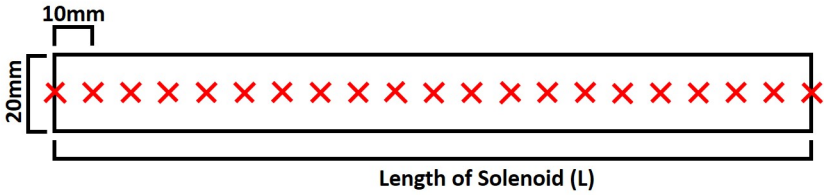

Figure 5.5: Schematic diagram of measuring the magnetic field strength of a solenoid of any given length (L) with a common aperture diameter of 20 mm, with every cross (X) indicating the position of the Hall probe measuring the magnetic field strength of the solenoid at every 10 mm increment.

Fig. 5.6 displayed the measured field strengths between the 100 mm (dotted black trend line) and 200 mm (dotted blue trend line) length solenoids

at 2 A of DC current. Both solenoids were compared to the calculated field ($\boldsymbol{B}$) from both solenoids (solid trend lines) using the equation,

$$B = \mu I \frac{N}{L} \tag{5.1}$$

where $\boldsymbol{B}$ is the solenoid's magnetic field induced by the driven current (I), μ is the permeability of free space ($4\pi \times 10^{-7}$), N is the number turns of the coiled wire and L is the length of the solenoid (Fig. 5.5).

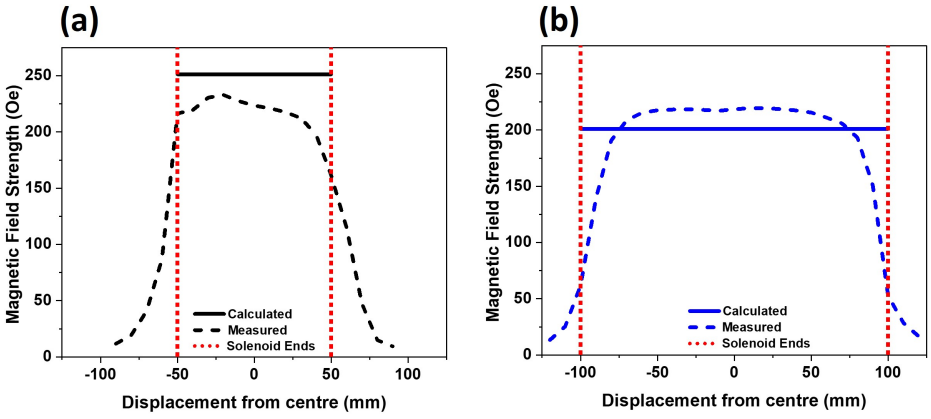

Figure 5.6: The measured magnetic field strength for (a) 100 mm solenoid and (b) 200 mm solenoid length, indicated by the red dotted lines. The x-axis indicates the distance the field strength was measured from the centre of the solenoid. The measured field strength was represented with a dotted trend line whereas the calculated field (using Eq. 5.2) was represented with a solid trend line.

The curve profile for both solenoids was as expected with a uniform central region and the field falling off rapidly once outside the solenoid body. The initial displayed asymmetry in which suggests the coil windings were unevenly distributed which was not the case for the 200 mm solenoid. The

100 mm solenoid displayed a slight underperformance than the calculated field strength whereas the 200 mm overperformed. This indicates the coil density (N/L) was either insufficient for the 100 mm solenoid ($\sim$28 Oe) or overdone for the 200 mm solenoid ($\sim$18 Oe). Moreover, the field rapidly declining within the body of the 200 mm solenoid suggests the coil density was higher within $\sim$160 mm instead of the expected 200 mm range.

Despite both solenoids having different curve profiles, the most important factor in accurately measuring the GMI response of the ribbon samples was the uniformity of the field strength. A non-uniform magnetic field will magnetise different parts of the ribbon sample differently, broadening the GMI curve and reducing the overall size of the GMI signal measured.

A simple method was to calculate the percentage difference of the field strength relative from the centre – $\sim$251 Oe for the 100 mm solenoid and $\sim$218 Oe for 200 mm solenoid – with an acceptable difference of the field strength by $\pm$10% (Fig. 5.7).

Fig. 5.7 demonstrated the 200 mm solenoid having a more consistent field strength between -60 mm to +60 mm positions of the solenoid in comparison to the 100 mm solenoid which lacked consistency. Within the allowable $\pm$10% difference field strength the 200 mm solenoid displays a total distance of 140 mm of a uniform field. Therefore, the 200 mm solenoid was selected to ensure a consistent field strength can be applied to ribbon samples (of lengths up to 200 mm) despite the large field strength changes at the ends of the ribbon. Here, measurements of GMI for ribbons of the same length of the solenoid were expected to show relatively minor broadening/suppression of the GMI response due to the 30 mm close to the ends of the solenoid where fields decayed rapidly.

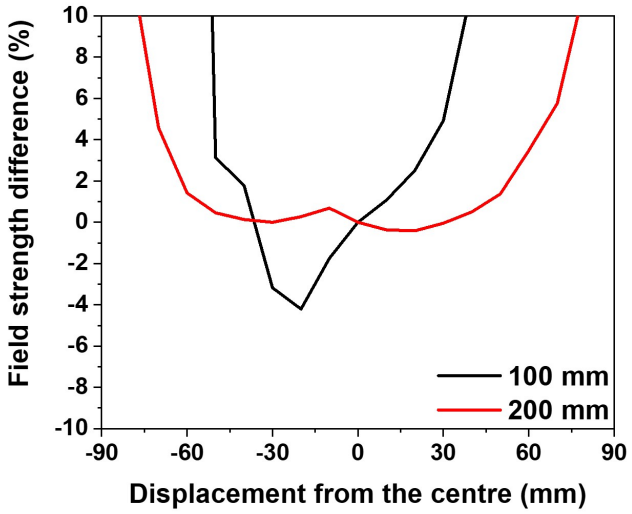

Figure 5.7: The ±10% (allowable) difference of the field strength between from the central position of the solenoid to the rest of the solenoid.

5.3.1.iii Helmholtz coil

A pre-existing Helmholtz coil pair was used for measuring ribbon samples with lengths $<$ 180 mm. This was because the 140 mm long test leads were too short to connect to the sample within the 200 mm length solenoid, whereas the Helmholtz Coil provide much to the sample.

The Helmholtz coil pair had an aperture of 160 mm in diameter, 150 mm between the outer edge of the two coils, and a total length of 250 mm. The coiled wires were supported and protected by a very thick plastic shell to prevent any environmental damage to the system. Between the two coils a rectangular hole was present (on the plastic covering), which was used for the test leads to access the centre of the Helmholtz Coil and connect to the sample (Fig. 5.8).

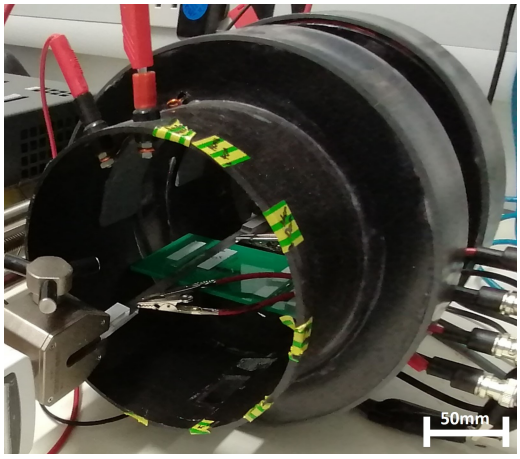

Figure 5.8: The Helmholtz coil used in this study.

The magnetic field strength of the Helmholtz Coil was characterised and mapped using a gaussmeter equipped with an axial probe as shown in Fig. 5.9.

Fig. 5.10 plots the field strength with 1 A of driven current across the Helmholtz Coil and compares this to the expected field derived from its manufacturer's specification (equivalent to 30 Oe/A). Measurements were taken along several different lines as illustrated in Fig. 5.10.

The magnetic field strength of the Helmholtz coil displayed a spike in field strength of over 30 Oe at -25 mm from the centre when measuring the edge of the Helmholtz coil. The sudden increase in field strength was associated with the close proximity to the coiling of the copper wire compared to the rest of the Helmholtz coil where field strengths were similar in strength throughout, with the highest measured up to 27.7 Oe. Excluding this spike, the applied field profile was consistent between central, mid-point, and edge line scans with the largest difference being 4.3 Oe at the -75 mm position.

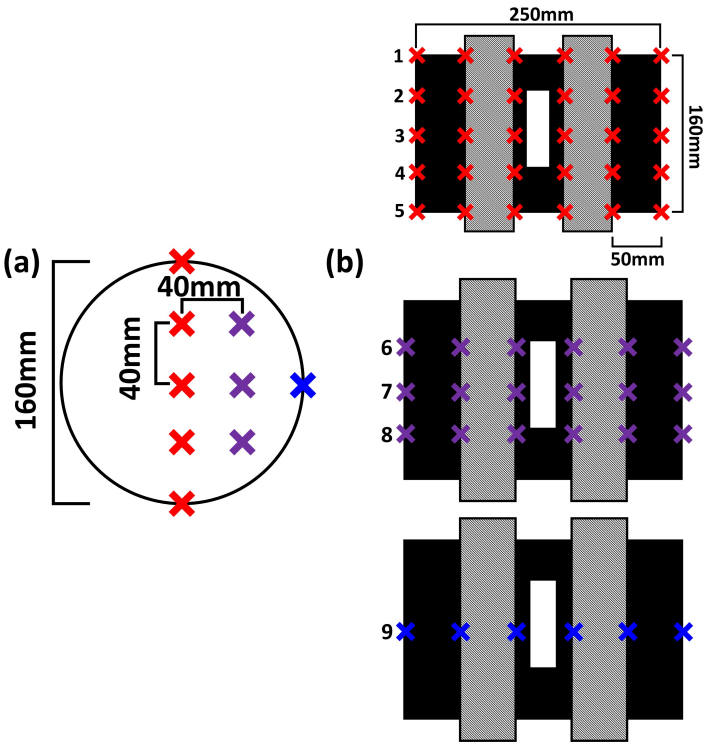

Figure 5.9: Mapping of the magnetic field of the Helmholtz Coil with (a) the cross-section of the Helmholtz Coil at the front and (b) the cross-section from the side of the Helmholtz Coil. The labelled (X) represents the position of the axial probe tip within the Helmholtz Coil when measuring its magnetic field strength. Furthermore, the different sections of the Helmholtz Coil being measured were labelled respectively; at the centre (X), mid-point (X), and edge (X). Within each section of the measured Helmholtz Coil a number was labelled for each row measured along the Helmholtz Coil within the section, e.g. X row 3 defines all magnetic field strengths measured at the centre section of the Helmholtz Coil. The positions of each cross (X) were equidistant from each other by 40 mm height $\times$ 40 mm width $\times$ 50 mm length. The two rectangles filled with a striped line pattern are the coiled wires and the white rectangle in the middle represents the hole on the plastic covering.

The percentage difference of the field strength relative to the centre was analysed with the acceptable variation from the uniform field to be the same as the solenoids (±10%). Following this parameter for the acceptable uniform field strength Fig. 5.10(b) demonstrated a distance between -50 and +50 mm was the most uniform - with a consistent field of ∼ ±27.7 Oe. This covered the desired distance required for ribbon samples with lengths between 50 mm and 100 mm.

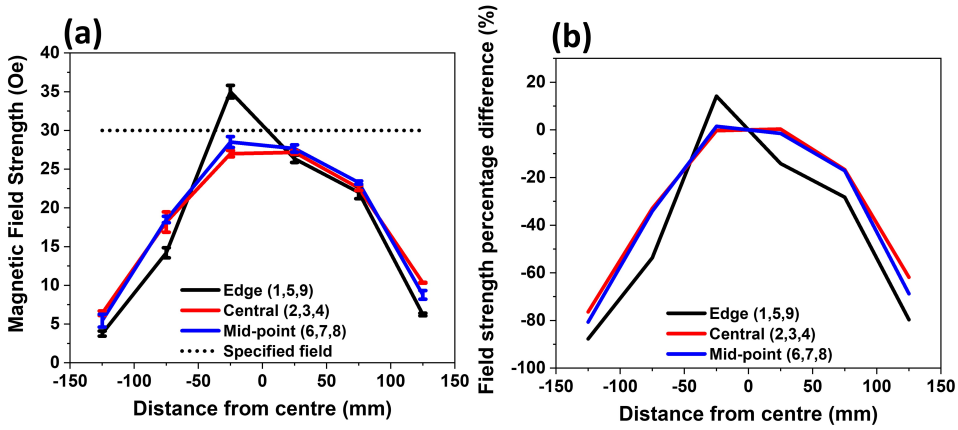

Figure 5.10: (a) Average field strength with respect to the distance from the centre of the Helmholtz coil for the edge, central, and mid-point regions of the electromagnet (highlighted in Fig. 5.9(a)). All measured fields were compared to its labelled specified field of 30 Oe/A with error bars representing the standard deviation from the mean field at every point of the electromagnet. (b) Percentage difference of field strength relative to the centre of the Helmholtz coil.

To measure the GMI response of ribbon samples with lengths over 100 mm the driven current was increased until the regions with the lowest field strengths were capable of magnetically saturating the ribbon samples. Although this did not resolve the effects of field non-uniformity on the precise

shape of the GMI curves, it meant that values of impedance in the absence of field and at magnetic saturation were as they would be for a perfectly uniform profile, and hence maximum GMI ratios would be measured correctly, as observed in chapter 6.

5.3.2 Automation and refinement of the GMI measurement system

The first and easiest problem to be resolved was the unclear distinction between single-peaked (SP) and double-peaked (DP) GMI curve profiles. This was achieved using an automated system to improve the field resolution of the measurements. This was achieved by creating a LabVIEW program (Appendix A) capable of sweeping the field while retrieving impedance measurements from the impedance analyser without any manual intervention. Additionally, the connection between the impedance analyser to the sample was changed from a 2T connection to a 4T connection using 4 BNC to crocodile clip test leads. All four test leads were secured using an adhesive tape to the table surface (similar in Fig. 5.1(b)) which limited the mobility of the ribbon sample and leads during measurement, improving the stability of the measurements.

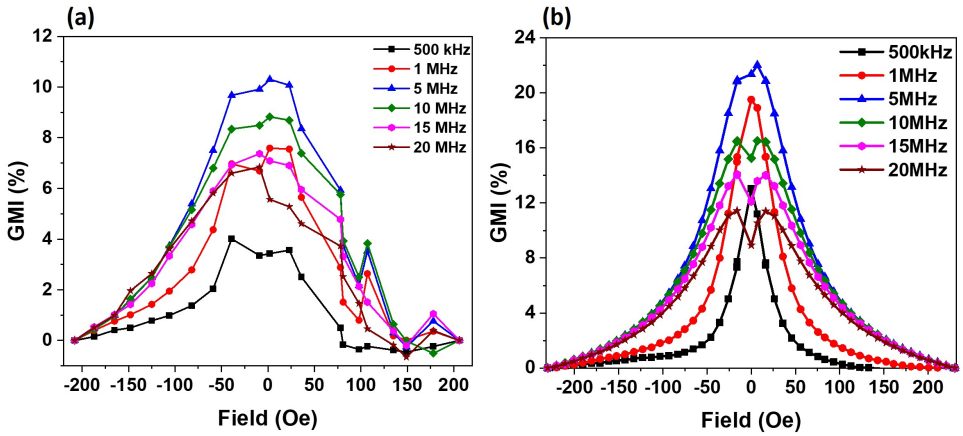

Figure 5.11: Comparison between the measured GMI ratio with respect to the field between the (a) initial experimental approach from Fig. 5.2(a) and the (b) automated GMI measurement system. The ribbon sample (CoFeCrSiB) used to measure in (b) was identical to the sample measured in Fig. 5.2(a).

Fig. 5.11(b) displays marginal improvements to the measuring technique compared to the initial setup. These improvements were:

1. Higher field resolution in which the field resolution improved from ∼0.2 Oe to 0.1 Oe meaning sharp single/ double peak responses can be clearly resolved.

2. Better compensation for the parasitic impedance present in the measurement provided the GMI response of the same material to double (from 12% to 24%).

3. Immobilisation of the test leads and automation reduced the noise in the data. This was summarised in Table 5.3 using the same method for measuring noise in Table 5.1.

ΔGMI (%) = GMI (%) (at -H) – GMI (%) (at +H)											
±H (Oe)	**0**	**26**	**36**	**76**	**83**	**93**	**103**	**133**	**152**	**180**	**230**
Frequency (MHz)											
0.5	0	0.53	0.61	0.66	0.58	0.45	0.37	0.31	0.08	-2.4×10^{-4}	0
1	0	0.41	0.42	0.48	0.36	0.26	0.20	0.20	-0.10	-0.11	0
5	0	-0.06	-0.07	-0.06	-0.07	-0.10	-0.14	-0.11	-0.01	0.02	0
10	0	-0.05	-0.05	-0.06	-0.10	-0.08	-0.08	-0.07	-0.02	1.2×10^{-3}	0
15	0	-0.10	-0.11	-0.10	-0.14	-0.16	-0.17	-0.14	0.01	4.2×10^{-4}	0
20	0	-0.08	-0.12	-0.14	-0.14	-0.10	-0.12	-0.10	9.4×10^{-4}	0.03	0

Table 5.3: Differences of measured GMI ratios between positive and negative fields.

The automation of the measurement system also meant that more data could be captured in order to make more detailed measurements and comparisons with data from the literature. An example is shown in Fig. 5.12(a) which compares the maximum GMI ratios as a function of frequency for the CoSiFeMo ribbon and two other ribbons with different chemical compositions; CoSiBFeNi and FeSiBC. All ribbons had the same length, width, and thickness: 200 mm x 3 mm x 25 μm.

Fig. 5.12(a) shows a common GMI behaviour between all three samples with the GMI ratio increasing with increasing frequency at low frequencies, followed by a decrease in GMI ratio at higher frequencies. The critical frequency (f_0) of the highest GMI ratio responses for all three samples was between 1 – 3 MHz. This behaviour corresponds to the GMI behaviour of magnetic materials at the intermediate-frequency regime (chapter 3) where, after exceeding f_0, eddy currents begin to dampen the domain wall motion and only magnetisation rotation contributes to the transverse permeability of the ribbons, thus decreasing the GMI ratio. The observed frequency depen-

dence of the GMI ratio also closely resembled that seen for similar samples in the literature, for example, the work of Lu et al. [249] (Fig 5.12(b)). In addition, the magnitude of the GMI response from the CoSiBFeNi ribbon sample was similar to the "as-prepared" CoFeCreSiB ribbon sample with values of ∼60% and ∼80%, respectively. This indicated the improvements to the characterisation technique for measuring GMI responses of magnetic ribbons improved in accuracy.

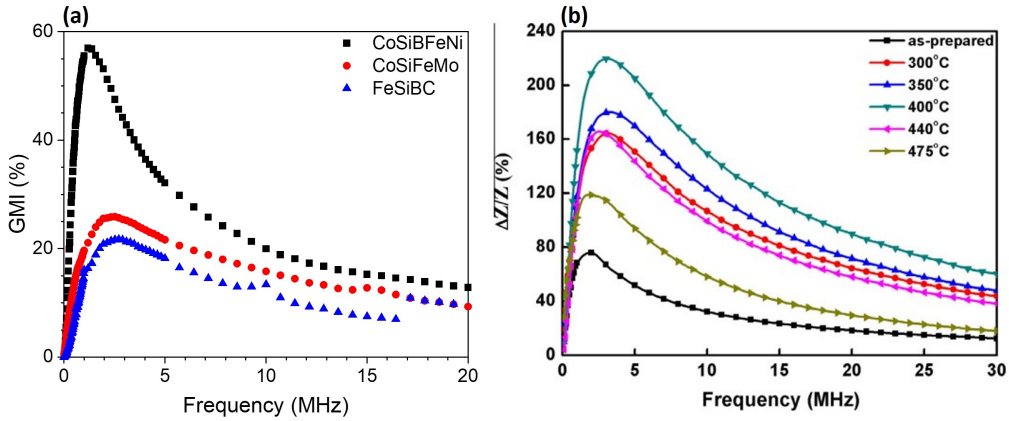

Figure 5.12: Comparison between two measured GMI responses ($\Delta Z/Z$) with respect to frequency (f) at a fixed field strength of 250 Oe for (a) automated system setup and 1 Oe for (b) literature source taken from [249]. Both data investigate the differing GMI responses of amorphous ribbon samples by (a) comparing multiple ferromagnetic materials and (b) comparing the same Co-rich (CoFeCrSiB) sample with different annealing conditions. All ribbon samples have amorphous crystal structures with dimensions of (a) 200 mm length x 3 mm width x 25 μm thickness and (b) 5 mm length x 1 mm width x 23 μm thickness.

Despite the improvements in data quality, measurements from the refined and automated system still contained substantial noise. This was especially

notable for the FeSiBC sample where the GMI ratio increased, instantaneously and unexpectedly, at ∼18 MHz. This suggested that the measurements were not reliable/repeatable, a hypothesis that was proven true when repeating measurements of the same sample multiple times (Fig. 5.13).

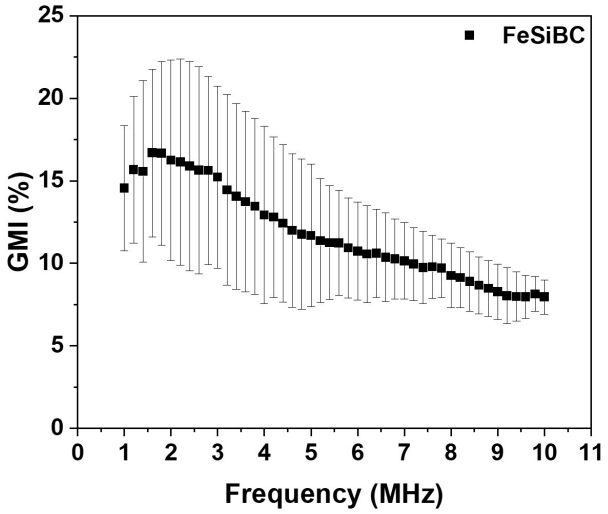

Figure 5.13: GMI ratio as a function of frequency for FeSiBC ribbon sample of 250 mm length, 3 mm width, and 25 μm thickness. The sample was repeatedly measured three times with error bars of a standard deviation of 2σ.

The repeating measurements were represented by the error bars with a standard deviation of 2σ, which means a 95% confidence the measured data (from each repeating measurement) lies within the error bars. Repeating measurements for the FeSiBC ribbon sample three times produced errors between $\pm 1\%$ to $\pm 6.3\%$ depending on the frequency (Fig. 5.13). This suggested that the characterisation technique still lacked the reliability and repeatability required for accurate and precise measurements.

5.3.3 Minimising parasitic impedances

To improve the reliability and repeatability of the measurements it was important to properly compensate any parasitic impedances that were influencing the measured impedance of the sample. This involved understanding how to properly calibrate the 42494A impedance analyser and test fixture adaptor to allow accurate measurements for materials with low impedances ($<$10 Ω), for which the impact of residual parasitic impedances was large.

Parasitic impedances are elements that are present in an electrical network that exhibits electrical properties (resistance, inductance, or capacitance) that are not their intended purpose. For example, a resistor is designed to possess pure resistance, but in reality, may also possesses parasitic capacitance. In GMI measurements the parasitic impedances provide a contribution to the measured impedances of the samples that do not vary with the applied field, thus suppressing the measured GMI ratios. In the measurement system, potential sources of parasitic impedances included the adapter unit, the coaxial cables, the test leads, and the contact between the sample surface and the crocodile clips.

Fig. 5.14 illustrated the influence of parasitic impedance on measurements of a CoSiFeMo ribbon sample. The ribbon sample used had dimensions of 250 mm length, 2 mm width, and 25 μm thickness and was measured using an initial experimental approach (2T connection, compensation in post-process). As a result, the observed impedance of the sample was close to 50 Ω at 20 MHz frequency with the measured GMI ratio to be at most 12%. Considering the GMI ratio was lower than expected for a typical Co-rich based material suggested parasitic impedances were prevalent in the measurement.

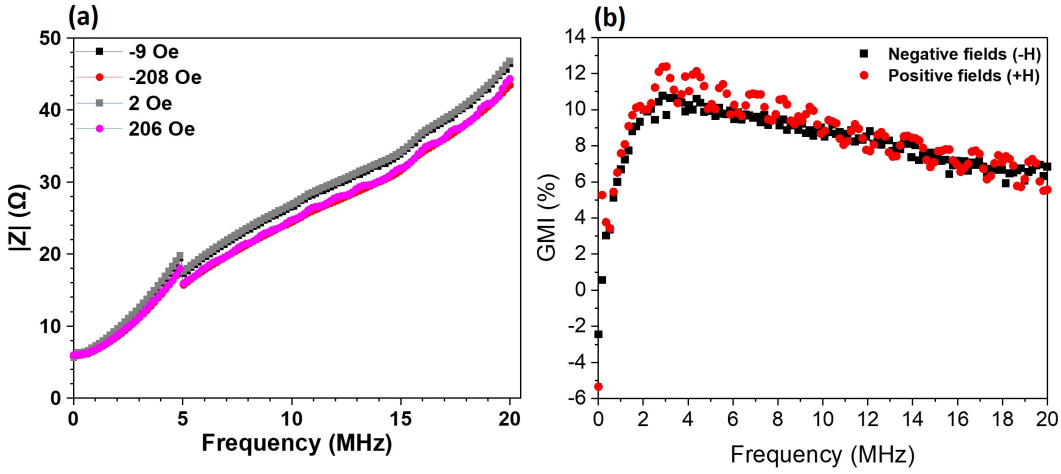

Figure 5.14: (a) The absolute impedance |Z| and (b) GMI ratio with respect to frequency up to 20 MHz. Amorphous ribbon sample, CoSiFeMo, with dimensions 200 mm length x 3 mm width x 25 μm thickness, with applied fields between -208 Oe to 206 Oe. The measurement was done during the initial experimental approach before using the automated system.

These suspicions were confirmed, comparatively, on another ribbon sample (with the same thickness) when the impedance analyser properly calibrated the parasitic impedances for low impedance materials where (at 10 MHz) it was ∼13 Ω instead of ∼27 Ω (more details in section 5.3.3.i "Test leads and adapter"). In addition, the sharp drop of impedance (∼3 Ω) at the 5 MHz frequency was consistently observed for all absolute impedance measurements which was related to a systematic error of the adapter unit not compensated into the measured impedance (Fig. 5.16).

The inclusion of parasitic impedance in the measured impedance lowers the expected GMI ratio of a sample as shown below:

$$GMI_{measured} = \frac{|Z(H)_S + Z_P| - |Z(H_{max})_S + Z_P|}{|Z(H_{max})_S + Z_P|} \times 100\% \qquad (5.2)$$

where $GMI_{measured}$ is the measured GMI, $Z(H)_S$ is the measured electrical impedance of the sample with respect to the field and Z_P is the parasitic impedance of the other electronic components. Clearly, when Z_P is of a similar order of magnitude to $Z(H)$ the measured GMI ratio will differ substantially from that of a "true" measurement. For example, a study performed by Raposo et al. [250] investigated the influence of the length of coaxial cables used to connect to a sample on its measured GMI ratio and saw a suppression of GMI ratio with increasing coaxial cable length (Fig. 5.15).

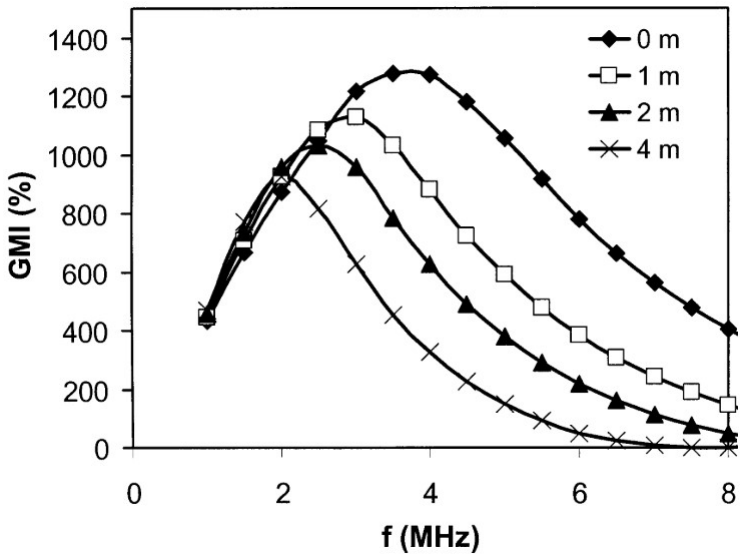

Figure 5.15: Maximum GMI ratio as a function of frequency with various coaxial cable lengths, taken from [250].

Some parasitic impedances can be directly calibrated/compensated, for example, those relating to the measurement cables, the adapter unit, and the

analyser itself. This can be achieved using the inbuilt compensation functionality of an impedance analyser. However, other residual parasitic impedances can exist and cannot be compensated, such as those at the connection between the sample and crocodile clips of the test leads. In this project, these were handled by characterising the approximate magnitudes of residual parasitic impedances considering these as producing residual, systematic errors in the experimental data. Both these topics are discussed in section 5.3.3.i.

5.3.3.i Calibration of the impedance analyser

The calibration procedure from the initial experimental approach was inadequate to compensate for the parasitic impedances as was evident from the ribbons' unnatural high impedances and low GMI responses. To confirm the suitability of the calibration process "Agilent Impedance Measurement Handbook: A Guide to Measurement Technology" [251] was used to identify the correct calibration procedures for the experimental setup. A number of key factors were identified. These included:

- the terminal configurations,
- the test leads,
- and the adapter unit.

5.3.3.ii Terminal configurations

In section 5.3.2 it was shown that the measured GMI ratio doubled when using a 4T connection rather than a 2T connection (Fig. 5.11(b)), implying that changing the terminal configuration substantially lowered the overall parasitic impedance within the circuit (Fig. 5.16).

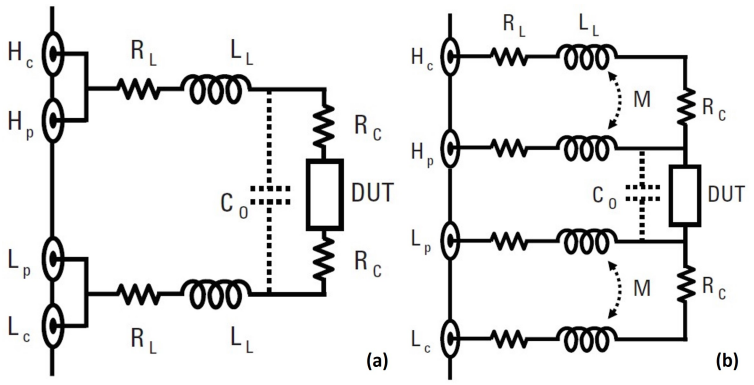

Figure 5.16: (Electrical equivalent circuit of residual parasitic impedances in (a) a 2T and (b) a 4T for test lead cables (L), test lead contacts (C) using a resistor (R)/ inductor (L)/ Capacitor (C) circuitry [251].

In a 2T measurement existing parasitic resistances (R_L), inductances (L_L), and stray capacitance (C_O) between the two test leads as well as parasitic resistances from the lead contacts (R_C) are included in the measured impedance measurement (along with the sample (DUT)). Thus, such an approach is only appropriate for measuring impedances in the range of 100 to 10 kΩ. Clearly, this was unsuitable for characterising the studied metallic glass ribbon samples with impedances of up to ∼13 Ω. Alternatively in the 4T configuration, the junctions are isolated using four test leads with the voltage sensing test leads unaffected by the parasitic elements since no current passes through them (H_P and L_P). This makes the 4T approach capable of accurately measuring impedances in the range 10 mΩ to 10 kΩ.

Potentially, parasitic impedances could be lowered further by shielding each test lead from parasitic capacitances and mutual coupling (M) from the magnetic flux induced by flowing current, potentially improving the measuring impedance range from 1 mΩ to 10 MΩ, without compensation. However, it was considered unnecessary to improve the measuring sensitivity of the

impedance analyser to detect impedance changes at such low magnitudes for the studied ribbon samples. Therefore, the simple 4T configuration was preferred in this project.

5.3.3.iii Compensation of the test leads and adapter unit

The test leads used initially were BNC cables attached to crocodile clips. When moving to the 4T configuration the test leads and fixtures were the same type with a shorter cable length.

In the initial experiments, an open/short compensation procedure was used, which was only suitable for a 2T configuration. Furthermore, instead of using the impedance analyser to compensate for the parasitic impedances in the adapter unit, cable length, and test leads, an Excel spreadsheet was used to manually compensate for the data in the process. These calculations were performed using:

$$Z_{correct} = \frac{Z_{measured}(f) - Z_{short}(f)}{1 - Z_{measured}(f) - Z_{short}(f)Y_{Open}(f)} \tag{5.3}$$

where $Z_{corrected}$ is the correct impedance value of the measured sample, $Z_{measured}$ is the measured impedance including the parasitic and sample impedances, Z_{short} is the impedance from the short measurement, and Y_{open} is the admittance from an open circuit measurement, with all impedances measured with respect to the driven frequency (f). A manual process was used because the adapter unit used (16048D) was nominally incompatible with the impedance analyser (4294A), meaning that the impedance analyser's inbuilt functionality could not be used.

For the 4T configuration, a more precise open/short/load compensation was used to correctly identify the parasitic impedances. The 16048D adapter

unit was replaced with a 16048H adapter unit which was both compatible with the impedance analyser and was capable of being used in a 4T configuration. In addition, a 04294-61001 100 Ω resistor was used to apply a phase/load compensation to the 16048H adapter unit. These changes enabled the impedance analyser to internally perform an open/short/load compensation on the test leads and coaxial cable, via the following formula:

$$Z_{correct} = \frac{(Z_{short}(f) - Z_{measured}(f))(Z_{load}(f) - Z_{open}(f))}{(Z_{measured}(f) - Z_{open}(f))(Z_{short}(f) - Z_{load}(f))} Z_{trueload}(f) \quad (5.4)$$

where Z_{load} is the measured impedance of the load device, and $Z_{(trueload)}$ is the true value of the load device. These changes drastically reduced the residual parasitic impedances in the measurements.

Fig. 5.17 compares the measured impedances and GMI ratios of a NiFeSi+BMo ribbon obtained using 2T and 4T configurations, both with and without parasitic compensations being applied. Even without compensation moving from a 2T (solid black line) to a 4T (solid red line) configuration produced a large reduction in the measured impedance. After applying their respective compensations impedances for both terminal configurations are substantially reduced, with the compensated 4T configuration (blank red line) exhibiting an impedance ∼5 Ω lower than that of the compensated 2T configuration due to minimisation of parasitic contributions. These differences were also reflected strongly in GMI measurements (Fig. 5.17(b)), where the 4T data exhibited notably higher GMI ratios due to the parasitic contributions still present in the 2T configuration data. Consequently, the 4T with open/short/load compensation was used for all future measurements.

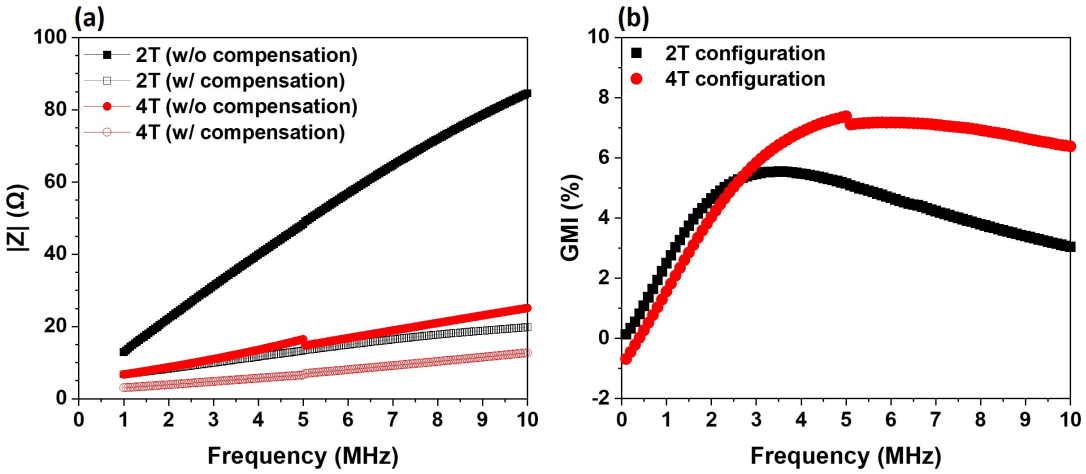

Figure 5.17: (Comparing the 2T (black dots) and 4T (red dots) configurations for measured (a) absolute impedance $|Z|$ and (b) GMI ratio with respect to frequency. The sample used was a NiFeSi+BMo ribbon sample with dimensions of 200 mm length x 3 mm width x 25 μm thickness.

5.3.3.iv Characterising residual parasitic impedance on the test lead contacts (R_C)

Although the test lead cables, coaxial cable, and adapter unit were compensated using the impedance analyser, there was a region in the circuit where the parasitic impedance was potentially still present: the physical contact between the sample and the crocodile clips of the test leads (R_C). Parasitic impedance generated from the physical contact between the test leads and the sample cannot be compensated by the impedance analyser, because the connection is often specific to the sample under test.

To gain an understanding of how much the results of measurements might be affected by this residual parasitic impedance, a simple methodology was created to characterise it. The method used was to place the voltage sensing

test leads next to each other (without touching) on a sample and measure the impedance between them, thus minimising the impedance of the sample under test (Fig. 5.18).

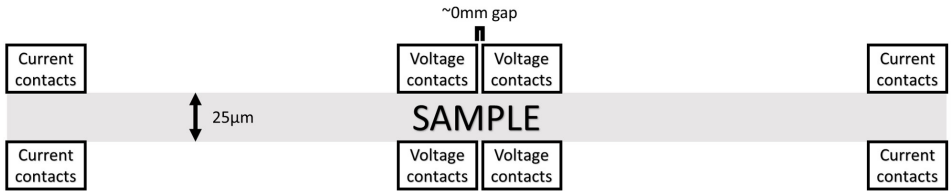

Figure 5.18: Cross-section of the parasitic impedance (R_C) characterised between the crocodile clips of the test leads and the surface of the sample. The voltage test leads were placed in close proximity with a gap close to 0mm (without them touching) and the impedance was measured with as little of the sample as possible.

The method used was under the assumption if the sample between the two voltage sensing contacts was close to zero – making the impedance present in the sample to be as close to 0 Ω as possible – any measured impedance should be the parasitic impedance generated by the physical interaction between the metal crocodile clips and the metallic surface of the sample. This was repeated multiple times to observe the highest (possible) parasitic impedance generated when taking the clips on and off each studied sample. The highest parasitic impedance – for each studied sample – was then used for the term (Z_P) and the corrected GMI value of the sample was calculated using equation 5.5.

$$GMI_{corrected} = \frac{|Z(H)_m - Z_P| - |Z(H_{max})_m - Z_P|}{|Z(H_{max})_m - Z_P|} \tag{5.5}$$

Equation 5.5 follows the assumption where the measured impedance can be expressed as $Z(H)_m = Z(H)_s + Z_P$, where $Z(H)_m$ is the measured

impedance and $Z(H)_s$ is the true impedance of the sample. Hence, rearranging this expression to find $Z(H)_s$ and substituting it into Eq. 5.5 provided the upper limit of the corrected GMI value for the studied samples. This approach is used extensively in chapter 6.

5.3.3.v Summary

Many changes were made from the initial experimental approach in order to improve the accuracy of the technique when measuring the impedance and the GMI signal of the studied samples. These changes included:

- Changing the adapter unit from 16048D to 16048H,
- Changing the terminal configuration from 2T to 4T,
- Calibrating the impedance analyser to apply a phase/load and an open/short/load compensation on the adapter unit, coaxial cable, and test leads, respectively.

Implementing these changes resulted in a substantial decrease in the parasitic impedance present in the experimental setup and substantially higher GMI ratios being measured. Furthermore, noise in the individual GMI curves was substantially reduced. The step that appears around the 5 MHz region is the result of implementing the phase and load corrections to the measured impedance of the sample.

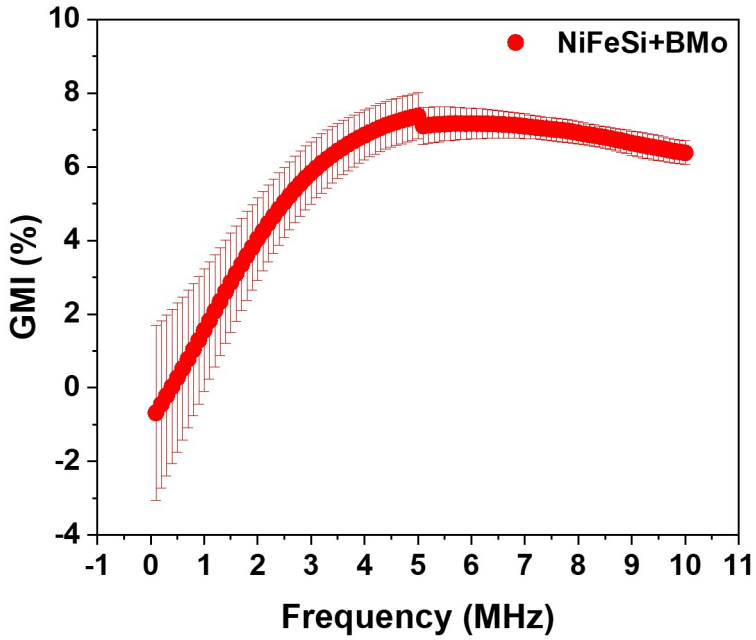

Figure 5.19: GMI measurement on NiFeSi+BMo ribbon sample with the length of 200 mm, width of 3 mm, and thickness of 25 μm. The impedance measurement was conducted with the 16048H adapter unit, 4T configuration, and calibrating the impedance analyser. The sample was repeatedly measured three times. The step at $\sim$5 MHz originates from the phase and load correction that has been applied to the sample.

In Fig. 5.19, the highest error was found to be $\pm$2.4% which was significantly smaller compared to the $\pm$6.3% error when measuring the FeSiBC amorphous ribbon (Fig. 5.13). The error measured for all three repeated measurements implied noise was still present in the improved characterisation technique. Implying, further refinement was required. The remaining area for improvement would be the immobilisation of the sample.

5.3.4 Immobilisation of the sample during measurement

It was expected that poor immobilisation of the ribbon samples would affect the measurements in four broad ways:

- The sample being twisted along an axis parallel to its length by forces from the test leads.
- The sample being pulled off axis in the solenoid by the forces from the test leads.
- The sample sagging under its own weight.
- The sample resonating (at very low vibrations) within the electromagnet.

The common source for all three issues was the poor mounting of the sample in the measurement system. This section discusses the solutions that were implemented to resolve this.

The setup used for measuring the impedances of the ribbons is shown in Fig. 5.20. The sample was placed inside the solenoid and the four test leads were attached using crocodile clips outside the solenoids end.

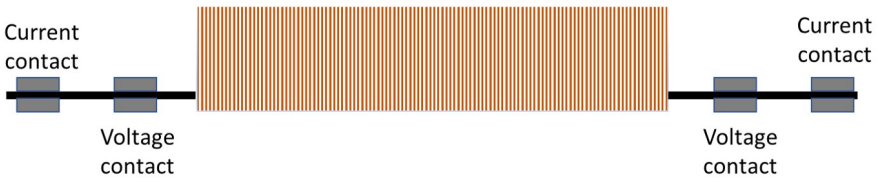

Figure 5.20: Schematic diagram of the sample placed through the solenoid and connected to the four test leads.

Fig. 5.21 illustrates the (initial) three problems with this setup: the sample could potentially be twisted by forces from the test leads, making it likely that the sample was not positioned parallel too, nor at the centre of, the solenoid. As a result, instead of lying flat and parallel to the solenoid, the sample could be in a variety of positions. Furthermore, the sample could move slowly and progressively throughout a measurement, which was typically $\sim$30 seconds. All of these effects were likely to result in a lack of repeatability between measurements, as observed in the previous section.

To resolve these issues a rectangular Perspex block (200 mm length, 14 mm width, 2 mm thickness) was placed in the middle of the solenoid, with the length and width of the block being the same as the length and diameter of the solenoid. The Perspex block then sat at the centre of the solenoid and acted as a platform for the sample to rest on, preventing it from sagging and twisting. Another rectangular Perspex block of the same dimensions was then placed on top of the sample (Fig. 5.22 (a)) and the two Perspex pieces were secured using adhesive tape (Sellotape) to prevent any further sample mobility, such as twisting, sagging or partial lifting. Together, these ensured the sample lay flat and parallel in the centre of the solenoid (Fig. 5.22 (b)). Furthermore, the placement of Perspex pieces for the ribbon in the solenoid further reduced any residual vibration of the ribbon due to electrical current noise in the electromagnet, or external mechanical noise.

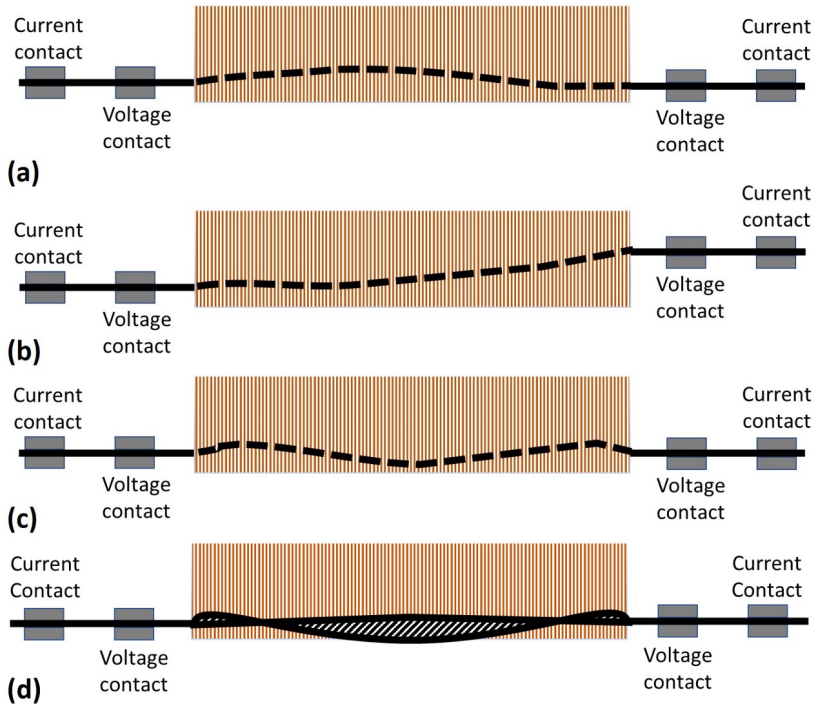

Figure 5.21: Schematic cross-section diagram of the test leads to possible positioning of the sample (black line) during measurement. (a) The bending stiffness of the test leads partially lifts the sample at one end than the other, (b) the bending stiffness completely lifts one side of the sample than the other, (c) the test leads are not bending but the sample is sagging at the centre due to its own weight and (d) the combination of the bending stiffness of the ribbon sample and test leads can twist the sample (shaded area represents the surface of the sample) on its longitudinal axis (along the solenoid) – these positions are exaggerated to illustrate the problem.

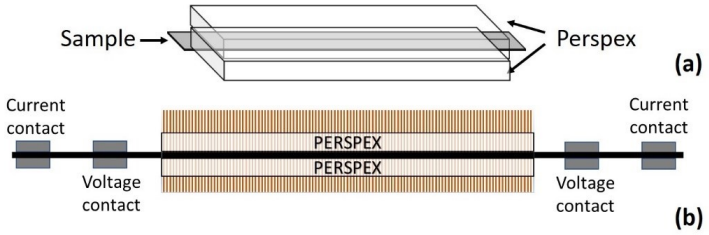

Figure 5.22: Illustration of (a) Perspex (of 200 mm length x 10 mm width x 2 mm thickness) placed on top and bottom of sample to secure it in place (with adhesive tape to wrap around the two Perspex pieces) and (b) a schematic cross-section diagram of the two Perspex pieces holding the sample at the centre of the solenoid.

While the Perspex blocks immobilised the parts of the ribbon within the solenoid, sections outside of the solenoid could still be bent/moved by the test leads. Thus the ends of the sample were also bonded between Perspex sheets using a chemical adhesive (Ethyl 2-cyanoacrylate) and securely held using tensile wedge grips (Mark 10 G1061) (Fig. 5.23). These Perspex pieces were necessary to clamp the ribbons due to the small thickness of the ribbons and their smooth surfaces, which made it difficult for the wedge grips to hold them in place under the tension of the test leads.

Figure 5.23: Illustration of four Perspex pieces securing the ends of the sample in the same manner as the two Perspex pieces in the middle. The Perspex pieces at the end of the sample are secured using a chemical adhesive.

For measurements using the Helmholtz coil a slightly different strategy was used since the diameter of the Helmholtz coil was 160 mm, which was

too large for the Perspex pieces solution designed for the solenoid. Therefore, a standing platform (made from Perspex) was created to allow the sample to be positioned at the centre of the Helmholtz coil, and a Perspex "roof" was placed over the top of the sample holder (highlighted area) to prevent the test leads from bending and moving during measurement (Fig. 5.24).

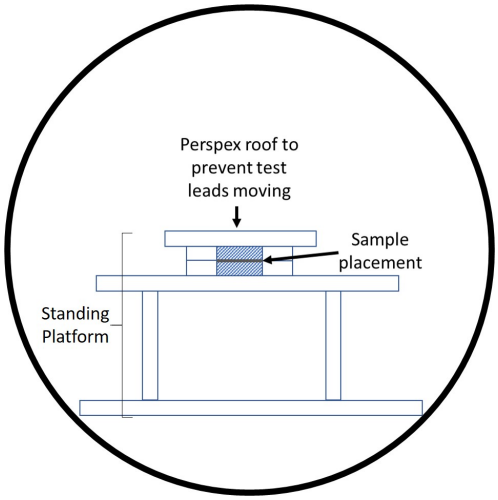

Figure 5.24: Schematic cross-section diagram of the standing platform placed inside the Helmholtz coil with the highlighted area representing the sample (same design as Fig. 5.20(a)) placed inside. The standing platform had dimensions of 61 mm height, 113 mm width, and length of 180 mm.

Fig. 5.25 illustrates the improved repeatability of the measurements when limiting the mobility of the samples. As in the previous cases, the GMI measurements for the NiFeSi+BMo ribbon sample were repeated three times, with the highest error being $\sim\pm 0.3\%$. This was the smallest error measured compared to both the measured NiFeSi+BMo and FeSiBC ribbon samples with earlier iterations of the characterisation technique. This demonstrated the technique was refined to the point that achieved both accuracy and repeatability when measuring the ribbon samples.

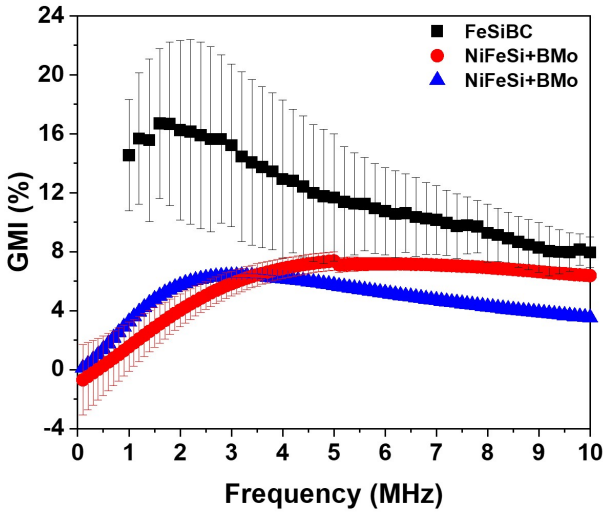

Figure 5.25: The measured GMI ratio for all iterations of the GMI characterisation technique. The same NiFeSi+BMo ribbon sample was used in both the previous iteration and the current iteration of the technique. The current iteration (blue trend) included the same procedure as the previous iteration (red trend) whilst also immobilising the ribbon sample. This minimised the noise in the measurements substantially evident by the small error bars with the highest value being $\sim\pm 0.3\%$.

5.3.5 Summary of Refinements to the GMI measurement process

Accurately measuring the GMI of large-scale amorphous ribbons was a challenging problem. The initial measurement setup was designed to measure high impedance samples, such as electroceramic materials, and was not suitable for characterising the much lower impedances of the ribbon samples. To overcome these challenges the following steps were taken:

- Stabilisation of the currents provided to the electromagnets by the KEPCO BOP power supply.
- Automating the measuring system using LabVIEW.
- Improving the solenoid design for more uniform field strength.
- Reducing/compensation parasitic impedances in the impedance analyser, adapter unit, coaxial cables, and test leads.
- Characterising residual parasitic impedance at the connection between the test leads and samples.
- Immobilising the sample during measurement.

The results of all these changes allowed a GMI characterisation technique that was fine-tuned to provide precise and accurate GMI measurements of large-scale amorphous ribbon samples. This was critical to the experimental results presented in the rest of this thesis.

5.4 Developing a GSI Characterisation System

The next step of the project was to investigate the relationship between the giant stress impedance (GSI) effect and the tensile stress/ strain of the studied sample. The characterisation technique for GSI follows the same principle as the GMI technique but a tensile testing machine was incorporated to apply tensile stresses/strains to the samples in addition/instead of applied fields.

5.4.1 Initial System Design

To characterise the GSI behaviour of the ribbon samples a tensile testing machine was needed to apply controlled forces to the ribbon samples while their impedances were measured. The tensile machine used was a Mark-10 ES30 Precision Hand Wheel Test Stand, which manually applied tensile forces to the studied sample via a hand-turned wheel. The tensile tester was equipped with two tensile wedge grip units (Mark 10 G1061), to hold samples, and a force meter (Mark-10 Series-5 Advanced Digital Force Gauge) to measure the applied forces (Fig. 5.26 (a)).

The sample was supported by a rectangular Perspex platform (120 mm length x 157 mm width x 2 mm thickness) placed inside the coil Helmholtz Coil to ensure the sample did not sag under its own weight. Test leads were fed through the gap between the two coils to connect to the samples (Fig. 5.26 (b)).

5.4.2 Calibrating the Zero-Load Position for the Tensile Test System

To accurately characterise GSI behaviour the position for which no force is applied to a ribbon must be determined, such that the force gauge can be "zeroed" thus calibrating subsequent measurements. However, determining this visually was very challenging. Furthermore, the force meter only displayed tensile force values regardless if the sample was in tension or in compression. Therefore, a procedure had to be developed to zero the force meter.

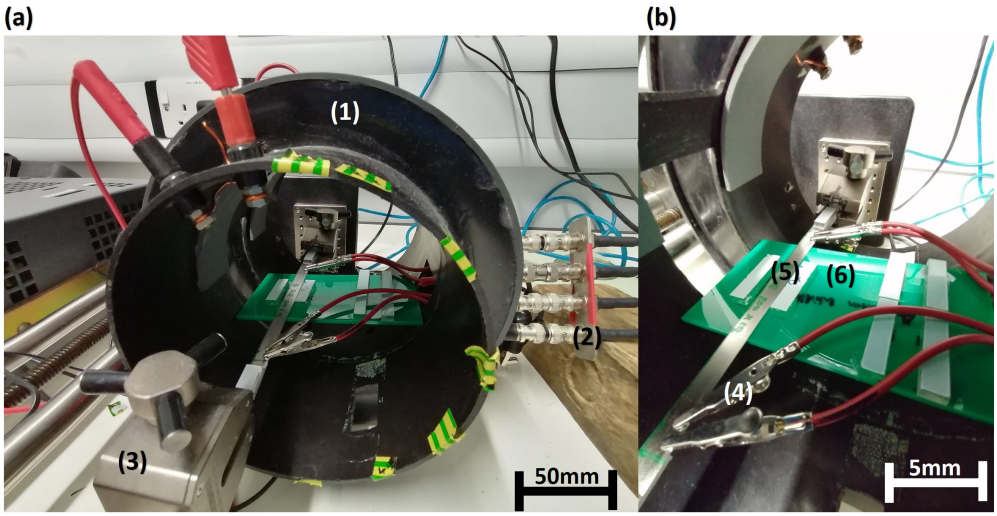

Figure 5.26: Image (a) of the experimental setup for characterising GSI measurements using (1) a Helmholtz coil, (2) the terminals (H_C, H_p, L_C and L_p) connecting the adapter to the test leads, (3) the tensile wedge grips holding the sample ends (secured with two Perspex pieces with a chemical adhesive between them). (b) A close-up of the setup where the (4) crocodile clip test leads are attached to the ribbon sample (5) where it is supported by a (6) rectangular Perspex piece resting on the inner circumference of the Helmholtz coil.

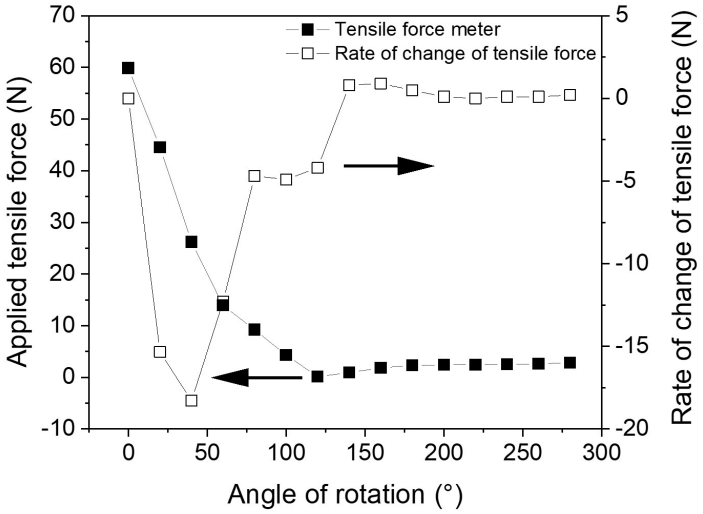

Figure 5.27: Applied tensile force (filled dots) and the rate of change of applied tensile force (blank dots) on the sample as a function of tensile machine wheel's angle of rotation. The force meter would be tarred at 0 N at the corresponding applied tensile force when rate of change of tensile force was near 0 N (in this case at 0.9 N, 140° angle of rotation from the sample under tension).

This was achieved by measuring the rate of change of the applied tensile force as the test stand wheel was rotated (Fig. 5.27). In this procedure, the sample was initially placed under tension (this was checked by observing the ribbon and/or by gently touching the sample to feel the increase in its stiffness) and the measured tensile force was recorded. The wheel angle was recorded at 0° as a reference. The wheel was then turned in 20° degree increments, lowering the tensile force applied to the sample and at each interval, the tensile force displayed on the force meter was recorded. This process was continued until the rate of change of applied tensile force (open dots) started to become constant, near 0 N. At this stage, the ribbon sample

was at a phase between a state of tension and a state of compression where the applied tensile force (filled dots) would display similar force values. This was considered the closest to the 0 N state. After locating the applied tensile force value that corresponded closely to where the sample just reached the 0 N state (in this case where the applied tensile force was 0.9 N at 140°) the force meter was zeroed.

5.4.3 Immobilising the sample during GSI measurements

Fig. 5.26 illustrates a ribbon sample being supported by a rectangular Perspex platform inside the Helmholtz coil which prevented the ribbon sample from sagging from its own weight during measurement. However, this setup did not entirely prevent minor deformations/movements of the ribbon sample when the test lead was attached. The combination of forces from test leads and the teeth of the crocodile clips on the sample gave rise to minor deformations and localised stress/ strains on the sample, which influenced its mechanical properties. These effects were more noticeable when the sample was under strain as this resulted in movement of the test leads from their initial positions.

Fig. 5.29(a) illustrates the effects of these forces on the repeatability of measurements. Here GSI measurements were repeated five times with an applied force ranging between 0 – 10 N (strains between 0 – 0.69×10^{-3}) on a FeSiBC ribbon sample while leaving the test leads in place. The standard deviation (2σ) of the measured GSI ratio was high at low frequencies (up to $\sim\pm3.75\%$ at 100 kHz) and gradually decreased at higher frequencies (at lowest to $\sim\pm1.25\%$ at 8 MHz), but given the modest size of the effect observed (max GSI $\sim$8%) were still too high for consistent and precise measurements (Fig. 5.29(b)).

To minimise these effects, two Perspex pieces and weights were used. One was placed on top of the ribbon sample to restrict its deformation/movement and the second was placed on top of the test leads to restrict cable movement (Fig. 5.28).

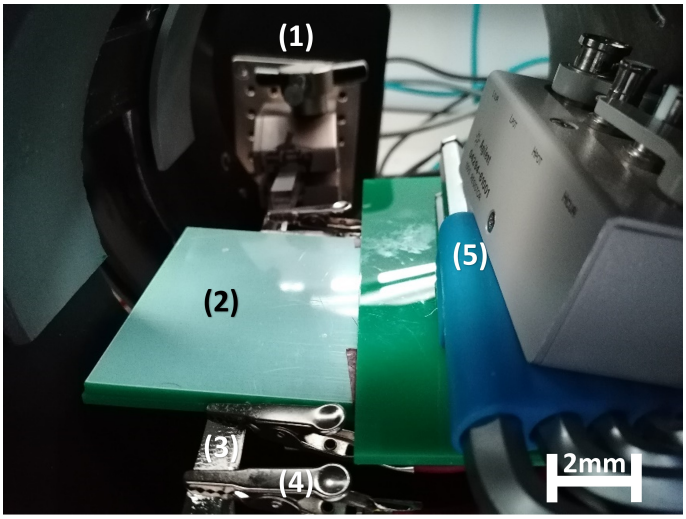

Figure 5.28: Image of the ribbon sample (3) being immobilised by placing: (1) tensile wedge grips at either end of the ribbon sample, (2) Perspex piece on top of the sample (same size as the previous piece in Fig. 5.26(b)), and (5) weights on top of the perspex piece. (4) Test leads were attached to the ribbon sample to measure the impedance once the sample was immobilised.

These modifications dramatically improved the consistency and precision of the GSI measurements. This is illustrated in Fig. 5.29(a) where the GSI curve (red line) displays both a higher GSI ratio (up to ∼-9%), and much greater repeatability than the previous measurements. The error decreased considerably to ∼±0.5%. These changes implied that confining the sample and test leads both restricted their movement and reduced the introduction of parasitic effects into the measurements.

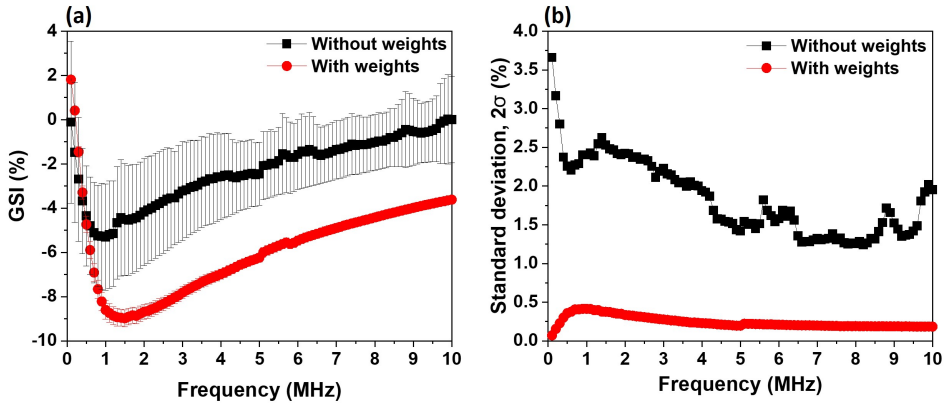

Figure 5.29: Comparing the influence of adding weights (red trend line) to restrict test lead cable motion for (a) measured GSI ratio and (b) standard deviation with both respect to frequency. FeSiBC ribbon sample was used for both measurements w/ and w/o weights with dimensions of 200 mm length, 10 mm width, and 25 μm thickness. The test lead contacts were not reattached to the sample throughout all measurements.

Following the measurements above the effect of detaching and reattaching the test leads between measurements was investigated. Here measurements where the test leads were detached and reattached for each of 5 repeat measurements with weights were compared to an equivalent set of six repeats without the weights but with the test leads were left in place between repeats (Fig. 5.30(a)). The measured GSI ratio was found to be lower in the setup where the test leads were detached and reattached (Fig. 5.29(a), black trend line), suggesting that this was due to parasitic impedances between the contacts of the test leads and sample surface, similar to those observed when refining the GMI technique (section 5.3.3.ii.). The exact source(s) of the parasitic effect was unclear but it was probable a combination of the reattachment of the test lead contacts (on the sample) and the minor movement of the test leads via straining the sample were the likely causes. However,

the overall repeatability of measurements was improved (max. $\sim\pm1.25\%$ variability), when the test leads were detached and reattached between measurements, but the sample was weighted Fig. 5.30(b). This further supported the hypothesis that the motion of the test lead was the primary contribution to inconsistency of the GSI measurements.

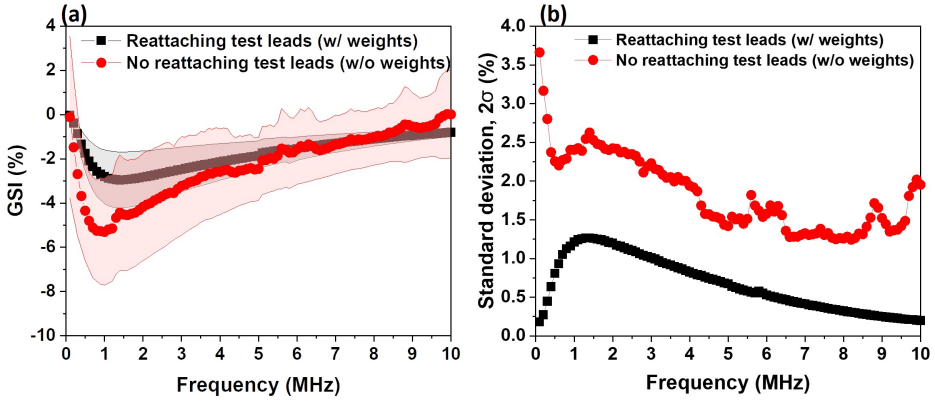

Figure 5.30: Comparing the influence of reattaching test lead contacts for every repeated measurement for (a) measured GSI ratio and (b) standard deviation both with respect to frequency. The ribbon sample used was identical to the sample used in Fig. 5.29.

The behaviour of the measurements at higher tensile forces (up to 150 N, equivalent to 600 MPa of tensile stress) to observe if the measured GSI response gets worse at higher strains (Fig. 5.31). Here, the GSI ratio was measured as a function of applied stress at a frequency of 1.5 MHz for all studied samples. The 1.5 MHz frequency was chosen as this was typically where errors in repeatability peaked. Repeatability for these measurements was assessed by performing five repeats with the test leads being detached and reattached at the sample for every repeat.

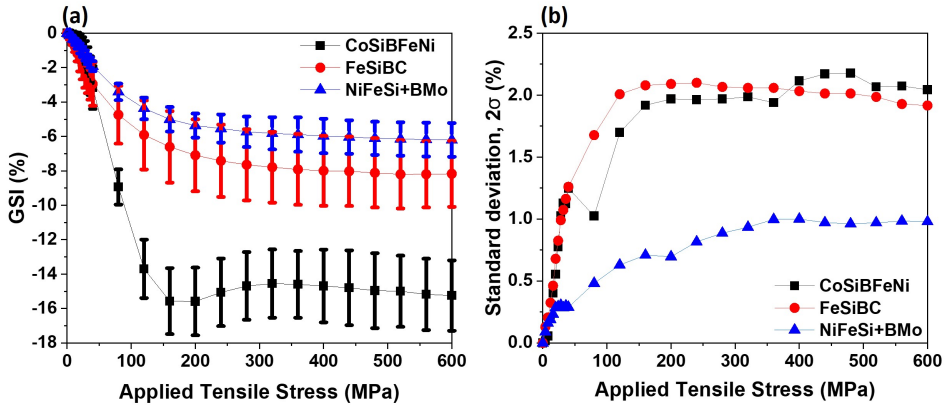

Figure 5.31: Comparing (a) GSI ratio and (b) standard deviation with respect to applied tensile stress for all three studied ribbon samples, at 1.5 MHz frequency. All three ribbon samples have the common dimensions of 200 mm length, 10 mm width, and 25 μm thickness.

For the FeSiBC ribbon sample, the variability was $\sim\pm1.25\%$ at 40 MPa, but continued to increase until reaching a consistent margin of error of $\sim\pm2.0\%$ from 120 MPa onwards. This basic curve profile of the variability with stress was consistent for all three ribbon samples, with the measurements of the NiFeSi+BMo ribbon sample having the lowest margin of error of $\sim\pm1.0\%$. However, the confidence intervals for the FeSiBC ribbon overlapped with those for the NiFeSi+BMo ribbon sample. This indicated the technique ideally required further refinement. However, due to time constraints, a full design of the system was impossible. Thus, instead, the GSI measurement of the FeSiBC ribbon sample for all repetitions was analysed to detect any anomalies that appeared in the data.

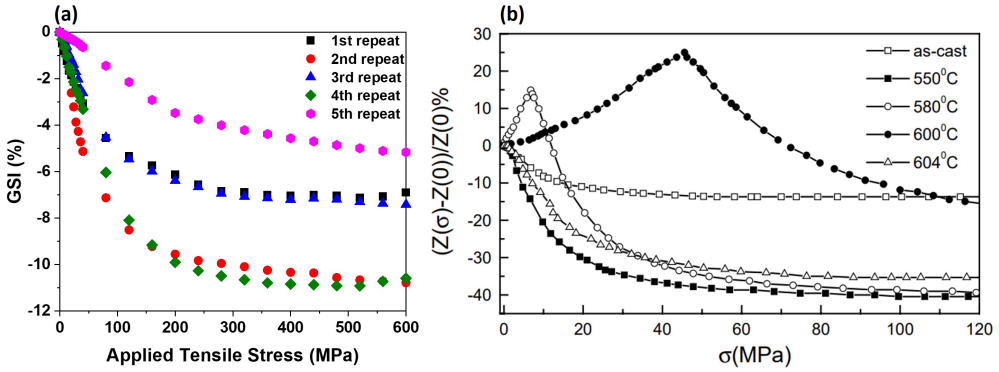

Figure 5.32: Comparing the GSI ratio with respect to applied tensile stress for Fe-rich amorphous ribbon sample from (a) thesis and (b) published literature from [44]. The Fe-based ribbon sample used in (a) was identical to the FeSiBC ribbon sample in Fig. 5.31 whereas (b) used an amorphous ribbon sample of chemical composition FeCuNbSiB with dimensions 65 mm length, 1 mm width, and 35 μm thickness. Both displayed different comparative GSI measurements with (a) compared the GSI ratios between multiple repetitions of the same FeSiBC ribbon sample whereas (b) compared the GSI ratios of the same FeCuNbSiB ribbon sample at different annealing temperatures. The frequency measured for (a) and (b) was at 1.5 MHz and 300 kHz, respectively.

All 5 repeats of the measurements for the FeSiBC ribbon are shown in (Fig. 5.32(a)). The two pairs of curves with similar GSI responses (1st and 3rd pair, 2nd and 4th pair) and was difficult to identify which of the two pair sets of data were anomalies. It was possible to use the average between the two pair sets of data which provided the highest average GSI ratio between all four measurements to be ∼-8.5% with error of ∼±1.6%. Looking to the literature to identify a typical GSI ratio for a Fe-based amorphous ribbons showed typical values ∼-10% (Fig. 5.32(b)) [44, 217, 252]. The 5th repeat had GSI ratios much lower than first four repetitions which indicates

parasitic impedance in the measurement. Taken into consideration the presence of the parasitic impedance it was appropriate to the take the subset of measurements that maximised the GSI ratio (i.e., the first four repetitions) which correlated well with the literature.

For the remaining two samples the same method was applied where the repeated measurement that had the lowest GSI response was ignored from their average GSI ratio, though this was rarely the case, since the remaining two samples exhibited more consistent values between each repeated measurements. A final comparison between all three studied samples GSI, including estimated error bounds at 1.5 MHz frequency is shown in Fig. 5.33.

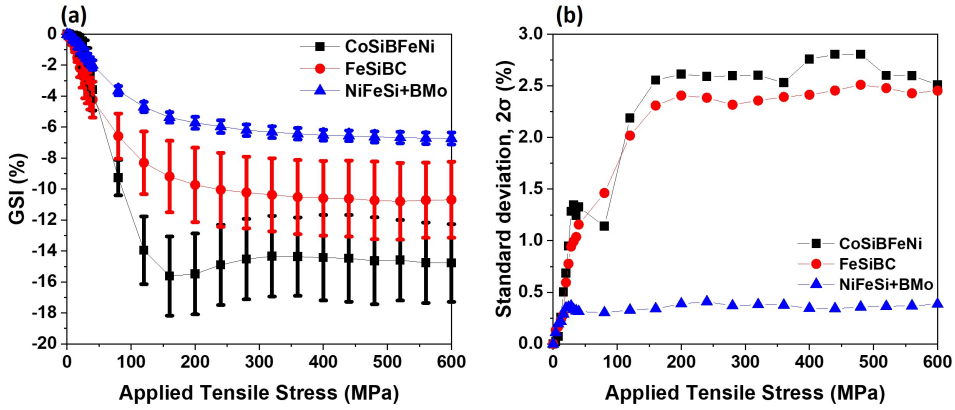

Figure 5.33: Modified data from Fig. 5.31 with (a) the average GSI ratio of each studied sample (excluding any anomalous measurements in the average) with respect to applied tensile stress and (b) the margin of error representing the potential parasitic effects present in the measurement.

5.4.4 Summary of Refinements to the GSI Measurement Process

As with section 5.3, there were many challenges in accurately measure the GSI of large amorphous ribbons. To address these the following steps were taken:

- Developing a technique to accurately determine the zero force state of the ribbons.
- Restricting the ribbon sample mobility by sandwiching the sample between two rectangular Perspex pieces.
- Restricting the mobility of the test leads as much as possible by placing a Perspex piece with a mass weight on top of them.

Despite these steps, and the improvements they produced, measurement repeatability was still challenging with errors in GSI ratios up to $\sim\pm 2.0\%$ being observed at high stress/strains. These errors resulted overlaps between the confidence intervals for measurements of the FeSiBC and NiFeSi+BMo ribbon samples. Due to time restrictions, it was not possible to further refine the experimental approach. Hence, an informed process of identifying outlier measurements and averaging of the remaining data was used to produce reliable data with defined confidence intervals. This allowed investigations of the GSI effect in chapter 7.

Chapter 6

Influence of geometry on the giant magnetoimpedance of high-aspect ratio amorphous ribbons

6.1 Outline

The chapter discusses the influence of geometry on the GMI behaviour in amorphous ribbons with aspect-ratios (l/w) up to 150, with a ribbon length of 300 mm. This is much larger compared to typically studied magnetostrictive ribbons, as shown in chapter 3, table 3.2, with them having ribbon lengths under 100 mm. Although, there are studies that have investigated the GSI and GMI responses on amorphous ribbons of aspect-ratios higher than 30 [253, 254] (which was based on the ribbon having a length of 300 mm and width of 10 mm) the large difference in the ribbon sizes was not convincing enough to ascertain the same (or similar) GMI response would occur.

Two, related, studies investigated the relationship between the GMI re-

sponse and the aspect ratio of amorphous ribbons. Both observed a “critical” aspect ratio at which the studied ribbon sample provided the maximum GMI response which it maintains when its aspect-ratio exceeds the "critical" value [2], [7]. However, the length of the studied ribbon samples was 43 mm and 10 mm with the highest aspect-ratio being 21.5 and 10, respectively. These lengths were not representative of the desired application where lengths would have to be 300 mm. Furthermore, both studies lacked any comparative investigations to other ferromagnetic samples of differing magnetic properties leaving a gap in the scientific knowledge if the observed behaviour would be consistent for any other soft magnetic materials.

Hence, this poses an important question for the design of the sensor technology since it is well understood that shape anisotropy has a substantial influence on the transverse susceptibility of an amorphous ribbon, and thus on its GMI behaviour. Here, we explore the GMI behaviour of three amorphous ribbon samples with differing magnetic properties at varying aspect-ratios (ranging between 2 - 150) to fill in the gap of understanding a sensor's performance when used for applications where large aspect-ratio ferromagnetic materials are desirable, which includes monitoring ILW nuclear waste packages.

The chapter is presented in a form of a paper for the Journal of Applied Physics (JAP) [1]. The paper contains minor errors in referencing the incorrect sample batch number, especially for figure 10 (in the paper) where in the caption it references Batch 3 to be DLEC and Batch 4 to be SLEC samples. This is meant to be the other way around which is later mentioned in the discussion of the figure.

Journal of Applied Physics ARTICLE scitation.org/journal/jap

Influence of geometry on the giant magnetoimpedance of high-aspect ratio amorphous magnetic ribbons

Cite as: J. Appl. Phys. **128**, 174504 (2020); doi: 10.1063/5.0022777
Submitted: 23 July 2020 · Accepted: 16 October 2020 ·
Published Online: 6 November 2020

Patrick Pan,[1,a)] Robert D. Moorehead,[2] and Thomas J. Hayward[1]

AFFILIATIONS

[1]Department of Materials Science and Engineering, The University of Sheffield, Sheffield, United Kingdom
[2]The Henry Royce Institute and Department of Materials Science and Engineering, The University of Sheffield, Sir Robert Hadfield Building, Sheffield, United Kingdom

[a)]**Author to whom correspondence should be addressed:** ppan4@sheffield.ac.uk

ABSTRACT

We study the influence of ribbon geometry on the giant magnetoimpedance (GMI) behavior of both low- and high-aspect ratio [*length (l)/width (w)* = 2–150] ribbons made from commercially available amorphous magnetic materials. Our results indicate that the variation of the ribbons' GMI with geometry is due to the combination of edge effects (due to damage created by the ribbon cutting process) and global shape anisotropy. In high-aspect ratio ribbons [*length (l)/width (w)* $\geq$ 20], we find that the GMI decreases with width, which we suggest is due to the cutting process creating induced stresses that suppress the transverse susceptibility at the edge of the material. In lower aspect ratio ribbons [*length (l)/width (w)* $\leq$ 20], shape anisotropy results in a relatively rapid increase in GMI with increasing length. We conclude that, with suitable optimization, high-aspect ratio ribbons prepared from commercially available materials are suitable for use as macro-scale sensors that detect small magnetic fields/strains over a large sensing area.

I. INTRODUCTION

There has been long-term interest in designing giant magnetoimpedance (GMI) sensors based on amorphous magnetic ribbons.[1–5] GMI sensors utilize the GMI effect, which is defined as a large change in electrical impedance of a magnetic material when subjected to an applied dc magnetic field. The magnitude of the GMI effect typically peaks at a "critical frequency" of AC current (f_0) between 2 and 7 MHz, with the precise value depending on the ribbon material and the conditions under which it has been processed.[2] At these frequencies, the GMI effect is dominated by the skin effect: applied magnetic fields alter a ribbon's transverse permeability, producing large changes in the skin depth of the AC current passing through it. Thus, large variations in electrical impedance are observed as the applied magnetic field is varied.[2,6] GMI ratios as large as several hundred percent[2] can be observed when both the microstructure and domain structure of the ribbons are well-optimized.[7,8]

It has been reported that the GMI effect is strongly dependent on the ribbon geometry.[9–14] For example, Ding *et al.*[10] observed that amorphous ribbons show a sharp decrease in the GMI ratio for ribbons with aspect ratios [length (l)/width (w)] below 5.4, and a similar trend was observed by Chaturvedi *et al.*[9] where a decrease in GMI was seen for ribbons with lengths below 8 mm. In both cases, these trends were attributed to demagnetizing effects/shape anisotropy. However, there have been relatively few studies on the geometry dependence of the GMI effect in high-aspect ratio ($l/w \geq 20$) amorphous ribbons. There are instances where high-aspect ratio ribbons could be useful as GMI sensors with the large signals available, meaning that macroscopic sensors could allow for the detection of relatively small stimuli distributed over large areas or local stimuli that affect only small areas of a larger sensor. For example, one can envisage such sensors being mass deployed to monitor the structural integrity of containers containing hazardous waste, where either global swellings or local deformations could be symptoms of container failure.

The magnitude of a ribbon's GMI response is also strongly influenced by its saturation magnetostriction coefficient λ_s.[15,16] This controls the strength and orientation of stress-induced anisotropies, which in turn dictate domain structure and permeability.

TABLE I. Magnetostriction coefficients, remanence ratio, and saturation flux density values for $Co_{66}Si_{15}B_{14}Fe_4Ni_1$, $Fe_{81}B_{13}Si_{3.5}C_2$, and $Ni_{40}Fe_{40}Si + B_{19}Mo_{1\text{-}2}$ ribbons, as quoted by the supplier.[23–25]

Ribbon sample	Magnetostriction Coefficient λ_s (ppm)	Remanence ratio (M_r/M_s)	Saturation Flux Density (T)
$Co_{66}Si_{15}B_{14}Fe_4Ni_1$ (Co-rich)	<1	0.82	0.55
$Fe_{81}B_{13}Si_{3.5}C_2$ (Fe-rich)	30	0.70	1.6
$Ni_{40}Fe_{40}Si + B_{19}Mo_{1-2}$ (Ni-rich)	8	<1	0.8

However, substantial changes in GMI ratios can also be induced by performing additional processing.[16,17] For example, many studies report that the GMI ratios of amorphous ribbons can be improved by post-fabrication thermal annealing due to the relaxation of induced strains.[10,18–20] Hence, the material becomes magnetically softer making it more effective as a GMI sensor. However, it is also interesting to examine whether manufactured, commercially available amorphous materials can show strong enough GMI performance to be technologically useful, as this would likely offer a cost-effective route to deployment where either modest quantity of sensors are required, or bespoke sensor geometries must be fabricated from generic feedstocks.

In this paper, we investigated how the GMI performance of three different, commercially available amorphous magnetic materials varies when they are fabricated into ribbon geometries with both high ($l/w \geq 20$) and low ($l/w \leq 20$) aspect ratios. Our results showed that there was substantial variation of the GMI ratio with geometry in both low- and high-aspect ratio ribbons due to the combination of global shape anisotropy and edge effects resulting from the ribbon cutting process.

II. EXPERIMENTAL METHODS

A. Basic characterization

Commercially available amorphous magnetic materials with chemical compositions $Co_{66}Si_{15}B_{14}Fe_4Ni_1$ (Co-rich), $Fe_{81}B_{13}Si_{3.5}C_2$ (Fe-rich), and $Ni_{40}Fe_{40}Si + B_{19}Mo_{1-2}$ (Ni-rich) were obtained as 25 μm thick foils from Goodfellow. We chose to study these three materials due to the relatively large differences in their magnetostriction constants (λ_s, Table I, as quoted by the supplier).

To confirm the material properties quoted by the supplier, we performed several basic characterizations of the foils: X-ray diffraction (XRD) with Cu K α radiation was conducted to analyze the crystal structure (2θ) of each material. Room temperature hysteresis loop measurements were performed using a superconducting quantum interference device (SQUID). For these measurements, each ribbon sample had common dimensions of 10 mm × 2 mm × 25 μm and was measured with magnetic fields (−150 Oe to 150 Oe) parallel to the ribbon samples' long axis. Finally, the surface roughness of each material was analyzed using atomic force microscopy (Bruker Fastscan AFM) in tapping mode.

B. Sample preparation

We prepared ribbons of the three materials by mechanically cutting them from the precursor foils. Four batches of samples were cut, as shown in Table II: Samples in Batch 1 had common lengths and widths of 400 mm and 3 mm, respectively; samples in Batch 2 had a fixed width of 10 mm and lengths between 20 mm and 150 mm. Thus, Batch 2 covers aspect ratios in the range of 2–15, similar to those that have been widely studied.[9,21,22,26] Samples in Batch 3 had fixed lengths of 300 mm and widths in the range of

TABLE II. List of ribbon samples made from each of the three materials studied, with either DLEC or SLEC edge profiles. Dimensions labeled with an * are fixed within a given batch of samples. To summarize, (DLEC) Batch 1 are ribbon samples with common dimensions of 400 mm × 3 mm; Batch 2 ribbon samples have a varying length with a fixed width of 10 mm; Batch 3 ribbon samples have a fixed length of 300 mm and varying widths; (SLEC) Batch 4 ribbon samples have a fixed length of 300 mm and varying widths.

	Double longitudinal edge cut (DLEC)					
	Batch 1		Batch 2		Batch 3	
Chemical Composition	Length	Width	Length	Width	Length	Width
$Co_{66}Si_{15}B_{14}Fe_4Ni_1$ (Co-rich)	400 mm	3 mm	20, 40, 60, 80, 100, 120, 140 and 150 mm	10 mm*	300 mm*	4, 5, 6, 7, 8, 9, and 10 mm
$Fe_{81}B_{13}Si_{3.5}C_2$ (Fe-rich)						2, 3, 4, 5, 6, 7, 8, 9, and 10 mm
$Ni_{40}Fe_{40}Si + B_{19}Mo_{1-2}$ (Ni-rich)						
	Single longitudinal edge cut (SLEC)					
	Batch 4					
			Length		Width	
$Co_{66}Si_{15}B_{14}Fe_4Ni_1$			300 mm*		4, 5, 6, 7, 8, 9, and 10 mm	
$Fe_{81}B_{13}Si_{3.5}C_2$					3, 4, 5, 6, 7, 8, 9, and 10 mm	
$Ni_{40}Fe_{40}Si + B_{19}Mo_{1-2}$						

J. Appl. Phys. **128,** 174504 (2020); doi: 10.1063/5.0022777 **128,** 174504-2

2–10 mm.[23–25] Thus, Batch 2 covered aspect ratio in the range of 20–150, higher than those that have been typically studied. The ribbons in Batch 2 and 3 had both edges mechanically cut from the precursor foils; we classify these samples as double longitudinal edge cut (DLEC) ribbons. To investigate how the cutting process affected the GMI response of the ribbons, we also manufactured Batch 4, which consisted of ribbons with dimensions equivalent to those in Batch 3, but where only a single edge was mechanically cut from the precursor foil (the other edge being that of the original foil). We classify these samples as single longitudinal edge cut (SLEC) ribbons. We chose to investigate the effects of the cutting process in samples with fixed width and varying lengths because we expected it to manifest as an edge effect, and thus have a more pronounced effect on samples with varying width than in those with varying length.

C. Magnetoimpedance measurements

The measurement geometry used to characterize the ribbons' GMI behaviors is illustrated schematically in Fig. 1. The impedance of the ribbons was measured in the range of 100 kHz–10 MHz using a four-terminal connection to an Agilent 4294A precision impedance analyzer. To prevent distortion of the ribbon sample during measurement, it was supported by a plastic mount that sandwiched the ribbon, which was then placed at the center of an electromagnet. The electromagnet supplied dc magnetic fields up to H = ±150 Oe to the ribbons.

Two electromagnets were used to apply magnetic fields to the ribbon samples: A Helmholtz coil with a uniform field region ~150 mm long was used to measure the Batch 1 samples, whereas a 200 mm long solenoid was used to measure Batch 2–4. When measuring with the Helmholtz coil both current contacts (I^+, I^-) and voltage contacts (V^+, V^-) were connected to the ends of the ribbons. When measuring using the solenoid, current contacts were connected at the ends of the ribbon, whereas the voltage contacts were connected to the ribbons at the ends of the solenoid, such that the impedance analyzer characterized only the sections of the ribbons to which the field was applied.

The field-dependent impedance values measured from the setup were used to calculate the GMI values of the ribbons using the standard expression,

$$GMI = \frac{|Z(H)| - |Z(H_{max})|}{|Z(H_{max})|} \times 100\%, \quad (1)$$

where $|Z(H_{max})|$ is the absolute impedance measured at the maximum DC magnetic field applied. Parasitic impedances were minimized by using short, 0.14 m long, BNC (Bayonet Neill-Concelman) to crocodile clip test leads[27] and by performing open, short, and load calibrations on the impedance analyzer.

Despite the steps taken to calibrate the impedance measurements, parasitic impedances were still present at the connection between the crocodile clips and the ribbon samples. To characterize these contributions, we placed the voltage contacts next to each other without touching (making the distance of the ribbon between the contacts negligible) and measured the impedance spectrum. The highest value of $|Z|$ measured in this way from each batch was selected and used as a representative value of the parasitic impedance Z_P. Assuming that the (as measured) values of $|Z(H)|$ and $|Z(H_{max})|$ in Eq. (1) contained parasitic impedances, the measured impedance could be expressed as $|Z(H)| = |Z_S(H) + Z_P|$ and $|Z(H_{max})| = |Z_S(H_{max}) + Z_P|$, where Z_S was the true impedance of the sample.[28] Thus, the measured GMI ratios were potentially suppressed by Z_P, which was primarily expected to increase the

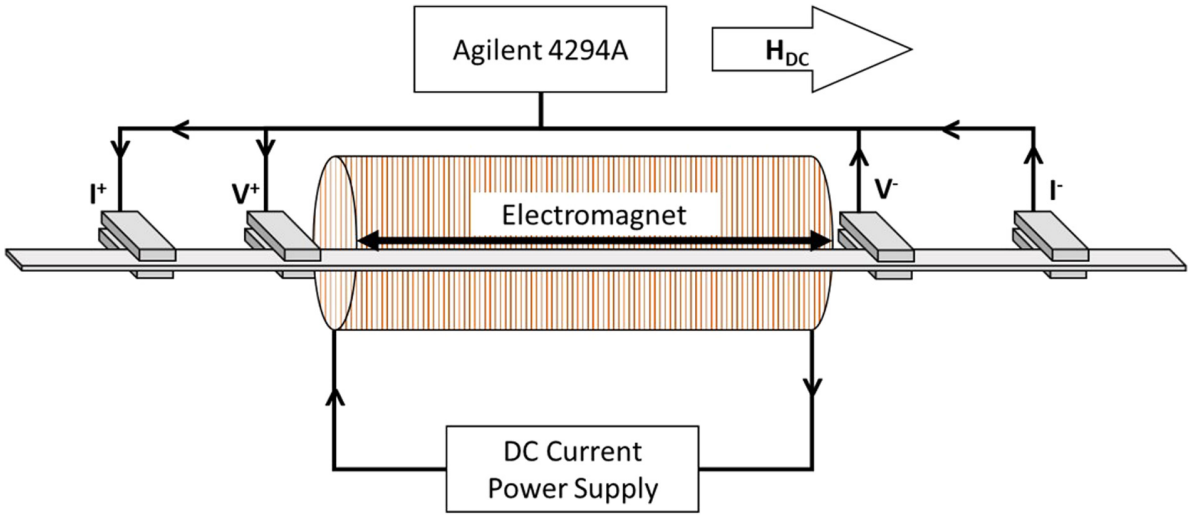

FIG. 1. Schematic diagram of experimental setup used to measure the magnetoimpedance of the amorphous ribbon samples.

J. Appl. Phys. **128,** 174504 (2020); doi: 10.1063/5.0022777

denominator in Eq. (1). Therefore, we also calculated a corrected GMI ratio for each ribbon sample using

$$GMI_{corrected} = \frac{|Z(H) - Z_P| - |Z(H_{max}) - Z_P|}{|Z(H_{max}) - Z_P|} \times 100\%. \quad (2)$$

In this paper, we will present measurements both with and without these corrections applied, thus representing the upper and lower limits of the ribbon samples' true GMI ratios.

D. Heat treating Fe-rich DLEC and SLEC samples

It is well established that heat treating amorphous ribbons relaxes induced stresses, leading to larger GMI responses. To investigate whether heat treatments were capable of relaxing stresses induced by our mechanical cutting process, SLEC and DLEC Fe-rich ribbons with length = 180 mm, width = 4 mm, and thickness = 25 μm were heat treated at 473 K for 30 min in an argon environment. Fe-rich ribbons were selected for this study because of their large λ_s values (Table I), which were expected to make these materials more sensitive to induced stresses than equivalent Co-rich and Ni-rich ribbons.

III. RESULTS AND DISCUSSION

A. Basic characterizations of Co-, Fe-, and Ni-rich ribbons

The XRD measurements for all of the materials exhibited a single broad peak around 2θ = 45° (Fig. 2). This is a typical trait for an amorphous crystal structure and indicated that the materials had the expected microstructure.[2,9,21,22]

Figure 3(a) presents hysteresis loops for each of the materials. The loops showed very small hysteresis and almost linear susceptibilities at low fields. The coercive fields measured for the samples were 0.01 Oe for $Co_{66}Si_{15}B_{14}Fe_4Ni_1$, 0.16 Oe for $Fe_{81}B_{13}Si_{3.5}C_2$, and 0.23 Oe for $Ni_{40}Fe_{40}Si + B_{19}Mo_{1-2}$ [Fig. 3(b)]. The data in Fig. 3 can be used to infer the susceptibility/permeability of the samples, with the Co-rich sample having the lowest susceptibility/permeability followed by the Fe-rich sample and the Ni-rich sample.

Figure 4 presents AFM images of each of the materials' surfaces. We quantified the surface roughness using a root mean square (R_q) value, which was found to be 4.15 nm for $Co_{66}Si_{15}B_{14}Fe_4Ni_1$, 15.3 nm for $Fe_{81}B_{13}Si_{3.5}C_2$, and 14.8 nm for $Ni_{40}Fe_{40}Si + B_{19}Mo_{1-2}$ samples [Figs. 4(a)–4(c)].

B. GMI behavior of Co-, Fe-, and Ni-rich ribbons

Figure 5(a) presents the field dependence of the GMI ratio for Batch 1 ribbon samples fabricated from each of the materials listed in Table I. All three materials exhibit single-peaked GMI behavior with GMI ratios of the order of tens of percent. Single-peaked behavior from amorphous ribbons is typically associated with low transverse anisotropies.[29] This would be expected for these ribbon samples where no special treatment was used to induce a transverse anisotropy following their cutting from the precursor foils. The Co-rich sample was found to have the highest GMI ratio (66.4%), with the Ni-rich (15.1%) and Fe-rich (10.2%) samples showing lower values. This was consistent with the previous literature studies where larger GMI ratios typically occur in Co-rich amorphous metals compared to Fe- and Ni-rich materials.[2,27,30,31] The GMI ratios also correlated well with the quasi-static magnetic susceptibilities/permeabilities implied by the ribbon's hysteresis loops. The Co-rich ribbon showed the highest GMI and was

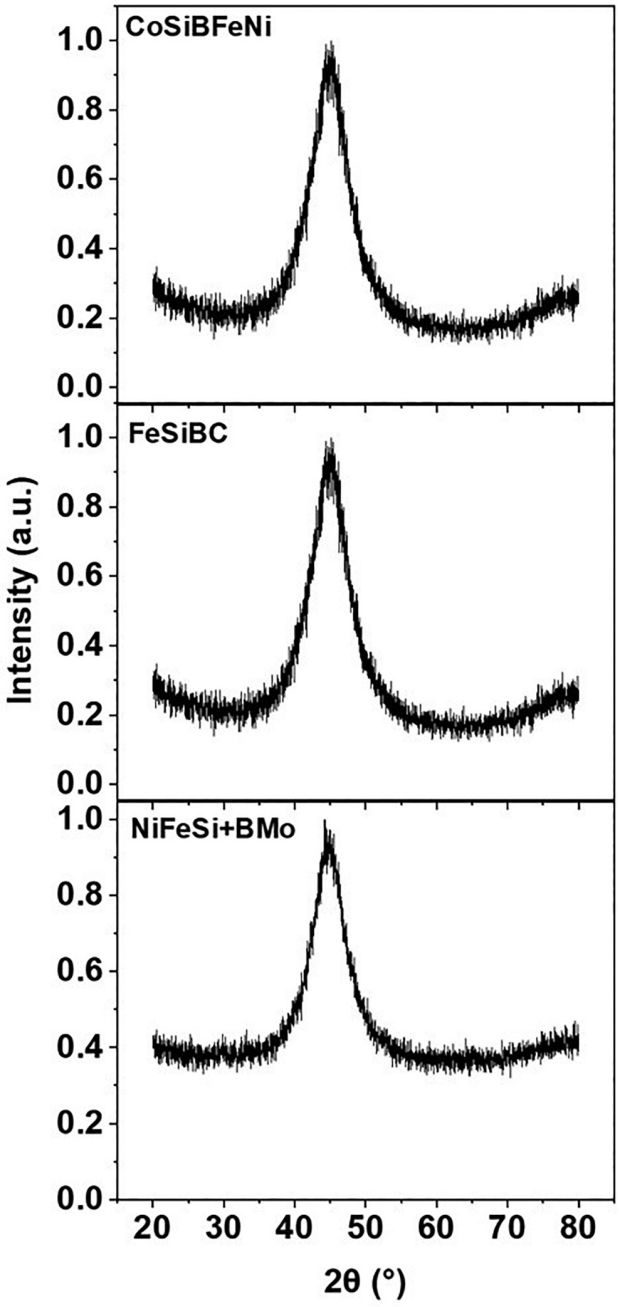

FIG. 2. XRD patterns measured from foils of $Co_{66}Si_{15}B_{14}Fe_4Ni_1$, $Fe_{81}B_{13}Si_{3.5}C_2$, and $Ni_{40}Fe_{40}Si + B_{19}Mo_{1-2}$ at ambient conditions.

J. Appl. Phys. **128,** 174504 (2020); doi: 10.1063/5.0022777

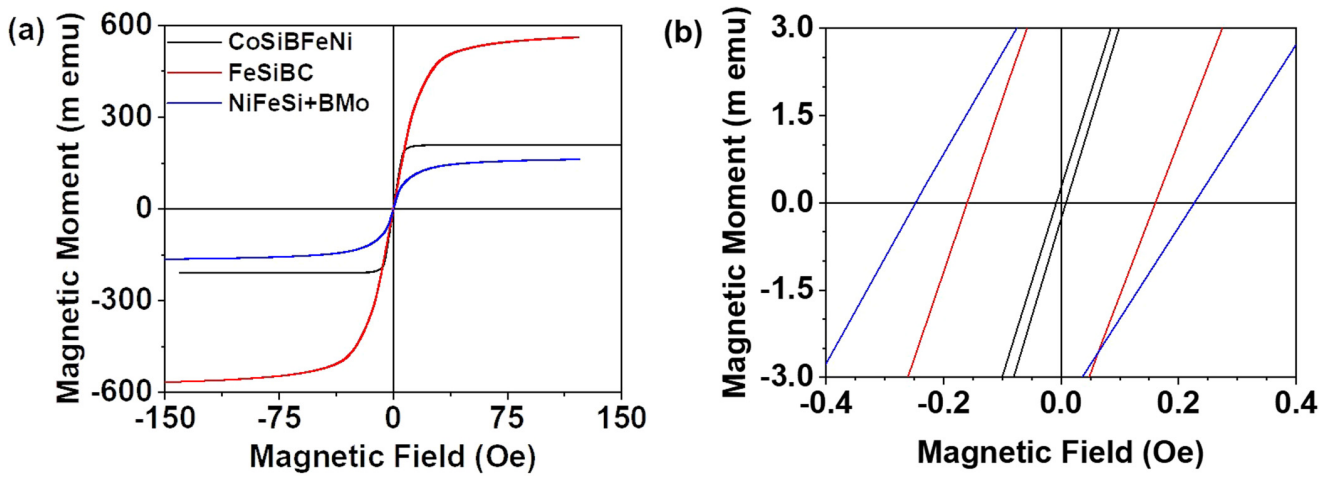

FIG. 3. (a) Hysteresis loops of $Co_{66}Si_{15}B_{14}Fe_4Ni_1$, $Fe_{81}B_{13}Si_{3.5}C_2$, and $Ni_{40}Fe_{40}Si + B_{19}Mo_{1-2}$ samples with common dimensions of 10 mm × 2 mm × 25 μm. (b) A more detailed image of the center of the loops, allowing their small coercive fields to be seen.

substantially magnetically softer than Ni-rich and Fe-rich ribbons, which showed sequentially higher coercivities/lower susceptibilities and lower GMI ratios.

The magnitudes of the materials' GMI responses correlated inversely, with the size of the λ_s constants listed in Table I, with the Co-rich ribbon having the smallest value of λ_s, followed by the Ni-rich and Fe-rich ribbons. A positive correlation between the ribbons' λ_s constants and coercivities was observed. These findings were again consistent with the previously published literature, where materials with negative and near-zero λ_s constants exhibited the largest GMI ratios.[2] Decreases in GMI ratios with increasing λ_s are typically attributed to increasing magnetoelastic anisotropies that suppress the ribbons' permeabilities.[16] However, we note that previous studies have also shown GMI ratios to be influenced by surface roughness.[32,33] In our samples, Fe- and Ni-rich ribbons had similar roughness, while the Co-rich ribbon had a much lower roughness. Therefore, it is possible that the differences in the ribbons' GMI responses resulted from a combination of differences in magnetostrictive properties and their surface topographies.

Figure 5(b) illustrates how the three ribbons' GMI ratios varied with frequency. The GMI ratios for all three ribbons peaked at a critical frequency (f_0) in the range of 2–3 MHz. This was consistent with the ribbons' magnetoimpedance responses being primarily due to the skin effect.[2,6] At these frequencies, the transverse permeability of the ribbons (which controls the skin depth) likely resulted from a combination of domain wall motion and domain rotation.[2,6,12] At higher frequencies beyond the f_0 domain, wall motion becomes progressively damped by the eddy current losses and only magnetization rotation contributes to the transverse permeability, thus decreasing the GMI ratio.

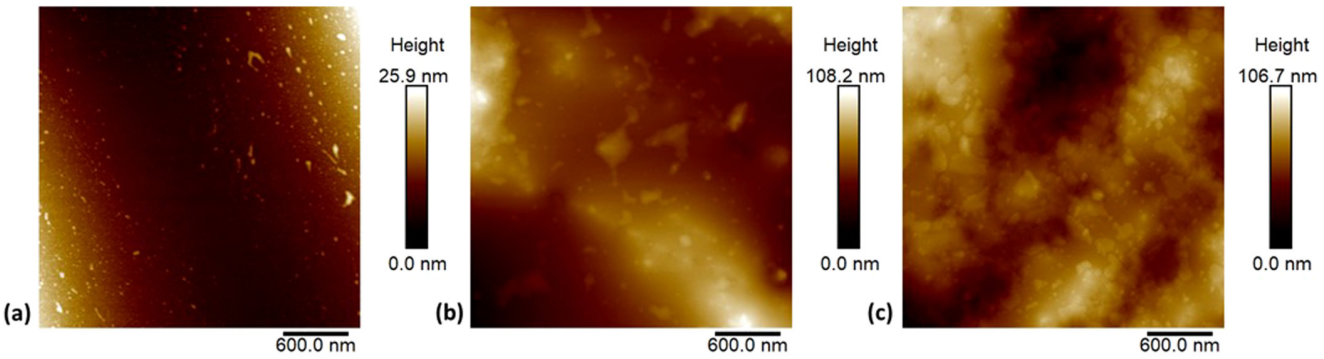

FIG. 4. AFM images of surface roughness of (a) $Co_{66}Si_{15}B_{14}Fe_4Ni_1$, (b) $Fe_{81}B_{13}Si_{3.5}C_2$, and (c) $Ni_{40}Fe_{40}Si + B_{19}Mo_{1-2}$ amorphous ribbon samples with common scanning area of 3 × 3 μm.

J. Appl. Phys. **128,** 174504 (2020); doi: 10.1063/5.0022777 **128,** 174504-5

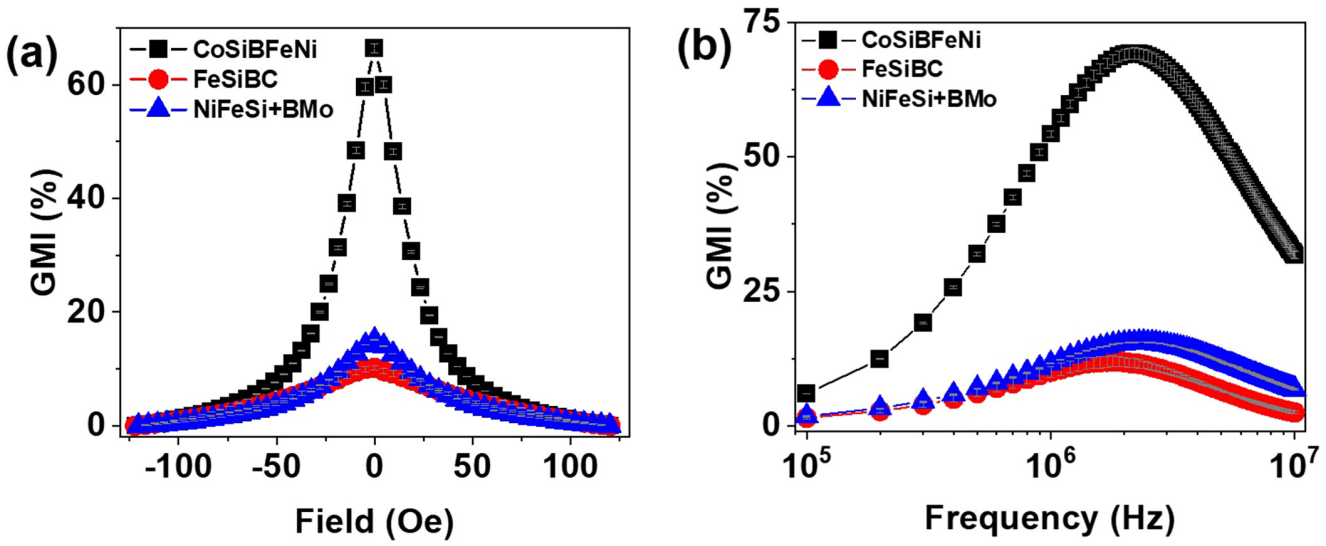

FIG. 5. (a) Variation of GMI with applied field at 3 MHz for three ribbons with different compositions and common dimensions of 400 mm × 3 mm × 25 μm and (b) frequency variation of the GMI ratio for the same ribbons.

C. Geometry dependence of GMI

1. Length dependence in low aspect ratio ribbons

Figure 6(a) presents the variation of the GMI ratio at f_0 with length for the Batch 2 ribbon samples. All three materials showed a common trend where the GMI ratio increased with the ribbon length and tended asymptotically toward a constant value for length >120 mm. Figure 6(b) presents equivalent data for $GMI_{corrected}$. In these data, the GMI ratios were enhanced over the uncorrected GMI values, but the basic trends remained. This indicated that the observed variations were genuinely due to effects of the ribbon geometry, rather than that of parasitic impedances, which were expected to be most significant when measuring the shortest ribbons.

The reduction of GMI ratio with decreasing ribbon length (and aspect ratio) was phenomenologically consistent with the results of previous studies on similar low aspect ratio ribbons,[9,11,12,34] where

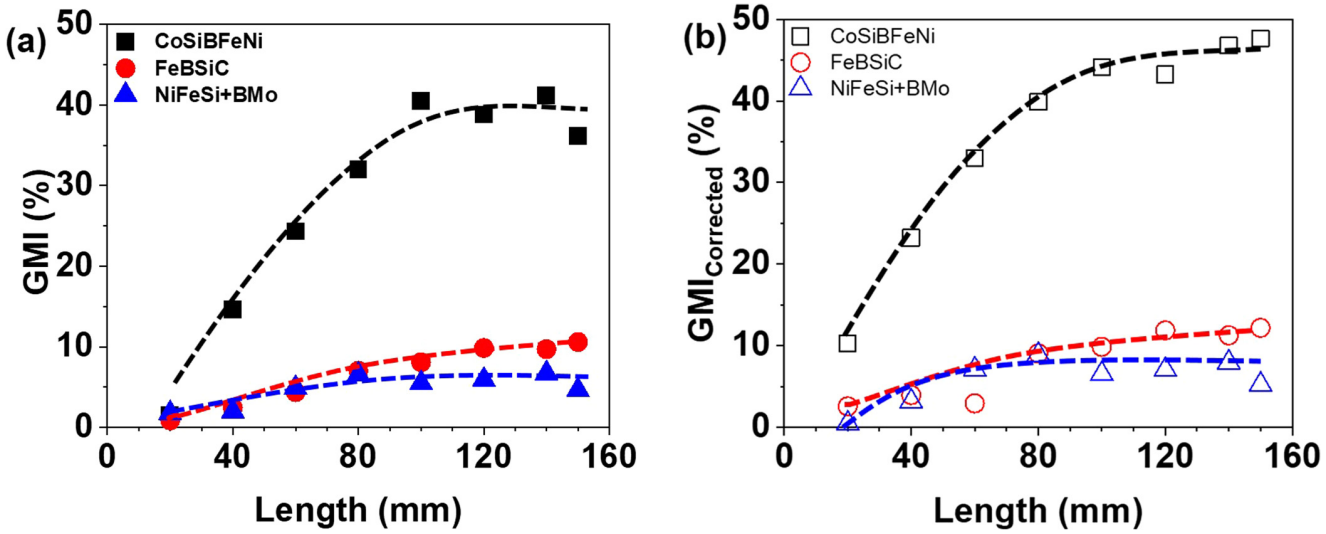

FIG. 6. (a) Variation of measured GMI ratio at f_0 with length for the Co-rich (black squares), Fe-rich (red circles), and Ni-rich (blue triangles) ribbons. (b) Equivalent data for $GMI_{corrected}$. All ribbons had width = 10 mm and thickness = 25 μm. Trendlines are plotted as guides to the eye.

J. Appl. Phys. **128,** 174504 (2020); doi: 10.1063/5.0022777

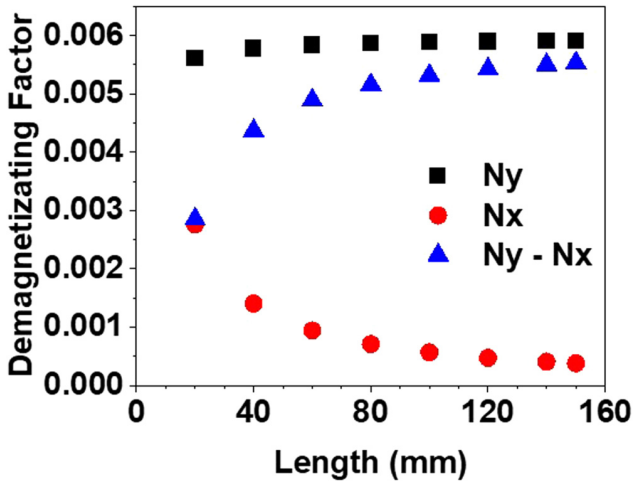

FIG. 7. Plots of N_y (black squares), N_x (red circles) and $(N_y - N_x)$ (blue triangles) as a function of ribbon length. Calculations assume consistent ribbon width = 10 mm and thickness = 25 μm.

the effects of geometric variations are attributed to shape anisotropy. To support this conclusion, we calculated the in-plane demagnetization factors of the ribbon samples, N_x and N_y, as a function of ribbon length (Fig. 7). Here, the subscripts x and y represent the directions along the length and width of the ribbon samples, respectively. Figure 7 also shows data for $(N_y - N_x)$, a factor proportional to the ribbons' in-plane shape anisotropy.

The data shown in Fig. 7 exhibited striking similarities to the form of the GMI data in Fig. 6. For example, both N_x and $(N_y - N_x)$ varied substantially for lengths below 80 mm, just as the GMI ratio did. Furthermore, at lengths over 80 mm, N_x, and $(N_y - N_x)$ both began to plateau. This was again consistent with the measured GMI ratios, which plateaued at a similar length.[35] Together, these results provided strong evidence that the variation of GMI ratio with length was due to the effects of shape anisotropy and that these effects were only significant in relatively low aspect ratio ribbons, i.e., those with aspect ratios less than 12–15. However, the physics underlying this was less clear. Shape anisotropy could have influenced the ribbons' transverse permeability in two distinct ways: First, variations in the ribbons' demagnetizing fields could have directly modified the transverse permeability of the domain structures that remained essentially consistent as the ribbons' geometry changes.[36] Second, changes in the ribbons' demagnetizing fields may have modified the ribbons' domain structure, resulting in configurations that inherently exhibited lower transverse permeability.[37] Previous studies have favored the latter explanation, suggesting that the variation of GMI with length was due to the formation of closure domains at the ends of the ribbons as their length decreased.[9,10,12,22] These closure domains were theorized to reduce the transverse permeability of the ribbon, sharply reducing the GMI response. However, we do not believe that this hypothesis is definitively proven in the literature, and our own results do not offer us any further detailed insight into this question.

2. Width dependence in high-aspect ratio ribbons

Figure 8(a) presents the variation of the GMI ratio at f_0 with width for Batch 4 (SLEC) ribbon samples. The Co-rich ribbons exhibited relatively little variation with a modest decrease in GMI ratio occurring at the largest widths. In contrast to this, the Fe-rich ribbon displayed a different behavior with the GMI ratio increasing at small widths and becoming flatter at larger widths (around

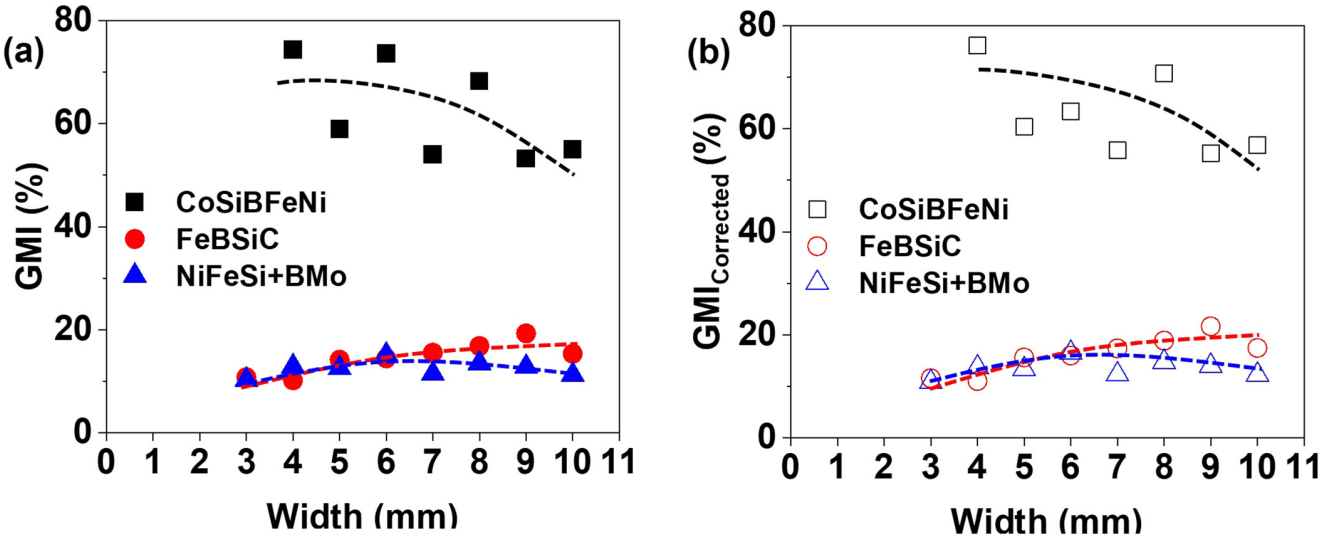

FIG. 8. (a) Variation of measured GMI ratio at f_0 with width for the Co-rich (black squares), Fe-rich (red circles), and Ni-rich (blue triangles) ribbons. (b) Equivalent data for $GMI_{corrected}$. All ribbons have length = 300 mm and thickness = 25 μm. Trendlines are plotted as a guide to the eye.

J. Appl. Phys. **128,** 174504 (2020); doi: 10.1063/5.0022777 **128,** 174504-7

8 mm). The Ni-rich ribbons exhibited characteristics from both the Fe-rich and Co-rich ribbon trendlines: At low widths, the GMI ratio increased until reaching a peak at ~6 mm, but at larger widths, GMI ratios decreased with the width. Figure 8(b) presents equivalent data for $GMI_{corrected}$. This followed the same trends as the uncorrected dataset, suggesting that parasitic impedances had very little effect on the observed results.

Following the example of our previous analysis, we calculated the variation of N_x, N_y, and $(N_y - N_x)$ as a function of ribbon width (Fig. 9). These calculations showed that the transverse demagnetizing factor (N_y) increased rapidly as the ribbon width decreased, while N_x remained negligible. The overall effect of this was to produce a rapid growth in the ribbons' in-plane shape anisotropy [proportional to $(N_y - N_x)$] as their widths decreased. However, there appeared to be little correlation between the variations of the GMI ratio observed and the variation of demagnetizing factors in these data series, indicating that shape anisotropy was not the primary origin of the trends seen in Fig. 8. We suggest that this was because, while the shape anisotropy was found to increase with the decreasing ribbon width, it did so from an already high level, which was perhaps already sufficient to saturate any effects on the ribbons' magnetization states and dynamics. Hence, it was believed that a different mechanism was contributing to the three distinct trends observed in the GMI ratio data.

To investigate whether the process of mechanically cutting the ribbons affected their GMI ratios, we studied the width variation of GMI ratios in both SLEC and DLEC ribbons. Figures 10(a)–10(c) present the variation of f_0 and the GMI ratio at f_0 with width for both Batch 3 (DLEC) and 4 (SLEC) ribbon samples.

It was clear that the different cutting processes had significant impacts on the samples' GMI ratios; the GMI ratios obtained for Batch 4 samples were consistently higher than those of Batch 3 samples. A possible explanation for this was that the primitive cutting process created strained regions at the edges of the ribbon. These would have induced local magnetoelastic anisotropies that may have either suppressed the transverse permeability directly or

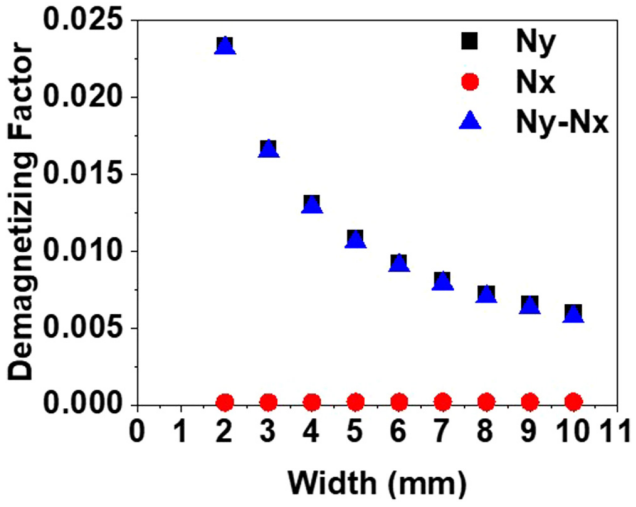

FIG. 9. Plots of N_y (black squares), N_x (red circles) and $(N_y - N_x)$ (blue triangles) as a function of ribbon width. Calculations assume consistent ribbon length = 300 mm and thickness = 25 μm.

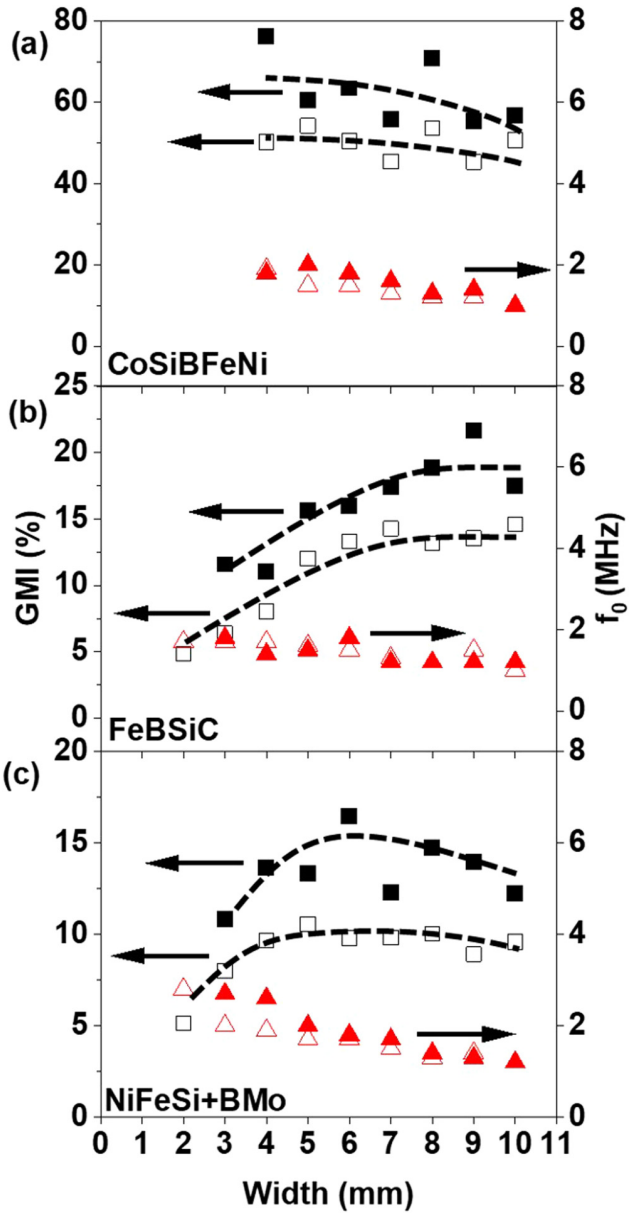

FIG. 10. Variation of GMI ratio (black squares) and critical frequency (f_0, red triangles) with ribbon width for ribbon samples composed of (a) $Co_{66}Si_{15}B_{14}Fe_4Ni_1$, (b) $Fe_{81}B_{13}Si_{3.5}C_2$, and (c) $Ni_{40}Fe_{40}Si + B_{19}Mo_{1-2}$. Data are shown for both Batch 3 (SLEC cut, closed symbols) and Batch 4 (DLEC cut, open symbols) ribbon samples. All ribbons have length = 300 mm and thickness = 25 μm. Trendlines are shown as a guide to the eye.

J. Appl. Phys. **128,** 174504 (2020); doi: 10.1063/5.0022777

indirectly through modification of the local domain structure. For example, the mixture of shear and tensile stress from the cutting motion may have induced a change in the orientation of the easy axis magnetization within the ribbon samples. We can associate the cutting process with applying torsion to the edges of the ribbon samples. Livingston and Morris observed that when they applied torsion to Fe-rich ribbon samples via twisting and untwisting, the orientation of the easy axis was different between the center and at the edges of the ribbon samples.[38] Additionally, edge roughness created by the cutting process could also have contributed to a local reduction of the transverse permeability by pinning the magnetization. A reduced transverse permeability at the edge of the ribbons would act to suppress the contribution of these regions to the GMI effect, with the DLEC ribbons having a greater proportion of their volume being affected, thus causing them to exhibit lower GMI ratios.[39]

Despite the differences in the magnitudes of the GMI ratios between Batch 3 (DLEC) and 4 (SLEC) ribbon samples, they showed very similar variations of their GMI ratios with the width. Both the Fe-rich and Ni-rich ribbons exhibited sharp drops in their GMI ratio at low widths. We suggest that this trend was due to the damaged/strained edge regions accounting for progressively larger proportions of the ribbons' volume as their widths decreased. The differences in the trends observed for the three materials can be explained by their differing magnetostriction constants, λ_s: The Fe-rich ribbons had the highest λ_s and so showed the onset of a decreasing GMI ratio at the largest width (~8 mm). The Ni-rich ribbons had a lower (but still sizeable) λ_s and so the GMI ratios began to decrease at a lower width (~5 mm). The Co-rich ribbons had near-zero λ_s and so did not show a decrease in GMI (ratio) with width within the studied range of geometries. We propose that the modest increases of GMI ratio with width observed at large widths in the Co-rich and Ni-rich ribbons are essentially a continuation of the trends due to the shape anisotropy observed when measuring the samples in Batch 2. Indeed, as we will show below, all Batch 2 and 3 samples appear to form a continuous curve when plotted as a function of the in-plane aspect ratio.

Another consistent feature observed in Batch 3 and 4 samples was that f_0 decreased from ~2 MHz at small widths to ~1 MHz at large widths. We are not sure of the underlying physics that caused this; however, it is likely to have been related to a shift in the balance of the mechanisms that contribute to the transverse susceptibility of the ribbons. For example, it is well established that domain wall motion becomes progressively damped as the frequency of excitation increases,[2,6] and so the observed trend may have been due to domain rotation becoming dominant in the lower width ribbons.

3. Variation of GMI ratio with aspect ratio

To unify the trends observed for the variation of GMI ratio with the ribbon length and width, we replotted the data as a function of the ribbons' aspect ratio (l/w) [Fig. 11(a)].

Data shown are for ribbon samples from Batches 3 and 4, as these had a consistent DLEC edge profile. Figure 11(b) presents equivalent data for $GMI_{corrected}$, which showed very similar trends to the uncorrected data.

For all three materials, a continuous curve was observed. The Fe-rich and Ni-rich dataset ribbons exhibited a peaked form, as noted previously in Sec. III B 2. We suggest that the peak was the result of competition between the effects of the strained/damaged edge regions and the global shape anisotropy. The increasing trend with the aspect ratio for $l/w < 20$ was due to shape anisotropy. The decreasing trend with the aspect ratio for $l/w > 20$ was caused by

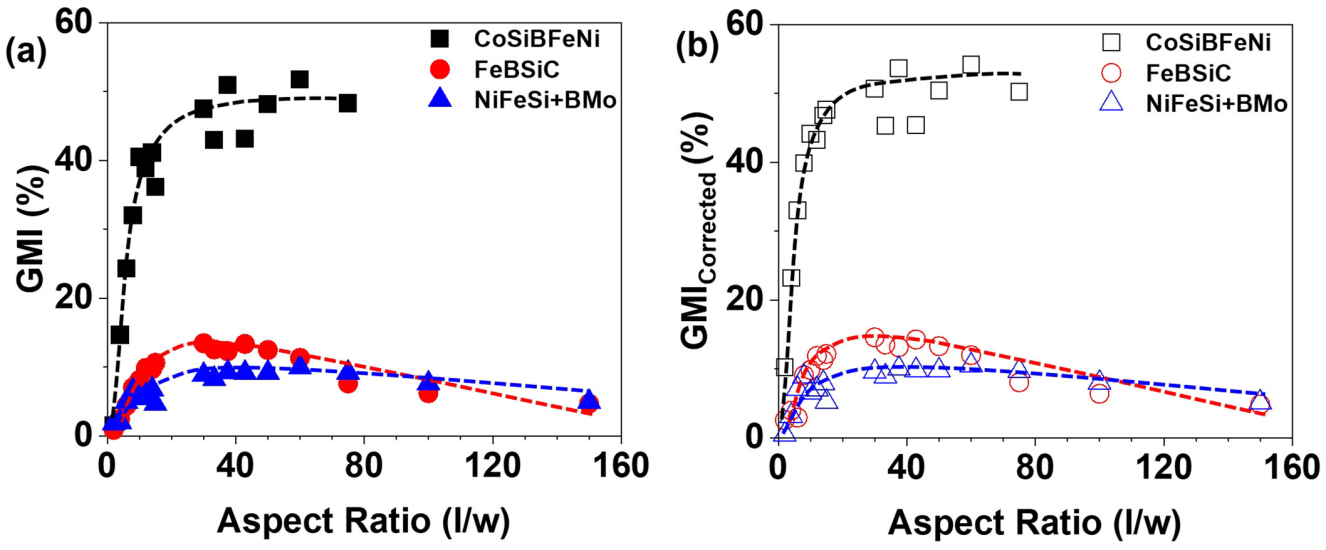

FIG. 11. (a) Peak GMI ratio as a function of in-plane aspect ratio (*length/width*). (b) Equivalent data for $GMI_{corrected}$.

J. Appl. Phys. **128,** 174504 (2020); doi: 10.1063/5.0022777

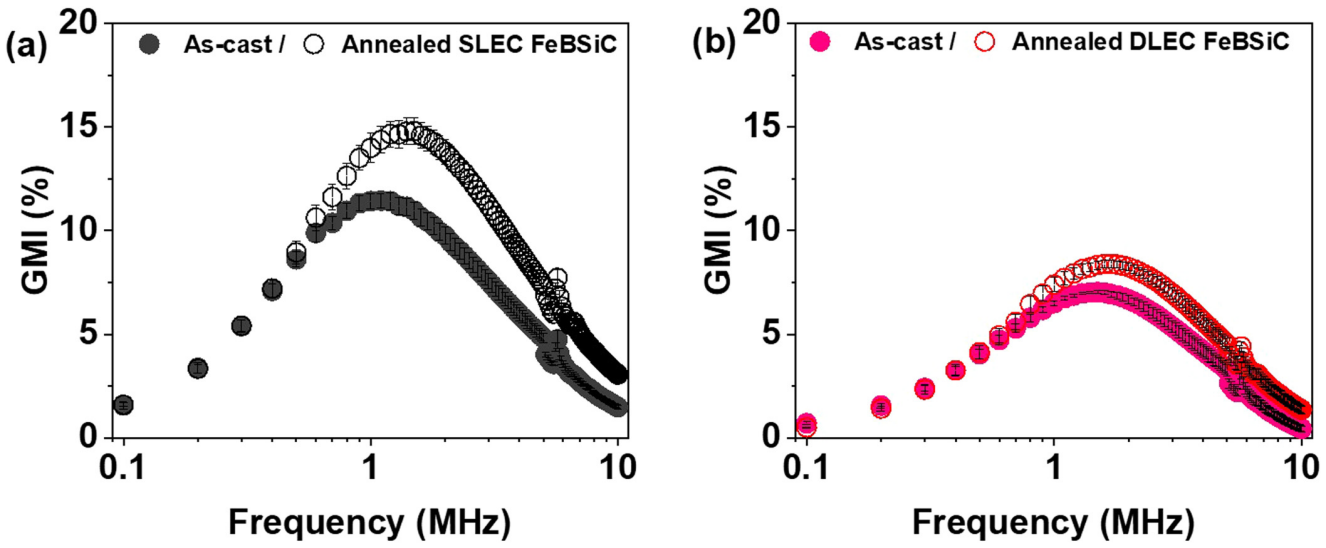

FIG. 12. GMI ratio vs frequency plots of as-cast and annealed (a) SLEC and (b) DLEC $Fe_{81}B_{13}Si_{3.5}C_2$ ribbons. The ribbons had length = 180 mm, width = 4 mm, and thickness = 25 μm.

our primitive cutting method, which suppressed the GMI ratio at lower widths (which translates to a high l/w). The Co-rich ribbons exhibited an asymptotic trend, which we attributed to their near-zero λ_s value.

D. Effects of heat treatment on SLEC and DLEC ribbons

To investigate whether the effects of our mechanical cutting process could be reversed by relaxing induced strains, we performed heat treatment of a SLEC ribbon and a DLEC Fe-rich ribbon with *length* = 180 mm, *width* = 4 mm, and thickness = 25 μm. Figures 11(a) and 11(b) present the frequency-dependent GMI ratios for both, ribbon samples before and after heat treatment.

We observed that the differences between the GMI ratios of the SLEC and DLEC ribbon samples persisted even after annealing, with the SLEC ribbon maintaining notably higher GMI ratios than the DLEC ribbon sample. Furthermore, there were differences in the degree to which the GMI ratio was enhanced by the heat treatment: the peak GMI ratio of the SLEC ribbon sample was enhanced by ~3.4%, while enhancement in the DLEC ribbon sample was ~1.4%. Many studies have correlated the effects of thermal treatment on a material's GMI ratio to the alleviation of internal stresses present in the sample from fabrication processes.[10,21] However, the heat treatment process applied here was clearly insufficient to completely restore parity between the GMI ratios of the SLEC and DLEC ribbons. Thus, we suggest that the differences in GMI behaviors between the SLEC and DLEC ribbon samples were caused either by inelastic deformations of the materials or by edge roughness, induced by the crude mechanical cutting process used to prepare the ribbons (Fig. 12).

IV. CONCLUSION

In this paper, we have studied the effects of geometry, the cutting process, and heat treatment on the GMI behavior of ribbons composed of commercially available amorphous magnetic materials. We have studied the width and length dependence of the peak GMI ratio, as well as how the GMI response changes when either one (SLEC) or both sides (DLEC) of the ribbon were mechanically cut when preparing the ribbons from precursor foils.

Our results suggest that, as expected, the GMI ratio of the materials we studied correlated with the size of their saturation magnetostriction coefficient λ_s, with low values promoting higher GMI ratios, even without additional field annealing. The roughness of the ribbon's surfaces may also have played a role in differentiating their GMI properties.

The geometry dependence of the GMI ratio was found to be complicated, with ribbons with non-zero λ_s constants exhibiting competition between the effects of shape anisotropy and those of edge regions damaged by a crude mechanical cutting process. In particular, we attributed a decrease in GMI ratios with the width in high-aspect ratio ribbons to magnetoelastic anisotropies or roughness induced at the edges of the ribbons during the cutting process. This conclusion is reinforced by the comparison between the GMI behavior of SLEC and DLEC ribbons, where it was found that SLEC ribbons always exhibited higher GMI ratios. Experiments in which the ribbons were heat treated after cutting enhanced the ribbons' GMI ratios, most likely due to the relaxation of induced strains, but were unable to restore parity between the SLEC and DLEC cut ribbons. GMI was found to increase with increasing length for aspect ratios l/w less than ~20, which we attributed to the effects of shape anisotropy. In combination, these two effects produce trends that were consistent with other works where a

J. Appl. Phys. **128,** 174504 (2020); doi: 10.1063/5.0022777

"critical aspect ratio" that maximized the GMI ratio was observed,[9,10] although we have proposed alternative explanations for these phenomena in our samples.

Most significantly for applications, our results suggest that high GMI ratios can be maintained in high-aspect ratio ribbons even when prepared from commercially available materials using relatively primitive cutting processes. This suggests that such ribbons could be successfully deployed as macro-scale sensors where either small magnetic fields/strain must be detected over large sensing areas or where more acute local stimuli must be detected if they occur at any point in a larger region of sensor coverage.

ACKNOWLEDGMENTS

The authors acknowledge the Nuclear Decommissioning Authority (NDA) for funding this project and the Henry Royce Institute for Advanced Materials, funded through EPSRC Grant Nos. EP/R00661X/1, EP/S019367/1, EP/P02470X/1, and EP/P025285/1, for the financial support and Bruker Fastscan AFM access at The University of Sheffield.

DATA AVAILABILITY

The data that support the findings of this study are available within the article.

REFERENCES

[1]C. Morón, C. Cabrera, A. Morón, A. Garcí, and M. González, "Magnetic sensors based on amorphous ferromagnetic materials: A review," Sensors **15**, 28340–28366 (2015).
[2]M. H. Phan and H. X. Peng, "Giant magnetoimpedance materials: Fundamentals and applications," Prog. Mater. Sci. **53**, 323–420 (2008).
[3]M. Knobel and K. R. Pirota, "Giant magnetoimpedance: Concepts and recent progress," J. Magn. Magn. Mater. **242–245**, 33–40 (2002).
[4]S. Dwevedi, G. Markandeyulu, P. R. Ohodnicki, A. Leary, and M. E. McHenry, "Stress-MI and domain studies in Co-based nanocrystalline ribbons," J. Magn. Magn. Mater. **323**(15), 1929–1933 (2011).
[5]J. Hu, H. Qin, J. Chen, and Y. Zhang, "Giant stress-impedance effect in $Fe_{73.5}CuNb_{3-x}V_xSi_{13.5}B_9$ amorphous ribbons," J. Magn. Magn. Mater. **266**, 290–295 (2003).
[6]M. Knobel, M. Vázquez, and L. Kraus, "Giant magnetoimpedance," Handb. Magn. Mater. **15**, 497–563 (2003).
[7]V. Zhukova *et al.*, "Effect of nanocrystallization on magnetic properties and GMI effect of Fe-rich microwires," J. Electron. Mater. **43**, 4540–4547 (2014).
[8]H. Q. Guo, H. Kronmüller, T. Dragon, Z. H. Cheng, and B. G. Shen, "Influence of nanocrystallization on the evolution of domain patterns and the magnetoimpedance effect in amorphous $Fe_{73.5}Cu_1Nb_3Si_{13.5}B_9$ ribbons," J. Appl. Phys. **89**, 514–520 (2001).
[9]A. Chaturvedi, T. P. Dhakal, S. Witanachchi, A. T. Le, M. H. Phan, and H. Srikanth, "Critical length and giant magnetoimpedance in $Co_{69}Fe_{4.5}Ni_{1.5}Si_{10}B_{15}$ amorphous ribbons," Mater. Sci. Eng. B Solid State Mater. Adv. Technol. **172**(2), 146–150 (2010).
[10]Y. H. Ding, K. Xue, W. Y. Wang, and X. Ma, "Influence of aspect ratio on giant magnetoimpedance effect for $Fe_{67}Co_{18}Si_{11}B_4$ amorphous ribbons," Acta Metall. Sin. (Engl. Lett.) **30**(12), 1236–1242 (2017).
[11]K. C. Mendes, "Enhanced GMI in ribbons of $Co_{70.4}Fe_{4.6}Si_{1.5}B_{10}$ alloy," J. Magn. Magn. Mater. **181**, 111–112 (1998).
[12]M. Zhao, S. Fang, Z. Han, J. Wei, H. Peng, and L. Chen, "Sample length dependence of giant magnetoimpedance in FeCuNbSiB nanocrystalline ribbons," Mater. Transfer **48**(3), 460–464 (2007).
[13]C. Zhao, X. Zhang, Q. Liu, and J. Wang, "GMI field sensitivity near a zero external field in Co-based amorphous alloy ribbons : Experiments and model," J. Phys. D: Appl. Phys. **49**(6), 065006 (2016).
[14]L. González-Legarreta *et al.*, "Magnetoimpedance dependence on width in $Co_{66.5}Fe_{3.5}Si_{12.0}B_{18.0}$ amorphous alloy ribbons," J. Appl. Phys. **113**(5), 0–6 (2013).
[15]L. A. P. Gonc, J. M. Soares, F. L. A. Machado, and W. M. De Azevedo, "GMI effect in the low magnetostrictive $Co_{70}Fe_5Si_{15}B_{10}$ alloys," Physica B: Condens. Mater. **384**, 152–154, (2006).
[16]K. R. Pirota, M. L. Sartorelli, M. Knobel, J. Gutierrez, and J. M. Barandiarah, "Influence of induced anisotropy and magnetostriction on the giant magnetoimpedance effect and its aftereffect in soft magnetic amorphous ribbons," J. Magn. Magn. Mater. **202**, 431–444 (1999).
[17]H. Chiriac and T. A. Óvári, "Amorphous glass-covered magnetic wires: Preparation, properties, applications," Prog. Mater. Sci. **40**(5), 333–407 (1996).
[18]A. Zhukov *et al.*, "Manipulation of magnetic properties of glass-coated microwires by annealing," J. Magn. Magn. Mater. **383**, 232–236 (2015).
[19]A. Zhukov *et al.*, "Effect of annealing on magnetic properties and magnetostriction coefficient of Fe-Ni-based amorphous microwires," J. Alloys Compd. **651**, 718–723 (2015).
[20]M. H. Phan, H. X. Peng, M. R. Wisnom, S. C. Yu, C. G. Kim, and N. H. Nghi, "Effect of annealing temperature on permeability and giant magneto-impedance of Fe-based amorphous ribbon," Sens. Actuators A Phys. **129**, 62–65 (2006).
[21]F. Jin, L. Zhou, W. Cheng, Y. Zhang, B. Tong, and Y. Xu, "Effect of shape and annealing on the giant magnetoimpendence properties of FeCoSiB ribbon," IEEE Trans. Magn. **50**(10), 1–4 (2014).
[22]Y. Ding, R. Tian, K. Xue, X. Wang, Y. Shi, and X. Ma, "Impact of ribbon width on magnetoimpedance and permeability of $Fe_{69.2}Co_{7.7}Cu_{0.6}Nb_{2.5}Si_{11}B_9$ soft magnetic alloy," Mater. Technol. **31**(6), 337–341 (2016).
[23]See http://www.goodfellow.com/catalogue/GFCat4I.php?ewd_token=t5Hi55VEn7gmigQ8omoaE3EsYo1a6W&n=H8vrxrqtUtiolf3A3HDcEcWGNXdgOH&ewd_urlNo=GFCat4B11&Catite=CO810250&CatSearNum=5 for "Cobalt/silicon/boron/iron/nickel foil CO810250—Goodfellow Catalog" (accessed October 9, 2019).
[24]See http://www.goodfellow.com/catalogue/GFCat4I.php?ewd_token=t5Hi55VEn7gmigQ8omoaE3EsYo1a6W&n=H8vrxrqtUtiolf3A3HDcEcWGNXdgOH&ewd_urlNo=GFCat4B11&Catite=FE800250&CatSearNum=5 for "Iron/boron/silicon foil FE800250—Goodfellow Catalog" (accessed October 9, 2019).
[25]See http://www.goodfellow.com/catalogue/GFCat4I.php?ewd_token=t5Hi55VEn7gmigQ8omoaE3EsYo1a6W&n=H8vrxrqtUtiolf3A3HDcEcWGNXdgOH&ewd_urlNo=GFCat4B11&Catite=NI800250&CatSearNum=5 for "Nickel/boron/silicon foil NI800250—Goodfellow Catalog" (accessed October 9, 2019).
[26]L. Jin, S. S. Yoon, P. Kollu, C. G. Kim, D. S. Suhr, and C. O. Kim, "Dependence of GMI profile on size of Co-based amorphous ribbon," J. Magn. **12**(1), 31–34 (2007).
[27]V. Raposo, J. I. Iñiguez, D. García, A. G. Flores, and M. Vázquez, "Internal magnetoimpedance of amorphous wires," in *Intermag 2003—Program of the 2003 IEEE International Magnetics Conference* (IEEE, 2003).
[28]P. Gazda and R. Szewczyk, "Novel giant magnetoimpedance magnetic field sensor," Sensors **20**(3), 1–15 (2020).
[29]C. Zhao, X. Zhang, Q. Liu, and J. Wang, "GMI field sensitivity near a zero external field in Co-based amorphous alloy ribbons: Experiments and model," J. Phys. D. Appl. Phys. **49**(6), 065006 (2016).
[30]D. García, V. Raposo, O. Montero, and J. I. Íñiguez, "Influence of magnetostriction constant on magnetoimpedance–frequency dependence," Sensors Actuators A Phys. **129**(1–2), 227–230 (2006).
[31]M. Knobel, M. L. Sanchez, J. Velazquez, and M. Vazquez, "Stress dependence of the giant magneto-impedance effect in armorphous wires," J. Phys.: Condens. Mater., 7 (1995).
[32]A. Chaturvedi, T. Dhakal, S. Witanachchi, A. T. Le, M. H. Phan, and H. Srikanth, "Correlation between magnetic softness, sample surface and

magnetoimpedance in $Co_{69}Fe_{4.5}X_{1.5}Si_{10}B_{15}$(X = Ni, Al, Cr) amorphous ribbons," Physica B **405**(13), 2836–2839 (2010).
[33]T. Eggers *et al.*, "Impact of the transverse magnetocrystalline anisotropy of a Co coating layer on the magnetoimpedance response of FeNi-rich nanocrystalline ribbon," J. Alloys Compd. **741**, 1105–1111 (2018).
[34]Z. M. Wu *et al.*, "Magnetoelastic resonance enhancement of longitudinally driven giant magnetoimpedance effect in FeCuNbSiB ribbons," Physica B **405**(1), 237–330 (2010).
[35]A. Aharoni, "Demagnetizing factors for rectangular ferromagnetic prisms," J. Appl. Phys. **83**(6), 3432–3434 (1998).
[36]C. Zhao, L. Pan, X. Li, L. Ma, Q. Liu, and J. Wang, "Optimization of magneto-impedance effect in Co-based ribbon by laser patterning for sensor arrays application," J. Phys. D. Appl. Phys. **51**(4), 1–4 (2018).
[37]T. Eggers *et al.*, "Correlation between domain structure, surface anisotropy and high frequency magneto-impedance in joule annealed CoFe-based melt-spun ribbons," J. Alloys Compd. 682, 799–804 (2016).
[38]J. D. Livingston and W. G. Morris, "Magnetic domains in twisted amorphous ribbons," IEEE Trans. Magn. **20**(5), 1379–1381 (1984).
[39]H. T. Tran *et al.*, "Anisotropic mechanical and giant magneto-impedance properties of cobalt-rich amorphous ribbons," J. Electron. Mater. **45**, 2278–2285 (2016).

J. Appl. Phys. **128,** 174504 (2020); doi: 10.1063/5.0022777

Chapter 7

Comparative study of the giant stress impedance behaviour of commercial amorphous ribbons for strain sensing applications

7.1 Outline

The chapter discusses the influence of mechanical stress/strain on the GMI and GSI behaviour in amorphous ribbons. Chapter 6 demonstrated the Co-rich ribbon sample had the highest GMI response out of all three samples due to its low λ_S value. However, it was believed not a viable option for a strain sensing technology since λ_S describes a ferromagnetic material's sensitivity to stress. Therefore, the Co-rich sample having a near-zero λ_S implies it's magnetic behaviour is not sensitive to stress implying a low GSI response. However, upon investigation, a more complex behaviour between λ_S and the

GSI effect was found in which (according to literature) was related to the sample's anisotropy field ($\boldsymbol{H}_{\mathrm{K}}$) [50]. Moreover, we have identified the strain performance are also limited by their mechanical properties, specifically, the Young's modulus (E).

In order to identify which amorphous sample has the best strain sensing performance, comparatively, a figure of merit (FOM) was used. The FOM was based on the linearity of the signal (R^2) and the gauge factor (GF) - which measures sensitivity - for all applied strains (up to 10×10^{-3}). Using the FOM, we identified the Ni-rich ribbon was suitable for low strain regimes (1×10^{-3}) and Co-rich ribbon was suitable for high strain regimes (10×10^{-3}) which covers the minimum strain requirement on monitoring an ILW waste package, 2.5×10^{-3}.

Details on these results and varying sensing applications are presented in the chapter as an article for the Journal of Applied Physics (JAP) [255]. It is important to note the GF presented for all three amorphous samples is smaller by a factor of 10, but the findings and discussion on the material behaviour are the same.

Journal of Applied Physics ARTICLE scitation.org/journal/jap

Comparative study of the giant stress impedance behavior of commercial amorphous ribbons for strain sensing applications

Cite as: J. Appl. Phys. 131, 214503 (2022); doi: 10.1063/5.0088988
Submitted: 21 February 2022 · Accepted: 4 May 2022 ·
Published Online: 2 June 2022

Patrick Pan[a] and T. J. Hayward

AFFILIATIONS

Department of Materials Science and Engineering, The University of Sheffield, Sheffield, United Kingdom

[a]Author to whom correspondence should be addressed: ppan4@sheffield.ac.uk

ABSTRACT

The giant magnetoimpedance (GMI) and giant stress impedance (GSI) behaviors of amorphous ribbons composed of three commercially available materials ($Co_{66}Si_{15}B_{14}Fe_4Ni_1$, $Fe_{81}B_{13}Si_{3.5}C_2$, and $Ni_{40}Fe_{40}Si + B_{19}Mo_{1-2}$) with differing saturation magnetostriction constants (λ_s) and Young's moduli (E) were studied under longitudinal stress/strain. The linearity of the ribbons' GSI responses and gauge factors was measured to create a figure of merit and compare their stress/strain sensing performance for strains up to $\varepsilon = 10 \times 10^{-3}$. We observed that the $Ni_{40}Fe_{40}Si + B_{19}Mo_{1-2}$ ribbon displayed the best performance for low strains ($\varepsilon < 1 \times 10^{-3}$), whereas the $Co_{66}Si_{15}B_{14}Fe_4Ni_1$ ribbon displayed the best performance for higher strains ($\varepsilon < 10 \times 10^{-3}$). We conclude that the suitability of a material for sensing strains in any given strain regime has a complex dependence on both λ_s and E, the former of which dictates both the absolute magnitude of the impedance variation materials exhibit (i.e., the dynamic range), while both λ_s and E control how their impedances vary with applied strain.

I. INTRODUCTION

The giant magnetoimpedance (GMI) effect has been studied extensively for use in technological applications.[1–3] The GMI effect is defined as the variation in absolute impedance, Z, of a ferromagnetic conductor when subjected to DC magnetic fields a DC magnetic field. Its magnitude usually peaks at low MHz frequencies, typically under $f = 10$ MHz,[3,4] where it results from variation in the skin depth (δ) of the electrical current with the magnetic field. The effect can be understood from classical electrodynamical theory, in which the skin depth may be expressed as $\delta = \sqrt{\frac{\rho}{\pi f \mu}}$, where f is the frequency of the electrical current, μ is the transverse magnetic permeability of the conductor, and ρ is the resistivity of the conductor.[3,4] Here, applying magnetic fields changes the value of μ, resulting in variation of the skin depth and, thus, Z with the applied field. GMI ratios can be as large as several hundred percent when the microstructure and domain structure of the (typically amorphous) materials are optimized to produce high values of μ.[5–7] Harnessing these phenomena can allow the creation of a highly sensitive magnetic field sensor[4,8] with promising applications in biosensing technologies.[9–12] Furthermore, other external stimuli can also affect μ, allowing the design of highly sensitive GMI sensors for detecting, e.g., temperature[13,14] and externally applied stresses/strains.[2,15,16]

In sensing applications, it is desirable to simply measure how the impedance of a ferromagnetic conductor varies with the target stimuli, rather than to perform full, field-swept GMI measurements in the presence of the stimuli. Such an approach was first reported in 1997 by Shen *et al.* who observed a direct correlation between applied stress and impedance in CoSiB amorphous wires,[17] a phenomenon known as the giant stress impedance (GSI) effect. Since then, there have been many studies investigating the GSI effect in wires[18–21] and ribbons[22–24] with a common understanding that the GSI effect results from the variation of μ with stress/strain due to magnetoelastic effects.

Recently, we reported on the GMI behavior of three commercialized amorphous ribbons with differing magnetic properties, including the saturation magnetostriction coefficient, λ_s.[25] It is widely agreed that λ_s determines the magnitude of the GMI response of a material, with lower λ_s coefficients resulting in higher

GMI ratios. This is because materials with near-zero (or negative) λ_s coefficients have higher transverse permeabilities.[4,26–28] Our results supported this view, with a $Co_{66}Si_{15}B_{14}Fe_4Ni_1$ ribbon with near-zero λ_s producing a much larger GMI response than the other materials studied. However, the situation for the GSI effect is more complex with λ_s not only affecting μ, but also how sensitive a material's magnetic properties are to changes in applied stress, and, in combination with a material's mechanical properties, how sensitive they are to applied strain. It is, therefore, unclear how λ_s should be optimized for any given stress/strain sensing application.

In this study, we have investigated correlations between the GSI effect, GMI effect, and λ_s in amorphous ribbons composed of three commercially available materials and assessed their applicability to strain sensing applications. Our results show that selecting materials with low λ_s will maximize both the GMI and GSI ratios. However, choosing a material for a given strain sensing application is more complex, with the best choice of material depending strongly on the range of stresses/strains that need to be sensed.

II. EXPERIMENTAL METHOD

A. Sample preparation

Three bulk amorphous foils were purchased from Goodfellow. The foils all had thicknesses of 25 μm, but different chemical compositions: $Co_{66}Si_{15}B_{14}Fe_4Ni_1$, $Fe_{81}B_{13}Si_{3.5}C_2$, and $Ni_{40}Fe_{40}Si + B_{19}Mo_{1-2}$. These three materials were chosen for the study due to each having different values of λ_s, as shown in Table I. For brevity, the ribbon samples will be referred to as Co-rich ($Co_{66}Si_{15}B_{14}Fe_4Ni_1$), Fe-rich ($Fe_{81}B_{13}Si_{3.5}C_2$), and Ni-rich ($Ni_{40}Fe_{40}Si + B_{19}Mo_{1-2}$), respectively.

In Ref. 25, we performed the basic characterization of the structural properties of all three materials to confirm the material properties quoted by the supplier. X-ray diffraction (XRD) measurements with Cu Kα radiation affirmed the amorphous crystal structure of all three materials with the single broad peak being observed at $2\theta \sim 45°$. In addition, each of the materials surface roughness was measured using Atomic Force Microscopy (AFM), with root mean square surface roughness (R_q) 4.15, 15.3, and 14.8 nm being observed for Co-rich, Fe-rich, and Ni-rich foils, respectively.

The three materials' (with common dimensions of 10 mm $\times$ 2 mm $\times$ 25 μm) hysteresis loops were measured at room temperature using a superconducting quantum interference device (SQUID) [Fig. 1(a)].[25] Of the three samples, the Co-rich sample exhibited the highest susceptibility when compared to the other two ribbon samples. Figure 1(b) presents the coercive fields (H_C) of all three samples with values of 0.01, 0.16, and 0.23 Oe of the observed Co-rich, Fe-rich, and Ni-rich foils, respectively.

In this study, two sets of ribbons composed of the three materials with common cross sections of 10 mm $\times$ 25 μm were prepared by mechanically cutting the foils. The first set of samples (batch 1) had lengths of 120 mm, while the second set of samples (batch 2) had lengths of 200 mm. The sample lengths batch 2 samples were chosen to give the ribbons an aspect ratio (l/w) of 20 where it was expected that GMI/GSI ratios would be maximized.[25] The shorter length of the batch 1 samples was chosen to allow uniform magnetic fields to be applied to them using a Helmholtz coil.

B. GMI and GSI measurements

Batch 1 samples were used to study the variation of the samples GMI under stress/strain. The ribbons were placed inside a Helmholtz coil with a uniform field region of ~150 mm long and a maximum field strength of $H_{DC} = \pm 150$ Oe. The ends of the sample were clamped to a manual tensile test stand (Mark-10 Model ES-30) (Fig. 2). Applied forces were measured using a force gauge (Mark—10 Series 5), and the applied longitudinal tensile stresses were calculated using the equation $\sigma = F/A$, where F was the applied tensile force and A was the ribbons' cross-sectional area. The samples' tensile strains were calculated using the equation $\varepsilon = \sigma/E$, using the values of E listed in Table I.

The ribbons' impedances were measured in the range 0.1–10 MHz by connecting them to an impedance analyzer (Agilent 4294A) using a four-terminal (4T) connection. Parasitic impedances from the test fixture and test leads were compensated using an open, short, and load calibration methodology. We note that parasitic impedances at the connection between the test leads and the sample were not accounted for in our de-embedding procedure. However, as we showed in a previous study, these effects are relatively minor and are not expected to substantially affect our measurements.[25]

GMI measurements under induced stress/strain were performed by measuring the samples' impedance spectra while sweeping the applied field between −150 and +150 Oe and applying constant longitudinal stresses of either 0 or 40 MPa. At both stresses, the ribbons' GMI ratios were then calculated using the expression

$$\mathrm{GMI} = \frac{|Z(H)| - |Z(H_{max})|}{|Z(H_{max})|} \times 100\%, \quad (1)$$

where $Z(H_{max})$ is the absolute impedance measured at the highest field ($H_{DC} = \pm 150$ Oe) and $Z(H)$ is the absolute impedance measured at field H. The peak GMI ratio (i.e., the highest magnitude GMI

TABLE I. Magnetic and mechanical properties for $Co_{66}Si_{15}B_{14}Fe_4Ni_1$, $Fe_{81}B_{13}Si_{3.5}C_2$, and $Ni_{40}Fe_{40}Si + B_{19}Mo_{1-2}$ ribbons, as quoted by the supplier.[29–31]

	Magnetic properties		Mechanical properties
Ribbon sample	Magnetostriction coefficient λ_s (ppm)	Saturation flux density (T)	Young's modulus (GPa)
$Co_{66}Si_{15}B_{14}Fe_4Ni_1$ (Co-rich)	<1	0.55	58
$Fe_{81}B_{13}Si_{3.5}C_2$ (Fe-rich)	30	1.6	61
$Ni_{40}Fe_{40}Si + B_{19}Mo_{1-2}$ (Ni-rich)	8	0.8	150

J. Appl. Phys. **131,** 214503 (2022); doi: 10.1063/5.0088988

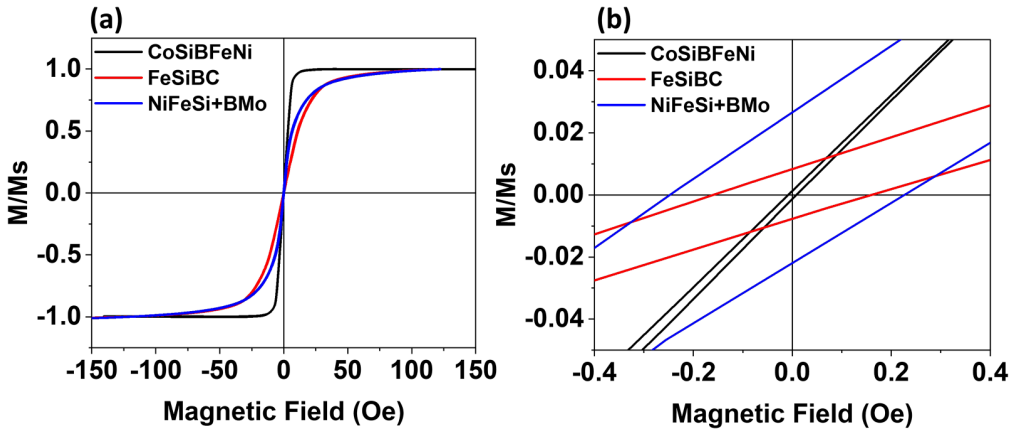

FIG. 1. (a) Normalized M-H hysteresis loops of Co-rich, Fe-rich, and Ni-rich samples with common dimensions of 10 mm × 2 mm × 25 μm. (b) A more detailed image of the center of the loops to enable each sample's coercive fields (H_C) to be seen. The applied field was parallel to the ribbon axis.

ratio), at both stresses, was obtained either at $H = 0$ Oe for samples that displayed single-peak GMI curve or at a positive/negative finite value of H for samples that displayed a double-peak GMI curve.

Batch 2 samples were used to characterize the ribbons' GSI behaviors. The ribbons were mounted in the same way as in Fig. 2; however, no fields were applied by the Helmholtz coil. The impedance spectra of each ribbon were measured under applied stresses up to 600 MPa. GSI ratios were calculated using the expression[22]

$$\mathrm{GSI} = \frac{|Z(\sigma)| - |Z(0)|}{|Z(0)|} \times 100\%, \tag{2}$$

where $Z(\sigma)$ is the absolute impedance at stress σ and $Z(0)$ is the absolute impedance measured at zero applied stress. The peak GSI ratio (the highest magnitude GSI ratio) was obtained either at finite values of σ or at the largest value of stress applied (σ_{max}) for samples that showed a monotonic trend of GSI with σ.

In order to analyze how the GSI behavior of the ribbons could be optimized for strain sensing applications, two factors were considered: the linearity of the ribbons' GSI responses and their average strain sensitivities ($\Delta GSI/\Delta\varepsilon$), also known as the gauge factor (GF). Both were calculated for each applied strain $\varepsilon(\sigma_i)$ by considering the GSI response over a strain range between $\varepsilon = 0$ and $\varepsilon(\sigma_i)$. The gauge factor for measurement up to strain value $\varepsilon(\sigma_i)$ was, thus, calculated using $GF(\sigma_i) = GSI(\sigma_i)/\varepsilon(\sigma_i)$. To characterize the linearity of the ribbons' GSI, we performed a linear regression of the GSI data between $\varepsilon = 0$ and $\varepsilon(\sigma_i)$, and calculated the value of R^2 to judge the quality of the linear fit. From these two values, we created a normalized figure of merit (FOM) in the range 0–1 to allow comparison between the differing responses of the three materials,

$$\mathrm{FoM} = R^2 \times \left(\frac{\mathrm{GF}}{\mathrm{GF}_{max}}\right), \tag{3}$$

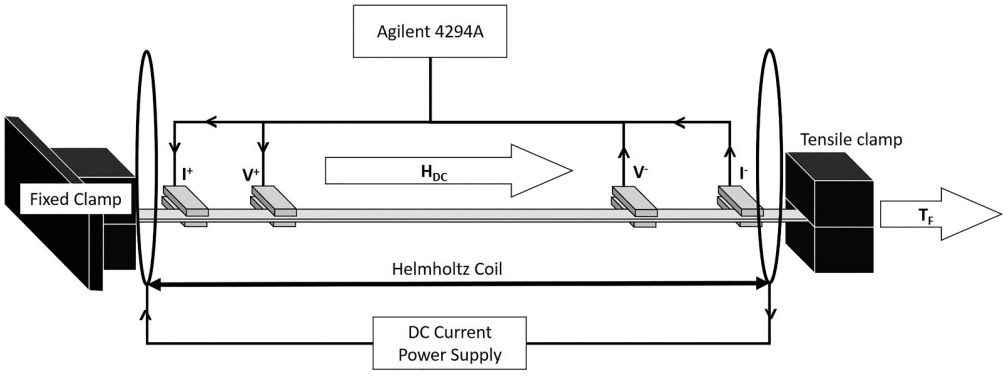

FIG. 2. Schematic diagram of the experimental setup used to perform GMI measurements under tensile stress/strain.

J. Appl. Phys. **131,** 214503 (2022); doi: 10.1063/5.0088988

where the GF_{max} was the largest gauge factor measured across all the samples, to allow direct comparisons between FOM for different materials. Thus, the higher the FOM value the better a sample's performance as a sensor was for a strain within a range bounded by ε_i.

III. RESULTS AND DISCUSSION

A. Influence of tensile stress/strain on GMI behavior

Figure 3 presents GMI data as a function of applied field (H) for all three samples at their respective critical frequencies (f_0), i.e., the frequency at which their peak GMI ratios were maximized. The Co-rich sample exhibited the highest GMI ratio (71.6%), followed by Fe-rich (14.6%) and Ni-rich (14.2%) samples. The difference in the GMI responses correlated to the ribbons differing λ_s coefficients, with the near-zero λ_s coefficient of the Co-rich ribbon produced a larger peak GMI response than the Fe-rich and Ni-rich ribbons, which had larger positive λ_s. This was consistent with the previously published literature, where materials with negative and near-zero λ_s produced larger GMI responses than materials with positive λ_s.[4,28,32] In addition, the GMI responses of all three samples were consistent with their magnetic properties with the hierarchy of coercive fields being the inverse of the hierarchy of GMI ratios (i.e., softer materials exhibited higher GMI ratios). The surface topography of the Co-rich sample may also have contributed to its high peak GMI ratio since it had much lower surface roughness than the other two materials. Surface roughness has previously been shown to be inversely correlated with GMI ratios in experimental studies.[33,34]

Figure 4 presents the three samples' peak GMI ratios as a function of frequency. For all samples, the peak GMI ratio was reached at $f_0 = 1$–2 MHz and then decreased as the frequency was increased further. The GMI ratio peaked at different f_0 for each sample; 1.3 MHz (Co-rich), 1.4 MHz (Fe-rich), and 1.7 MHz (Ni-rich). The frequency variation of the peak GMI ratio could be attributed to changes in the magnetization dynamics that contributed to the ribbons' transverse permeabilities. At lower frequencies, both domain wall motion and magnetization rotation contributed; however, at frequencies higher than f_0, the domain wall motion was damped by eddy currents and so magnetization rotation alone contributed to the transverse permeability (μ), resulting in a decrease in the GMI ratio.[3,4]

Figures 3 and 4 also present GMI curves measured at f_0 under $\sigma = 40$ MPa of tensile stress. Under stress, the peak GMI ratios of all three samples decreased, but each with varying amounts as listed in Table II. Furthermore, the GMI curve for the Co-rich sample changed from a single-peak to a double-peak form, indicating a change in the direction and strength of the anisotropy field within the sample.[35–37] The Fe- and Ni-rich samples exhibited single-peak GMI curves at both $\sigma = 0$ and $\sigma = 40$ MPa.

Figure 4 illustrates how the observed reduction of peak GMI ratios by applied stress extended to all the frequencies studied. This suppression of the GMI ratio occurred due to the creation of additional magnetoelastic anisotropies that decreased the peak value of μ, thus increasing the minimum skin depth and the maximum value of impedance that the materials exhibited. One might, therefore, expect materials with larger λ_s to show greater sensitivity to stress/strain. Indeed, at the first glance, the degree to which GMI ratios were suppressed from their initial values appeared correlated with the size of the materials λ_s coefficients, with the Fe-rich ribbons, which had the largest value of λ_s showing a much larger *proportional* decrease in the GMI ratio than the Co-rich ribbon, which had the smallest λ_s. Furthermore, the degree to which the peak GMI ratios were suppressed from their initial values correlated with the size of the materials λ_s coefficient, with the Fe-rich ribbons, having the largest value of λ_s showing a much larger decrease in the GMI ratio than the Co-rich ribbon. However, closer examination of the data presented evidence of a more complicated picture. For example, at $H = 0$ Oe [Fig. 5(a)], the change in the GMI ratio of the Co-rich ribbon was much larger than the other two materials exhibited at any applied field, with an absolute stress-induced GMI ratio change of 15.7% (Fe-rich ribbon peak: 9.9%, Ni-rich ribbon peak: 3.8%) [see the inset of Fig. 3(a)].

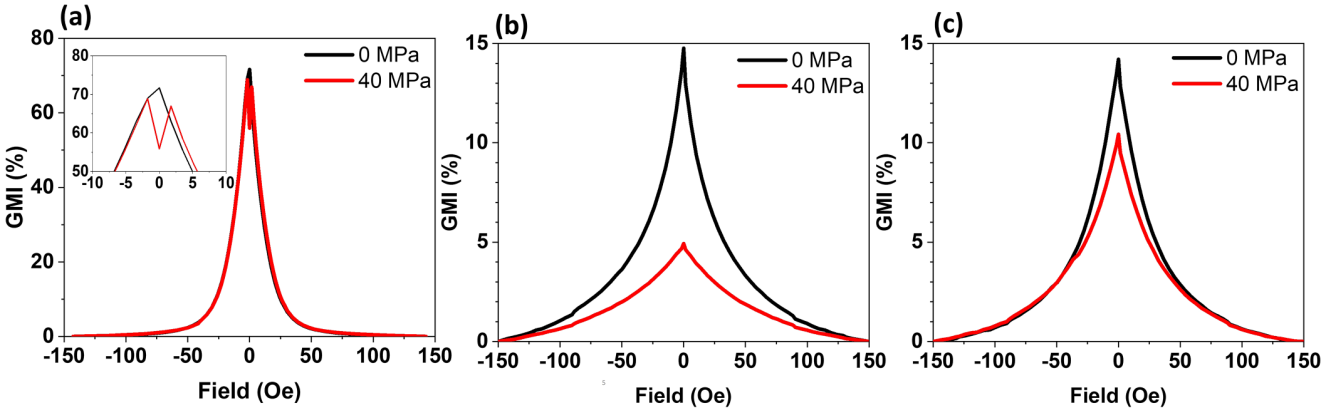

FIG. 3. GMI data measured for (a) Co-rich, (b) Fe-rich, and (c) Ni-rich ribbon samples at their respective f_0; 1.3, 1.4, and 1.7 MHz. Data are shown for tensile stresses of 0 MPa (black lines) and 40 MPa (red lines).

J. Appl. Phys. **131,** 214503 (2022); doi: 10.1063/5.0088988

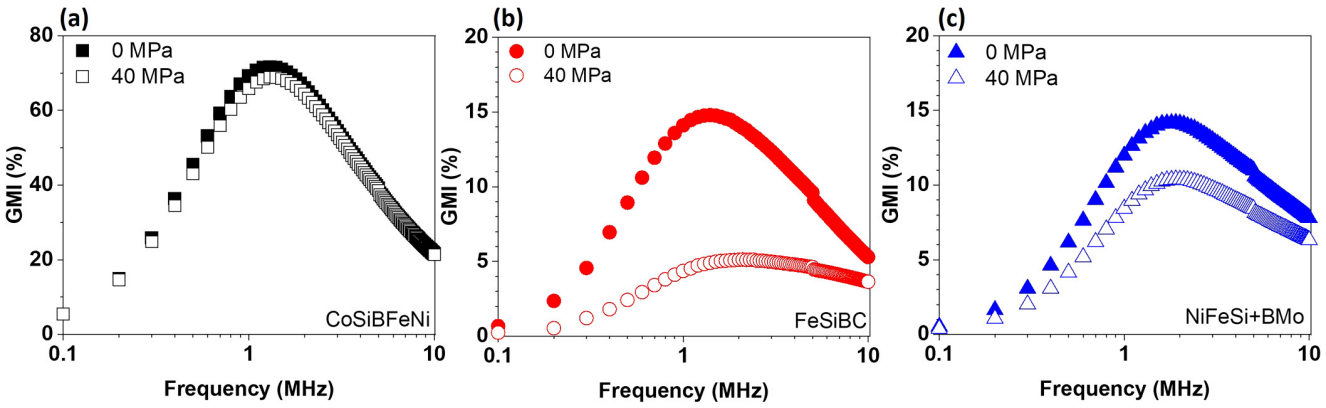

FIG. 4. Frequency dependence of peak GMI ratios for (a) Co-rich, (b) Fe-rich, and (c) Ni-rich ribbon samples under tensile stresses of 0 (measured at $H = 0$ Oe for all samples) and 40 MPa (measured at $H = \pm 1.7$ Oe for Co-rich sample and $H = 0$ Oe for Fe- and Ni-rich samples).

These data illustrate the conflicting considerations of materials selection for a stress/strain sensor: while the Fe- and Ni-rich ribbons with large λ_s clearly showed larger changes in their peak GMI ratios than the Co-rich ribbon, at zero field the Co-rich ribbon sample displayed an even larger effect, despite its low λ_s. This can be understood as follows: the size of a ribbon's GMI response is defined by the difference in its skin depth at the point where magnetic permeability is maximized, and the point where a strong applied field almost entirely suppresses the permeability. For ribbons with near-zero (or negative) λ_s, the difference in skin depth is large, and these materials have a large range of impedance values they can potentially exhibit, but these would be expected to vary relatively slowly with additional stress/strain, as induced anisotropies will be weak. For ribbons with a higher λ_s, the range of available impedance values is more limited (as the maximum permeability observed is lower due to pre-existing magnetoelastic anisotropies), but variation with applied stress would be expected to be more rapid and dramatic. Out of the studied materials, at this single stress value, the dominating factor was clearly the total range of available impedance values; hence, the Co-rich ribbon with its large dynamic range produced the largest absolute change in the GMI ratio on the application of stress.

A further interesting observation for the Co-rich ribbon (measured at H = 0 Oe) was that at frequencies in the range $f < 0.3$ MHz the sample displayed a slightly higher GMI ratio (by ~1.5%–2%) at $\sigma = 40$ MPa than it did at $\sigma = 0$ MPa (Fig. 5). This was counter to expectations, as additional anisotropies are typically expected to reduce the permeability nd, thus, increase skin depth. However, at these low frequencies, the addition of a weak magnetoelastic anisotropy aided the magnetization dynamics, resulting in an increased permeability and reduced skin depth. At higher frequencies, GMI was always decreased by the application of stress. This suggested that the additional anisotropy increased domain wall mobility within the ribbons, but did not similarly assist magnetization rotation, as typically the former mechanism dominates over the latter at lower frequencies.[22,38] Comparatively, Fe- and Ni-rich ribbon samples displayed a monotonic trend at all frequencies between both stresses, which suggests that the magnetoelastic anisotropy only reduced the transverse permeability of these samples. These results suggested a further complication in materials selection for strain sensing; clearly, the addition of stronger magnetoelastic anisotropies would eventually result in decreases in GMI for all materials; thus, it was likely that the Co-rich ribbon exhibited a non-monotonic variation of GMI with stress at some frequencies, a highly undesirable property for a sensor. Such behaviors are discussed in more detail in Secs. III B and III C.

B. GSI behavior

Having characterized the GMI behavior of the samples under stress, we turned our attention to characterizing their GSI behavior

TABLE II. Maximum GMI ratio of each sample before and after applied stress, and the stress-induced change in the GMI ratios. The ribbons' magnetostriction coefficients λ_s are also shown.

		GMI behavior		
Ribbon sample	λ_s (ppm)	Peak GMI ratio ($\sigma = 0$ MPa) (%)	Peak GMI ratio ($\sigma = 40$ MPa) (%)	Stress-induced change in GMI ratio (%)
Co-rich	<1	71.6	68.9	2.5
Fe-rich	30	14.8	4.9	9.9
Ni-rich	8	14.2	10.4	3.8

J. Appl. Phys. **131,** 214503 (2022); doi: 10.1063/5.0088988

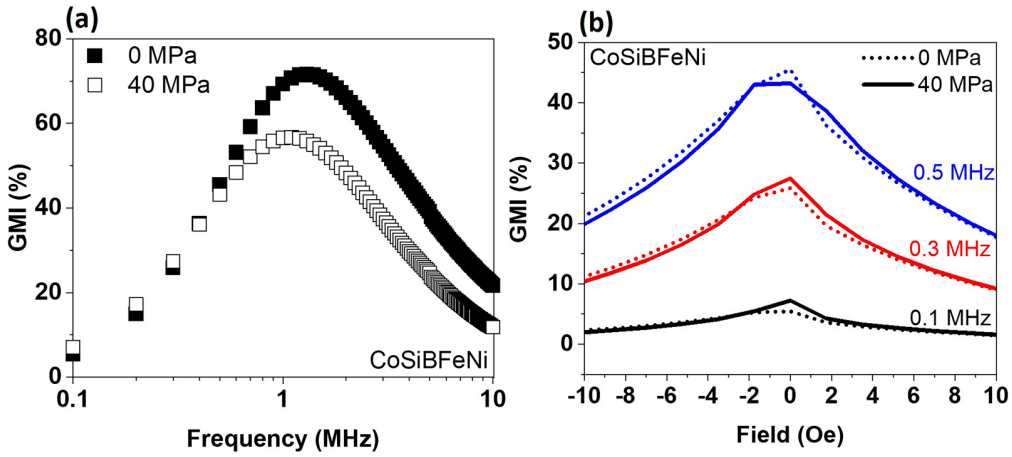

FIG. 5. The GMI ratio of the Co-rich ribbon sample with respect to (a) frequency (measured at $H = 0$ Oe) and (b) field (at frequencies of 0.1, 0.3, and 0.5 MHz).

in the absence of applied field. Figure 6 presents exemplar GSI behavior curves measured from the three materials at $f = 0.3$ MHz [Fig. 6(a)] and $f = 2$ MHz [Fig. 5(b)] under tensile stresses up to $\sigma = 600$ MPa. At both frequencies, the Fe- and Ni-rich samples exhibited monotonic behaviors, where GSI ratios were negative and consistently decreased as the stress increased, with the Fe-rich ribbon consistently exhibiting higher GSI ratios than the Ni-rich ribbon. In contrast, the GSI curves for the Co-rich sample exhibited two distinct behaviors: at $f = 0.3$ MHz [Fig. 6(a)], positive GSI ratios were observed for stresses under $\sigma = 150$ MPa. These peaked at 50 MPa (~3.3%) and then decreased monotonically for higher stresses. This behavior was equivalent to that observed in the GMI data at low frequencies. At $f = 2$ MHz, a different behavior was observed. For stress up to $\sigma = 200$ MPa, the data were like the Fe- and Ni-rich samples, with a monotonic trend and negative GSI ratios. However, beyond $\sigma = 200$ MPa, the sample's GSI ratios decreased again, before tending toward a constant value as the stress approached $\sigma = 600$ MPa. The peak GSI ratios of the Co-rich ribbon were universally higher than those of the Fe-rich and Ni-rich ribbons.

Figure 7 presents frequency-dependent GSI ratios of the three materials for $\sigma = 0$–600 MPa and $f = 0.1$–10 MHz. Like the GMI behavior, the GSI behavior exhibited a critical frequency, f_0, where the sample's highest peak GSI ratio was observed; this was 2.5 MHz for Co-rich and 1.5 MHz for Fe- and Ni-rich samples. The maximum peak GSI ratio was observed in the Co-rich ribbon (−18.3%), followed by the Fe-rich (−10.8%) and Ni-rich (−6.8%) ribbons. This indicated that the peak GSI behaved in a similar manner to the peak GMI ratios, with both ultimately being determined by the maximum possible transverse permeability available

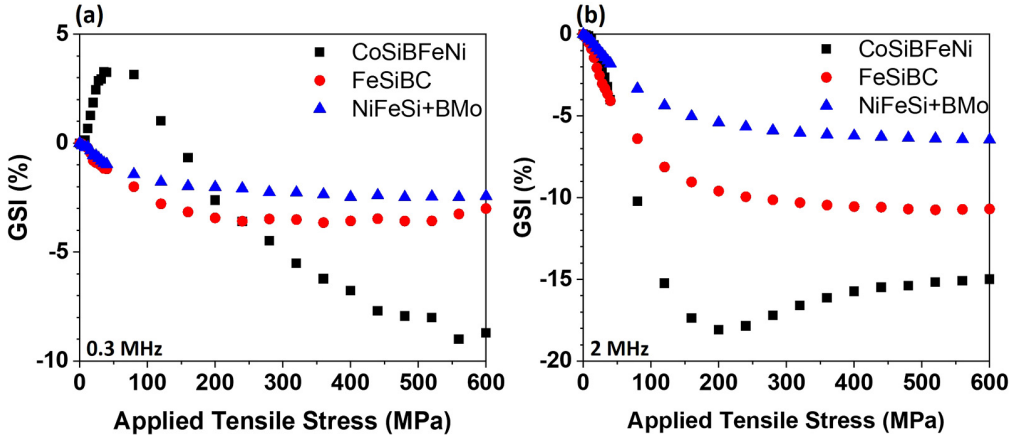

FIG. 6. Stress dependence of the GSI ratio of the Co-rich (black squares), Fe-rich (red circles), and Ni-rich (blue triangles) ribbons at $f =$ (a) 0.3 MHz and (b) 2 MHz.

J. Appl. Phys. **131,** 214503 (2022); doi: 10.1063/5.0088988

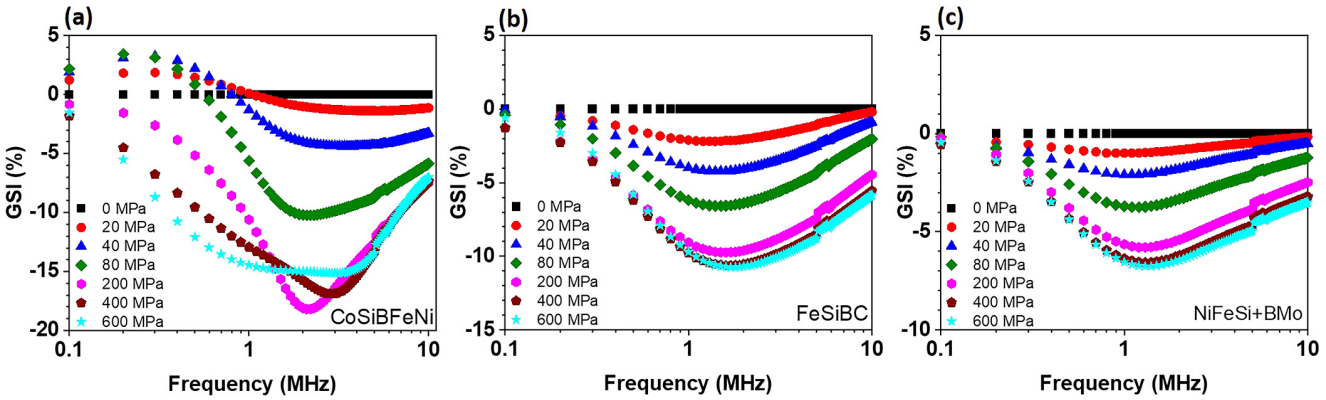

FIG. 7. Frequency dependence of GSI ratio for (a) Co-rich, (b) Fe-rich, and (c) Ni-rich ribbon samples under tensile stresses up to $\sigma = 600$ MPa.

in each sample. Thus, the materials with near-zero (or negative) λ_s coefficients exhibited larger peak GSI ratios than those with high λ_s.[4,26–28] GSI curves for each material at their respective f_0 are shown in Fig. 8.

Figure 7 also further illustrates the frequency-dependent, non-monotonic GSI behaviors exhibited by the Co-rich ribbon. Behavior like those shown in Fig. 6(a), where positive GSI ratios were measured for low stresses before monotonically decreasing, was observed for $f < 1$ MHz. For $f > 1$ MHz, behaviors similar to those shown in Fig. 6(b) were observed, with the samples always exhibiting negative GSI ratios which peaked between $\sigma = 200$ and 400 MPa and then began to decrease at higher stresses. The Fe- and Ni-rich samples exhibited simple, monotonic trends at all frequencies.

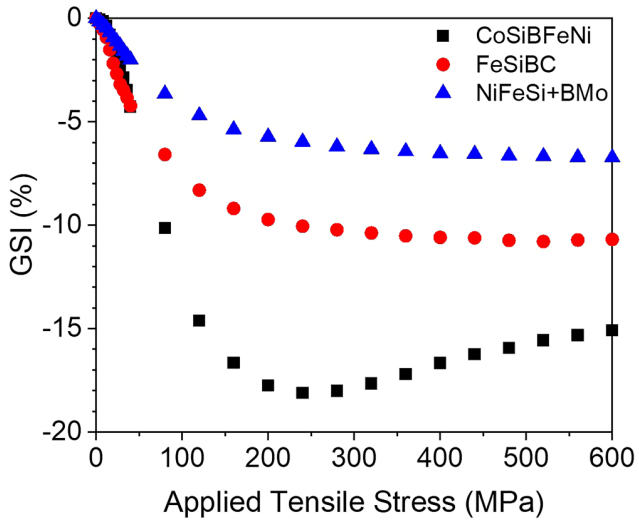

FIG. 8. Stress dependence of the GSI ratio measured for Co-rich (black squares), Fe-rich (red circles), and Ni-rich (blue triangles) ribbons. Each sample was measured from their respective critical frequency (f_0) (Co-rich sample $f_0 = 2.5$ MHz, Fe-rich and Ni-rich samples $f_0 = 1.5$ MHz).

The differences in GSI behaviors between the materials implied that the transverse permeabilities of the samples responded differently to each other as the induced magnetoelastic anisotropies combined with other anisotropic energies terms. Typically, λ_s defines the domain structure of amorphous ribbons. Previous studies have generally found that ribbon samples with negative (or near-zero) λ_s coefficient have a greater tendency toward transverse-oriented domain structures than those with positive λ_s, which translates to materials with negative (or near-zero) λ_s coefficient having higher transverse permeability than those with positive λ_s coefficients.[4,24,39,40] This clearly correlates with the data presented here, in Fig. 3 and Fig. 8, where the Co-rich samples displayed both higher peak GSI and GMI ratios than equivalent Fe- and Ni-rich ribbons. Furthermore, previous studies[40–42] have shown a correlation between the size of a material's GSI response and the strength of its anisotropy field, with lower anisotropy fields resulting in higher GSI ratios. This suggests that, in the absence of induced stress, the Co-rich sample possessed a lower anisotropic field than Fe- and Ni-rich samples. However, in general, the anisotropy field was a combination of three effects: shape anisotropy and magnetocrystalline anisotropy, which were both fixed, and magnetoelastic anisotropy, which increased as stress was induced, potentially rotating the axis and modifying the strength of the net anisotropy of the samples.[43] Both rotations of anisotropy axis and modulations of the strength of the anisotropic field would be expected to intrinsically modify the transverse permeability and may have also modified the domain structure and magnetization dynamics exhibited by the ribbons, thus resulting in second order effects that further influenced the sample's transverse susceptibility.

Further complication was added by the facts that the magnetization dynamics contributing to the transverse permeability (i.e., domain wall motion and domain rotation) were likely to be affected differently by these changes and that the balance of those mechanisms would have been different at different frequencies, with

J. Appl. Phys. **131,** 214503 (2022); doi: 10.1063/5.0088988 **131,** 214503-7

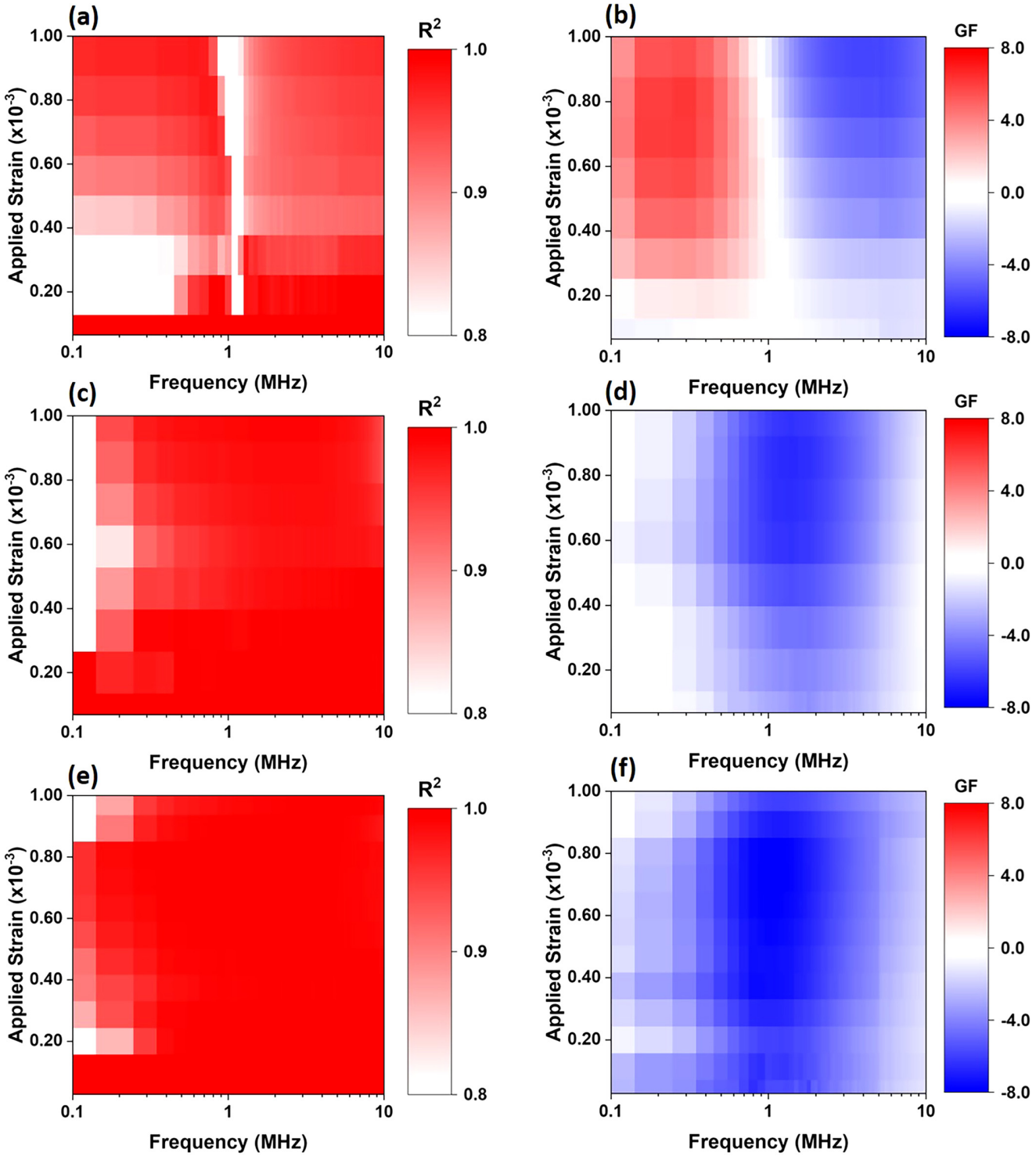

FIG. 9. Heatmaps of R^2 and gauge factors (GFs) for Co-rich ribbon [(a) and (b)], Fe-rich ribbon [(c) and (d)], and Ni-rich ribbon [(e) and (f)] for strains up to $\varepsilon = 1 \times 10^{-3}$.

J. Appl. Phys. **131,** 214503 (2022); doi: 10.1063/5.0088988

domain wall motion dominating at low frequencies and domain rotation progressively playing a more important role as frequency increased. As a result, the samples' GSI responses would not necessarily have been expected to be the same at all frequencies, potentially explaining the differing trends observed for the Co-rich sample at frequencies above and below $f = 1$ MHz. Untangling the details of these effects from our measurements is difficult, but the following is clear: For $f < 1$ MHz, the addition of small magnetoelastic anisotropies increased the transverse permeability (resulting in a positive GSI ratio) but decreased it at high stress/strains, thus resulting in the negative GSI ratios. In contrast to this, for $f > 1$ MHz frequency initial increases of stress/strain decreased the transverse permeability, while those over 200 MPa induced a modest recovery.

C. Optimization of samples strain performance

Having characterized the basic GSI characteristics of the three ribbon materials, we turned our attention to understanding how they could be best applied and optimized for strain sensing applications. Here, we split our analysis into two regimes: a low-strain regime ($\varepsilon < 1 \times 10^{-3}/\sigma < 40$ MPa) and a high-strain regime ($\varepsilon < 10 \times 10^{-3}/\sigma < 600$ MPa). We made this distinction semi-arbitrarily as it provided an interesting illustration of how different measurement tasks require different choices of material and measurement frequencies. As noted previously, we characterized a ribbons performance for any given maximum strain value within these ranges by the linearity of its response (as characterized by R^2) and the strength of the signal produced (as characterized by its GF) up to that value of the applied stimulus. These were also combined into a normalized FOM as an overall measure of applicability [Eq. (3)].

1. Low-strain sensor performance

Figure 9 presents the R^2 values and GFs as a function of frequency, for maximum strains within the low-strain regime, for all three materials. Here, the Co-rich sample exhibited a larger range of R^2 and $\Delta GSI/\Delta\varepsilon$ values than the other materials, due to the non-monotonic GSI trends at low strains discussed previously. In particular, the Co-rich sample exhibited highly non-linear behavior for strains lower than $\varepsilon = 0.4 \times 10^{-3}$ at $f < 1$ MHz, and at all strains in the frequency window $f = 0.9$–1.2 MHz. Comparing the sample's R^2 plot with its GF plot explained the low R^2 values in these regions [Figs. 9(a) and 9(b)]. The low R^2 values for $f < 1$ MHz and maximum $\varepsilon < 0.4 \times 10^{-3}$ were due to the initial lack of sensitivity to strain seen in the GF plot. Furthermore, the poor linearity seen in the 0.9–1.2 MHz range for all strain values was due to this region representing a boundary between frequencies that resulted in positive GSI ratios (highlighted red) to negative GSI ratios (highlighted blue) due to the two different non-monotonic behaviors discussed in Sec. III B.

While the Fe- and Ni-rich samples both showed poor linearity at frequencies below 0.3 MHz, they exhibited a consistently high R^2 value for all other frequencies, with linearity being particularly strong for Ni-rich ribbon [Figs. 9(e) and 9(f)]. The GF plots showed the Ni-rich sample to generally have higher GF than the Fe-rich sample, being consistently in the range −4.5% to −6%, at frequencies with peak sensitivity (0.6–2 MHz). In contrast, the GFs of the Fe-rich ribbons gradually increased from −3% to −6% in their own window of peak sensitivity (1–2 MHz), a fact that also explained these samples' slightly poorer linearity characteristics. The difference in GF values and linearity between the Ni- and Fe-rich samples was associated with the difference in their Young's modulus, E; the modulus of the Ni-rich sample was more than twice that of the Fe-rich sample. This difference caused the Ni-rich sample to exhibit a lower strain for any given stress value, thus causing its GSI to vary more rapidly with strain.

Figure 10 presents FOM data for all three samples. As expected, the Co-rich sample performed worse than the other two samples with its highest FOM being ~0.55, primarily because of the non-linearity of its response. The Fe- and Ni-rich samples both displayed higher performance, with the Ni-rich being well optimized to sense with good fidelity (FOM = 0.6–1) in the low-strain regime at around $f = 1$ MHz.

2. High-strain sensor performance

For the high stress/strain regime, all samples were subjected to a maximum tensile stress of $\sigma = 600$ MPa which translated to

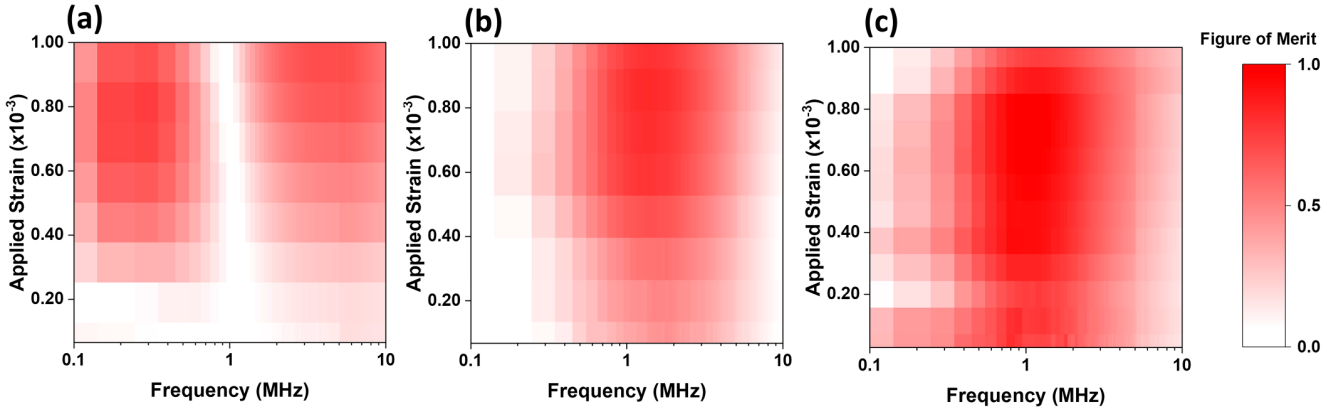

FIG. 10. Heatmap of figure of merit for (a) Co-rich, (b) Fe-rich, and (c) Ni-rich ribbons for strains up to $\varepsilon = 1 \times 10^{-3}$.

J. Appl. Phys. **131,** 214503 (2022); doi: 10.1063/5.0088988

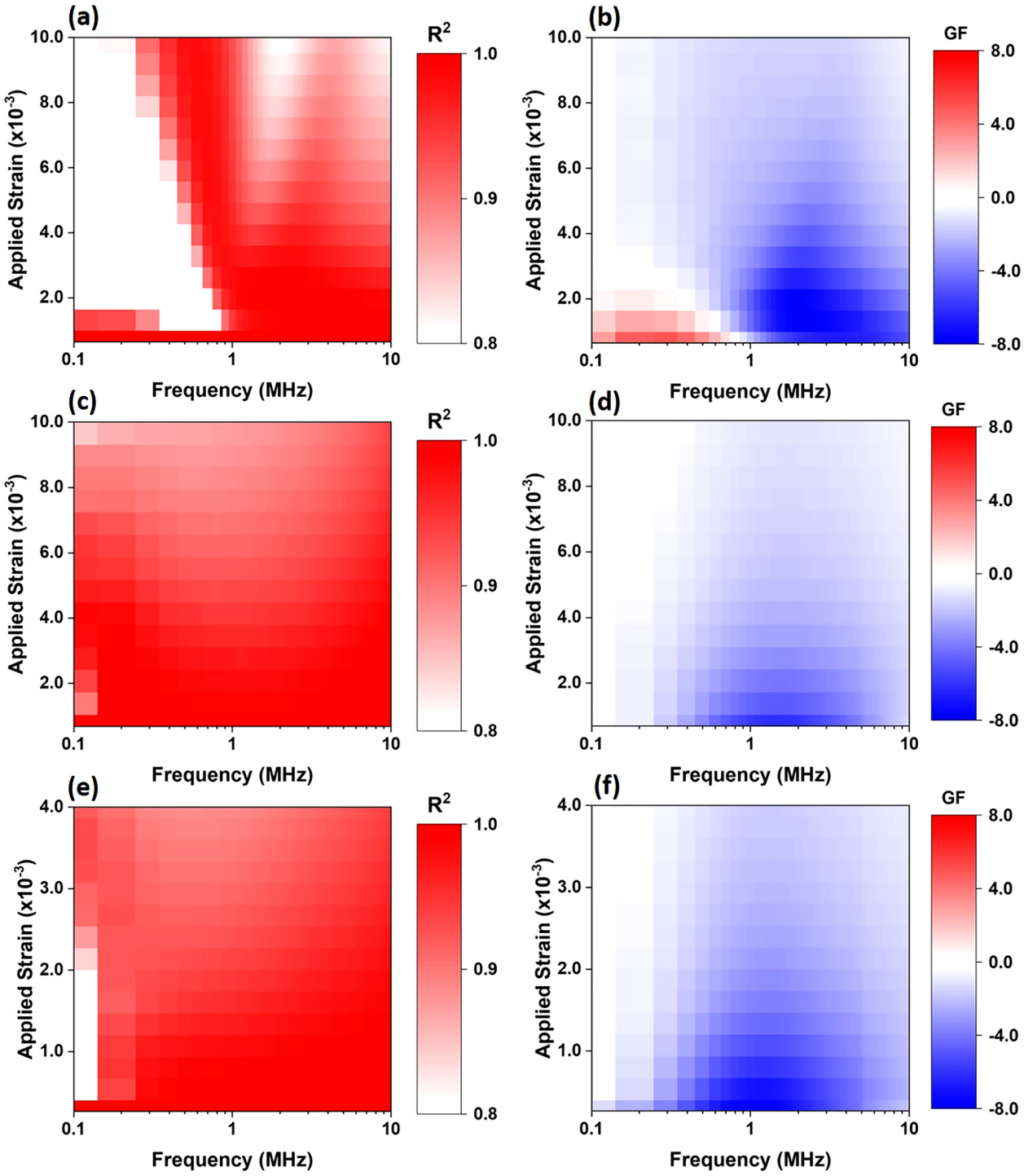

FIG. 11. Heatmaps of R^2 and gauge factors (GFs) for Co-rich ribbon [(a) and (b)], Fe-rich ribbon [(c) and (d)], and Ni-rich ribbon [(e) and (f)] for strains up to $\varepsilon = 10 \times 10^{-3}$.

J. Appl. Phys. **131,** 214503 (2022); doi: 10.1063/5.0088988

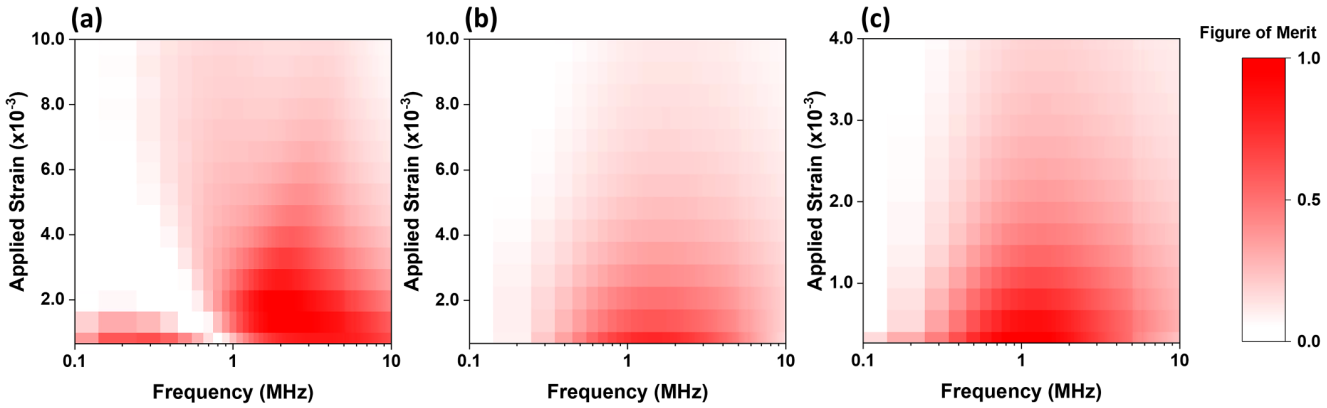

FIG. 12. Heatmap plots illustrating the figure of merit for (a) Co-rich, (b) Fe-rich, and (c) Ni-rich ribbon for strains up to $\varepsilon = 1 \times 10^{-3}$.

$\varepsilon = 10 \times 10^{-3}$ strain for Co- and Fe-rich samples due to their similar Young's moduli but a smaller strain of $\varepsilon = 4 \times 10^{-3}$ for the Ni-rich sample due to its higher Young's modulus.

Figure 11 presents the R^2 values and GFs as a function of frequency for maximum strains in the high-strain regime for all three materials. As in the low-strain regime, the Co-rich sample exhibited a larger range of R^2 values than the other two samples and was highly non-linear for $f < 1$ MHz for all values of maximum strain. This was caused by the low frequency, non-monotonic behavior discussed earlier, which can also be seen in the presence of both positive and negative in the GF plot at these frequencies. At higher frequencies, R^2 values increased and for $f > 1$ MHz, high linearity was observed up to $\varepsilon \sim 3 \times 10^{-3}$ with the material showing only negative GSI ratios. As the strain increased to values $\varepsilon > 4.0 \times 10^{-3}$, R^2 again decreased due to saturation of the GSI response and the onset of the high frequency non-monotonic behavior discussed previously. Fe- and Ni-rich samples exhibited relatively linear behaviors at low values of maximum strain but became less linear at high strains ($\varepsilon > 1.5 \times 10^{-3}$ for Fe-rich samples and $\varepsilon > 1.0 \times 10^{-3}$ for Ni-rich samples) due to the saturation of their GSI responses.

All three ribbons exhibited their greatest GF values for $f > 1$ MHz, with the Co-rich ribbon presenting the largest GFs due to its superior peak GSI ratio. Furthermore, the GFs for the Fe- and Ni-rich ribbons dropped rapidly with strain due to their larger λ_s values (and E in the case of Ni) causing saturation of their GSI response at lower strain. In contrast, for $f = 1$–3 MHz, the Co-rich sample retained high GF values up to $\varepsilon \sim 3 \times 10^{-3}$ as its lower λ_s led to a less rapid saturation of its GSI response.

Figure 12 presents FOM data for all three materials in the high-strain regime. Here, the Co-rich ribbon exhibited the best performance of all three materials, being able to detect strains up to 3×10^{-3} with good FOM, when working in the frequency range 2–3 MHz. As would be expected from the low-strain regime previously studied, the Fe-rich and Ni-rich samples initially showed good performance, but their FOM began to drop rapidly at $\varepsilon > 1 \times 10^{3}$, respectively, due to saturation of their GSI response resulting in drops in R^2, GF, and consequently FOM. None of the ribbons were able to effectively act as sensors for strain beyond $\sim 3 \times 10^{-3}$ no matter what measurement frequency was selected.

The data presented above illustrate the complexity of selecting a material for a given strain sensing application. While one might naively argue that materials with large λ_s would be preferable, as these would maximize the size of induced magnetoelastic anisotropies, or that small λ_s would be preferable as this would maximize the broadly equivalent GMI effect and, thus, a sensor's dynamic range, the reality is much more complex and nuanced with differing magnetic and mechanical properties being optimal in different measurement regimes.

IV. CONCLUSION

In this study, we have explored the differences between the GMI and GSI behaviors of ribbons composed of three commercial amorphous materials ($Co_{66}Si_{15}B_{14}Fe_4Ni_1$, $Fe_{81}B_{13}Si_{3.5}C_2$, and $Ni_{40}Fe_{40}Si + B_{19}Mo_{1-2}$) under longitudinal tensile stresses up to $\sigma = 600$ MPa, equivalent to strains up to $\varepsilon = 10 \times 10^{-3}$. We have also assessed the linearity and gauge factor of the GSI effect in these materials in order to understand how they could be optimized for different strain sensing tasks.

We observed a simple relationship between a material's peak GMI and GSI ratios and the size of their saturation magnetostriction constants (λ_s) with the smaller values of λ_s producing the largest GMI and GSI responses. This occurred because ribbons with lower λ_s were magnetically softer and so exhibit higher maximum permeabilities, and thus a larger range of impedance values. While Fe-rich and Ni-rich samples always exhibited monotonic variations of impedance with applied stimuli, the Co-rich sample exhibited a variety of non-monotonic behaviors for both its GMI and GSI responses depending on the frequency and strain applied to the ribbons. We attributed these differing responses to the gradual transition from domain wall motion-based dynamics to domain rotation as the frequency increased and suggest that these mechanisms reacted differently to the shifting balance of magnetoelastic, magnetocrystalline, and shape anisotropies as the stress/

J. Appl. Phys. **131,** 214503 (2022); doi: 10.1063/5.0088988

strain increased. Further study will be required to understand these effects in detail.

While the peak GSI ratio of the ribbons was easily understood, we observed that optimizing the response of the ribbons for strain sensing in different regimes was more complex. λ_s simultaneously determined the range of available impedances that a material could exhibit (i.e., a sensor's dynamic range), and in conjunction with the material's Young's modulus, E, the rate of their impedance changes with respect to stress/strain (i.e., sensitivity), and how quickly this saturated. These conflicting considerations meant that the optimal parameters for λ_s and E depended strongly on the range of strains to be sensed. In general, we observed that the Ni-rich ribbons, with modest λ_s with high E performed best in low-strain regimes, while Co-rich ribbons with near-zero λ_s and lower Young's modulii performed better in high-strain regimes. Fe-rich ribbons, which had the highest λ_s (and, therefore, hypothetically had the most stress sensitive magnetic properties), did not excel in either regime, but were broadly suitable for detecting low strains $\varepsilon < 1.5 \times 10^{-3}$. Our work indicates the challenge and complexity of optimizing the material properties of a GSI sensor for operation in any given stress/strain regime.

ACKNOWLEDGMENTS

The authors thank the Nuclear Decommissioning Authority (NDA) for funding this project.

AUTHOR DECLARATIONS

Conflict of Interest

The authors have no conflicts to disclose.

DATA AVAILABILITY

The data that support the findings of this study are available within the article.

REFERENCES

[1]M. Kuźmiński, K. Nesteruk, and H. K. Lachowicz, "Magnetic field meter based on giant magnetoimpedance effect," Sens. Actuators, A **141**(1), 68–75 (2008).
[2]A. F. Cobeño, A. Zhukov, J. M. Blanco, V. Larin, and J. Gonzalez, "Magnetoelastic sensor based on GMI of amorphous microwire," Sens. Actuators, A **91**(1–2), 95–98 (2001).
[3]M. Knobel, M. Vázquez, and L. Kraus, "Giant magnetoimpedance," in *Handbook of Magnetic Materials* (Elsevier, 2003), Vol. 15, pp. 497–563.
[4]M. H. Phan and H. X. Peng, "Giant magnetoimpedance materials: Fundamentals and applications," Prog. Mater. Sci. **53**(2), 323–420 (2008).
[5]V. Zhukova *et al.*, "Effect of nanocrystallization on magnetic properties and GMI effect of Fe-rich microwires," J. Electron. Mater. **43**(12), 4540–4547 (2014).
[6]H. Q. Guo, H. Kronmüller, T. Dragon, Z. H. Cheng, and B. G. Shen, "Influence of nanocrystallization on the evolution of domain patterns and the magnetoimpedance effect in amorphous $Fe_{73.5}Cu_1Nb_3Si_{13.5}B_9$ ribbons," J. Appl. Phys. **89**(1), 514–520 (2001).
[7]Z. Lotfollahi, A. García-Arribas, A. Amirabadizadeh, I. Orue, and G. V. Kurlyandskaya, "Comparative study of magnetic and magnetoimpedance properties of CoFeSiB-based amorphous ribbons of the same geometry with Mo or W additions," J. Alloys Compd. **693**, 767–776 (2017).
[8]T. Wang, Y. Zhou, C. Lei, J. Luo, S. Xie, and H. Pu, "Magnetic impedance biosensor: A review," Biosens. Bioelectron. **90**, 418–435 (2017).
[9]L. Chen *et al.*, "A prototype of giant magnetoimpedance-based biosensing system for targeted detection of gastric cancer cells," Biosens. Bioelectron. **26**(7), 3246–3253 (2011).
[10]G. V. Kurlyandskaya, M. L. Sánchez, B. Hernando, V. M. Prida, P. Gorria, and M. Tejedor, "Giant-magnetoimpedance-based sensitive element as a model for biosensors," Appl. Phys. Lett. **82**(18), 3053–3055 (2003).
[11]G. V. Kurlyandskaya, V. Fal Miyar, A. Saad, E. Asua, and J. Rodriguez, "Giant magnetoimpedance: A label-free option for surface effect monitoring," J. Appl. Phys. **101**(5), 054505 (2007).
[12]J. Torrejón, L. Kraus, K. R. Pirota, G. Badini, and M. Vázquez, "Magnetostatic coupling in soft/hard biphase magnetic systems based on amorphous alloys," J. Appl. Phys. **101**(9), 09N105 (2007).
[13]P. Corte-Leon *et al.*, "Engineering of magnetic properties and magnetoimpedance effect in Fe-rich microwires by reversible and irreversible stress-annealing anisotropy," J. Alloys Compd. **855**, 157460 (2021).
[14]F. Jin, L. Zhou, W. Cheng, Y. Zhang, B. Tong, and Y. Xu, "Effect of shape and annealing on the giant magnetoimpendence properties of FeCoSiB ribbon," IEEE Trans. Magn. **50**(10), 1–4 (2014).
[15]J. Nabias, A. Asfour, and J.-P. Yonnet, "The impact of bending stress on the performance of giant magneto-impedance (GMI) magnetic sensors," Sensors **17**(3), 640 (2017).
[16]J. J. Beato-Lopez, J. M. Algueta-Miguel, C. A. De La Cruz Blas, L. G. Santesteban, J. I. Perez-Landazabal, and C. Gomez-Polo, "GMI magnetoelastic sensor for measuring trunk diameter variations in plants," IEEE Trans. Magn. **53**(4), 1–5 (2017).
[17]L. P. Shen, T. Uchiyama, K. Mohri, E. Kita, and K. Bushida, "Sensitive stress-impedance micro sensor using amorphous magnetostrictive wire," IEEE Trans. Magn. **33**(5), 3355–3357 (1997).
[18]J. M. Blanco, A. Zhukov, and J. Gonzalez, "Effect of tensile and torsion on GMI in amorphous wire," J. Magn. Magn. Mater. **196–197**, 377–379 (1999).
[19]S. L. Zhang, J. F. Sun, D. W. Xing, F. X. Qin, and H. X. Peng, "Large GMI effect in Co-rich amorphous wire by tensile stress," J. Magn. Magn. Mater. **323**(23), 3018–3021 (2011).
[20]L. De-Ren, L. Zhi-Chao, Z. Shao-Xiong, Z. Jun-Feng, L. Hui, and H. Wei, "Giant stress-impedance effect in amorphous and high-current-density electropulsing annealed $Fe_{73.5}Cu_1Nb_3Si_{13.5}B_9$ ribbons," Chin. Phys. Lett. **19**(7), 1000 (2002).
[21]F. X. Qin, H. X. Peng, V. V. Popov, and M. H. Phan, "Giant magnetoimpedance and stress-impedance effects of microwire composites for sensing applications," Solid State Commun. **151**(4), 293–296 (2011).
[22]J. J. Beato-López, G. Vargas-Silva, J. I. Pérez-Landazábal, and C. Gómez-Polo, "Giant stress-impedance (GSI) sensor for diameter evaluation in cylindrical elements," Sens. Actuators, A **269**, 269–275 (2018).
[23]J. Hu, H. Qin, J. Chen, and Y. Zhang, "Giant stress-impedance effect in $Fe_{73.5}CuNb_{3-x}V_xSi_{13.5}B_9$ amorphous ribbons," J. Magn. Magn. Mater. **266**(3), 290–295 (2003).
[24]S. Dwevedi, G. Markandeyulu, P. R. Ohodnicki, A. Leary, and M. E. McHenry, "Stress-MI and domain studies in co-based nanocrystalline ribbons," J. Magn. Magn. Mater. **323**(15), 1929–1933 (2011).
[25]P. Pan, R. D. Moorehead, and T. J. Hayward, "Influence of geometry on the giant magnetoimpedance of high-aspect ratio amorphous magnetic ribbons," J. Appl. Phys. **128**(17), 174504 (2020).
[26]V. Raposo, J. I. Iniguez, D. Garcia, A. G. Flores, and M. Vazquez, "Internal magnetoimpedance of amorphous wires," in *Digest of INTERMAG 2003. International Magnetics Conference (Cat. No. 03CH37401)*, (2003), p. CB-05.
[27]D. García, V. Raposo, O. Montero, and J. I. Íñiguez, "Influence of magnetostriction constant on magnetoimpedance–frequency dependence," Sens. Actuators, A **129**(1–2), 227–230 (2006).
[28]C. Morón, M. T. Carracedo, J. G. Zato, and A. García, "Stress and field dependence of the giant magnetoimpedance effect in Co-rich amorphous wires," Sens. Actuators, A **106**(1–3), 217–220 (2003).

[29]See http://www.goodfellow.com/catalogue/GFCat4I.php?ewd_token=t5Hi55VEn7gmigQ8omoaE3EsYo1a6W&n=H8vrxrqtUtiolf3A3HDcEcWGNXdgOH&ewd_urlNo=GFCat4B11&Catite=CO810250&CatSearNum=5 for Cobalt/Silicon/Boron/Iron/Nickel Foil CO810250—Goodfellow Catalog (accessed 9 October 2019).
[30]See http://www.goodfellow.com/catalogue/GFCat4I.php?ewd_token=t5Hi55VEn7gmigQ8omoaE3EsYo1a6W&n=H8vrxrqtUtiolf3A3HDcEcWGNXdgOH&ewd_urlNo=GFCat4B11&Catite=FE800250&CatSearNum=5 for Iron/Boron/Silicon Foil FE800250—Goodfellow Catalog (accessed 9 October 2019).
[31]See http://www.goodfellow.com/catalogue/GFCat4I.php?ewd_token=t5Hi55VEn7gmigQ8omoaE3EsYo1a6W&n=H8vrxrqtUtiolf3A3HDcEcWGNXdgOH&ewd_urlNo=GFCat4B11&Catite=NI800250&CatSearNum=5 for Nickel/Boron/Silicon Foil NI800250—Goodfellow Catalog (accessed 9 October 2019).
[32]A. Zhukov *et al.*, "Manipulation of magnetic properties of glass-coated microwires by annealing," J. Magn. Magn. Mater. **383**, 232–236 (2015).
[33]A. Chaturvedi, T. Dhakal, S. Witanachchi, A.-T. Le, M.-H. Phan, and H. Srikanth, "Correlation between magnetic softness, sample surface and magnetoimpedance in $Co_{69}Fe_{4.5}X_{1.5}Si_{10}B_{15}$ (X = Ni, Al, Cr) amorphous ribbons," Phys. B: Condens. Matter **405**(13), 2836–2839 (2010).
[34]T. Eggers *et al.*, "Impact of the transverse magnetocrystalline anisotropy of a Co coating layer on the magnetoimpedance response of FeNi-rich nanocrystalline ribbon," J. Alloys Compd. **741**, 1105–1111 (2018).
[35]L. González-Legarreta *et al.*, "Magnetoimpedance dependence on width in Co66.5Fe3.5Si12.0B18.0 amorphous alloy ribbons," J. Appl. Phys. **113**(5), 053905 (2013).
[36]C. Zhao, X. Zhang, Q. Liu, and J. Wang, "GMI field sensitivity near a zero external field in Co-based amorphous alloy ribbons: Experiments and model," J. Phys. D: Appl. Phys. **49**(6), 065006 (2016).
[37]Y.-H. Ding, K. Xue, W.-Y. Wang, and X. Ma, "Influence of aspect ratio on giant magnetoimpedance effect for Fe67Co18Si11B4 amorphous ribbons," Acta Metall. Sin. (Engl. Lett.) **30**(12), 1236–1242 (2017).
[38]J. Hu, H. Qin, J. Chen, and Y. Zhang, "Giant stress-impedance effect in $Fe_{73.5}CuNb_{3-x}V_xSi_{13.5}B_9$ amorphous ribbons," J. Magn. Magn. Mater. **266**(3), 290–295 (2003).
[39]M. H. Phan, H. X. Peng, M. R. Wisnom, S. C. Yu, C. G. Kim, and N. H. Nghi, "Effect of annealing temperature on permeability and giant magneto-impedance of Fe-based amorphous ribbon," Sens. Actuators, A **129**(1–2), 62–65 (2006).
[40]D. Li, Z. Lu, and S. Zhou, "Induced magnetic anisotropy and stress-impedance effect in nanocrystalline $Fe_{73.5}Cu_1Nb_3Si_{13.5}B_9$ ribbons," IEEE Sens. J. **6**(4), 924–927 (2006).
[41]S. Mansourian, A. Bakhshayeshi, and R. Taghavi Mendi, "Giant magneto-impedance variation in amorphous CoFeSiB ribbons as a function of tensile stress and frequency," Phys. Lett. A **384**(26), 126657 (2020).
[42]D. R. Li, Z. C. Lu, and S. X. Zhou, "Magnetic anisotropy and stress-impedance effect in Joule heated $Fe_{73.5}Cu_1Nb_3Si_{13.5}B_9$ ribbons," J. Appl. Phys. **95**(1), 204–207 (2004).
[43]Z. Guo *et al.*, "Electric field induced non-90° rotation of the easy axis of a ferromagnetic film," Appl. Phys. Lett. **112**(5), 052904 (2018).

Chapter 8

Initial testing on a proof-of-concept for a prototype Co-rich amorphous ribbon GSI strain sensor

8.1 Outline

This chapter investigated the feasibility of using the GSI effects of amorphous magnetic ribbons for detecting distortions in ILW waste packages, by examining their behaviour under strains of similar orders of magnitude to those that would be experienced if they were attached to ILW packages in real-world conditions. The selection of the sensor material and geometry are first discussed, before the response of that sensor to strains, and the repeatability/reproducibility of this response, of are characterised. Finally, there is a discussion of other variables/factors that would need to be considered for

real-world applications.

8.2 Selection of Co-rich amorphous metal as the prototype GSI strain sensing material

In chapter 3 the criteria requirement for a strain sensor for monitoring ILW waste packages were summarised as:

- The sensor needs to detect strains of (at least) up to 0.25% strain – which means the sensor must be capable of detecting strains of at least 0.025%, per year.
- The sensor's sensitivity on detecting strains of either ∼0.025%/year or ∼0.25%/decade with a gauge factor of at least in the double digits.
- The sensor needs to be flexible enough to be attached to a curved surface of a waste package.
- Ease of access to the sensor technology should be easy to obtain such as, the technology is commercially available or can be fabricated easily. This would minimise cost and time considering the number of ILW waste packages required to be monitored are in the thousands.
- The sensor needs to be designed to cover a surface area of at least 3000 mm^2, assuming the ribbon sensor was designed with a 10 mm width and 300 mm length. The length of 300 mm is approx. length of the bottom third of the waste package in which has been reported by John Jowsey to be where deformation of either localised or global expansions initiate.

All of these criteria were to monitor a waste package which had dimensions of 1166 mm total height and 800 mm diameter (information on the waste package design were from John Jowsey, a staff member of Sellafield Ltd [1]. According to John, the deformation of localised and/or global expansions typically initiate at the bottom third of the waste package, which is the main area of interest for monitoring.

After investigating the capabilities of the GMI and GSI effect for amorphous magnetostrictive materials, such as Co-, Fe-, and Ni-rich amorphous ribbons, it was found they satisfied the majority of the criteria requirements for a GSI strain sensing technology. Chapter 3 highlighted high GF values in the double and triple digits for existing GMI and GSI effect magnetostrictive materials when measuring strains as small as 1%. This was later shown in chapter 7 where all three amorphous ribbon samples displayed GF values as high as ± 80 for strains up to 10×10^{-3}. Chapter 6 identified the material behaviour can retain its GMI behaviour if the material's aspect ratio was 20 or over, with ribbon lengths over 200 mm. This showed promise in the potential application of high-aspect ratio ribbons since it showed the material can cover large surface areas at the highest sensing performance as long the aspect ratio is over 20. Moreover, the chapter identified the Co-rich ribbon sample to have the best GMI performance out of the samples due to its low λ_S value. However, a low λ_S was considered unfavourable for a strain sensing magnetic material since it defines the material's capability of detecting stress. This was not the case when investigating the GSI performance for all three amorphous ribbons (in chapter 7) with the Co-rich ribbon, objectively, having the best GMI and GSI responses, strain detection, and sensitivity out of the rest of the ribbon samples (Fig. 8.1). At this stage of the project, the Co-rich ribbon sample satisfied majority of the criteria, excluding the second bullet point where there was no time to investigate the influence of irradiation to the magnetic and mechanical behaviour of an amorphous metal.

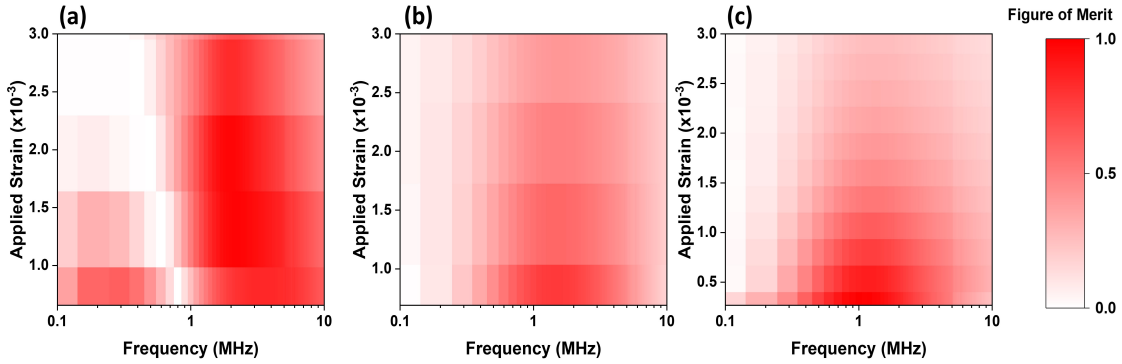

Figure 8.1: Heatmap plots illustrating the figure of merit (FOM) of GSI response with respect to strain for (a) Co-rich, (b) Fe-rich, and (c) Ni-rich ribbon samples. All were measured with a common frequency range between 0 - 10 MHz. The data was adpated from ref. [255] to illustrate the sensor performance for each material up to 2.5×10^{-3} (0.25%) strain.

Figure 8.1 displays the figure of merit (FOM) values for all three amorphous ribbons in which is defined by Eq. 7.3, thus illustrating the GSI sensing performance for all three materials. This quantitatively demonstrates the Co-rich ribbon having the highest sensing performance where at frequencies between 1 to 3 MHz the FOM values are close to 1 for all strains up to 2.5×10^{-3}. The remaining ribbons display the highest FOM around 0.8 to 2 MHz range at strains as high as 1.0×10^{-3} in which Fe-rich ribbon displays the highest FOM value of around 0.5 and Ni-rich ribbon with a FOM value of around 1. Hence, the Co-rich material was considered the best candidate as a prototype GSI strain sensor and was selected for this chapter.

8.3 Methodology

The ends of the Co-rich ribbon were clamped to the manual tensile test machine as shown in Fig. 4.16. No weights were applied on top of the ribbon since, in a realistic scenario, the sensor applied on top of the waste package surface would be open to the environment. Tensile forces were manually applied to the ribbon and monitored by the force gauge (with a precision of 0.05 N. The force gauge was zeroed at the 0 N mark as described in chapter 4, section 4.4 to ensure no strain was initially applied. Tensile stresses of up to 480 MPa were applied to the sample with 8 MPa increments between 0 – 200 MPa and 40 MPa increments between 200 – 480 MPa. The resulting strain of the sample was then calculated using Young's modulus (E) of the sample (61 GPa [256]) using the formula:

$$\varepsilon = \frac{\sigma}{E} \tag{8.1}$$

This resulted in strains up to a maximum of 0.79% being applied.

To measure the ribbons impedance, the impedance analyser's adaptor was calibrated using a PHASE and LOAD compensation, and the test fixture (i.e. BNC to crocodile clip test leads) was calibrated using an OPEN, SHORT and LOAD compensation. The impedance ($|Z|$) of the sample was measured between frequencies of 0.1 – 10 MHz at every increment of the tensile force applied. At each applied force the ribbons impedance was measured 5 times, with the crocodile clips being detached and reattached to the sample between each sample. This was done to mimic a realistic scenario of monitoring the expansion of a waste package over time, where continuous connection to a sample was unlikely to be possible.

8.4 Initial performance of the prototype strain sensor

The efficacy of the sensor's performance was determined by its linearity (R^2), sensitivity (GF), and the product lifetime, all with respect to strain (ε). The linearity and sensitivity have the same definition as stated in chapter 7 whereas the sensor's lifetime is dependent on the strain of the material. This is assuming John Jowsey's (and other members of Sellafield Ltd) observations and estimations on the change in the waste package size are valid. Assuming this to be the case, then it can be used as a parameter to estimate the product lifetime of a Co-rich GSI strain sensor with the basic unit of every 0.25% strain being equivalent to 10 a year lifetime. Hence, if the strain sensor can reach strains higher than 0.25% it can potentially have a lifetime longer than 10 years. In this case, the strain of the Co-rich ribbon sample was measured to be 0.79% which provided an estimated lifetime of nearly ∼32 years (Fig. 8.3(b)). However, this estimated lifetime would only be beneficial if any noticeable signal changes were observed at strains higher than 0.25% (i.e., the linearity and sensitivity parameters). Another parameter that was important was the strain sensor's capability of differentiating between two different states of the waste package: no expansion and with expansion. This was analysed using a signal-to-noise ratio (SNR) with respect to strain.

The sensor's behaviour was analysed in two strain regimes, up to ∼0.26% and up to ∼0.79%. The regime up to 0.26% strain was based on information from Sellafield Ltd [2], who estimated the expansion of the circumference of a waste package could result in strains ∼0.25% per decade. Whereas, 0.79% strain was the maximum strain applied to the ribbon sample. These two strains were selected based on the timescales for monitoring an expanding nuclear waste package to be in several decades, thus it was used as a rough es-

timate of the lifetime of the strain sensor. As the sensitivity of the GSI strain sensor was dependent on the frequency of the AC current. The variation of the sensors R^2 and GF values was characterised as a function frequency, at strains of 0.25% and 0.79% (Fig. 8.2).

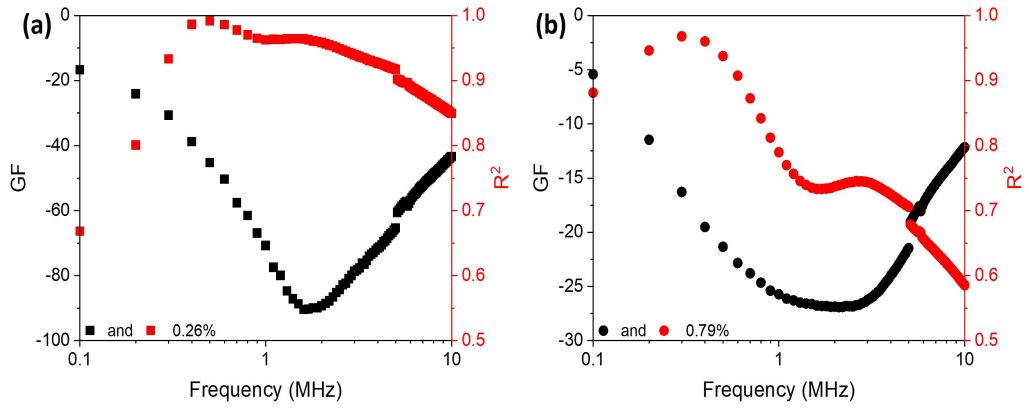

Figure 8.2: Frequency dependence to the GF value and R^2 value of the ribbon sample at (a) 0.26% and (b) 0.79% strains.

Figure. 8.2 illustrates a trade-off between linearity and sensitivity as the frequency increased. This was especially apparent for 0.79% strain where R^2 drastically dropped at ∼0.4 MHz, despite further increases in GF being observed beyond this point. As frequency increased further, the sensor's sensitivity decreased as visible in the sharp decrease in the GF value at ∼2 MHz for both strains. The data indicated the sensor was capable of detecting strains up to 0.26% with high linearity (∼0.96, at 0.5 MHz) and at high sensitivity (∼-86, at 1.6 MHz), but at higher strains, there was a trade-off between linearity and sensitivity. Therefore, the sensor could potentially detect higher strains with good linearity if lower sensitivity could be tolerated. For example, at 0.3 MHz frequency a R^2 value of ∼0.96 and a GF value of ∼-17 are obtained for 0.79% strain.

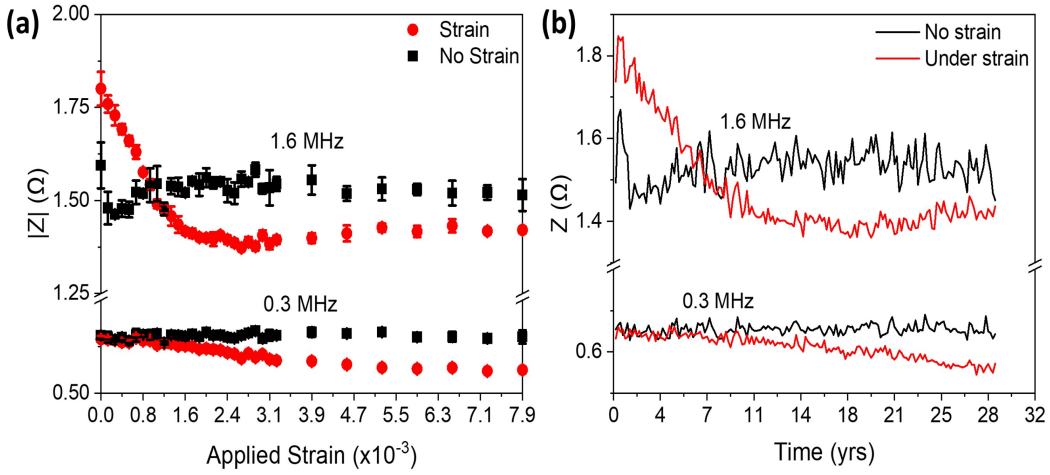

Figure 8.3: Impedance changes at frequencies 0.3 MHz and 1.6 MHz for when under strain (0.26% and 0.79% strains) and absence of strain with respect to (a) applied strain and (b) estimated lifetime based on the rate of 0.25% per decade.

Figure 8.3(a) illustrates the variation of average impedance (across the five repeat measurements) as a function of strain for frequencies of 0.3 MHz and 1.6 MHz. These frequencies represented regimes in which the sensor could measure large strains with high linearity, but with lower sensitivity (0.3 MHz) and smaller strains, but with high sensitivity (1.6 MHz) respectively. Figure 8.3(b) presents the individual impedance measurements with a pseudo-time axis created by assuming the strain changes by a rate of 0.25% every decade. Measurements at 1.6 MHz offered good sensitivity and strong linearity up to strains ∼0.16%, which translated to timescales of the order of a decade. However, beyond the GSI response began to saturate, reducing sensitivity and linearity with additional strain. On the other hand, the measurements at 0.3 MHz showed a relatively linear trend across the full 0.79% strain range (equivalent timescale ∼28 years), but with greatly reduced sen-

sitivity, which made it difficult to discern a noticeable signal difference for the no strain waste package for the initial ∼0.16% strain, which could mean unreliable measurements for the initial ∼7 years of sensor life.

Furthermore, the noise of the no-strain sample was noticeably larger for both frequencies which causes means it may be difficult to differentiate the data when the sample begins to strain. The noise observed across the repeated measurements as a function of strain was (Fig. 8.4) using a signal-to-noise ratio (SNR) with the formula:

$$SNR = \frac{S(\varepsilon)}{N(\varepsilon)} \tag{8.2}$$

where the S is the signal and N is the noise. The signal represents the average measured impedance for all five repeated measurements, at a particular strain, with the noise being the deviation from the average impedance with each measurement. The signal was obtained using multiple steps. Initially, the difference between the measured impedance of strain and no strain was calculated for each repeated measurement at all strains. This was labelled as the reference impedance (Z_{ref}),

$$Z_{ref}(\varepsilon) = Z_S(\varepsilon) - Z_{NS}(\varepsilon) \tag{8.3}$$

where $Z_{S/NS}$ represent the measured impedance when under strain or absence of strain. Afterwards, the difference of the reference impedance δZ_{ref} was calculated by subtracting the reference impedance at ε from the reference impedance at 0,

$$\delta Z_{ref}(\varepsilon) = Z_{ref,\varepsilon} - Z_{ref,0} \tag{8.4}$$

resulting in five $\delta Z_{ref}(\varepsilon)$ values at all strains for all repeated measure-

ments. The signal was the average of all five values, $\overline{\delta Z_{ref}}$. The noise was calculated using the standard deviation (σ_{SD}) formula:

$$\sigma_{SD} = \sqrt{\frac{1}{N}\sum_{\varepsilon}^{N}(\delta Z_{ref,\varepsilon} - \overline{\delta Z_{ref}})^2} \tag{8.5}$$

where N is the number of repeated measurements which is 5. Plotting $\overline{\delta Z_{ref}}$ against ε should represent the "actual" signal detected when the ribbon is under strain with the error bars representing the reliability of the measurement (Fig. 8.4).

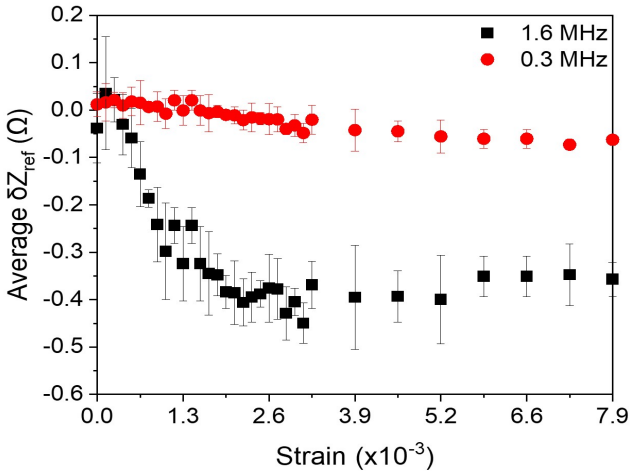

Figure 8.4: The average δZ_{ref} with applied strain for 0.3 MHz and 1.6 MHz frequencies.

The SNR ratio for both frequencies is calculated and plotted with strain, as shown in Fig. 8.5.

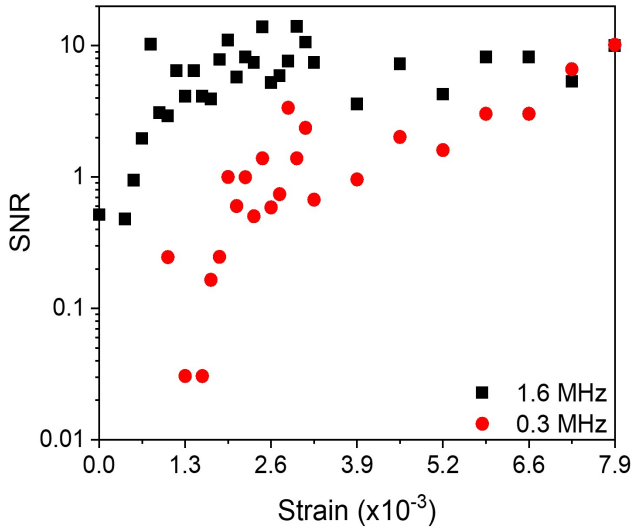

Figure 8.5: SNR ratio with increasing strain for 0.3 MHz and 1.6 MHz frequencies.

Fig. 8.5 illustrates the strong signal detection for strains under $\sim 3 \times 10^{-3}$ (0.3%) followed by a flat line with no change in signal at higher strains due to the saturation of the GSI effect. However, at higher strains, the 0.3 MHz frequency displays a continuous linear increase in signal with a comparable SNR ratio to the 1.6 MHz. This suggests the Co-rich GSI strain sensor can be capable of detecting strains higher than the minimum requirement of 0.25% to 0.79% strain by switching the operating frequency at ~0.3% strain.

This shows the prototype GSI strain sensor is capable of monitoring expanding ILW waste packages with strains larger than 0.25% by switching the operating frequency from 1.6 MHz to 0.3 MHz, without losing much of its sensing performance. In addition, it can be estimated the lifetime of the GSI strain sensor can operate as long as (at most) ~30 years.

8.5 Other variables that may affect the performance of a GSI strain sensor

Although we have provided a proof of concept that high-aspect ratio amorphous ribbons could be used as flexible strain sensors to monitor nuclear waste package(s) there are still some obstacles before real-world application. Firstly, there are strict guidelines within the nuclear waste industry about placing additional material on top of an existing nuclear waste package. While, a sensor could be bonded to the outside of a package, or integrated within it, either of these approaches would require careful evaluation to ensure that they did not compromise the integrity of the packages in any way. Thus, it is difficult to make more precise estimations of the strains a sensor would experience during package expansion. Depending on the final shape of the material a different set of simulations and experiments would be required to observe any effects on its strain sensor performance. Secondly, other external variables (that are time-dependent) could influence the material's magnetic behaviour thus influencing its sensor performance These time-dependent variables include:

- Radiation from the nuclear waste package (typically beta radiation) [257, 46, 258].
- Environmental influences on the sensor material (i.e. moisture in the air) [259, 151, 46].
- Creep behaviour of the sensor material when under constant strain (relaxation of the strain of the sensor material leading to a GMI aftereffect [260]).

Thirdly, the operability of the strain sensor has yet to be investigated but

it is heavily dependent on the methodology of monitoring the strain of the magnetic sensor. There are two methods in which the strain of the magnetic sensor can be monitored; i) self-sustained or ii) aided by external means.

The first method assumes that the sensor is self-sufficient and can operate without any external influences and can broadcast the measured data wirelessly over the life-expectancy of the sensor. This has a major hurdle where any electronic design integrated into the sensor [261] would need to consider the size and weight of the electronics in order to have ease of access and usage when monitoring the expansion of ILW waste packages - possibly requiring a power supply if the energy harnessing cannot provide a large enough energy footprint. Moreover, the specification for the electronics could be demanding and expensive considering it requires; a power source, RF electronics capable of supplying MHz frequency currents and accurately measuring impedance at these same frequencies; and circuitry (that may contain components similar to an Arduino) that would enable the device to automatically measure the change in impedance on a daily basis and wirelessly sending the data to a database that stores the information. On top of all the above, all the electronics will need to be sufficiently shielded from potential irradiation from the ILW waste package to prevent any errors or faults in the device. However, when the electronics are successfully implemented to the sensor the parasitic impedance can then easily be calibrated which would improve the signal-to-noise ratio and as a result the sensor's performance. In this chapter, the method involved using clip contacts to physically attach on and off the sample to measure the impedance which may have lowered the sensor performance due to the inclusion of parasitic impedance.

The second method assumes that the monitoring on ILW waste packages is a multi-step process where the sensor is measured via external connection (e.g. robotic arm/ probe etc). Here, the sensor would not require any elec-

tronic devices and could be a simple magnetic strip which is securely mounted on the desired region of the ILW waste package. The complicated electronics can be placed on a separate unit which has the capability to minimise the damage to the electronics from the irradiated environment by moving away from the waste package. This possibility grants fewer considerations for the design of the sensor and only concerns the time dependent variables, mentioned before, influencing its sensor performance. However, this method sacrifices ease of access to the magnetic sensor since it requires another device to monitor the sensor and will have to be done for every single waste package. Furthermore, if this method cannot reliably reproduce the same/ similar measurements from the connection between the external source and the sensor material will produce a greater error, as we have battled throughout this project.

8.6 Summary

This chapter presents proof-of-concept that the GSI response of high-aspect ratio amorphous ribbons could be used as a strain sensor to monitor swelling in intermediate level nuclear waste packages. The prototype sensor presented a measurable decrease in impedance when subjected to strains, comparable to those expected of the surface of an ILW waste package, and the response was clearly different from measurements of the same material in the absence of strain. Therefore, this indicated a possible detection method to (at least) identify the progressive global expansion of nuclear waste package from start (little to no expansion) to end (a strain of $\sim$0.26%) at the waste package surface over a timescale of (approximately) a decade. It has also demonstrated the possibility of monitoring strains higher than 0.26% by switching the operating frequency with little impact on its performance, thus extend-

ing the operating timescale by a factor of three. This shows good promise in the application of a GSI magnetostrictive sensor for monitoring ILW waste packages (and similarly large applications).

However, a number of challenges remain to be implemented to realise such a sensor, which includes understanding how such a sensor could be integrated with the waste package, the detection electronics that would be required for monitoring large numbers of waste packages, and whether the changes observed over relatively short timescales (∼minutes-to-hours) in the well-controlled environment of a laboratory could be genuinely observable over the much longer periods of time ILW waste packages need to be monitored (years-to-decades), and under less ideal conditions.

Chapter 9

Conclusion

In this thesis, the giant magnetoimpedance (GMI) and giant stress impedance (GSI) behaviours of three amorphous metals; $Co_{66}Si_{15}B_{14}Fe_4Ni_1$ (Co-rich), $Fe_{81}Si_{13.5}B_{13}C_2$ (Fe-rich) and $Ni_{40}Fe_{40}Si+B_{19}Mo_{1\text{-}2}$ (Ni-rich) have been studied to understand their suitability for use as sensors for monitoring swelling in intermediate level waste canisters. These results have provided both a general understanding of the GMI and GSI behaviour of these materials and demonstrated proof-of-concept that a ribbon sensor technology using the GSI effect could be used to monitor the rate of swelling of ILW waste.

Chapter 3 explored the state-of-the-art, smart material, flexible strain sensors with strains as high as 18,100%. The flexible strain sensors were categorised by the flexible material used for their compliant nature which were; polymer-based, elastomer-based, hydrogel-based, textile-based, paper-based, carbon-based, and magnetostrictive/magnetoelastic. Each strain sensor was investigated against the criteria that outline the desirable traits of a strain sensor monitoring ILW waste packages. In the end, four strain technologies were considered to be the best candidate for the application

which were; GWF/PDMS, rGO/PDMS, graphite/paper, and cobalt-based alloy smart materials. The cobalt-based alloy (and magnetostrictive materials as a whole) was selected as an interest of study because of its potential strain sensing capabilities that can achieve gauge factors (GF) values in the triple digits (if the conservative estimates were valid). Further investigation on magnetostrictive strain sensors identified the best magnetoelectric effect to monitor the rate of expansion was the GSI effect. To identify the physical variables that could affect the GSI performance of the GSI strain sensor a literature review was conducted, but due to the lack of extensive research on the GSI effect we also looked at the literature on the GMI effect – since the GMI effect has close parallels to the GSI effect. The variables identified that affect the GSI performance of amorphous material was; the driving frequency, magnetostriction coefficient, fabrication process, aspect ratio, and applied tensile stress/strain. Most of the variables were investigated on the studied samples in later chapters.

Chapter 6 investigated the design specification for ribbon-shaped amorphous metals by observing the influence of chemical structure, aspect ratio and heat treatment on their GMI properties. It was observed that the Co-rich sample exhibited a higher GMI response, up to $\sim$70%, compared to Fe- and Ni-rich samples with a GMI ratio of $\sim$15% and $\sim$13%, respectively. This was associated with the difference in the λ_S values between them where near-zero (or negative) λ_S would always exhibit a higher GMI ratio compared to the positive λ_S which correlates to the existing literature. Furthermore, all samples exhibited a peak GMI response with an increasing aspect ratio illustrating the influence of the manufacturing process on the GMI responses of the ribbons. This provided significant insight that with minimal damage to the edge profiles – minimising the influence of the edge effects – of the amorphous ribbons it was possible to retain and maintain strong GMI ratios at high aspect ratios (observed to be an aspect ratio of 20 and higher for

all three amorphous samples). Furthermore, heat-treating amorphous metals (between 450 K - 700 K at times up to 30 minutes) that were cut into a ribbon shape would not improve/recover the GMI properties of the amorphous metal because the manufacturing process creates physical permanent defects on the amorphous metal. The presence of permanent defects suppresses the GMI behaviour of the amorphous metal thus reducing the effects of heat treating the amorphous metal to a small degree. As a result, for a ribbon ferromagnetic sensor to be at its best performance the λ_S value has to be near-zero (or negative), the aspect ratio of 20 or higher and any permanent defects have to be avoided or minimised when patterning the sensing material.

Chapter 7 investigated the GSI strain performance of the three samples to probe their capabilities of detecting the rate of expansion of ILW waste packages, by applying a stress/strain on the sensing material, with an aspect ratio of 20 (following from chapter 6 on the design specification for the best sensor performance). Initially, the influence of applied stress/strain on the amorphous metal's GMI behaviour was observed, and it was observed that amorphous metals' impedances decreased with increasing applied stress/strain. This led to another observation, that the rate of GMI decrease with strain was higher in Fe-rich and Ni-rich samples compared to Co-rich samples. This suggested that positive λ_S were better at detecting small changes of stress/strain, but Fe- and Ni-rich ribbon samples have a much lower available GMI ratio than the Co-rich ribbon sample (with a negative λ_S) with GSI ratio values of $\sim$-10% and $\sim$-5%, respectively. Hence, such a sensor could not be applied well for the detection of higher stresses/strains. This correlated with their GSI behaviour where the Co-rich sample displayed the greatest GSI response magnitude of $\sim$-20%. There was evidence of differing GSI behaviours between the amorphous metals depending on their λ_S value and its relation to the anisotropy field. This was observed when the

Co-rich sample displayed a non-monotonic GSI response whereas Fe- and Ni-rich samples displayed purely monotonic responses. Nevertheless, when comparing the sensor performance between the three amorphous metals it was evident that a near-zero (or negative) λ_S material was better at detecting strains in the regimes expected to be present at the surfaces of ILW canisters.

As a result, from the results of chapters 6 and 7, it was determined that the best material for use as a strain sensor for ILW canisters was the Co-rich ribbon sample with its near-zero λ_S with an aspect ratio of 20 or over, and with minimal or no permanent defects present. In chapter 8, the sample was then tested under stresses/strains that were equivalent to the observed swelling expected in ILW waste packages. In chapter 7, the Co-rich sample displayed two modes of detecting changes of strain depending on the frequency used; 1.6 MHz for the highest sensitivity and 0.3 MHz for the linear sensitivity. The impedance response at both frequencies displayed two different trends with 1.6 MHz displaying a sharp decrease in signal until reaching a flat line with increasing strain whereas 0.3 MHz was a decreasing linear trend with increasing strain. Both trends were compared to the same sample at the same frequencies with the absence of strain with 1.6 MHz clearly defining two different trends with the 0.3 MHz showing similar trends until it diverges at higher strains. SNR analysis was conducted to identify the signal difference between strained and unstrained samples at both frequencies for all strains. The SNR analysis illustrated that 1.6 MHz had a strong distinct signal difference between the unstrained and strained sample of an SNR value $\sim$10 a magnitude higher than 0.3 MHz with an SNR value $\sim$1 at the same strain of $2.6\times^{1}0-3$. This suggests the Co-rich sample performs best at 1.6 MHz in which it will be capable to detect strains as low as $\sim 0.7\times 10^{-3}$. However, at higher strains, 0.3 MHz has been shown to display signals comparable to 1.6 MHz where at the maximum applied strain $7.9\times^{1}0-3$ the SNR value was at

$\sim$10. At this point in time, it provided a proof-of-concept that a GSI strain sensor was basically feasible for monitoring an ILW nuclear waste package.

In summary, this thesis has provided evidence that high aspect ratio amorphous magnetic ribbons could be used as GSI strain sensors for detecting the (global) expansion of ILW waste packages. However, there are numerous challenges remaining in order for a practical realisation of such a sensor to come to fruition. Chapter 8 discussed some of the challenges that needed to be investigated on the sensor to reach a practical stage, such as beta radiation from the waste package, environmental influences, and creep behaviour, but are considered for research in the near future. For research in the long-term other variables to research outside of the sensor could be:

- Low power electronics – that the sensor can remain operational for long periods of time (expected for months to years).
- Wireless communication technologies – to accurately measure and record the change of impedance from the sensor with as little data loss as possible.
- Energy harvesting methods – the power source of the electronic sensor device where it could operate without being dependent on an AC power source.
- Mounting methods – methods to reliably and safely mount the sensor technology without violating the strict regulations on the ILW waste packages.
- Investigating the metallic properties of an amorphous metal in an irradiating environment for long periods of time – this is a key parameter that was briefly discussed in chapter 8 where the metallic behaviour

could change at long periods of time (such as creep). However, researching the relationship between all metallic behaviour (i.e. thermal, electrical and mechanical) with respect to time and irradiation would provide crucial insight on the realistic nature of a functioning strain sensor for an extreme environment.

- Bending angle of an amorphous metal to its GSI performance – this study only investigated a linear deformation of applied strains that were comparable to observations to ILW waste packages. However, a more accurate simulation of various bending angles may provide insight how the GSI performance of the material may behave.

- Robotic drone – Using a robotic drone equipped with the sensor technology that can apply and measure the sensor technology (with other complex functions).

- Composite material – embedding the magnetic material inside a matrix that is capable of resisting the extreme environment whilst sensing the expansion of the ILW waste packages.

Appendix

Appendix A

LabVIEW virtual instrument (VI) design to characterise the GMI effect of samples

This section contains the details of the LabVIEW VI designs for operating the KEPCO power supply and the Agilent 4294A precision impedance analyser.

Fig. A.1 shows a part of the larger design of the VI where it contains the functions of controlling the settings of the impedance analyser, including; PHASE, LOAD, OPEN, SHORT compensations for adapter and coaxial cable; the minimum and maximum frequency settings and changing the measuring unit (e.g. impedance, phase angle, resistance etc.).

Fig. A.2 displays the functions required to operate the impedance analyser to measure the change of impedance of the sample. It involves controlling the; sweep of the frequency, the number of times of sweeping the frequency, the start/stop measuring frequency, the steps within a frequency sweep, trigger function (starts the measurement), and a data transfer to the computer interface, shown in Appendix A.6.

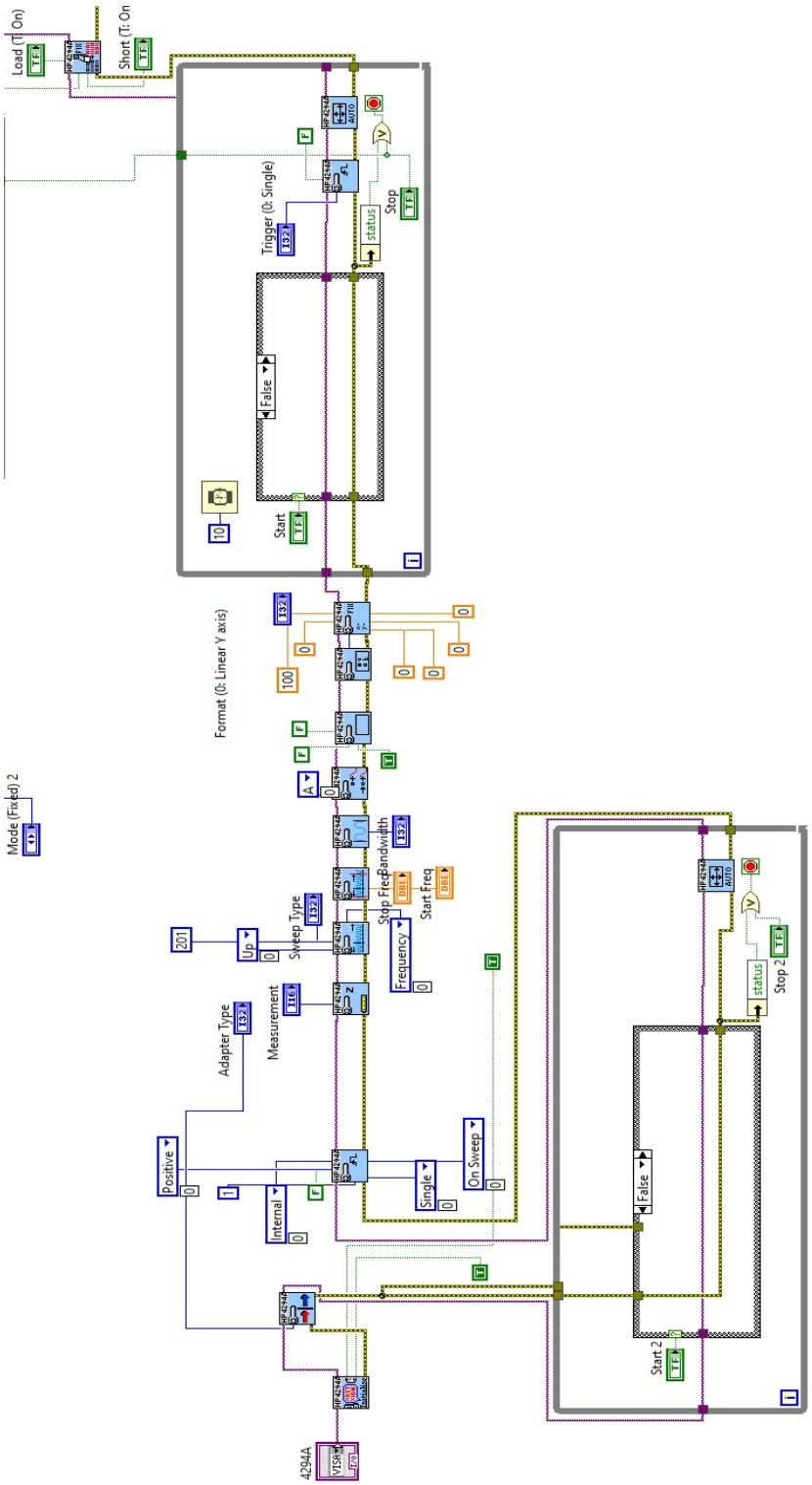

Figure A.1: LabVIEW VI design for operating the Agilent 4294A Impedance Analyser.

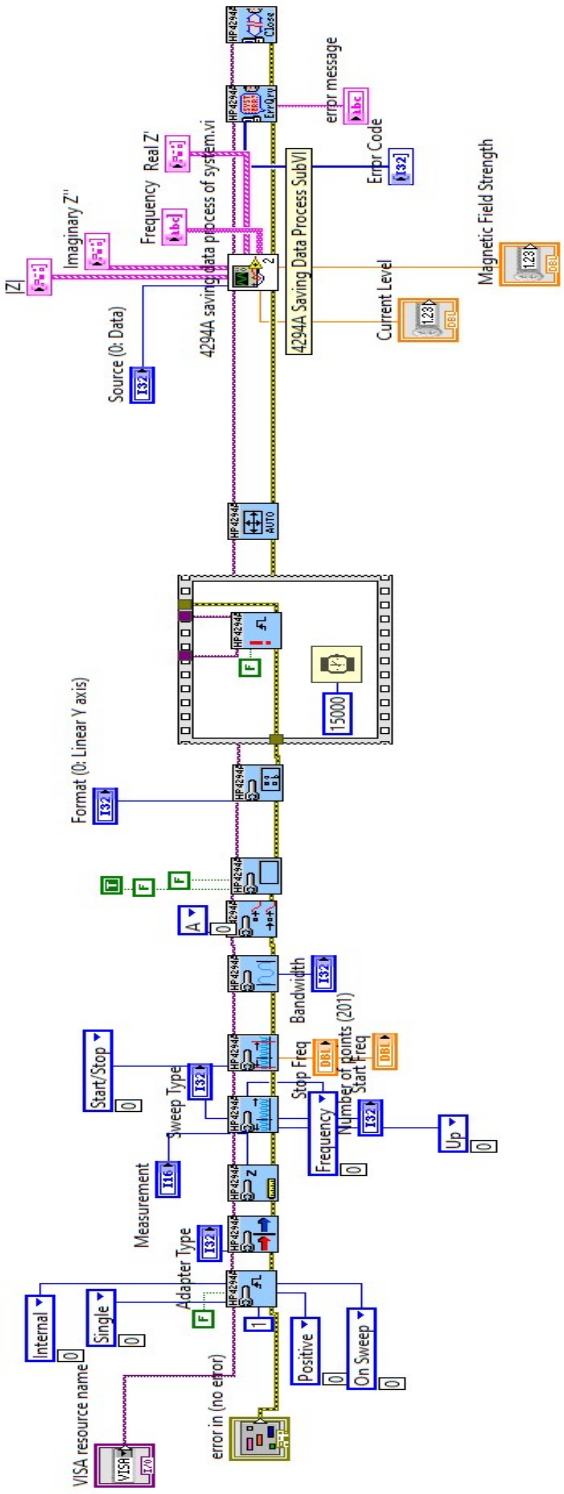

Figure A.2: LabVIEW VI design for measuring the impedance of the sample.

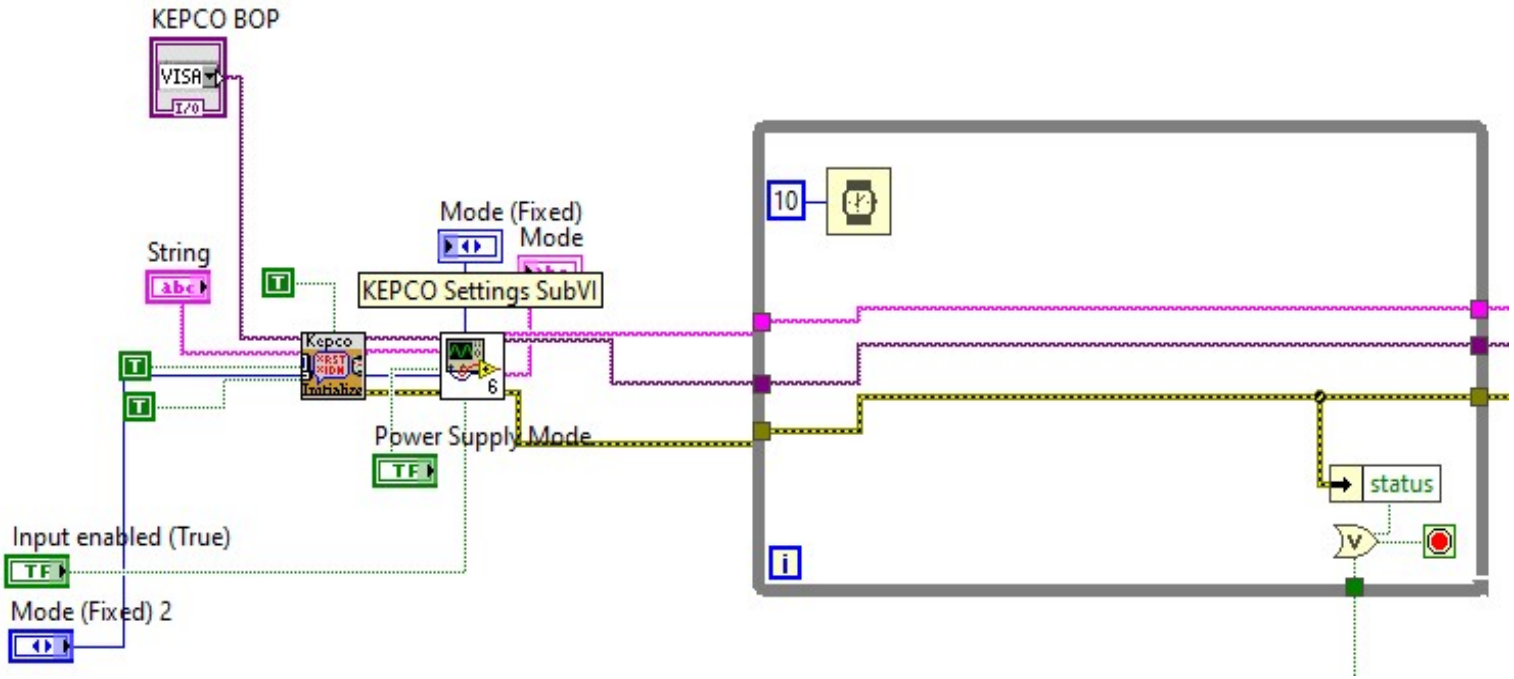

Figure A.3: LabVIEW VI design for operating the KEPCO power supply.

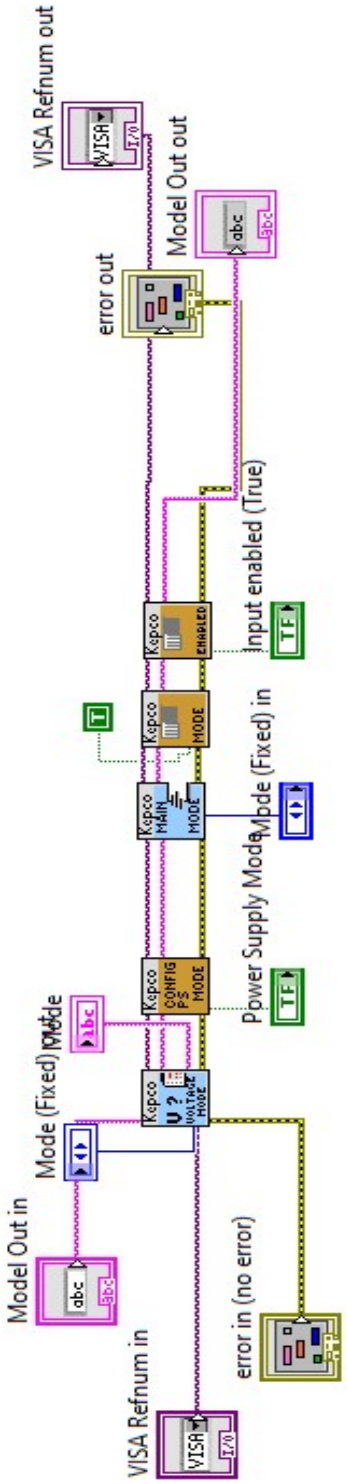

Figure A.4: LabVIEW VI design for the settings of the KEPCO power supply.

Fig. A.3 shows the KEPCO section of the LabVIEW VI design with Fig. A.4 showing the KEPCO parameters that can be controlled using LabVIEW. These functions of controlling the KEPCO power supply, includes; current/ voltage modes and the magnitude and limit for both parameters.

Fig. A.5 shows a part of the larger design of the VI where it contains the functions of sweeping the field and frequency (Fig. A.2). The loop box controls the steps for the magnetic field sweep with the "Voltage Input" function (manually) inputting the desired magnetic field strength, based on the magnitude of the voltage. Since voltage and current are linear (following Ohm's law) the higher the voltage the higher the current and this increases the magnetic field strength of the solenoid/ Helmholtz Coil. It operates by initially setting a magnetic field strength and stabilising it by "waiting" for a period of time - in this case it was 3000 milliseconds. After stabilising the magnetic field strength a frequency sweep is placed through the sample and the impedance analyser measures the impedance of the sample between the desired frequency range. Once it has finished measuring it sends the data to a computer interface (Fig. A.6) as a .DAT file. Then it moves onto the next magnetic field strength, from the voltage input boolean array, and repeats the cycle again.

Fig. A.6 shows the process of transferring and saving the data to the computer interface. It sorts the measured data into an array of measured frequency, absolute impedance $|Z|$, real part of the impedance R, and imaginary part of the impedance X. In addition, it contains the measured magnetic field strength and magnitude of the current for the electromagnet with the material's name and material property measured (e.g. GMI).

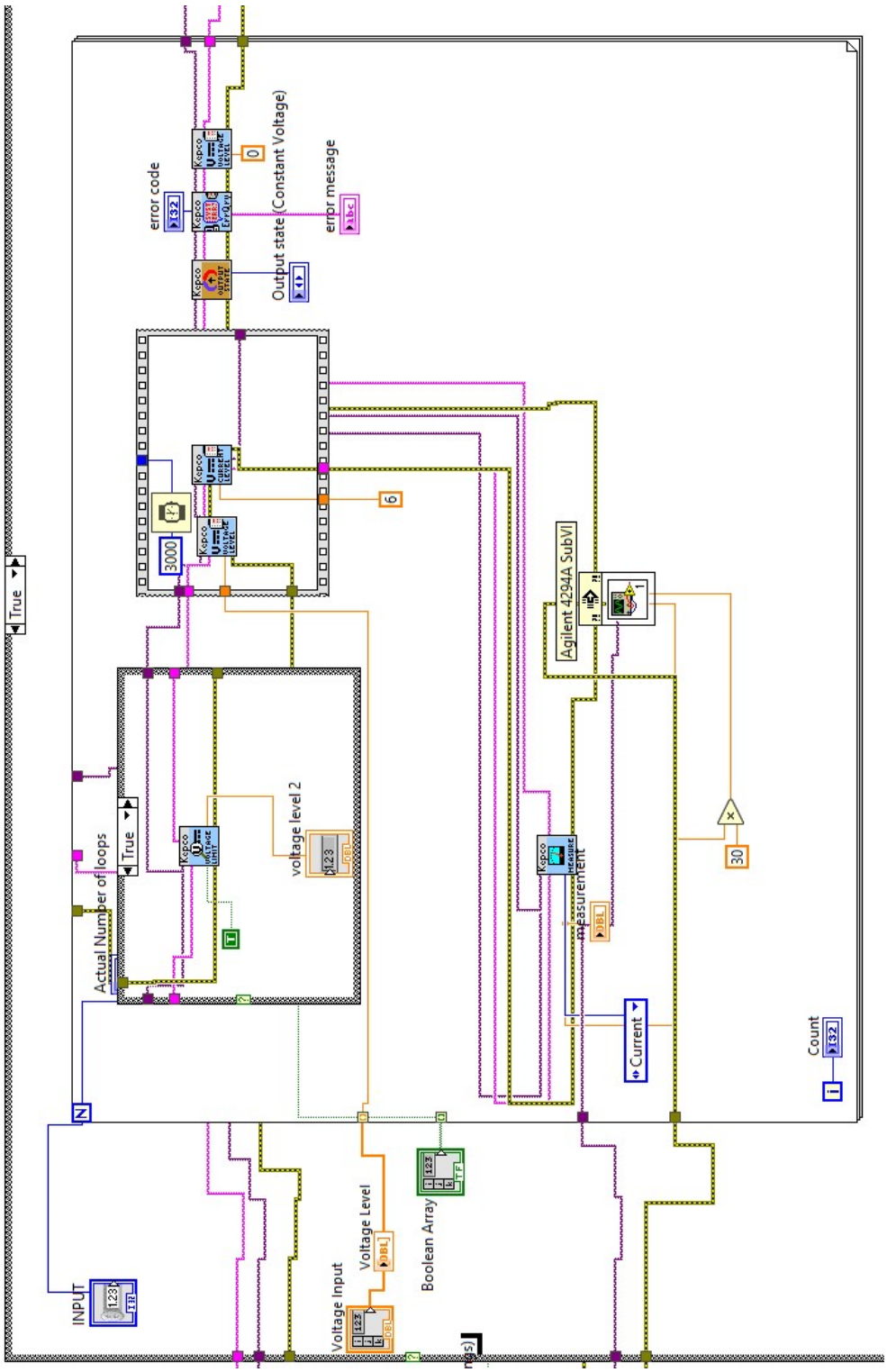

Figure A.5: LabVIEW VI design for measuring the change in impedance of a sample.

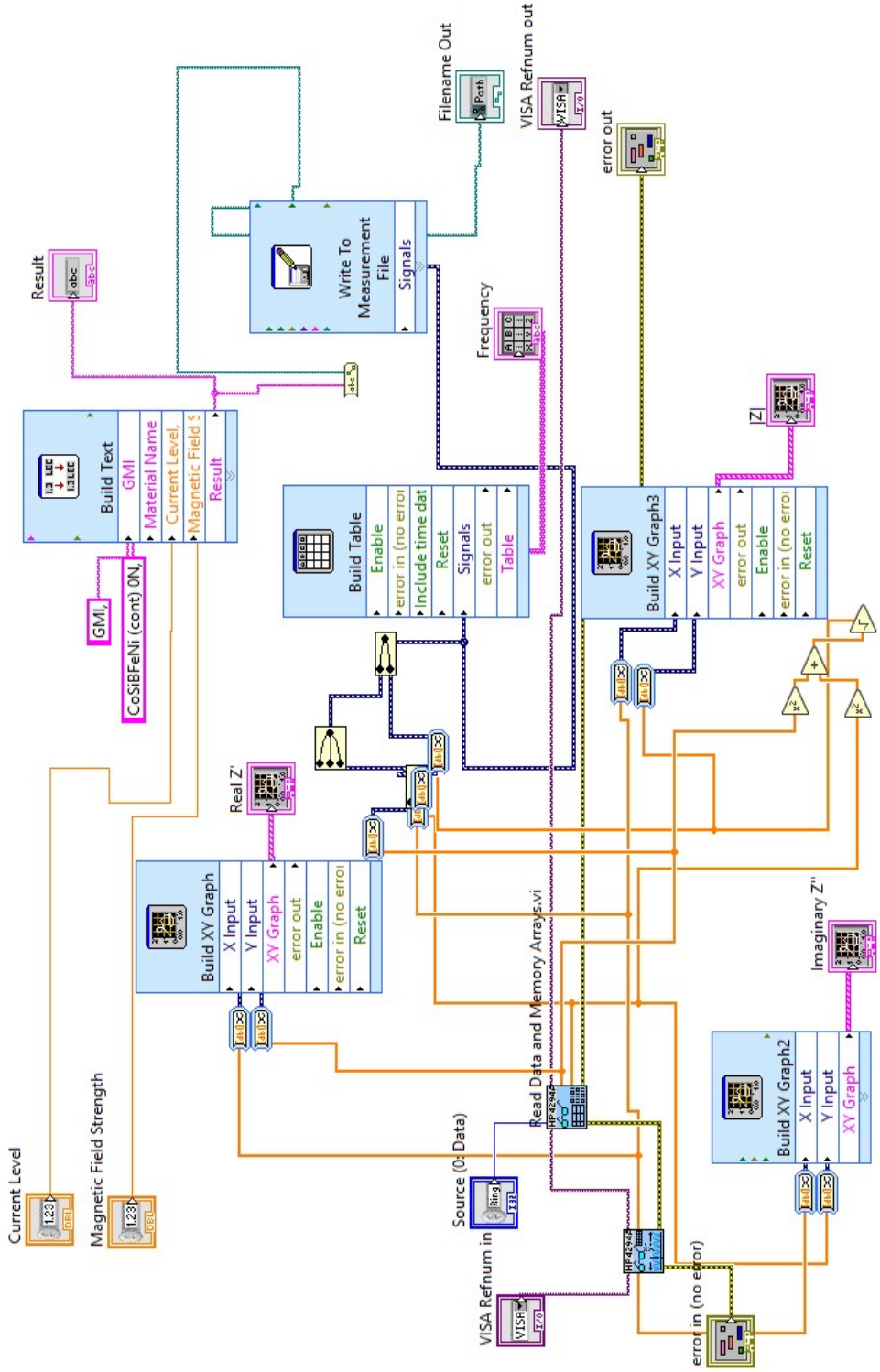

Figure A.6: LabVIEW VI design for transferring and saving measured data to the computer interface.

The collected data is then used to calculate the GMI ratio and plot it against either measured field or measured frequency. In addition, the characteristion of the GSI effect only utlises the impedance analyser thus, only Fig. A.1,2, and 6 were required to measure the change in impedance with respect to applied stress/strain.

References

[1] "Private communication, john jowsey (senior technology manager, operation technical, sellafield ltd)."
Communicated: 19-Jan-2021.

[2] C. Corkhill and N. Hyatt, *Nuclear Waste Management*. 2399-2891, IOP Publishing, 2018.

[3] N. D. Authority, "Radioactive wastes in the uk: A summary of the 2016 inventory," *Department for Business, Energy & Industrial strategy*, 2017.

[4] "What is radiation? | uk radioactive waste inventory (ukrwi)."
https://ukinventory.nda.gov.uk/about-radioactive-waste/what-is-radioactivity/.
Accessed: 01-Nov-2021.

[5] M. Ojovan and W. Lee, "Waste processing schemes," pp. 117–135, 2014.

[6] "Overview of the production and management of radioactive waste in the uk."
https://ukinventory.nda.gov.uk/wp-content/uploads/2021/03/20201222-Official-Rep-PO023346_fact-sheet-03.pdf/.
Accessed: 01-Nov-2021.

[7] R. W. Management and N. W. Services, "Inventory for geological disposal, main report," 2021.

[8] C. Paraskevoulakos, C. Stitt, K. Hallam, A. Banos, M. L. Olloqui, C. Jones, G. Griffiths, A. Adamska, J. Jowsey, and T. Scott, "Monitoring the degradation of nuclear waste packages induced by interior metallic corrosion using synchrotron x-ray tomography," *Construction and Building Materials*, vol. 215, pp. 90–103, 2019.

[9] G. Ausanio, V. Iannotti, and L. Lanotte, "Giant magnetic induction in magneto-elastic resonators and its application for magnetic field sensors," *Sensors and Actuators A: Physical*, vol. 153, no. 2, pp. 162–165, 2009.

[10] C. Blache and G. Lamarquand, "New structures for linear displacement sensor with high magnetic field gradient," *IEEE transactions on magnetics*, vol. 28, no. 5, pp. 2196–2198, 1992.

[11] W. R. Scott, "Electromagnetic induction sensor with a spinning magnet excitation," in *IGARSS 2019-2019 IEEE International Geoscience and Remote Sensing Symposium*, pp. 3542–3545, IEEE, 2019.

[12] W. R. Scott, "Differential electromagnetic induction sensor using a spinning magnet excitation," in *IGARSS 2020-2020 IEEE International Geoscience and Remote Sensing Symposium*, pp. 1401–1404, IEEE, 2020.

[13] S. Atalay, P. Ripka, and N. Bayri, "Coil-less fluxgate effect in (co0.94fe0.06)72.5si12.5b15 amorphous wires," *Journal of Magnetism and Magnetic Materials*, vol. 322, no. 15, pp. 2238–2243, 2010.

[14] O. Dezuari, E. Belloy, S. Gilbert, and M. Gijs, "Printed circuit board

integrated fluxgate sensor," *Sensors and Actuators A: Physical*, vol. 81, no. 1, pp. 200–203, 2000.

[15] M. Dressler, M. Janosek, and M. Butta, "Reduction of magnetic noise limits of orthogonal fluxgate sensor," *AIP Advances*, vol. 11, no. 1, p. 015347, 2021.

[16] P. Ripka, "Advances in fluxgate sensors," *Sensors and Actuators A: Physical*, vol. 106, no. 1, pp. 8–14, 2003. Proceedings of the 4th European Magnetic Sensors and Actuators Conference.

[17] L. Ejsing, M. F. Hansen, A. K. Menon, H. Ferreira, D. Graham, and P. Freitas, "Planar hall effect sensor for magnetic micro-and nanobead detection," *Applied Physics Letters*, vol. 84, no. 23, pp. 4729–4731, 2004.

[18] Y. Y. Lee, R.-H. Wu, and S. T. Xu, "Applications of linear hall-effect sensors on angular measurement," in *2011 IEEE International Conference on Control Applications (CCA)*, pp. 479–482, 2011.

[19] P. Liu, K. Skucha, M. Megens, and B. Boser, "A cmos hall-effect sensor for the characterization and detection of magnetic nanoparticles for biomedical applications," *IEEE Transactions on Magnetics*, vol. 47, no. 10, pp. 3449–3451, 2011.

[20] R. Popovic, Z. Randjelovic, and D. Manic, "Integrated hall-effect magnetic sensors," *Sensors and Actuators A: Physical*, vol. 91, no. 1, pp. 46–50, 2001. Third European Conference on Magnetic Sensors Actuators.

[21] E.-H. Toh, Y. Sun, P. Zheng, M. Shajan, P. Cao, M. N. Islam, J.-Y. Wong, P. Arikath, R. Jain, T. L. Tan, and E. Quek, "A modular three-dimensional hall effect sensor for performance optimization," *IEEE Sensors Journal*, vol. 22, no. 12, pp. 11256–11263, 2022.

[22] D. A. Allwood, G. Xiong, M. D. Cooke, and R. P. Cowburn, "Magneto-optical kerr effect analysis of magnetic nanostructures," *Journal of Physics D: Applied Physics*, vol. 36, p. 2175, sep 2003.

[23] Y. Didosyan, H. Hauser, H. Wolfmayr, J. Nicolics, and P. Fulmek, "Magneto-optical rotational speed sensor," *Sensors and Actuators A: Physical*, vol. 106, no. 1, pp. 168–171, 2003. Proceedings of the 4th European Magnetic Sensors and Actuators Conference.

[24] M. Koschny and M. Lindner, "Magneto-optical sensors accurately analyze magnetic field distribution of magnetic materials," *Advanced Materials & Processes*, vol. 170, no. 2, pp. 13–17, 2012.

[25] C. Liu, T. Shen, H.-B. Wu, Y. Feng, and J.-J. Chen, "Applications of magneto-strictive, magneto-optical, magnetic fluid materials in optical fiber current sensors and optical fiber magnetic field sensors: A review," *Optical Fiber Technology*, vol. 65, p. 102634, 2021.

[26] V.-D. Doan, J.-T. Jeng, H.-T. Nguyen, C.-H. Dinh, D.-V. Dao, and T.-T. Pham, "Magnetization measurement system with giant magnetoresistance zero-field detector," *IEEE Transactions on Magnetics*, vol. 58, no. 2, pp. 1–5, 2022.

[27] F. Mancoff, J. H. Dunn, B. Clemens, and R. White, "A giant magnetoresistance sensor for high magnetic field measurements," *Applied Physics Letters*, vol. 77, no. 12, pp. 1879–1881, 2000.

[28] C. Reig, S. Cardoso, and S. C. Mukhopadhyay, "Giant magnetoresistance (gmr) sensors," *Smart Sensors, Measurement and Instrumentation*, vol. 6, no. 1, pp. 1–301, 2013.

[29] R. Weiss, R. Mattheis, and G. Reiss, "Advanced giant magnetoresistance technology for measurement applications," *Measurement Science and Technology*, vol. 24, p. 082001, jul 2013.

[30] F. Beato and A. Palacios-Laloy, "Second-order effects in parametric-resonance magnetometers based on atomic alignment," *EPJ Quantum Technology*, vol. 7, no. 1, pp. 1–14, 2020.

[31] F. Hartmann, "Resonance magnetometers," *IEEE Transactions on Magnetics*, vol. 8, no. 1, pp. 66–75, 1972.

[32] A. Weis, G. Bison, and Z. Grujić, *Magnetic Resonance Based Atomic Magnetometers*, vol. 19. 2017.

[33] C. Amorim, F. Mohseni, R. Dumas, V. Amaral, and J. Amaral, "A geometry-independent moment correction method for the mpms3 squid-based magnetometer," *Measurement Science and Technology*, vol. 32, no. 10, p. 105602, 2021.

[34] A. Eulenburg, E. Romans, C. Carr, A. Millar, G. Donaldson, and C. Pegrum, "Highly balanced long-baseline single-layer high-t c superconducting quantum interference device gradiometer," *Applied physics letters*, vol. 75, no. 15, pp. 2301–2303, 1999.

[35] R. Fagaly, "Superconducting quantum interference device instruments and applications," *Review of scientific instruments*, vol. 77, no. 10, p. 101101, 2006.

[36] S. Lee, W. Myers, H. Grossman, H.-M. Cho, Y. Chemla, and J. Clarke, "Magnetic gradiometer based on a high-transition temperature superconducting quantum interference device for improved sensitivity of a biosensor," *Applied physics letters*, vol. 81, no. 16, pp. 3094–3096, 2002.

[37] T. Morooka, S. Nakayama, A. Odawara, N. Shimizu, K. Chinone, and T. A. Kasai, "Development of integrated direct current superconducting quantum interference device gradiometer for nondestructive evaluation," *Japanese Journal of Applied Physics*, vol. 35, p. L486, apr 1996.

[38] L. Chen, C.-C. Bao, H. Yang, D. Li, C. Lei, T. Wang, H.-Y. Hu, M. He, Y. Zhou, and D.-X. Cui, "A prototype of giant magnetoimpedance-based biosensing system for targeted detection of gastric cancer cells," *Biosensors and Bioelectronics*, vol. 26, no. 7, pp. 3246–3253, 2011.

[39] B. Dufay, S. Saez, C. Dolabdjian, A. Yelon, and D. Ménard, "Physical properties and giant magnetoimpedance sensitivity of rapidly solidified magnetic microwires," *Journal of Magnetism and Magnetic Materials*, vol. 324, no. 13, pp. 2091–2099, 2012.

[40] P. Gazda and R. Szewczyk, "Novel giant magnetoimpedance magnetic field sensor," *Sensors*, vol. 20, no. 3, 2020.

[41] J. Liu, Z. Du, S. Jiang, H. Shen, Z. Li, D. Xing, W. Ma, and J. Sun, "Tailoring giant magnetoimpedance effect of co-based microwires for optimum efficiency by self-designed square-wave pulse current annealing," *Journal of Magnetism and Magnetic Materials*, vol. 385, pp. 145–150, 2015.

[42] A. Zhukov, M. Ipatov, J. Gonzalez, J. Blanco, and V. Zhukova, "Recent advances in studies of magnetically soft amorphous microwires," *Journal of Magnetism and Magnetic Materials*, vol. 321, no. 7, pp. 822–825, 2009. Proceedings of the Forth Moscow International Symposium on Magnetism.

[43] J. Beato-López, G. Vargas-Silva, J. Pérez-Landazábal, and C. Gómez-Polo, "Giant stress-impedance (gsi) sensor for diameter evaluation in cylindrical elements," *Sensors and Actuators A: Physical*, vol. 269, pp. 269–275, 2018.

[44] D. Li, Z. Lu, and S. Zhou, "Giant stress-impedance effect in amorphous and thermally annealed fe73.5cu1nb3si13.5b9 ribbons," *Sensors and Actuators A: Physical*, vol. 109, no. 1, pp. 68–71, 2003.

[45] L. Shen, T. Uchiyama, K. Mohri, E. Kita, and K. Bushida, "Sensitive stress-impedance micro sensor using amorphous magnetostrictive wire," *IEEE Transactions on Magnetics*, vol. 33, no. 5, pp. 3355–3357, 1997.

[46] M.-H. Phan and H.-X. Peng, "Giant magnetoimpedance materials: Fundamentals and applications," *Progress in Materials Science*, vol. 53, no. 2, pp. 323–420, 2008.

[47] F. Jin, L. Zhou, W. Cheng, Y. Zhang, B. Tong, and Y. Xu, "Effect of shape and annealing on the giant magnetoimpendence properties of fecosib ribbon," *IEEE Transactions on Magnetics*, vol. 50, no. 10, pp. 1–4, 2014.

[48] Y.-H. Ding, K. Xue, W.-Y. Wang, and X. Ma, "Influence of aspect ratio on giant magnetoimpedance effect for fe67co18si11b4 amorphous ribbons," *Acta Metallurgica Sinica (English Letters)*, vol. 30, no. 12, pp. 1236–1242, 2017.

[49] A. Chaturvedi, T. P. Dhakal, S. Witanachchi, A.-T. Le, M.-H. Phan, and H. Srikanth, "Critical length and giant magnetoimpedance in co69fe4.5ni1.5si10b15 amorphous ribbons," *Materials Science and Engineering: B*, vol. 172, no. 2, pp. 146–150, 2010.

[50] D. Li, Z. Lu, and S. Zhou, "Induced magnetic anisotropy and stress-impedance effect in nanocrystalline $Fe_{73.5}Cu_1Nb_3Si_{13.5}B_9$ ribbons," *IEEE Sensors Journal*, vol. 6, no. 4, pp. 94–927, 2006.

[51] N. A. Spaldin, *Magnetic materials: fundamentals and applications*. Cambridge university press, 2010.

[52] Q. A. Pankhurst, J. Connolly, S. K. Jones, and J. Dobson, "Applications of magnetic nanoparticles in biomedicine," *Journal of physics D: Applied physics*, vol. 36, no. 13, p. R167, 2003.

[53] B. D. Cullity and C. D. Graham, *Introduction to magnetic materials*. John Wiley & Sons, 2011.

[54] P. Langevin, "Sur la théorie du magnétisme," *J. Phys. Theor. Appl.*, vol. 4, no. 1, pp. 678–693, 1905.

[55] N. Cusack, *The Electrical and Magnetic Properties of Solids: An Introductory Textbook*. Longmans, Green, 1958.

[56] T. Hayward, *Exquisitely balanced magnetic switching in microscopic ferromagnetic rings*. PhD thesis, University of Cambridge, 2007.

[57] J. C. Slater, "Cohesion in monovalent metals," *Physical Review*, vol. 35, no. 5, p. 509, 1930.

[58] A. Sommerfeld and H. Bethe, *Elektronentheorie der metalle*, vol. 19. Springer-Verlag, 2013.

[59] R. Cardias, A. Szilva, A. Bergman, I. D. Marco, M. Katsnelson, A. Lichtenstein, L. Nordström, A. Klautau, O. Eriksson, and Y. O. Kvashnin, "The bethe-slater curve revisited; new insights from electronic structure theory," *Scientific reports*, vol. 7, no. 1, pp. 1–11, 2017.

[60] J. Fedotova, J. Kasiuk, V. Bayev, O. Kupreeva, A. Nguyen, D. Manh, and D. Vu, *CORRELATED EVOLUTION OF SURFACE MORPHOLOGY, STRUCTURE AND MAGNETIC PROPERTIES OF NANOPOROUS Co/Pd FILMS WITH PERPENDICULAR MAGNETIC ANISOTROPY: Reviews and Short Notes to Nanomeeting-2017*, pp. 333–340. 06 2017.

[61] P. Nieves, S. Arapan, S. Zhang, A. Kądzielawa, R. Zhang, and D. Legut, "Maelas 2.0: A new version of a computer program for the calculation of magneto-elastic properties," *Computer Physics Communications*, vol. 271, p. 108197, 2022.

[62] S. Somkun, A. J. Moses, and P. I. Anderson, "Magnetostriction in grain-oriented electrical steels under ac magnetisation at angles to the rolling direction," *IET Electric Power Applications*, vol. 10, no. 9, pp. 932–938, 2016.

[63] T. Wakiyama, H. Brooks, E. Gyorgy, K. Bachmann, and D. Brasen, "Magnetostriction of hcp and dhcp co-fe single crystals," *Journal of Applied Physics*, vol. 49, no. 7, pp. 4158–4160, 1978.

[64] C. Gao, Z. Zeng, S. Peng, and C. Shuai, "Magnetostrictive alloys: Promising materials for biomedical applications," *Bioactive Materials*, vol. 8, pp. 177–195, 2022.

[65] L. Bernard, X. Mininger, L. Daniel, G. Krebs, F. Bouillault, and M. Gabsi, "Effect of stress on switched reluctance motors: a magneto-elastic finite-element approach based on multiscale constitutive laws," *IEEE Transactions on Magnetics*, vol. 47, no. 9, pp. 2171–2178, 2011.

[66] S. Chikazumi and C. D. Graham, *Physics of ferromagnetism*. No. 94, Oxford university press, 1997.

[67] F. Akagi, "Magnetic domain structures and techniques in micromagnetics simulation," in *Magnetic Material for Motor Drive Systems*, pp. 165–179, Springer, 2019.

[68] "Hysteresis - definition, meaning, hysteresis loop, loss, curve." Accessed: 2022-05-12.

[69] F. Colaiori, "Exactly solvable model of avalanches dynamics for barkhausen crackling noise," *Advances in Physics*, vol. 57, no. 4, pp. 287–359, 2008.

[70] "Magnetic hysteresis loop including the b-h curve." Accessed: 2022-05-12.

[71] R. Grössinger, "Characterisation of hard magnetic materials," *Journal of Electrical Engineering*, vol. 59, no. 7, pp. 15–20, 2008.

[72] J. D. Coey, "Magnetic materials," *Journal of Alloys and Compounds*, vol. 326, no. 1-2, pp. 2–6, 2001.

[73] M. Campos, "Different coercivity mechanisms for hard and soft magnetic materials," 09 2014.

[74] H. Yibole, B. Lingling-Bao, J. Xu, H. Alata, O. Tegus, W. Hanggai, N. van Dijk, E. Brück, and F. Guillou, "(fe, co) 2 (p, si) rare-earth free permanent magnets: From macroscopic single crystals to submicron-sized particles," *Acta Materialia*, vol. 221, p. 117388, 2021.

[75] L. Straka, L. Fekete, M. Rameš, E. Belas, and O. Heczko, "Magnetic coercivity control by heat treatment in heusler ni–mn–ga (–b) single crystals," *Acta Materialia*, vol. 169, pp. 109–121, 2019.

[76] N. Patelli, F. Cugini, D. Wang, S. Sanna, M. Solzi, H. Hahn, and L. Pasquini, "Structure and magnetic properties of fe-co alloy nanoparticles synthesized by pulsed-laser inert gas condensation," *Journal of Alloys and Compounds*, vol. 890, p. 161863, 2022.

[77] E. A. Gorbachev, L. A. Trusov, A. E. Sleptsova, E. S. Kozlyakova, L. N. Alyabyeva, S. R. Yegiyan, A. S. Prokhorov, V. A. Lebedev, I. V. Roslyakov, A. V. Vasiliev, *et al.*, "Hexaferrite materials displaying ultra-high coercivity and sub-terahertz ferromagnetic resonance frequencies," *Materials Today*, vol. 32, pp. 13–18, 2020.

[78] D. S. Mathew and R.-S. Juang, "An overview of the structure and magnetism of spinel ferrite nanoparticles and their synthesis in microemulsions," *Chemical engineering journal*, vol. 129, no. 1-3, pp. 51–65, 2007.

[79] J. Sung Lee, J. Myung Cha, H. Young Yoon, J.-K. Lee, and Y. Keun Kim, "Magnetic multi-granule nanoclusters: A model system that exhibits universal size effect of magnetic coercivity," *Scientific reports*, vol. 5, no. 1, pp. 1–7, 2015.

[80] J. Mohapatra, J. Fischbacher, M. Gusenbauer, M. Xing, J. Elkins, T. Schrefl, and J. P. Liu, "Coercivity limits in nanoscale ferromagnets," *Physical Review B*, vol. 105, no. 21, p. 214431, 2022.

[81] M. I. Dar and S. Shivashankar, "Single crystalline magnetite, maghemite, and hematite nanoparticles with rich coercivity," *RSC Advances*, vol. 4, no. 8, pp. 4105–4113, 2014.

[82] Y. G. Pastushenkov, K. P. Skokov, E. S. Antonova, T. I. Ivanova, and J. S. Bartolomé, "Domain structure transformation and magnetic susceptibility of ho2fe17 single crystals," *Journal of Alloys and Compounds*, vol. 689, pp. 894–898, 2016.

[83] A. Ramazani, M. Almasi Kashi, and A. Montazer, "Fabrication of single crystalline, uniaxial single domain co nanowire arrays with high coercivity," *Journal of Applied Physics*, vol. 115, no. 11, p. 113902, 2014.

[84] G. Herzer, "Grain size dependence of coercivity and permeability in nanocrystalline ferromagnets," *IEEE Transactions on magnetics*, vol. 26, no. 5, pp. 1397–1402, 1990.

[85] M. Vopsaroiu, M. Georgieva, P. Grundy, G. Vallejo Fernandez, S. Manzoor, M. Thwaites, and K. O'Grady, "Preparation of high moment cofe films with controlled grain size and coercivity," *Journal of applied physics*, vol. 97, no. 10, p. 10N303, 2005.

[86] G. Herzer, "Modern soft magnets: Amorphous and nanocrystalline materials," *Acta Materialia*, vol. 61, no. 3, pp. 718–734, 2013. The Diamond Jubilee Issue.

[87] J. Moulin, F. Mazaleyrat, A. Mendez, and E. Dufour-Gergam, "Internal stress influence on the coercivity of fecunbsib thin films," *Journal of Magnetism and Magnetic Materials*, vol. 322, no. 9, pp. 1275–1278, 2010. Proceedings of the Joint European Magnetic Symposia.

[88] K. Uestuener, M. Katter, and W. Rodewald, "Dependence of the mean grain size and coercivity of sintered nd–fe–b magnets on the initial powder particle size," *IEEE Transactions on Magnetics*, vol. 42, no. 10, pp. 2897–2899, 2006.

[89] J. Dho, E. Lee, J. Park, and N. Hur, "Effects of the grain boundary on the coercivity of barium ferrite bafe12o19," *Journal of Magnetism and Magnetic Materials*, vol. 285, no. 1, pp. 164–168, 2005.

[90] G. Han, R. Gao, S. Yan, H. Liu, S. Fu, W. Feng, W. Li, and X. Li, "Effect of exchange–coupling interaction on the effective anisotropy in nanocrystalline nd2fe14b material," *Journal of Magnetism and Magnetic Materials*, vol. 281, no. 1, pp. 6–10, 2004.

[91] X. Liang, T. Kulik, J. Ferenc, M. Kowalczyk, G. Vlasák, W. Sun, and B. Xu, "Influence of structure on coercivity in nanocrystalline (fe1xcox)86hf7b6cu1 alloys," *Physica B: Condensed Matter*, vol. 370, no. 1, pp. 151–157, 2005.

[92] L. Varga, L. Novák, and F. Mazaleyrat, "Effective magnetic anisotropy and internal demagnetization investigations in soft magnetic nanocrystalline alloys," *Journal of Magnetism and Magnetic Materials*, vol. 210, no. 1, pp. 25–30, 2000.

[93] R. Gao, W. Feng, H. Liu, B. Wang, W. Chen, G. Han, P. Zhang, H. Li, W. Li, Y. Guo, *et al.*, "Exchange-coupling interaction, effective anisotropy and coercivity in nanocomposite permanent materials," *Journal of applied physics*, vol. 94, no. 1, pp. 664–668, 2003.

[94] K. Dewangan, K. Shrivas, and R. Kurrey, "Chapter 9 - hybrid nanomaterials as chemical sensors," in *Multifunctional Hybrid Nanomaterials for Sustainable Agri-Food and Ecosystems* (K. A. Abd-Elsalam, ed.), Micro and Nano Technologies, pp. 213–239, Elsevier, 2020.

[95] W. Zhang, S. R. Valloppilly, X. Li, R. Skomski, J. E. Shield, and D. J. Sellmyer, "Coercivity enhancement in zr_2co_{11} -based nanocrystalline materials due to mo addition," *IEEE Transactions on Magnetics*, vol. 48, no. 11, pp. 3603–3605, 2012.

[96] A. Chrobak, G. Ziółkowski, N. Randrianantoandro, J. Klimontko, D. Chrobak, K. Prusik, and J. Rak, "Ultra-high coercivity of

(fe86xnbxb14)0.88tb0.12 bulk nanocrystalline magnets," *Acta Materialia*, vol. 98, pp. 318–326, 2015.

[97] K. Suzuki and J. Cadogan, "The effect of the spontaneous magnetization in the grain boundary region on the magnetic softness of nanocrystalline materials," *Journal of applied physics*, vol. 85, no. 8, pp. 4400–4402, 1999.

[98] A. Bolyachkin and S. Komogortsev, "Power-law behavior of coercivity in nanocrystalline magnetic alloys with grain-size distribution," *Scripta Materialia*, vol. 152, pp. 55–58, 2018.

[99] S. Komogortsev and R. Iskhakov, "Magnetization curve and magnetic correlations in a nanochain of ferromagnetic grains with random anisotropy," *Physics of the Solid State*, vol. 47, no. 3, pp. 495–501, 2005.

[100] T. Hysen, S. Al-Harthi, I. Al-Omari, P. Geetha, R. Lisha, R. Ramanujan, D. Sakthikumar, and M. Anantharaman, "Annealing induced low coercivity, nanocrystalline co–fe–si thin films exhibiting inverse cosine angular variation," *Journal of Magnetism and Magnetic Materials*, vol. 341, pp. 165–172, 2013.

[101] C. S. Boland, U. Khan, C. Backes, A. O'Neill, J. McCauley, S. Duane, R. Shanker, Y. Liu, I. Jurewicz, A. B. Dalton, and J. N. Coleman, "Sensitive, high-strain, high-rate bodily motion sensors based on graphene–rubber composites," *ACS Nano*, vol. 8, no. 9, pp. 8819–8830, 2014. PMID: 25100211.

[102] M. Stoica, V. Kolesar, J. Bednarčic, S. Roth, H. Franz, and J. Eckert, "Thermal stability and magnetic properties of partially co-substituted

(fe71. 2b24y4. 8) 96nb4 bulk metallic glasses," *Journal of Applied Physics*, vol. 109, no. 5, p. 054901, 2011.

[103] W. Yang, H. Liu, L. Xue, J. Li, C. Dun, J. Zhang, Y. Zhao, and B. Shen, "Magnetic properties of (fe1xnix)72b20si4nb4 (x=0.0–0.5) bulk metallic glasses," *Journal of Magnetism and Magnetic Materials*, vol. 335, pp. 172–176, 2013.

[104] L. Hou, M. Li, C. Jiang, X. Fan, Q. Luo, S. Chen, P. Song, and W. Li, "Thermal and magnetic properties of fe(co)bccu amorphous alloys with high saturation magnetization of 1.77 t," *Journal of Alloys and Compounds*, vol. 853, p. 157071, 2021.

[105] H. Lassri, M. Tlemçani, M. Slimani, S. Sayouri, M. Abid, H. Hamouda, and A. Mikou, "Random anisotropy studies in amorphous fe80xnixb12si8 alloys," *Physica B: Condensed Matter*, vol. 239, no. 3, pp. 274–277, 1997.

[106] R. Hasegawa, "Static bubble domain properties of amorphous gd–co films," *Journal of Applied Physics*, vol. 45, no. 7, pp. 3109–3112, 1974.

[107] A. H. Morrish, *The Physical Principles of Magnetism*. 2001.

[108] R. Parsons, K. Onodera, H. Kishimoto, T. Shoji, A. Kato, and K. Suzuki, "Effect of tensile stress during ultra-rapid annealing on the soft magnetic properties of fe-b based nanocrystalline alloys," *Journal of Alloys and Compounds*, vol. 924, p. 166374, 2022.

[109] B. Chandra Sekhar, G. Rao, O. Caltun, B. Dhana Lakshmi, B. Parvatheeswara Rao, and P. Subba Rao, "Magnetic and magnetostrictive properties of cu substituted co-ferrites," *Journal of Magnetism and Magnetic Materials*, vol. 398, pp. 59–63, 2016.

[110] J. Barandiarán, J. Gutiérrez, and A. García-Arribas, "Magnetoelasticity in amorphous ferromagnets: Basic principles and applications," *physica status solidi (a)*, vol. 208, no. 10, pp. 2258–2264, 2011.

[111] E. Callen and H. B. Callen, "Magnetostriction, forced magnetostriction, and anomalous thermal expansion in ferromagnets," *Phys. Rev.*, vol. 139, pp. A455–A471, Jul 1965.

[112] Y. Li, J. Zhu, Y. Li, H. Wang, and L. Zhu, "Modeling dynamic magnetostriction of amorphous core materials based on jiles–atherton theory for finite element simulations," *Journal of Magnetism and Magnetic Materials*, vol. 529, p. 167854, 2021.

[113] B. Huang, Y. Yang, A. Wang, Q. Wang, and C. Liu, "Saturated magnetization and glass forming ability of soft magnetic fe-based metallic glasses," *Intermetallics*, vol. 84, pp. 74–81, 2017.

[114] S. Bahl, H. Nagar, I. Singh, and S. Sehgal, "Smart materials types, properties and applications: A review," *Materials Today: Proceedings*, vol. 28, pp. 1302–1306, 2020. International Conference on Aspects of Materials Science and Engineering.

[115] M. Sobczyk, S. Wiesenhütter, J. R. Noennig, and T. Wallmersperger, "Smart materials in architecture for actuator and sensor applications: A review," *Journal of Intelligent Material Systems and Structures*, vol. 33, no. 3, pp. 379–399, 2022.

[116] H. Tai, Z. Duan, Y. Wang, S. Wang, and Y. Jiang, "Paper-based sensors for gas, humidity, and strain detections: A review," *ACS Applied Materials & Interfaces*, vol. 12, no. 28, pp. 31037–31053, 2020. PMID: 32584534.

[117] D. Zhang, B. Ren, Y. Zhang, L. Xu, Q. Huang, Y. He, X. Li, J. Wu, J. Yang, Q. Chen, Y. Chang, and J. Zheng, "From design to applications of stimuli-responsive hydrogel strain sensors," *J. Mater. Chem. B*, vol. 8, pp. 3171–3191, 2020.

[118] L. Duan, D. R. D'hooge, and L. Cardon, "Recent progress on flexible and stretchable piezoresistive strain sensors: From design to application," *Progress in Materials Science*, vol. 114, p. 100617, 2020.

[119] S. Seyedin, P. Zhang, M. Naebe, S. Qin, J. Chen, X. Wang, and J. M. Razal, "Textile strain sensors: a review of the fabrication technologies, performance evaluation and applications," *Mater. Horiz.*, vol. 6, pp. 219–249, 2019.

[120] D. Chung, "A critical review of piezoresistivity and its application in electrical-resistance-based strain sensing," *Journal of Materials Science*, vol. 55, no. 32, pp. 15367–15396, 2020.

[121] A. Dehghani and F. Aslani, "Piezoresistive sensing of cementitious composites reinforced with shape memory alloy, steel, and carbon fibres," *Construction and Building Materials*, vol. 267, p. 121046, 2021.

[122] H. Nesser and G. Lubineau, "Strain sensing by electrical capacitive variation: From stretchable materials to electronic interfaces," *Advanced Electronic Materials*, vol. 7, no. 10, p. 2100190, 2021.

[123] M. A. Khan, J. Sun, B. Li, A. Przybysz, and J. Kosel, "Magnetic sensors-a review and recent technologies," *Engineering Research Express*, vol. 3, p. 022005, jun 2021.

[124] H. Chiriac, N. Lupu, V. Dobrea, and S. Corodeanu, "Mechanical properties of magnetic fe-based and co-based amorphous wires and microwires," *physica status solidi (a)*, vol. 206, no. 4, pp. 648–651, 2009.

[125] J. Konieczny, L. Dobrzański, L. Pešek, P. Zubko, and P. Komenkeho, "Mechanical properties of co-based amorphous ribbons," *Journal of Achievements in Materials and Manufacturing Engineering*, vol. 31, no. 2, pp. 254–261, 2008.

[126] J. Zhao, G. Wang, R. Yang, X. Lu, M. Cheng, C. He, G. Xie, J. Meng, D. Shi, and G. Zhang, "Tunable piezoresistivity of nanographene films for strain sensing," *ACS Nano*, vol. 9, no. 2, pp. 1622–1629, 2015. PMID: 25658857.

[127] X. Li, R. Zhang, W. Yu, K. Wang, J. Wei, D. Wu, A. Cao, Z. Li, Y. Cheng, Q. Zheng, *et al.*, "Stretchable and highly sensitive graphene-on-polymer strain sensors," *Scientific reports*, vol. 2, no. 1, pp. 1–6, 2012.

[128] S. Zhao, L. Guo, J. Li, N. Li, G. Zhang, Y. Gao, J. Li, D. Cao, W. Wang, Y. Jin, *et al.*, "Binary synergistic sensitivity strengthening of bioinspired hierarchical architectures based on fragmentized reduced graphene oxide sponge and silver nanoparticles for strain sensors and beyond," *Small*, vol. 13, no. 28, p. 1700944, 2017.

[129] S. Chen, Y. Wei, S. Wei, Y. Lin, and L. Liu, "Ultrasensitive cracking-assisted strain sensors based on silver nanowires/graphene hybrid particles," *ACS Applied Materials & Interfaces*, vol. 8, no. 38, pp. 25563–25570, 2016. PMID: 27599264.

[130] J. Yuan, A. Luna, W. Neri, C. Zakri, A. Colin, and P. Poulin, "Giant electrostriction of soft nanocomposites based on liquid crystalline graphene," *ACS Nano*, vol. 12, no. 2, pp. 1688–1695, 2018. PMID: 29353484.

[131] Q. Yu, R. Ge, J. Wen, T. Du, J. Zhai, S. Liu, L. Wang, and Y. Qin,

"Highly sensitive strain sensors based on piezotronic tunneling junction," *Nature communications*, vol. 13, no. 1, pp. 1–9, 2022.

[132] Y.-G. Kim, J.-H. Song, S. Hong, and S.-H. Ahn, "Piezoelectric strain sensor with high sensitivity and high stretchability based on kirigami design cutting," *npj Flexible Electronics*, vol. 6, no. 1, pp. 1–8, 2022.

[133] T. Hu, S. Xuan, L. Ding, and X. Gong, "Liquid metal circuit based magnetoresistive strain sensor with discriminating magnetic and mechanical sensitivity," *Sensors and Actuators B: Chemical*, vol. 314, p. 128095, 2020.

[134] S. Ryu, P. Lee, J. B. Chou, R. Xu, R. Zhao, A. J. Hart, and S.-G. Kim, "Extremely elastic wearable carbon nanotube fiber strain sensor for monitoring of human motion," *ACS Nano*, vol. 9, no. 6, pp. 5929–5936, 2015. PMID: 26038807.

[135] Z. Lei, Q. Wang, S. Sun, W. Zhu, and P. Wu, "A bioinspired mineral hydrogel as a self-healable, mechanically adaptable ionic skin for highly sensitive pressure sensing," *Advanced Materials*, vol. 29, no. 22, p. 1700321, 2017.

[136] H. Zhang, W. Niu, and S. Zhang, "Extremely stretchable and self-healable electrical skin with mechanical adaptability, an ultrawide linear response range, and excellent temperature tolerance," *ACS Applied Materials & Interfaces*, vol. 11, no. 27, pp. 24639–24647, 2019. PMID: 31257840.

[137] X. Shi, H. Wang, X. Xie, Q. Xue, J. Zhang, S. Kang, C. Wang, J. Liang, and Y. Chen, "Bioinspired ultrasensitive and stretchable mxene-based strain sensor via nacre-mimetic microscale "brick-and-mortar" architecture," *ACS Nano*, vol. 13, no. 1, pp. 649–659, 2019.

[138] H. Zhao, Y. Zhang, P. D. Bradford, Q. Zhou, Q. Jia, F.-G. Yuan, and Y. Zhu, "Carbon nanotube yarn strain sensors," *Nanotechnology*, vol. 21, p. 305502, jul 2010.

[139] Z. Li, X. Qi, L. Xu, H. Lu, W. Wang, X. Jin, Z. I. Md, Y. Zhu, Y. Fu, Q. Ni, and Y. Dong, "Self-repairing, large linear working range shape memory carbon nanotubes/ethylene vinyl acetate fiber strain sensor for human movement monitoring," *ACS Applied Materials & Interfaces*, vol. 12, no. 37, pp. 42179–42192, 2020. PMID: 32822534.

[140] T. Lee, W. Lee, S.-W. Kim, J. J. Kim, and B.-S. Kim, "Flexible textile strain wireless sensor functionalized with hybrid carbon nanomaterials supported zno nanowires with controlled aspect ratio," *Advanced Functional Materials*, vol. 26, no. 34, pp. 6206–6214, 2016.

[141] X. Xi and D. Chung, "Capacitance-based self-sensing of flaws and stress in carbon-carbon composites, with reports of the electric permittivity, piezoelectricity and piezoresistivity," *Carbon*, vol. 146, pp. 447–461, 2019.

[142] X. Liao, Q. Liao, X. Yan, Q. Liang, H. Si, M. Li, H. Wu, S. Cao, and Y. Zhang, "Flexible and highly sensitive strain sensors fabricated by pencil drawn for wearable monitor," *Advanced Functional Materials*, vol. 25, no. 16, pp. 2395–2401, 2015.

[143] J. J. Beato-López, J. M. Algueta-Miguel, C. A. de la Cruz Blas, L. G. Santesteban, J. I. Pérez-Landazábal, and C. Gómez-Polo, "Gmi magnetoelastic sensor for measuring trunk diameter variations in plants," *IEEE Transactions on Magnetics*, vol. 53, no. 4, pp. 1–5, 2017.

[144] Z. Wang, X. Wang, M. Li, Y. Gao, Z. Hu, T. Nan, X. Liang, H. Chen, J. Yang, S. Cash, *et al.*, "Highly sensitive flexible magnetic sensor based

on anisotropic magnetoresistance effect," *Advanced Materials*, vol. 28, no. 42, pp. 9370–9377, 2016.

[145] S. Ota, A. Ando, and D. Chiba, "A flexible giant magnetoresistive device for sensing strain direction," *Nature Electronics*, vol. 1, no. 2, pp. 124–129, 2018.

[146] A. Tavassolizadeh, P. Hayes, K. Rott, G. Reiss, E. Quandt, and D. Meyners, "Highly strain-sensitive magnetostrictive tunnel magnetoresistance junctions," *Journal of Magnetism and Magnetic Materials*, vol. 384, pp. 308–313, 2015.

[147] S. Zhang, J. Sun, D. Xing, F. Qin, and H. Peng, "Large gmi effect in co-rich amorphous wire by tensile stress," *Journal of Magnetism and Magnetic Materials*, vol. 323, no. 23, pp. 3018–3021, 2011.

[148] F. Qin, H. Peng, V. Popov, and M. Phan, "Giant magneto-impedance and stress-impedance effects of microwire composites for sensing applications," *Solid State Communications*, vol. 151, no. 4, pp. 293–296, 2011.

[149] S. Shuai, S. Lu, Z. Xiang, and W. Lu, "Stress-induced giant magneto-impedance effect of amorphous cofenisipb ribbon with magnetic field annealing," *Journal of Magnetism and Magnetic Materials*, vol. 551, p. 169131, 2022.

[150] L. Panina, K. Mohri, K. Bushida, and M. Noda, "Giant magneto-impedance and magneto-inductive effects in amorphous alloys," *Journal of Applied Physics*, vol. 76, no. 10, pp. 6198–6203, 1994.

[151] L. Kraus, "Gmi modeling and material optimization," *Sensors and Actuators A: Physical*, vol. 106, no. 1, pp. 187–194, 2003. Proceedings of the 4th European Magnetic Sensors and Actuators Conference.

[152] M. Knobel, M. Vázquez, and L. Kraus, *Giant Magnetoimpedance*, vol. 15. 2003.

[153] M. Knobel and K. Pirota, "Giant magnetoimpedance: concepts and recent progress," *Journal of Magnetism and Magnetic Materials*, vol. 242-245, no. Part 1, pp. 33–40, 2002.

[154] K. Mohri, T. Kohsawa, K. Kawashima, H. Yoshida, and L. Panina, "Magneto-inductive effect (mi effect) in amorphous wires," *IEEE Transactions on Magnetics*, vol. 28, no. 5, pp. 3150–3152, 1992.

[155] P. Squire, "Phenomenological model for magnetization, magnetostriction and δe effect in field-annealed amorphous ribbons," *Journal of Magnetism and Magnetic Materials*, vol. 87, no. 3, pp. 299–310, 1990.

[156] F. Machado and S. Rezende, "A theoretical model for the giant magnetoimpedance in ribbons of amorphous soft-ferromagnetic alloys," *Journal of Applied Physics*, vol. 79, no. 8, p. 6558, 1996.

[157] F. Machado, C. Martins, and S. Rezende, "Giant magnetoimpedance in the ferromagnetic alloy $Co_{75\text{-}x}Fe_xSi_{15}B_{10}$," *Physical Review B*, vol. 51, no. 6, pp. 3926–3929, 1995.

[158] L. Panina, K. Mohri, T. Uchiyama, M. Noda, and K. Bushida, "Giant magneto-impedance in co-rich amorphous wires and films," *IEEE Transactions on Magnetics*, vol. 31, no. 2, pp. 1249–1260, 1995.

[159] L. Panina and K. Mohri, "Magneto-impedance effect in amorphous wires," *Applied Physics Letters*, vol. 65, no. 9, pp. 1189–1191, 1994.

[160] L. Gonzalez-Legarreta, P. Corte-León, V. Zhukova, J. Blanco, M. Churyukanova, S. Taskaev, and A. Zhukov, "Route of magnetoimpedance and domain walls dynamics optimization in co-based microwires," *Journal of Alloys and Compounds*, vol. 830, p. 154576, 2020.

[161] A. Yelon, D. Ménard, M. Britel, and P. Ciureanu, "Calculations of giant magnetoimpedance and of ferromagnetic resonance response are rigorously equivalent," *Applied Physics Letters*, vol. 69, no. 20, pp. 3084–3085, 1996.

[162] D. Ménard, A. Yelon, L. Melo, P. Ciureanu, M. Britel, M. Rouabhi, and R. Cochrane, "Modeling the magnetoimpedance in anisotropic wires," *Journal of Applied Physics*, vol. 87, no. 9, pp. 4801–4803, 2000.

[163] M. Vazquez and A. Hernando, "A soft magnetic wire for sensor applications," *Journal of Physics D: Applied Physics*, vol. 29, no. 4, p. 939, 1996.

[164] M. Vázquez and A. Hernando, "A soft magnetic wire for sensor applications„" *Journal of Physics D: Applied Physics*, vol. 29, no. 29, pp. 939–949, 1996.

[165] M. Phan, H. Peng, M. Wisnom, S. Yu, C. Kim, and N. Nghi, "Effect of annealing temperature on permeability and giant magneto-impedance of fe-based amorphous ribbon," *Sensors and Actuators A: Physical*, vol. 129, no. 1, pp. 62–65, 2006. EMSA 2004.

[166] D. Garcia, V. Raposo, O. Montero, and J. Íñiguez, "Influence of magnetostriction constant on magnetoimpedance–frequency dependence," *Sensors and Actuators A: Physical*, vol. 129, no. 1-2, pp. 227–230, 2006.

[167] K. Pirota, J. Schoenmaker, M. Sartorelli, M. Knobel, J. Gutiérrez, and J. M. Barandiarán, "Influence of induced anisotropy and magnetostriction in the magnetoimpedance and its aftereffect in cofesib amorphous ribbons," in *Magnetism, Magnetic Materials and their Applications*, vol. 302 of *Materials Science Forum*, pp. 229–233, Trans Tech Publications Ltd, 1 1999.

[168] E. J. Lavernia and T. S. Srivatsan, "The rapid solidification processing of materials: science, principles, technology, advances, and applications," *Journal of Materials Science*, vol. 45, no. 2, pp. 287–325, 2010.

[169] T. Gotō, "Fendash;b and fendash;sindash;b system alloy filaments produced by glass-coated melt spinning," *Transactions of the Japan Institute of Metals*, vol. 21, no. 4, pp. 219–225, 1980.

[170] Y. Waseda, S. Ueno, M. Hagiwara, and K. T. Aust, "Formation and mechanical properties of fe- and co-base amorphous alloy wires produced by in-rotating-water spinning method," *Progress in Materials Science*, vol. 34, no. 2, pp. 149–260, 1990.

[171] I. Ogasawara and S. Ueno, "Preparation and properties of amorphous wires," *IEEE Transactions on Magnetics*, vol. 31, no. 2, pp. 1219–1223, 1995.

[172] G. F. Taylor, "A method of drawing metallic filaments and a discussion of their properties and uses," *Phys. Rev.*, vol. 23, pp. 655–660, May 1924.

[173] H. Wiesner and J. Schneider, "Magnetic properties of amorphous fe p alloys containing ga, ge, and as," *physica status solidi (a)*, vol. 26, no. 1, pp. 71–75, 1974.

[174] H. Chiriac, "Preparation and characterization of glass covered magnetic wires," *Materials Science and Engineering: A*, vol. 304-306, pp. 166–171, 2001. RQ10, Tenth International Conference on Rapidly Quenched and Metastable Materials.

[175] M. Vázquez and A. Zhukov, "Magnetic properties of glass-coated amorphous and nanocrystalline microwires," *Journal of Magnetism and*

Magnetic Materials, vol. 160, pp. 223–228, 1996. Proceedings of the twelfth International Conference on Soft Magnetic Materials.

[176] V. Vega, V. Prida, B. Hernando, M. Ipatov, A. Chizhik, V. Zhukova, A. Zhukov, L. Domínguez, and J. González, "Improvement of high frequency giant magnetoimpedance effect in cofesib amorphous ribbon with vanishing magnetostriction by electrodeposited co coating surface layer," *Journal of Materials Research and Technology*, vol. 15, pp. 6929–6939, 2021.

[177] J. Garcia, J. Sinnecker, A. Asenjo, and M. Vázquez, "Enhanced magnetoimpedance in cop electrodeposited microtubes," *Journal of Magnetism and Magnetic Materials*, vol. 226-230, pp. 704–706, 2001. Proceedings of the International Conference on Magnetism (ICM 2000).

[178] M. McHenry, A. Willard, and D. Laughlin, "Amorphous and nanocrystalline materials for applications as soft magnets," *Progress in Materials Science*, vol. 44, no. 4, pp. 291–433, 1999.

[179] C. Rong and B. Shen, "Nanocrystalline and nanocomposite permanent magnets by melt spinning technique*," *Chinese Physics B*, vol. 27, p. 117502, nov 2018.

[180] R. Thomas, J. Perepezko, and J. Wiley, "Crystallization of sputter deposited amorphous metal thin films," *Applied Surface Science*, vol. 26, no. 4, pp. 534–541, 1986.

[181] L. Panina and K. Mohri, "Magneto-impedance in multilayer films," *Sensors and Actuators A: Physical*, vol. 81, no. 1-3, pp. 71–77, 2000.

[182] L. Chen, Y. Zhou, C. Lei, and Z.-M. Zhou, "Effect of sputtering parameters and sample size on giant magnetoimpedance effect in nife and

nife/cu/nife films," *Materials Science and Engineering: B*, vol. 172, no. 2, pp. 101–107, 2010.

[183] Z. Zhang, B. Li, W. Cui, and J. Xie, "Influence of glass coating thickness and metallic core diameter on gmi effect of glass-coated co68fe4.5si13.5b14 amorphous microwires," *Journal of Magnetism and Magnetic Materials*, vol. 323, no. 12, pp. 1712–1716, 2011.

[184] F. Qin, H. Peng, and M. Phan, "Influence of varying metal-to-glass ratio on gmi effect in co70.3fe3.7b10si13cr3 amorphous glass-coated microwires," *Solid State Communications*, vol. 150, no. 1, pp. 114–117, 2010.

[185] Y. Geng, Y. Wang, J. Qiang, G. Zhang, C. Dong, O. Tegus, and J. Sun, "Fe–b–si–zr soft magnetic bulk glassy alloys," *Intermetallics*, vol. 67, pp. 138–144, 2015.

[186] S. Jiang, T. Eggers, O. Thiabgoh, D. Xing, W. Fei, H. Shen, J. Liu, J. Zhang, W. Fang, J. Sun, *et al.*, "Relating surface roughness and magnetic domain structure to giant magneto-impedance of co-rich melt-extracted microwires," *Scientific Reports*, vol. 7, no. 1, pp. 1–8, 2017.

[187] N. Laurita, A. Chaturvedi, C. Bauer, P. Jayathilaka, A. Leary, C. Miller, M.-H. Phan, M. E. McHenry, and H. Srikanth, "Enhanced giant magnetoimpedance effect and field sensitivity in co-coated soft ferromagnetic amorphous ribbons," *Journal of Applied Physics*, vol. 109, no. 7, p. 07C706, 2011.

[188] M. Liu, S. Du, F. Wang, R. Adam, Q. Li, X. Ma, X. Guo, X. Chen, J. Yu, Y. Song, J. Xu, S. Li, and D. Cao, "Influence of surface pinning in the domain on the magnetization dynamics in permalloy striped

domain films," *Journal of Alloys and Compounds*, vol. 869, p. 159327, 2021.

[189] A. Chaturvedi, T. Dhakal, S. Witanachchi, A.-T. Le, M.-H. Phan, and H. Srikanth, "Correlation between magnetic softness, sample surface and magnetoimpedance in co69fe4.5x1.5si10b15 (x=ni, al, cr) amorphous ribbons," *Physica B: Condensed Matter*, vol. 405, no. 13, pp. 2836–2839, 2010.

[190] A. A. Taysioglu, A. Peksoz, Y. Kaya, N. Derebasi, G. Irez, and G. Kaynak, "Gmi effect in cuo coated co-based amorphous ribbons," *Journal of Alloys and Compounds*, vol. 487, no. 1, pp. 38–41, 2009.

[191] J. Yi, X. Li, J. Ding, and H. Seet, "Study of the grain size, particle size and roughness of substrate in relation to the magnetic properties of electroplated permalloy," *Journal of Alloys and Compounds*, vol. 428, no. 1, pp. 230–236, 2007.

[192] "Influence of microstructure evolution on gmi properties and magnetic domains of melt-extracted zr-doped amorphous wires with accumulated dc annealing," *Journal of Alloys and Compounds*, vol. 644, pp. 180–185, 2015.

[193] M. H. Phan, H. X. Peng, M. R. Wisnom, S. C. Yu, and N. Chau, "Enhanced gmi effect in a co70fe5si15b10 ribbon due to cu and nb substitution for b," *physica status solidi (a)*, vol. 201, no. 7, pp. 1558–1562.

[194] A. Zhukov, M. Churyukanova, S. Kaloshkin, V. Semenkova, S. Gudoshnikov, M. Ipatov, A. Talaat, J. Blanco, and V. Zhukova, "Effect of annealing on magnetic properties and magnetostriction coefficient of

fe–ni-based amorphous microwires," *Journal of Alloys and Compounds*, vol. 651, pp. 718–723, 2015.

[195] K. Wanjun, F. Ge, and J. Zhu, "Effect of magnetic field annealing on the giant magnetoimpedance in fecumosib ribbons," *Journal of Applied Physics*, vol. 82, no. 10, pp. 5050–5053, 1997.

[196] A. Gonzalez, V. Zhukova, M. Ipatov, P. Corte-Leon, J. Blanco, and A. Zhukov, "Effect of joule heating on gmi and magnetic properties of fe-rich glass-coated microwires," *AIP Advances*, vol. 12, no. 3, p. 035021, 2022.

[197] V. Zhukova, M. Ipatov, A. Talaat, J. Blanco, M. Churyukanova, and A. Zhukov, "Effect of stress annealing on magnetic properties and gmi effect of co- and fe-rich microwires," *Journal of Alloys and Compounds*, vol. 707, pp. 189–194, 2017. Selected papers presented at ISMANAM 2016, July 3rd-8th, Nara, Japan.

[198] Y. Zhang, T. Gan, T. Wang, F. Wang, and W. Shi, "Giant magnetoimpedance effect in fe75.5cu1nb3si13.5b7 ribbon/fega film composite," *Journal of Magnetism and Magnetic Materials*, vol. 417, pp. 37–41, 2016.

[199] H. Chiriac, V. Goian, and S. Corodeanu, "Gmi effect in amorphous glass covered microwires as a function of the internal induced stresses," *IEEE Transactions on Magnetics*, vol. 42, no. 10, pp. 3359–3361, 2006.

[200] M. Vazquez, Y.-F. Li, and D.-X. Chen, "Influence of the sample length and profile of the magnetoimpedance effect in fecrsibcunb ultrasoft magnetic wires," *Journal of applied physics*, vol. 91, no. 10, pp. 6539–6544, 2002.

[201] F. Qin, H. Peng, and M. Phan, "Wire-length effect on gmi in co70.3fe3.7b10si13cr3 amorphous glass-coated microwires," *Materials Science and Engineering: B*, vol. 167, no. 2, pp. 129–132, 2010.

[202] D. Park, E. Moon, Y. Rheem, C. Kim, and J. Hong, "The gmi profiles of surface-removed amorphous ribbon," *Physica B: Condensed Matter*, vol. 327, no. 2, pp. 357–359, 2003. Proceedings of the International Symposium on Advanced Magnetic M aterials.

[203] F. Amalou and M. Gijs, "Giant magnetoimpedance of chemically thinned and polished magnetic amorphous ribbons," *Journal of Applied Physics*, vol. 90, no. 7, pp. 3466–3470, 2001.

[204] M. Knobel, C. Gómez-Polo, and M. Vázquez, "Evaluation of the linear magnetostriction in amorphous wires using the giant magnetoimpedance effect," *Journal of Magnetism and Magnetic Materials*, vol. 160, pp. 243–244, 1996.

[205] C. Garcia, A. Zhukov, V. Zhukova, M. Ipatov, J. Blanco, and J. Gonzalez, "Effect of tensile stresses on gmi of co-rich amorphous microwires," *IEEE Transactions on Magnetics*, vol. 41, no. 10, pp. 3688–3690, 2005.

[206] L. Kraus, "The theoretical limits of giant magneto-impedance," *Journal of Magnetism and Magnetic Materials*, vol. 196-197, pp. 354–356, 1999.

[207] D. Li, Z. Lu, and S. Zhou, "Induced magnetic anisotropy and stress-impedance effect in nanocrystalline$hboxfe_7$3.5$hboxcu_1hboxnb_3hboxsi_1$3.5$hboxb_9$ribbons," *IEEE Sensors Journal*, vol. 6, no. 4, pp. 924–927, 2006.

[208] S. Yoon, S. Yu, G. Ryu, and C. Kim, "Effect of annealing on anisotropy field in fe 84 zr 7 b 8 cu 1 amorphous ribbons evaluated by giant magne-

toimpedance," *Journal of applied physics*, vol. 85, no. 8, pp. 5432–5434, 1999.

[209] Z. Guo, X. Yang, X. Liu, J. Ou-Yang, B. Zhu, S. Chen, and Y. Zhang, "Electric field induced non-90° rotation of the easy axis of a ferromagnetic film," *Applied Physics Letters*, vol. 112, no. 5, p. 052904, 2018.

[210] C. Zhao, X. Zhang, Q. Liu, and J. Wang, "Gmi field sensitivity near a zero external field in co-based amorphous alloy ribbons: experiments and model," *Journal of Physics D: Applied Physics*, vol. 49, p. 065006, jan 2016.

[211] S. Mansourian, A. Bakhshayeshi, and R. T. mendi, "Giant magneto-impedance variation in amorphous cofesib ribbons as a function of tensile stress and frequency," *Physics Letters A*, vol. 384, no. 26, p. 126657, 2020.

[212] G. H. Ryu, S. C. Yu, C. G. Kim, and S. S. Yoon, "Evaluation of anisotropy field in amorphous fe71+xnb7b22x alloys by gmi measurement," *Journal of Magnetism and Magnetic Materials*, vol. 215-216, pp. 359–361, 2000.

[213] M. Knobel, M. L. Sanchez, J. Velazquez, and M. Vazquez, "Stress dependence of the giant magneto-impedance effect in amorphous wires," *Journal of Physics: Condensed Matter*, vol. 7, p. L115, feb 1995.

[214] N. Bayri and S. Atalay, "Giant stress-impedance effect in fe71cr7si9b13 amorphous wires," *Journal of Alloys and Compounds*, vol. 381, no. 1, pp. 245–249, 2004.

[215] M. Moradi, A. Dadsetan, S. M. Mohseni, and A. J. Gharehbagh, "Magnetoimpedance and field sensitivity of cofesib amorphous ribbons under

applied tensile stress," *Journal of Superconductivity and Novel Magnetism*, vol. 28, no. 7, pp. 2059–2062, 2015.

[216] B. Kaviraj and S. Ghatak, "Influence of stress on magneto-impedance in co71xfexcr7si8b14 (x=0, 2) amorphous ribbons," *Journal of Materials Processing Technology*, vol. 202, no. 1, pp. 119–124, 2008.

[217] J. Hu, H. Qin, J. Chen, and Y. Zhang, "Giant stress-impedance effect in fe73.5cunb3xvxsi13.5b9 amorphous ribbons," *Journal of Magnetism and Magnetic Materials*, vol. 266, no. 3, pp. 290–295, 2003.

[218] P. Pan, R. D. Moorehead, and T. J. Hayward, "Influence of geometry on the giant magnetoimpedance of high-aspect ratio amorphous magnetic ribbons," *Journal of Applied Physics*, vol. 128, no. 17, p. 174504, 2020.

[219] A. Bushby, N. Tarakina, and N. Gavara, "Lecture: Mat400 - structural characterisation, week 2 - diffraction," *Queen Mary Univeristy of London (QMUL), School of Enginering and Materials Science (SEMS)*, p. 18, 2015.

[220] "D2 phaser - dataquality."
https://d2phaser.com/en/126-dataquality.
Accessed: 17-Oct-2021.

[221] A. Bushby, N. Tarakina, and N. Gavara, "Lecture: Mat400 - structural characterisation, week 3 - diffraction," *Queen Mary Univeristy of London (QMUL), School of Enginering and Materials Science (SEMS)*, p. 43, 2015.

[222] B. Cullity, *Elements of X-ray diffraction*. Addison-Wesley Publishing Company, Inc., 1957.

[223] X. Sun, J. Du, Z. Zhu, J. Wang, and Q. Liu, "Enhanced gmi effect in nizn-ferrite-modified fe-based amorphous ribbons," *Applied Physics A*, vol. 119, no. 4, pp. 1277–1281, 2015.

[224] I. Kozlov, G. Elmanov, K. Prikhodko, L. Kutuzov, B. Tarasov, V. Mikhalchik, R. Svetogorov, V. Mashera, E. Gorelikov, and S. Gudoshnikov, "The evolution of structure and magnetoimpedance characteristics of amorphous co69fe4cr4si12b11 microwires under heat treatment," *Journal of Magnetism and Magnetic Materials*, vol. 493, p. 165681, 2020.

[225] Y. Ding, R. Tian, K. Xue, X. Wang, Y. Shi, and X. Ma, "Impact of ribbon width on magnetoimpedance and permeability of fe69.2co7.7cu0.6nb2.5si11b9 soft magnetic alloy," *Materials Technology*, vol. 31, no. 6, pp. 337–341, 2016.

[226] T. Eggers, D. Lam, O. Thiabgoh, J. Marcin, P. Švec, N. Huong, I. Škorvánek, and M. Phan, "Impact of the transverse magnetocrystalline anisotropy of a co coating layer on the magnetoimpedance response of feni-rich nanocrystalline ribbon," *Journal of Alloys and Compounds*, vol. 741, pp. 1105–1111, 2018.

[227] "Atomic force microscope diagram."
https://commons.wikimedia.org/wiki/File:Atomic_force_microscope_block_diagram.svg.
Accessed: 01-Feb-2021.

[228] S. Maghsoudy-Louyeh, M. Kropf, and B. Tittmann, "Review of progress in atomic force microscopy," *The Open Neuroimaging Journal*, vol. 12, no. 1, pp. 86–104, 2018.

[229] A. Bushby, N. Tarakina, and N. Gavara, "Lecture: Mat804 - structural

charachterisation, week 10 - scanning probe microscopy," *Queen Mary Univeristy of London (QMUL), School of Enginering and Materials Science (SEMS)*, p. 58, 2015.

[230] A. Bushby, N. Tarakina, and N. Gavara, "Lecture: Mat804 - structural charachterisation, week 11 - scanning probe microscopy," *Queen Mary Univeristy of London (QMUL), School of Enginering and Materials Science (SEMS)*, 2015.

[231] A. Ruiz, D. Mukherjee, J. Devkota, M. Hordagoda, S. Witanachchi, P. Mukherjee, H. Srikanth, and M. Phan, "Enhanced giant magneto-impedance effect in soft ferromagnetic amorphous ribbons with pulsed laser deposition of cobalt ferrite," *Journal of Applied Physics*, vol. 113, no. 17, p. 17A323, 2013.

[232] "Vibrating sample magnetometry - j. arregi."
http://magnetism.eu/esm/2019/practical/VSM_practical.pdf.
Accessed: 01-Nov-2021.

[233] "Vibrating sample magnetometry - swt physics department."
https://gato-docs.its.txstate.edu/jcr:7543b8ec-f619-49c3-888f-01c3ad13c7da/vsm.pdf.
Accessed: 01-Nov-2021.

[234] "Vsm image."
https://commons.wikimedia.org/wiki/File:VSM_en.svg.
Accessed: 01-Feb-2021.

[235] "Squid magnetometer and josephson junctions."
http://hyperphysics.phy-astr.gsu.edu/hbase/Solids/Squid.htmlc3.
Accessed: 02-Apr-2021.

[236] M. Buchner, K. Höfler, B. Henne, V. Ney, and A. Ney, "Tutorial: Basic principles, limits of detection, and pitfalls of highly sensitive squid magnetometry for nanomagnetism and spintronics," *Journal of Applied Physics*, vol. 124, no. 16, p. 161101, 2018.

[237] G. V. Kurlyandskaya, D. S. Portnov, I. V. Beketov, A. Larrañaga, A. P. Safronov, I. Orue, A. I. Medvedev, A. A. Chlenova, M. B. Sanchez-Ilarduya, A. Martinez-Amesti, and A. V. Svalov, "Nanostructured materials for magnetic biosensing," *Biochimica et Biophysica Acta (BBA) - General Subjects*, vol. 1861, no. 6, pp. 1494–1506, 2017. Recent Advances in Bionanomaterials.

[238] B. Li, A. M. Morsy, and J. Kosel, "Optimization of autonomous magnetic field sensor consisting of giant magnetoimpedance sensor and surface acoustic wave transducer," *IEEE Transactions on Magnetics*, vol. 48, no. 11, pp. 4324–4327, 2012.

[239] C. Zhao, L. Pan, X. Ma, J. Li, Q. Liu, and J. Wang, "Cycle rapid cooling treatment effect on the magnetic properties and giant magnetoimpedance properties of co-based amorphous alloy ribbons," *Journal of Magnetism and Magnetic Materials*, vol. 444, pp. 198–205, 2017.

[240] L. Jin, S. Yoon, P. Kollu, C. Kim, D. Suhr, and C. Kim, "Dependence of gmi profile on size of co-based amorphous ribbon," *Journal of Magnetics*, vol. 12, no. 1, pp. 31–34, 2007.

[241] H. Chiriac, T.-A. Óvári, and C. Marinescu, "Giant magneto-impedance effect in nanocrystalline ribbons," *Nanostructured Materials*, vol. 12, no. 5-8, pp. 775–778, 1999.

[242] A. Zhukov, A. Talaat, M. Churyukanova, S. Kaloshkin, V. Semenkova, M. Ipatov, J. Blanco, and V. Zhukova, "Engineering of magnetic proper-

ties and gmi effect in co-rich amorphous microwires," *Journal of Alloys and Compounds*, vol. 664, pp. 235–241, 2016.

[243] V. Zhukova, M. Ipatov, A. Talaat, J. Blanco, M. Churyukanova, S. Taskaev, and A. Zhukov, "Effect of stress-induced anisotropy on high frequency magnetoimpedance effect of fe and co-rich glass-coated microwires," *Journal of Alloys and Compounds*, vol. 735, pp. 1818–1825, 2018.

[244] A. Zhukov, M. Ipatov, M. Churyukanova, A. Talaat, J. Blanco, and V. Zhukova, "Trends in optimization of giant magnetoimpedance effect in amorphous and nanocrystalline materials," *Journal of Alloys and Compounds*, vol. 727, pp. 887–901, 2017.

[245] G. Kurlyandskaya, S. Shcherbinin, S. Volchkov, S. Bhagat, E. Calle, R. Pérez, and M. Vazquez, "Soft magnetic materials for sensor applications in the high frequency range," *Journal of Magnetism and Magnetic Materials*, vol. 459, pp. 154–158, 2018. The selected papers of Seventh Moscow International Symposium on Magnetism (MISM-2017).

[246] J. Nabias, A. Asfour, and J.-P. Yonnet, "The impact of bending stress on the performance of giant magneto-impedance (gmi) magnetic sensors," *Sensors*, vol. 17, no. 3, p. 640, 2017.

[247] M.-H. Phan, H.-X. Peng, M. R. Wisnom, S.-C. Yu, and N. Chau, "Valve behavior of giant magnetoimpedance in field-annealed co 70 fe 5 si 15 nb 2.2 cu 0.8 b 7 amorphous ribbon," *Journal of applied physics*, vol. 97, no. 10, p. 10M108, 2005.

[248] L. Chen, Y. Zhou, C. Lei, Z.-M. Zhou, and W. Ding, "Effect of meander structure and line width on gmi effect in micro-patterned co-based

ribbon," *Journal of Physics D: Applied Physics*, vol. 42, p. 145005, jun 2009.

[249] W. Lu, Y. Xu, J. Shi, Y. Song, and X. Li, "Soft magnetic properties and giant magnetoimpedance effect in thermally annealed amorphous co68fe4cr3si15b10 alloy ribbons," *Journal of Alloys and Compounds*, vol. 638, pp. 233–238, 2015.

[250] V. Raposo, J. Iniguez, D. Garcia, A. Flores, and M. Vazquez, "Internal magnetoimpedance of amorphous wires," *Digest of INTERMAG 2003. International Magnetics Conference (Cat. No.03CH37401)*, pp. CB–05, 2003.

[251] "Agilent impedance measurement handbook a guide to measurement technology and techniques." Keysight Technologies.

[252] W. Han, D. Li, Z. Lu, S. Zhou, and H. Zhang, "Giant stress-impedance effect in amorphous and current annealed $Fe_{73.5}Cu_1Nb_3Si_{13.5}B_9$ wires," *Journal of Magnetism and Magnetic Materials*, vol. 239, no. 1-3, pp. 567–569, 2002.

[253] L. González-Legarreta, V. Prida, B. Hernando, M. Ipatov, V. Zhukova, A. Zhukov, and J. González, "Magnetoimpedance dependence on width in co66. 5fe3. 5si12. 0b18. 0 amorphous alloy ribbons," *Journal of Applied Physics*, vol. 113, no. 5, p. 053905, 2013.

[254] S. Zhang, J. Sun, D. Xing, F. Qin, and H.-X. Peng, "Large gmi effect in co-rich amorphous wire by tensile stress," *Journal of Magnetism and Magnetic Materials*, vol. 323, no. 23, pp. 3018–3021, 2011.

[255] P. Pan and T. Hayward, "Comparative study of the giant stress impedance behavior of commercial amorphous ribbons for strain

sensing applications," *Journal of Applied Physics*, vol. 131, no. 21, p. 214503, 2022.

[256] "Cobalt/silicon/boron/iron/nickel foil - technical information." http://www.goodfellow.com/.
Accessed: 09-Oct-2019.

[257] M. Miglierini and M. Hasiak, "Impact of ion irradiation upon structure and magnetic properties of nanoperm-type amorphous and nanocrystalline alloys," *Journal of Nanomaterials*, vol. 2015, 2015.

[258] H. Song and D.-g. Park, "Dependence of the giant magnetoimpedance on electron irradiation for bio-sensor design," *Journal of the Korean Physical Society*, vol. 61, no. 10, pp. 1641–1645, 2012.

[259] J. Devkota, N. T. Huong, H. Srikanth, and M.-H. Phan, "Magnetoimpedance-based probe of various concentrations of corrosive chemicals," *IEEE Transactions on Magnetics*, vol. 50, no. 6, pp. 1–4, 2014.

[260] M. Sartorelli, M. Knobel, J. Schoenmaker, J. Gutierrez, and J. Barandiarán, "Giant magneto-impedance and its relaxation in co–fe–si–b amorphous ribbons," *Applied physics letters*, vol. 71, no. 15, pp. 2208–2210, 1997.

[261] M. Li, Y. Pei, Y. Cao, S. Chen, and X. Guo, "Flexible strain sensors: from devices to array integration," *Flexible and Printed Electronics*, vol. 6, p. 043002, nov 2021.